The role of oceanic mesoscale in the tropical Atlantic Ocean on salinity and air-sea CO2 flux

Léa Olivier

To cite this version:

Léa Olivier. The role of oceanic mesoscale in the tropical Atlantic Ocean on salinity and air-sea CO2 flux. Earth Sciences. Sorbonne Université, 2023. English. NNT : 2023SORUS149 . tel-04166813

HAL Id: tel-04166813
https://theses.hal.science/tel-04166813v1

Submitted on 20 Jul 2023

THESE DE DOCTORAT DE SORBONNE UNIVERSITÉ

École doctorale : 129 - Sciences de l'Environnement d'Île-de-France

Spécialité: Océanographie physique

Présentée par

Léa OLIVIER

Pour obtenir le titre de

DOCTEUR DE SORBONNE UNIVERSITÉ

Role de la méso-échelle dans l'océan Atlantique tropical sur la salinité et les flux air-mer de CO_2

Soutenance prévue le 28 Février 2023

Composition du jury :

M.	Laurent BOPP	Président
Mme.	Dorothee BAKKER	Rapportrice
M.	Peter BRANDT	Rapporteur
M.	Peter LANDSCHÜTZER	Examinateur
Mme.	Sabrina SPEICH	Examinatrice
Mme.	Jacqueline BOUTIN	Directrice de thèse
Mme.	Nathalie LEFÈVRE	Co-directrice de thèse
Mr.	Gilles REVERDIN	Invité

Laboratoire d'Océanographie et du Climat: Expérimentation et Approches Numériques

Scientific activities during this PhD

Teaching at Ecole normale supérieure

- Master 1 and 2 "Geophysical Fluid Dynamics" (course referent: Vladimir Zeitlin)
- Master 1 "Physical Oceanography" (course referent: Sabrina Speich)
- License 3 "Introduction to Dynamical Oceanography" (course referent: Sabrina Speich)
- Master 1 and 2 "Dynamical Meteorology" (course referent: Caroline Muller)

Oceanographic cruises

- EUREC^{4}A - Carribean - 1 month - 2020
- Tara - Amazone - 1.5 months - 2021
- Tara - Antarctique - 1.5 months - 2022
- SASSIE - Arctic - 1 month - 2022

Outreach

- Tara Education: Three sessions with middle-school classes to present oceanography and sensibilise to climate change
- Strasbourg Science Congress: presentation to 100 middle school and high-school students from 11 different structures in Alsace on the ocean and the climate
- Festival Culture Océan: Member of the roundtable on life and science on board the schooner Tara. Responsible of the plancton discovery workshop, were we educated the public to the micro-organism living in the water from microscope phytoplancton activities.
- Académie du Climat: presentation on the ocean and climate to high school students from all over the Ile de France region.

Publications

- **Olivier L**., Reverdin, G.,Boutin, J., Laxenaire,R.,Iudicone,D.,Pesant,S., ... & Speich, S. (2022). Late summer northwestward Amazon plume pathway under the action of the North Brazil Current rings. Under review in Journal of Geophysical Research: Oceans.
- **Olivier L**., Boutin, J., Reverdin, G., Lefèvre, N., Landschützer, P., Speich, S., ... & Wanninkhof, R. (2022). Wintertime process study of the North Brazil Current rings reveals the region as a larger sink for CO_2 than expected. Biogeosciences, 19(12), 2969-2988.
- **Olivier L**, Reverdin G, Hasson A, Boutin J. Tropical Instability Waves in the Atlantic Ocean: investigating the relative role of sea surface salinity and temperature from 2010 to 2018. Journal of Geophysical Research: Oceans. 2020 Dec;125(12):e2020JC016641.
- Reverdin G, **Olivier L**, Foltz GR, Speich S, Karstensen J, Horstmann J, Zhang D, Laxenaire R, Carton X, Branger H, Carrasco R. Formation and evolution of a freshwater plume in the northwestern tropical Atlantic in February 2020. Journal of Geophysical Research: Oceans. 2021 Apr;126(4):e2020JC016981.
- Reverdin G, **Olivier L**, Cabanes C, Boutin J, et al. Argo floats profiling in the Amazon river plume. (2022). To be submitted to Journal of Atmospheric and Oceanic Technology.
- Stevens, B., Bony, S., Farrell, D., Ament, F., Blyth, A., Fairall, C., Karstensen, ...,**Olivier L**, et al. , 2021. EUREC 4 a. Earth System Science Data, 13(8), pp.4067-4119. Vancouver

- Boutin J, Reul N, Köhler J, Martin A, Catany R, Guimbard S, Rouffi F, Vergely JL, ..., **Olivier L**, et al. Satellite-Based Sea Surface Salinity Designed for Ocean and Climate Studies. Journal of Geophysical Research: Oceans. 2021 Nov;126(11):e2021JC017676.

Conferences

- PIRATA - Tropical Atlantic Variability, 2020, online (oral)
- EGU General Assembly, 2021, online (oral)
- ICOS, 2021, Reims, France (oral)
- ESA: Ocean Carbon from Space, 2022, online (poster)
- Ocean Sciences Meeting, 2022, online (oral)
- Ocean Salinity Conference, New-York, US (oral - online)

Résumé

L'océan Atlantique tropical contrôle les échanges d'un hémisphère à l'autre et est un lieu de fortes interactions avec l'atmosphère. Cinq des plus grands fleuves du monde s'écoulent dans cet océan et la zone de convergence intertropicale (ITCZ) y est une source d'intenses précipitations. Cela induit une grande variabilité de la salinité et des flux air-mer de CO_2. Alors que l'océan global est un fort puits de CO_2, cette région est une source importante de CO_2 en raison des eaux profondes riches en carbone inorganique qui remontent à la surface au niveau de l'équateur. Cependant, ce phénomène est atténué par le panache de l'Amazone, dont les eaux douces sont pauvres en carbone inorganique, riches en nutriments et favorisent le développement du phytoplancton. C'est dans ce cadre que se propagent les ondes tropicales d'instabilité (TIW) et les anneaux du courant Nord Brésil (NBC), les deux formes de mésoéchelle dominantes de l'Atlantique tropical. L'objectif de ce travail est de décrire et de comprendre la variabilité de la salinité et des flux air-mer de CO_2 associée à la mésoéchelle. Pour cela, des observations in-situ sont couplées à des données satellitaires de salinité, température et chlorophylle-a de surface.

Dans l'Atlantique équatorial, le gradient de salinité entre l'eau douce provenant des précipitations sous l'ITCZ et l'eau salée de l'upwelling équatorial est très fort en mai-juin. Les TIW déforment ce gradient, et l'observation de leur signature en salinité fournit des informations sur leur variabilité saisonnière et interannuelle complémentaires à celles de la température de surface. La salinité couplée à la température détermine les contrastes de densité de surface, ce qui influence l'énergie associée aux TIW. Le gradient horizontal de salinité contribue à la moitié de l'énergie potentielle générée par la déformation du gradient horizontal de densité. Ainsi, les TIW modifient et sont modifiés par les contrastes de salinité dans l'Atlantique équatorial.

Sur le bord ouest du bassin, le panache de l'Amazone induit une variabilité de la salinité encore plus importante que celle observée dans l'Atlantique équatorial. Les anneaux du NBC, tourbillons de 200 km de diamètre, sont des structures très contrastées. Ils piègent les eaux salées et riches en CO_2 du NBC, mais leur rotation advecte l'eau peu salée et appauvrie en CO_2 du panache de l'Amazone. L'eau du panache renforce donc les échanges de CO_2 et de chaleur entre l'océan et l'atmosphère. En février 2020, l'Atlantique tropical nord-ouest est un puits de carbone 10 fois plus fort qu'anticipé, et cela est dû à plus de 40% à l'effet des tourbillons. Leur rôle est double, d'une part ils entrainent le panache qui devient un fort puits de carbone, et d'autre part, ils ne gardent pas la signature de surface riche en CO_2 des eaux qu'ils piègent. La situation en été est très différente de celle en hiver. Le NBC change son orientation de 90° et au lieu de suivre la côte sud-américaine, il s'écoule vers l'Afrique. Il passe au large de l'embouchure du fleuve Amazone, qui a alors un fort débit, et devrait entraîner le panache vers l'est. Cependant, les anneaux du NBC et les vents modifient ce schéma. La formation et la propagation de tourbillons interrompent cette circulation, et les vents favorisent un transport d'eau douce vers le nord-ouest. Ainsi, en août-septembre, alors qu'une part du panache est entrainée vers l'est, une autre part est advectée vers les Petites Antilles. L'été 2021 présente des exemples particulièrement forts de ce phénomène.

Ces travaux montrent l'importance de la méso-échelle océanique pour la compréhension de phénomènes clés, comme la propagation des ondes tropicales d'instabilité, du panache de l'Amazone et le flux de CO_2 dans l'océan Atlantique tropical.

Abstract

The tropical Atlantic Ocean (TAO) controls exchanges from one hemisphere to the other and is a place of strong interactions with the atmosphere. The TAO is home to five of the world's largest rivers as well as intense rainfall in the intertropical convergence zone (ITCZ). This induces large spatial variability of salinity and of air-sea CO2 flux. While the global ocean is a strong CO2 sink, the TAO is a strong source of CO2 to the atmosphere due to the deep waters rich in inorganic carbon upwelled to the surface at the equator. However, this source is mitigated by the low CO2 concentrations in the Amazon River plume whose freshwater is low in inorganic carbon and favours phytoplankton blooms. It is in this context that propagate the tropical instability waves (TIWs) and the North Brazil current (NBC) rings, the two dominant mesoscale forms in the TAO. The objective of this work is to describe and understand the variability of the surface salinity and CO2 fluxes associated with the mesoscale. In-situ observations collected during cruises and Argo floats are coupled to surface satellite salinity, temperature and chlorophyll-a.

In the equatorial Atlantic the salinity gradient between the fresh water from rainfall under the ITCZ and the salty water of the equatorial upwelling is very strong in May-June. The TIWs strongly distort this gradient, and are therefore particularly well observed in surface salinity. The observation of TIWs in salinity provides complementary information to their observation in surface temperature on their seasonal and interannual variability. Furthermore, salinity does not only play the role of a passive tracer, as together with temperature, it determines the seawater surface density. This affects the energy that allows TIWs to develop and propagate. One of the energy sources is the potential energy generated by the deformation of the density gradient. The effect of salinity on this energy is as strong as that of temperature, which means that by adding the contribution of salinity, the potential energy is doubled. TIWs modify and are modified by the salinity in the equatorial Atlantic.

On the western edge of the basin, the Amazon plume results in even more salinity variability than in the equatorial Atlantic. The NBC rings, eddies that are 200 km in diameter, are highly contrasted structures. They trap the salty, CO2-rich waters of the NBC, but their rotation stirs water from the Amazon plume. The fresh water of the plume enhances the exchanges of CO2 and heat with the atmosphere. The northwestern TA in February 2020 was found to be a CO2 sink 10 times stronger than expected, and more than 40% of this flux is due to the effect of eddies. Their role is twofold, on the one hand they stir the plume which becomes a strong carbon sink, but also, they do not retain the CO2-rich surface signature of the waters they trap, and instead often stir freshwater filaments. The situation in summer is very different from the one in winter. The NBC changes its orientation by 90° and instead of following the South American coastline, it flows towards Africa. The NBC passes the mouth of the Amazon that is close to its maximum discharge and advects the plume eastwards. However, the NBC rings and the winds change this classical pattern. The formation and propagation of eddies make the plume discontinuous, and the winds favour a northwestward transport of fresh water. Thus, in August -September, whereas part of the plume indeed flows eastwards, another part is advected towards the Lesser Antilles. Particularly strong examples of this were observed in late summer 2021.

This work shows the importance of the oceanic mesoscale for understanding key phenomena, such as the propagation of the TIWs and of the Amazon plume and the TAO carbon budget.

Contents

GENERAL INTRODUCTION 1

DATA AND METHODS 27

List of Figures

GENERAL INTRODUCTION

Introduction 1

1.1 Ocean circulation

Powered by the sun, the ocean is constantly moving intricate patterns. Due to the spheric shape of the Earth, more solar energy arrives in the equatorial band than at the poles. It creates large temperature gradients between the poles and the equator. It is the role of winds and currents, i.e. the oceanic and atmospheric circulation, to redistribute this heat excess around the globe. In addition, the Earth is a rotating sphere, and this geometry generates the swirling ocean currents patterns. The ocean is a complex system. Some currents flow at the surface, while others flow in the deep ocean. Some of them flow on short distances, some other cross entire basins. But what make ocean currents flow?

The circulation at large temporal and spatial scales, characterised by the transport of heat from the low latitudes to the higher latitudes and involving return flows at depth all over the world's ocean is called the Meridional Overturning Circulation (MOC). The thermohaline part of the MOC is driven by the changes of salinity and temperature, the two variables that control density through the equation of state. The solar radiation induces changes in the water temperature while salinity varies with freshwater fluxes, such as rainfall, ice melt and river runoff. This circulation is slow, connects all the ocean basins and ventilates the deep layers by allowing movements between the surface and the bottom. It sets the ocean at the heart of the climate system, by storing heat and carbon though exchanges with the atmosphere. In regions of convection and deep water mass formation, such as the North Atlantic and the Weddell and Ross seas, the surface waters sink to the bottom of the ocean and store carbon on long time scales, while driving the deep part of the MOC. The ocean is the largest carbon reservoir, and on large time scales it determines the atmospheric concentration of carbon dioxide (CO_2). Human activities have raised the atmospheric CO_2 concentration by 132 ppm since the beginning of the pre-industrial era (Friedlingstein et al., 2020). Changes in atmospheric CO_2 have large effects on the planetary climate (as indicated by the geologically recent past) and the ocean contributes to mitigating these changes by pumping CO_2 from the surface to the depths, where it can remain for hundreds of years. The properties (temperature, salinity) acquired at the surface therefore reflects exchanges of energy, carbon and salt.

The ocean and the atmosphere are components of a coupled system. By forcing winds, the sun forces the wind driven oceanic circulation. The wind's energy is transferred to the ocean upper layer through friction. The wind driven circulation is fast and represents most of the surface component of the MOC. The winds and the density, through the heat and freshwater fluxes, are therefore the two driving mechanisms of the large-scale oceanic circulation (figure 1.1). Large-scale currents, such as the Gulf stream, flow across basins over more than 5000 km and are mostly organised in large gyres (tropical, subtropical and subpolar gyres).

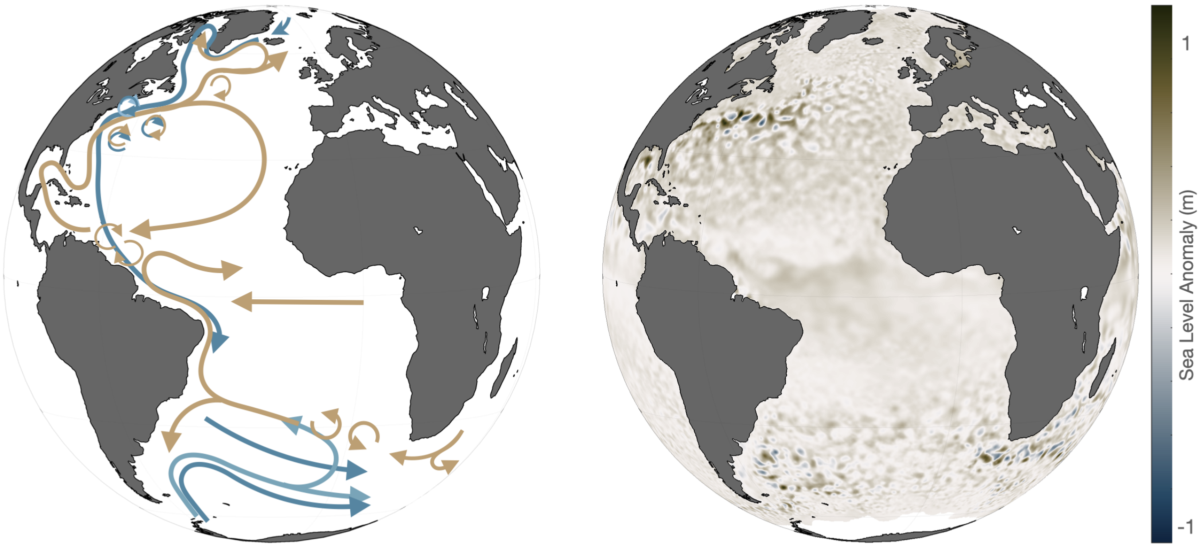

Figure 1.1: On the left, large scale circulation in the Atlantic Ocean. Warm (cold) flows are coloured in orange (blue). On the right, mesoscale circulation in the tropical Atlantic from a snapshot of altimetric sea level anomaly on August, 27th 2021.

1.2 Mesoscale dynamics

The oceanic circulation is nevertheless very diverse and happens at a continuum of scales, from basin wide currents to small filaments (Figure 1.1). The eddies, waves, currents and fronts that forms the mesoscale class of phenomena occur on spatial scales of tens to hundreds of kilometres.

1.2.1 A rapid history of mesoscale observations

The first Greek sailors who ventured into the unknown waters of the western Mediterranean poetically expressed the dangers they faced. In the Odyssey (Homer, VIII century BC), Circe says to Odysseus: "There, under a wild fig tree, which, laden with thick foliage, casts a dark shadow over the sea, dwells the dreaded Charybdis; there she opens her devouring mouth: three times a day she swallows up the black waves, and three times she vomits them up with horrible roars. Woe to you if your ship should approach her, when the torrents are lost in this abyss; when Neptune would take you out of it, Neptune himself would fail". In fact, Charybdis is the imperfect personification of an eddy and tides, while Scylla is, according to a frequent interpretation, a rock or a reef (Figure 1.2).

Myths and legends participate in creating the confusion between eddies and oceanic whirlpools, but still hold part of the truth and show that mesoscale phenomena are ubiquitous features of the ocean circulation.

Figure 1.2: Two creatures surrounded by large waves: Scylla (right) and Charybdis (left). Oil on canvas, by Ary Renan, 1894

After the Challenger expedition in the 1870s, oceanography in a scientific context developed strongly, driven by the work of the Bjerknes (Bjerknes et al., 2013), Nansen's expeditions and the "Bergen School" (including H. Solberg, W. Ekman, H.U. Sverdrup and C.G. Rossby). In 1909, Bjørn Helland-Hansen and Fritjof Nansen summarised years of observations and oceanographic cruises in the pioneering book "The Norwegian Sea". They noticed apparent irregularities in the horizontal distribution of temperature, salinity, and density. The equilines (isotherms, isohalines, as well as isopycnals) formed bends or undulations like waves, sometimes great, sometimes small. This study is of crucial importance, and is the first to dismantle the theory of a stationary ocean circulation. Helland-Hansen and Nansen could not solve the problem of the exact nature and mode of formation of these "waves" and their movements at the time of their observations, but they demonstrate how these "irregularities" may be formed in three different ways: (1) by "waves, of some kind, on the boundary between water-strata of different densities; (2) by sudden variation or direction of the surface currents; (3) by great vortex movements or horizontal movements with vertical axes, as shown by the sections of the Lofoten." Helland-Hansen and Nansen are the first to observe the ocean mesoscale variability, that they represented in figure 1.3. At the time, the underlying theory was the one of a steady ocean circulation. Therefore, most of the time differences between stations were attributed to the difference in station position, not the difference in station time. Almost 30 years later observations by Iselin and colleagues in 1936 in the Gulf Stream showed repeated temperature anomalies that were not coherent with the position of the current and were later attributed to the Gulf stream rings. In the 1950s the meandering of the Gulf Stream is well established, and the multiple ship operation CABOT under the leadership of Fritz Fuglister demonstrated the shedding of a cold-core eddy (Fuglister and Worthington, 1951). Swallow, building on an idea of Stommel, demonstrated thanks to the now called Swallow buoyant floats (Swallow, 1955, ancestor of the Argo float) that variability at mesoscale in space and time was not confined to boundary current, but was present everywhere (Munk, 2002).

During the second half of the XXth century, mesoscale eddies have been observed in most of the boundary currents, such as the Kurushio (Uda, 1938), the Agulhas (Duncan, 1968) and the East Australian current (Hamon, 1965) as well as in the Antarctic Circumpolar current (Savchenko et al., 1978). It is partly the advent of satellite oceanography in the 1980s that revealed the ubiquity of mesoscale phenomena (gyres, eddies, jets, fronts, meanders).

In 1992 U.S./French altimetry satellite TOPEX/Poseidon was launched, and together with Geosat (launched in 1985) revolutionised the way the ocean is studied by revealing for the first time how transient phenomena that affect the seas. Walter Munk considered it "the most successful ocean experiment of all times" (Munk, 2002). Since then, oceanography has made numerous progress, and the measurement of ocean topography from space is still one of the most important data, fuelling intense research on the large, meso and sub-meso scales of the ocean. It has recently been completed by satellite sea surface salinity (SSS), that brings new information on the characteristics of these features, and their role in the global circulation, air-sea exchanges and water cycle. The first observation of eddies in SSS were also the gulf steam rings, showing that cold-core eddies are also fresh, and that this salinity signal is not dampen by short-therm air-sea exchanges and so sometimes easier to detect (Reul, Chapron, et al., 2014).

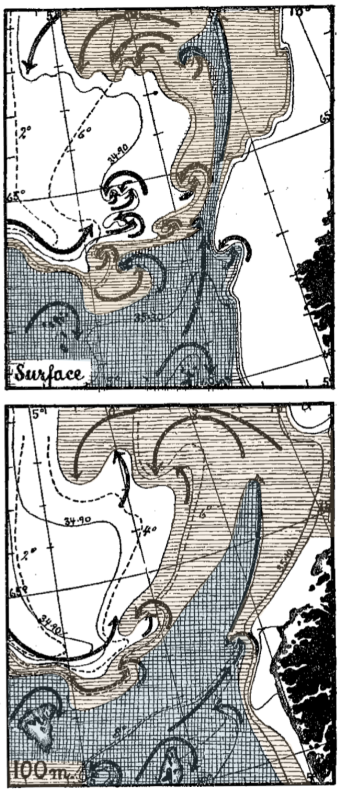

Figure 1.3: Horizontal Distribution of Salinity and Temperature and possible Vortex Movements, May-June, 1904. Yellow single hatching for salinity from 35.0-35.2; blue cross hatching for salinity above 36.2. Extracted from Helland-Hansen and Nansen, 1909's figure 37 and coloured.

1.2.2 Background informations

Mesoscale phenomena are omnipresent in the ocean. They are so important that the mesoscale energy exceeds the one of the mean flow by an order of magnitude or more (Wyrtki et al., 1976, Richardson, 1983).

Dynamically, they are in many ways the oceanic counterpart of the atmospheric weather. Mesoscale motions are in approximate geostrophic and hydrostatic balance, that however breaks down close to the equator. They are commonly formed by instability processes of the background currents and ocean density structure. Mesoscale flows occur within a continuum of scales. On the one end of the spectrum they are bounded by the large scale, which sets the mean gradients from which eddies or waves are generated. At the other end of the spectrum, they are bounded by the submesoscale, where motions are also significantly influenced by rotation and stratification, but ageostrophic effects remain important in the balance of forces.

The length of mesoscale processes is intimately related to the first baroclinic Rossby radius of deformation (or near the equator, an equivalent equatorial scale). It represents the scale of baroclinic variability beyond which internal vortex stretching is more important than relative vorticity. It is strongly related to the main length scale of unstable waves in a stratified shear flow (Chelton et al., 1998). There is therefore a strong variation in the length scale of mesoscale processes with latitude. The Coriolis force is weak in the vicinity of the equator, so the Rossby radius reaches hundred of kilometres. On the contrary, near the poles, the mesoscale processes are rather on the order of tens of kilometres.

Mesoscale structures move in their environment. When they are not advected by an underlying current, it can be observed and shown theoretically that except very close to the equator most of them move toward

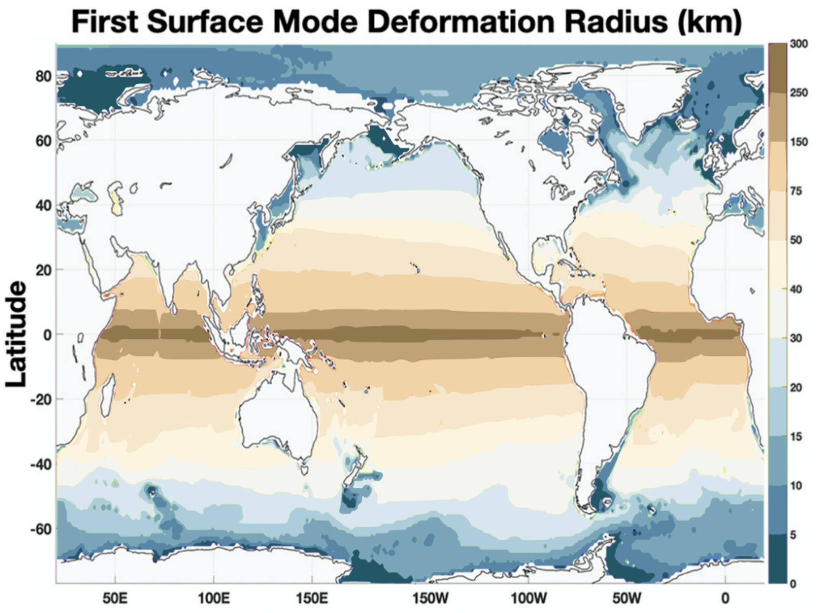

Figure 1.4: Map of the first baroclinic radius of deformation (Rossby Radius). Adapted from LaCasce and Groeskamp, 2020

the west (Nof, 1981, Cushman-Roisin et al., 1990, Chelton et al., 2011) due to the intensity of the coriolis force changing with latitude (beta effect). This is the case for most waves and for eddies. A small initial zonal movement leads to a meridional displacement of the surrounding water. The surrounding water will therefore gain or lose relative vorticity to compensate for the change of planetary vorticity and to conserve potential vorticity.

1.2.3 Impact of mesoscale features

Mesoscale structures strongly influence their surroundings in many ways. At the surface, two mechanisms dominate, called water stirring and trapping. While waves mainly stir water (non-linear waves can also induce transport), non-linear eddies, i.e. eddies whose speed of rotation is faster than their travelling speed, can also trap water in their core.

Stirring

Eddies, waves and fronts generate strong horizontal advection that stir their surrounding along the same density level (isopycnal surfaces). This stirring impacts basin-scale tracer distributions, such as heat, salt, nutrients and influences physical and biological systems. It is a strong source of phytoplankton patchiness in the ocean (Martin, 2003), that can strongly influence ecosystem stability, diversity, dynamics and regional productivity (Steele, 1974; Hobson, 1989; Martin et al., 2002). This mechanism is detailed on Figure 1.5 for the example of an eddy or a wave stirring water along a front or a strong gradient.

Trapping

Non-linear eddies, can trap water in their core. They are important in the transport of hydrological or biogeochemical properties, such as heat, salt and CO_2 when they can carry them over a long time and for large distance, before mixing them in the environment. Eddies can be formed by a meandering large scale current, such as the Gulf Stream. The extreme case of a meandering current is a retroflecting current (the current turns back on itself in a tight loop), as is the case for the Agulhas and North Brazil Currents. The pinching of the retroflection forms an eddy that carries the properties of the watermass it was formed in, that can then travel in another environment (Figure 1.5).

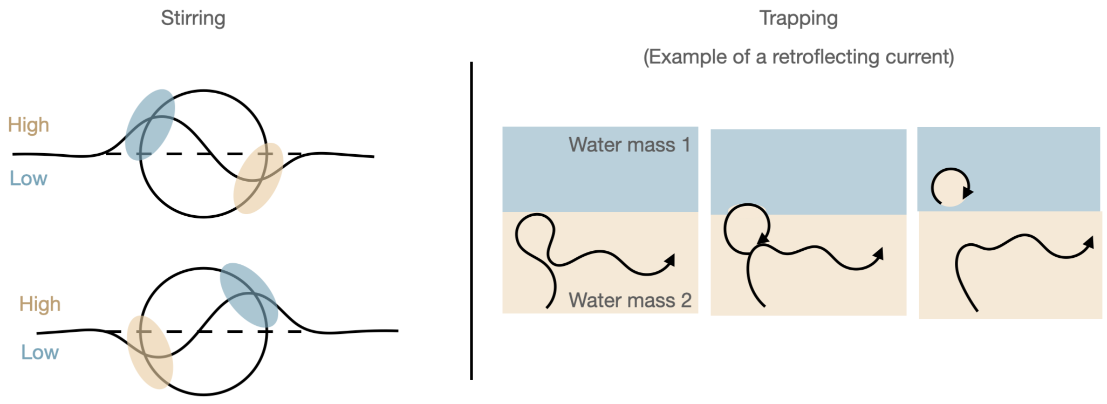

Figure 1.5: Schematics showing how eddies trap and stir water, adapted from Chelton et al., 2011

Impacts

Through these two mechanisms (and others, such as eddy pumping, see McGillicuddy (D. J. McGillicuddy, 2016), for a full review of eddy processes influence on biology), mesoscale play a key role on the physics, biogeochemistry and biology of the ocean at many scales. In 2008, McWilliams gave an extensive list of the eddy roles identified from models: they help to the maintenance of boundary and equatorial currents, they contribute to the lateral and vertical buoyancy fluxes and to the kinetic and available potential energy conversion, they disperse, mix and advect the ocean properties; they provide dissipation routes through energy cascades; they contribute to the surface-layer density stratification and to the biological pumping and quenching; they help the ventilation and subduction of water masses, they form fronts, they exert a topographic form stress, and finally they generate intrinsic climate variability. In the following part, we will present in more details some of these impacts.

Mesoscale processes are known to explain most of the total kinetic energy in the ocean (Ferrari & Wunsch, 2009). Through energy dissipation, mixing and transport, they influence the physical properties of the ocean on a large range of scales. They are crucial to understand and to better characterize their role on the Atlantic part of the meridional overturning circulation AMOC for example, as eddies strongly contribute to the meridional transport of heat (Zhao et al., 2018) and salt (Treguier et al., 2012) in the North Atlantic. The mixing induced by the ocean mesoscale impacts the local dynamics such as the ones involved in the El Nino Southern Oscillation (ENSO) in the equatorial pacific, by explaining part of the interdecadal variability in ENSO amplitude (Gnanadesikan et al., 2017) Mesoscale mixing is also correlated to the main ocean climate variability (ENSO, North Atlantic Oscillation and Pacific Decadal Oscillation, Busecke and Abernathey, 2019).

The near-surface mixed layer is the conduit by which the atmosphere influences the ocean interior. Gaube et al. (2019) showed the influence of eddies on the Mixed Layer Depth (MLD) globally, with warm anticyclones deepening the MLD and cold cyclones shallowing the MLD. This deepening of the MLD in winter in some areas is associated to the formation of mode waters (Y. Chen et al., 2022; Kouketsu et al., 2012).The small-scale mixing induced by mesoscale and sub-mesoscale processes also participates in the transformation of the water masses (Groeskamp et al., 2017; Lévy et al., 2012).

As the mesocale circulation explains most of the turbulent dispersion and transport of tracers such as heat and salt in oceanic basins, they influence the interactions between the ocean and the atmosphere. This can happen through the modulation of the MLD, but also directly through the transport of heat anomalies. This impact is particularly strong in the tropics where ocean and atmosphere are tightly coupled. Changes in the surface temperature, due to waves or eddies, have an important effect on the large scale atmospheric circulation from winds to clouds and rainfall (Chelton et al., 2001; Hashizume et al., 2001).

Oceanic mesoscales play a profound role in mixing tracers, not only heat, but also carbon and nutrients (McWilliams, 1985) thereby contributing in regulating regional and global climate. Through their direct impact on the physical ocean properties, they participate in mixing and in the horizontal and vertical advection of biogeochemical properties. The oceanic mesoscale is important for the oceanic carbon cycle but is still poorly understood, especially in the tropical oceans. Processes in the Agulhas Current have been particularly studied. Agulhas rings absorbs and transport anthropogenic carbon, playing a role in the faster acidification of the South Atlantic Central Water (Orselli et al., 2019). Carbon transport by eddies has been observed in the Antarctic circumpolar current (Moreau et al., 2017), where they can also regulate the seasonal iron supply and resulting phytoplankton bloom and carbon drawdown. Globally, isopycnal mixing by mesoscale eddies significantly impacts oceanic anthropogenic carbon uptake (Gnanadesikan et al., 2015). Mesoscales can also bring nutrients in oligtrophic waters, that are then able to influence the new production (fraction of total primary production in surface waters fuelled by externally supplied nutrients) of the region (D. McGillicuddy et al., 1998).

The ocean is the largest habitat on earth, representing 99% of the biosphere (Game et al., 2009). Mesoscale processes happen at scales affecting biological communities, from lower trophic levels (Martin, 2003) to marine mammals (Cotté et al., 2015; Cotté et al., 2007), bird (Scales et al., 2014), fishes (Arostegui et al., 2022) and turtles (Gaube et al., 2017). Through entrainment effects, eddies and waves affect organisms drifting down the food chain. They create and displace frontal zones which can favour the growth of phytoplankton following the upwelling of nutrients present under the mixed layer (Lévy et al., 2012). They disturb the environment, and this spatial heterogeneity influences the stability, diversity, dynamics and regional productivity of ecosystems. A coherent vortex can preserve the diversity of a population by isolating it from the surrounding fluid (Bracco et al., 2000), while a strong front can genetically isolate pelagic populations (Giachini Tosetto et al., 2022). For example, blue sharks that use the Gulf stream anticyclonic eddies to feed on vertically migrating mesopelagic prey during dives (Braun et al., 2019).

"The small-scale of the ocean may hold the key to surprises" (Hewitt et al., 2020). Mesoscale structures are a key part of the global understanding of the ocean, its role on climate and marine life. On long time-scales, recent observations show that the mesoscale variability will increase significantly of 2-5% per decade in eddy-rich regions, while the tropical oceans show a decrease in mesoscale variability (Martínez-Moreno et al., 2022) in response to the increasing anthropic CO_2 forcing. Fronts and eddies are still not well resolved in climate models, while these small processes can play a key role in how the atmosphere and the ocean evolve under a changing climate, challenging the climate models (Hewitt et al., 2020). As an example of the key area identified by the IPCC Sixth Assessment Report (AR6), there is less confidence in the future projection associated with the AMOC. There is therefore a need to better understand the transport of heat and salt in the whole Atlantic, either to better parametrize the models or to push for a direct representation of mesoscale processes. Algulhas rings transport the warm and salty water from the Indian Ocean to the Atlantic, while the North Brazil Current rings transport these salty water masses across the equator.

1.3 The tropical Atlantic Ocean

The tropical oceans are a great part of the climate system as they receive most of the excess heat from the sun. The tropical Atlantic ocean is involved and influenced by the AMOC, driving the exchanges of water from one hemisphere to another. This part of the ocean is highly dynamic, with numerous large scale currents generating a strong variability of oceans properties, such as temperature and salinity at all scales.

1.3.1 Dynamics of the tropical Atlantic Ocean

Circulation

While the Coriolis force organises most of the oceanic circulation in gyre-like pattern, the coriolis force is null at the equator. Currents are therefore mainly dominated by the wind direction and geostrophic compensation. The surface currents in the tropical Atlantic Ocean are among the least sampled in the world's ocean (Ardhuin et al., 2019), mostly because surface drifters are quickly expelled from the region by the divergent currents associated with the Equatorial upwelling (Lumpkin & Garzoli, 2005).

Trade winds dominate the atmospheric circulation in the tropics, and participate in creating a strongly zonal oceanic circulation (Figure 1.6). The South Equatorial Current (SEC) flows westward toward south America

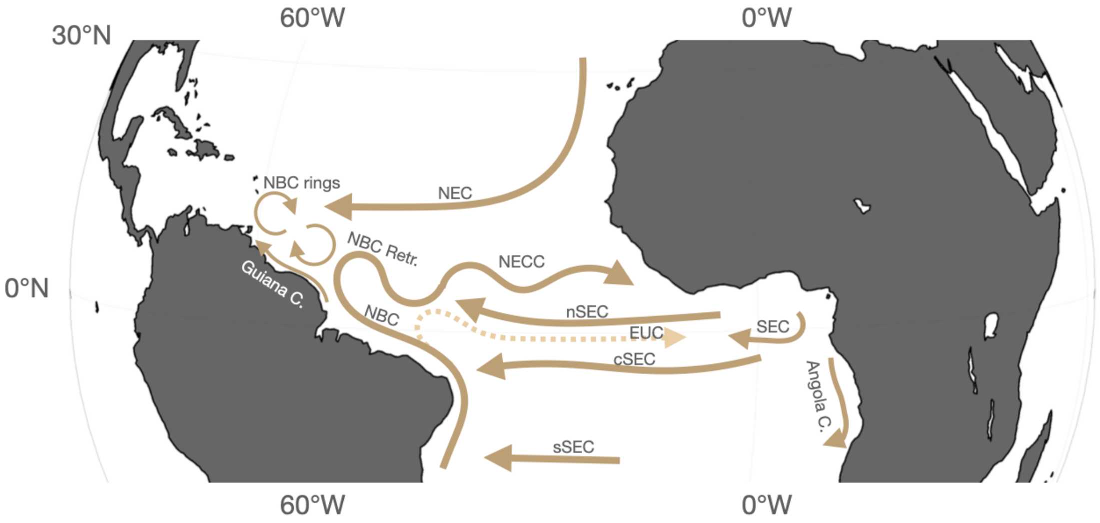

Figure 1.6: Schematic of the oceanic circulation of the tropical Atlantic Ocean, inspired by Lumpkin and Garzoli (2005). NEC: North Equatorial Current, NECC: North Equatorial Counter Current,NBC: North Brazil Current, NBC Retro: NBC Retroflection, SEC: South Equatorial Current, EUC: Equatorial UnderCurrent, nSEC: northern branch of the SEC, cSEC: central branch of the SEC, sSEC: southern branch of the SEC, Angola C: Angola Current, Guiana C: Guiana Current.

and separates to feed two western boundary currents: the Brazil Current to the south, and the North Brazil Current (NBC) to the north.

Stommel (1948) described the western boundary currents as "one of the most striking features of general oceanic wind-driven circulation". The tropical Atlantic western boundary current is quite unique. The NBC flows northward from the South (15°S) to the North (8°N) Atlantic, and extends down to 800 m, carrying surface water down through the Antarctic Intermediate Water. It is continuously fed by the SEC and crosses the equator. Upon crossing the equator, the planetary vorticity changes sign. To conserve potential vorticity the flow must change the sign of its relative vorticity. Part of the NBC retroflects around 2°N and creates the Equatorial UnderCurrent (EUC). The rest of the NBC continues northwestward until it retroflects at approximately 7°N; 48°W and joins the eastward flowing North Equatorial Counter Current (NECC). This flow is easily destabilized and breaks up into eddies (Edwards & Pedlosky, 1998; Jochum & Malanotte-Rizzoli, 2003). These eddies are called the North Brazil Current rings and travel toward the Lesser Antilles, as is the Guiana Current. The EUC and NECC compensate the overpressure on the western side of the basin created by the trade winds. North of the NECC, the westward flowing North Equatorial Current (NEC) bounds the tropical Atlantic circulation and closes the wind-driven north Atlantic gyre.

Seasonal variability

The surface currents in the Tropical Atlantic Ocean display a strong seasonal variability (Molinari, 1983; Reverdin & McPhaden, 1986; Richardson & Reverdin, 1987; Richardson & McKee, 1984), that reflects, in response to seasonally varying wind field, the migration of the Intertropical Convergence Zone (ITCZ, Stramma and Schott, 1999, Lumpkin and Garzoli, 2005).

From spring to summer, as the ITCZ moves northward, so do the zonals NEC and SEC. By the beginning of August, the southeast trade winds reach across the equator and the NBC retroflects eastward into the NECC. In early November, the NECC, current presenting the largest seasonal variation, reaches its maximum seasonal strength. The northern part of the tropical Atlantic circulation is then invigorated, with a strong NECC and a strong NEC, whereas the Guiana Current weakens in mid-August, and strengthens significantly only by late February. From January to April, as the ITCZ moves southward, the NBC retroflection and western NECC weaken. By early April, the retroflection has almost disappeared and the NECC reverses and flows westward, whereas the Guiana current intensifies. In the central Atlantic, the horizontal currents are less sensitive to seasonal variation, but the migration of the ITCZ has strong impacts on the temperature and salinity.

From spring to summer, the ITCZ moves northward, and the trade wind are reinforced close to the equator. It strengthens the Ekman transport driven equatorial upwelling. The waters brought up by the upwelling are cold, saline, rich in nutrients and create the Atlantic "cold tongue". It fertilises a region that is strongly depleted in macronutrients such as nitrogen, phosphate and silicium. The seasonal cycle in the central part of the tropical Atlantic is mainly driven by the position of the ITCZ, where strong precipitations lower the SSS. In the eastern tropical Atlantic, the seasonal cycle of the Congo and Niger is important, with both river discharges peaking in December, and the dry period happening end of spring. On the western side of the basin, the Amazon river has an opposite seasonal cycle, with a maximum discharge in May, and a minimum one in late autumn.

Interannual variability

The modes of interannual variability in the tropical Atlantic is more numerous than in the Pacific Ocean where the ENSO is the single mode of variability. Atlantic Niños, equatorial warm events analogous to ENSO, do occur in the tropical Atlantic as well (Zebiak, 1993). They are also maintained by the Bjerknes feedback involving ocean and atmospheric dynamics, even though their amplitude is much smaller than in the Pacific. In addition to this zonal mode of variability, the tropical Atlantic also presents a meridional one (Chiang & Vimont, 2004; Servain et al., 1999). The Atlantic Meridional Mode (AMM) is characterized by a meridional SST gradient near the ITCZ location; with surface winds that flow toward the warm water anomaly and turn to the right in the northern hemisphere, and a meridional displacement of the ITCZ toward the warmer hemisphere.

This complex interannual variability is still not well understood, and has impact on large scale phenomena such as the intensity of the African monsoon or the tropical cyclone season (Vimont & Kossin, 2007). Moreover, the large-scale ocean dynamics show strong interannual variability that overlaps with the global warming signal and disturbs its detection and attribution. However, the processes that govern this low-frequency variability are still poorly understood for a variety of reasons, including a lack of long-term observations.

1.3.2 The Amazon river

The Amazon is the largest river in the world and one of the most important feature of the tropical Atlantic. The Amazon is fed by the world's largest drainage basin, which spreads over a large part of South America, including Peru, Bolivia, Ecuador, Colombia, Venezuela, Guiana, Suriname, French Guiana and most notably Brazil and covers almost 6 million km^2 (Vörösmarty et al., 2000). The part of the Amazon drainage basin in Brazil alone is larger than any other drainage basin. The Amazon basin receives ~2000 mm of precipitation annually. Most of the basin is therefore covered by the Amazon rainforest, the richest tropical forest in the world in terms of biodiversity (Albert & Reis, 2011). It is home to more than one-fifth of all known species in the world. The Amazon river also supports thousands species of fishes, as well as crabs, dolphins, turtles and algae. In 2016, a unique carbonate reef system of ~ 9500 km^2 was discovered at the mouth of the river, that includes mainly large sponges but also rhodolith beds (Moura et al., 2016). It supports a diverse ecosystem, showing a mixture of estuarine, coastal and oceanic communities (Neumann-Leitão et al., 2018).

Every second, the Amazon delivers about 200 000 m^3 of turbid freshwater rich in nutrients and organic matter, contributing alone to almost 20% of the freshwater inflow to the ocean (Dai & Trenberth, 2002). The discharge of the Amazon is greater than that of the seven other largest rivers combined,and produces a plume that spreads over up to 1.6 millions of km^2, (Coles et al., 2013; Dai & Trenberth, 2002).The Amazon's discharges is minimum in December and increases progressively from January onwards to reach its maximum in May. January to March is therefore the period of minimum extension of the plume, that contrasts with June-July when the plume covers more than 15% of the western tropical Atlantic at that time, with a strong contribution of the Para River discharge.

The Amazon plume modifies the physical, biogeochemical and biological properties of the ocean. The advent of SSS observation from space brought to light many key phenomena and allowed for a better characterisation of the tropical freshwater plumes (Reul, Fournier, et al., 2014; Tzortzi et al., 2013). The difference in water masses between the Amazon plume and the western tropical Atlantic creates a barrier to animal dispersion, it isolates the Caribbean Sea and tropical Brazil ecoregion and spatially structures animal species diversity (Giachini Tosetto et al., 2022). The plume waters brings nutrients and organic matter in a highly oligotrophic region, maintaining a large phytoplankton bloom (Smith & Demaster, 1996). Indeed, as water vertically mixes and turbidity decreases, the primary producer's growth and associated biological drawdown are stimulated (C.-T. A. Chen et al., 2012). Dissolved nitrate is rapidly consumed, and nitrogen fixation by diazotrophs becomes the main pathway of carbon sequestration in the plume (Subramaniam et al., 2008). Far from the mouth, the low salinity associated to the plume explains more than 80% of the primary productivity (Gouveia et al., 2019). This strong carbon drawdown leads to a significant sink of atmospheric CO_2 of global importance, often overlooked (Körtzinger, 2003; Lefévre et al., 2010). Not taking into account the Amazon plume would result in overestimating the tropical Atlantic air-sea CO_2 flux by 10%(Ibánhez et al., 2016). The Amazon plume pathways are driven by the dynamics of the western tropical Atlantic and by the winds. From January to March, the Amazon outflow is low and winds are mainly zonal, they confine the water on the shelf. From April to mid-July, the Amazon outflow reaches its maximum, and the plumes spreads out towards the north-west and reaching the Lesser Antilles Arc and up to 24°N. In mid-July, the NBC) retroflection sets up, and brings the Amazon water toward the East in the NECC) (Coles et al., 2013; Muller-Karger et al., 1988).

Rivers are the link between continent and ocean. They are at the heart of the water cycle and many biogeochemical cycles. The weathering of the rocks and of the soils through which the river flows gives it unique chemical properties, and makes it a natural source of carbon and nutrients to the ocean. Ocean waters from rivers are therefore extremely productive and support ecologically and socially important ecosystems (Biber et al., 2004) They are however highly subject to human influence. Human development in coastal river basins has greatly increased sediment and nutrient loads to coastal waters (Paerl, 1997; Peierls et al., 1991). This leads to deterioration of water quality, loss of habitat and fisheries resources, and to a general decline in the ecological and economic condition of the region (Boesch et al., 2001; Costanza et al., 1997). These impacts are greatly exacerbated by climate change (Paerl & Huisman, 2009), which accentuate the need for understanding and monitoring the Amazon plume waters.

1.3.3 Air-sea exchanges

Air-sea interactions are key for understanding a global climate system, and ocean-atmosphere coupling is the strongest at low latitude. Heat fluxes from the ocean to the atmosphere drives a large part of the global atmospheric circulation. CO_2 fluxes at the surface and carbon export at depth drive the global ocean carbon sink, who absorbs 23% of the carbon emitted in the atmosphere by human activities (Friedlingstein et al., 2020). However, it was very difficult to accurately estimate global air-sea fluxes because of the sparsity of ocean observation data. Near-surface stratification play a key role in controlling these air-sea exchanges.

Stratification

The ocean forms stratified layers with lighter water near the surface and denser water at greater depths. This stable configuration acts as a barrier to mixing of the waters, which has an impact on the efficiency of vertical exchanges of heat, carbon and oxygen among others.

The stratification is determined by the density of the surface layers (vertical density gradient). The properties acquired at the surface such as temperature and salinity are thoroughly mixed vertically by turbulent motions within this layer, called the mixing layer. This create a very homogeneous layer that acts as a bridge between the atmosphere and the deeper parts of the ocean. These two layers are separated by the pycnocline, a thin layer with a very high density gradient, preventing strong vertical exchanges between surface and depth (Fieux, 2019). In the general case, the properties of the mixing layer being homogeneous, the strong density gradient mirrors a strong temperature gradient, the thermocline and salinity gradient, the halocline. In some cases, the temperature and salinity gradient can be observed at distinct depths, where the halocline is shallower than the thermocline. In these circumstances, the salinity controls the stratification, and in addition to the mixing layer there is a barrier layer (BL) between the halocline and the thermocline (Lukas & Lindstrom, 1991). The northwestern tropical Atlantic is a region with very thick and long BLs (Mignot et al., 2012; Mignot et al., 2007). This is in part due to the various and intense sources of freshwater in the tropical Atlantic : the rainfall under the ITCZ and the freshwater input from rivers. The Amazon and the Congo, the two rivers with the highest discharge, flow into the tropical Atlantic, as do the Orinoco ($4^t h$), the Para-Tocantin ($17^t h$) and the Niger ($20^t h$).

In the presence of BL, the surface layer is shallower and well isolated from the deep ocean, which enhances the exchanges between the surface layer and the atmosphere (Vialard & Delecluse, 1998). BLs may contribute to maintain the heat build-up necessary for El Niño development (Maes et al., 2005; Meinen & McPhaden, 2000; Wyrtki, 1975) and thus play an important role on the onset of ENSO events (Maes et al., 2002, 2005). In the tropical Atlantic, it has been showed that BLs can raise offshore SST by 0.5-1°C (Foltz & McPhaden, 2009) and up to 4°C close to the shore (Ffield, 2007). Amazon-influenced SST anomalies are large enough to influence regional precipitation, hurricane frequency and intensity (Vizy & Cook, 2010). BLs are in the path of tropical cyclones, and play a role in the tropical cyclone intensification (Balaguru et al., 2012; Grodsky et al., 2012; Reul, Fournier, et al., 2014).

The tropical Atlantic is a region where surface density can be controlled by both temperature and salinity. This means that the spatial distribution of salinity must be as well known as that of temperature in order to have an accurate estimate of the air-sea exchange in this region. However, the mechanisms responsible for the meso and small-scale variability of salinity in this region are still poorly observed and understood.

Carbon dioxide

The surface conditions impact the exchange of heat but also gases. The ocean plays an important role in the carbon cycle by it's ability to take up CO_2 from the atmosphere, thus reducing the increase of atmospheric CO_2 due to the combustion of fossil fuels by human activities and land use change. The global ocean is taking up 23 % of total anthropogenic CO_2 emissions (Friedlingstein et al., 2020). The ocean anthropogenic carbon storage rates continue to be determined by the ocean sink in response to growing CO_2 emissions (McKinley et al., 2020). Over the last decades, the air-sea CO_2 exchanges got enhanced through the strengthening of the CO_2 partial pressure gradient. The growing CO_2 sink is beginning to drive observable large-scale changes in ocean carbonate chemistry (IPCC 2019, 2021). CO_2 dissolves in sea water and turns into carbonic acid which in turn is transformed into bicarbonate (HCO_3^-) and carbonate ions (CO_3^{2-}). During this chemical reaction, free hydrogen ions (H^+ ions) are released, decreasing the ocean pH. It tremendously impacts shelled organisms and marine calcifying organisms such as coral or some species of plankton (like coccolithophorids). Plankton is at the basis of the food chain, a decrease in its population or a change in its geographical distribution will have huge consequences on the entire global food chain.

The ocean is not homogeneous and the different oceanic regions do not have the same capacity to absorb a portion of the atmospheric CO_2 (Figure 1.7). Globally, the high-latitude surface waters are considered as a sink for the atmospheric CO_2, and the upwelling regions of the low and middle latitudes are rather a source (Landschützer et al., 2014; Takahashi et al., 2009). The divergence created by the winds in upwelling regions such as the equator draws water rich in DIC that releases CO_2 to the atmosphere.

The equatorial Atlantic is indeed the second biggest source of CO_2, after the equatorial Pacific (Landschützer et al., 2014; Takahashi et al., 2009). The biogeochemistry of the tropical Atlantic is complex because it is at the boundary between different biogeochemical regimes and is subject to a strong seasonal variability. The equatorial upwelling generates CO_2 supersaturation over a large area of the equatorial band. It is an observed source of CO_2, notably thanks to ships of opportunity equipped with CO_2 systems and the PIRATA campaigns (Bourlès et al., 2019), but some large, less-well studied areas of the tropical Atlantic surface are characterized by CO_2 undersaturation. It can be associated to freshwater sources to the basin (Amazon, Congo, Niger), and to the SST seasonal changes of the subtropical part of the tropical Atlantic (>10° in latitude).

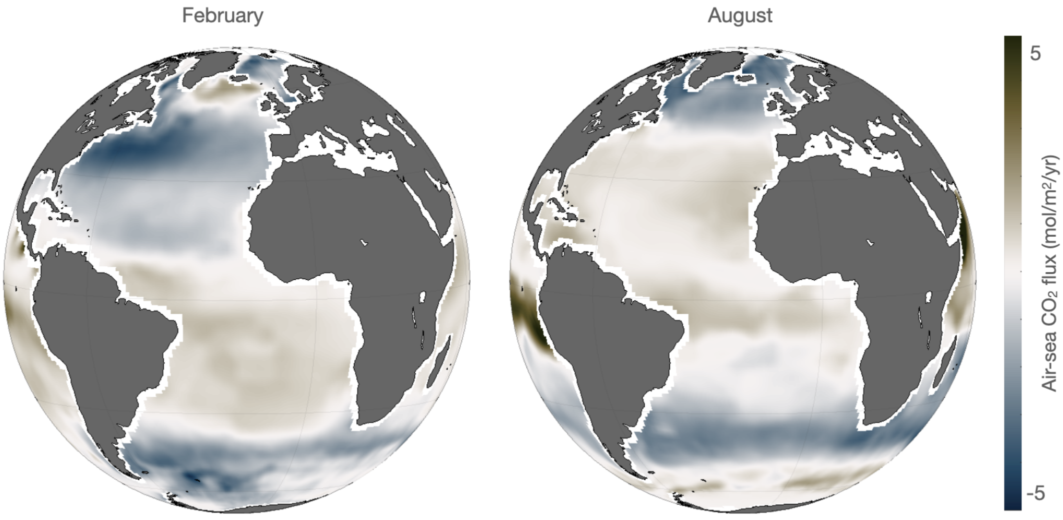

Figure 1.7: Air-sea CO_2 fluxes climatology from Landschützer et al. (2014) in February and August.

Figure 1.7 presents the CO_2 flux climatology for the months of February and August. The equatorial Atlantic outgasses all year long, and the warmer waters in the west of the basin drive higher fluxes (Andrié et al., 1986). The subtropics have a strong seasonal cycle, switching from a sink in winter to a source of CO_2 in summer. The general knowledge based on all observations available is mainly large-scale, and some individual studies have refined this view. A few cruises have reported strong CO_2

undersaturation in the northwestern tropical Atlantic, attributed to the discharge of the Amazon outflow (Körtzinger, 2003; Lefévre et al., 2010). Ibánhez et al. (2016) showed that sea-air CO_2 flux for the tropical Atlantic could be overestimated by about 10% due to neglecting the CO_2 sink associated to the Amazon plume. The high precipitation associated with the presence of the ITCZ also leads to local CO_2 undersaturation, migrating with the ITCZ (Ibánhez et al., 2022; Lefévre et al., 2010; Oudot et al., 1987). There is a strong link between the carbonate chemistry and the sea surface salinity in the tropical Atlantic, due to the omnipresence of freshwater.

The discrepancies between the global climatology and the regional studies rise doubts on current sea-air CO_2 estimations for the basin and the role of the tropical Atlantic in the global sea-air CO_2 exchange. Only by understanding the freshwater pathways, sources, and variability in the tropical Atlantic ocean will we be able to better assess the CO_2 flux of the region. This depends on the large, meso and sub-mesoscale variability of currents, salinity and temperature, that will impact the ones of the biogeochemistry and biology.

The latest IPCC report (2021) highlights that the subtropics and highly variable regions are still large sources of uncertainties, and that the sparsity of data is a problem for understanding the ocean CO_2 sink. Moreover the tropical oceans contribute the most to the global mean interannual variability signal, that is crucial to understand to better untangle the internal variability from the one forced by the increasing CO_2 emissions. Further research is needed to understand the drivers of changes in the CO_2 sink rate, and this implies understanding the mechanisms responsible for the spatial and temporal variability of CO_2, in particular in under-observed regions.

1.3.4 Mesoscale variability in the tropical Atlantic ocean

The mesoscale features of the tropical Atlantic are largely formed by the destabilisation of the large-scale currents in the region, which are located relatively close to the equator. With sizes on the order of several hundred kilometres, they is therefore easier to observe, either from space or by ship, than at high latitudes. The tropical Atlantic is very dynamic, with numerous mesoscale phenomena, and we will focus on two phenomena that dominate the medium-scale variability, the tropical instability waves (TIWs) and the North Brazil Current rings.

Tropical instability waves

The mean circulation in the central tropical Atlantic Ocean is dominated by vigorous zonal currents (Brandt et al., 2006). As the ITCZ migrates northward in boreal spring/summer, the strengthened westerlies intensify the northern branch of the SEC (nSEC) and the NECC. The strong shear between these two currents, and between the SEC and the EUC leads to barotropic instabilities generating tropical instability waves (Philander, 1976, 1978).

These waves were first discovered more than 40 years ago when Düing et al. (1975) in current data records observed fluctuations near the equator in the Atlantic. Two years later, Legeckis (1977) observed with infrared satellite images the undulations of the Pacific cold tongue's temperature front.

The TIWs propagate just off the equator, and distort in cusp like features the strong gradient of temperature and salinity generated by the upwelling (Figure 1.8). They propagate toward the west, with a large wave length of approximately a thousand kilometres, and a period of 20-30 days (Legeckis & Reverdin, 1987; Qiao & Weisberg, 1995; Steger & Carton, 1991).

The TIWs were extensively studied, with models and observations, because of of their strong link with the cold tongue, and therefore their influence over the physical, biogeochemical, biological and atmospheric dynamics of the region.

They contribute in reducing the equatorial shear of the background currents (Weisberg & Weingartner, 1988), and they also contribute in redistributing heat and freshwater through both advection and mixing (Foltz et al., 2020; Hummels et al., 2013; Jochum et al., 2007; Jochum & Murtugudde, 2006; Moum et al., 2009). They cool and bring saline waters to the northern part of the tropics, and warm and freshen the cold tongue, reducing the strong horizontal density gradient created by the equatorial upwelling. The rigorous mixing at the edges of the waves may also explain why the vertical heat flux is the largest during the TIWs period (Moum et al., 2009).

This strong link with the cold tongue results in their seasonal and interannual variability, which although studied, is still only understood at a superficial level. In theory, the seasonality of TIWs follows the one of the cold tongue, forming in spring and weakening at the end of summer, but has mainly been studied in SST only. Regarding their interannual variability, during periods of Atlantic Niño (that is itself linked to the Pacific Niño), the trade winds and the cold tongue are reduced, weakening the TIWs (An, 2008; Im et al., 2012; Perez et al., 2012). The interannual variability of the Atlantic TIWs is more complex than their Pacific counterpart due to the different modes of variability of the equatorial Atlantic, and long time-series are a key element in its understanding (Perez et al., 2012; Tuchen et al., 2022).

Through the modification of the surface stratification, they influence the air-sea coupling that is already particularly strong in the tropics. It has consequences on winds, cloudiness and precipitations (Caltabiano et al., 2005; Chelton et al., 2001; Seo et al., 2007). TIWs warm the mixed layer in the equatorial band (Jochum et al., 2007) and play a crucial role in the heat exchanges between the surface and the deeper ocean (Jochum & Murtugudde, 2006). Indeed, TIWs radiate internal waves, that are energy pathway to turbulent mixing, influencing the thermocline and deeper part of the ocean.

The equatorial Atlantic is considered to be a low-nutrient low-chlorophyll (LNLC) region, which means that nutrients, and in particular nitrogen, are hypothesized to be a factor limiting the phytoplankton growth (Davey et al., 2008; Mills et al., 2004; Moore et al., 2008). Through advection and mixing, TIWs affect the biogeochemistry of the equatorial upper ocean by influencing the distribution of nutrients (Murray et al., 1994; Radenac et al., 2020) and therefore chlorophyll concentration (Jochum et al., 2004; Shi & Wang, 2021; Strutton et al., 2001) and ecosystem distribution (Martinez et al., 2018; Menkes et al., 2002).

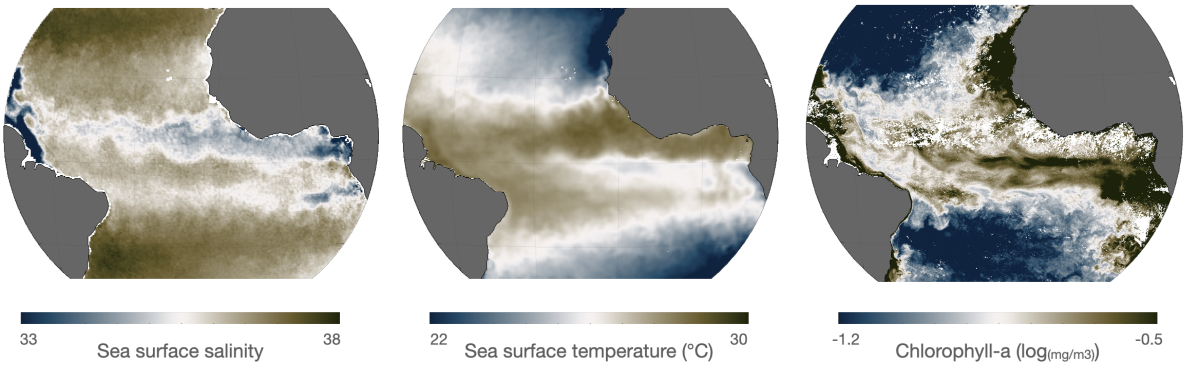

Figure 1.8: From left to right, snapshots of SSS, SST and chlorophyll-a on June $5^t h$, 2017 showing the propagation of TIWs just north of the Equator.

Despite the consensus on the importance of the TIWs, the complexity of these waves and of their environment means that some of their characteristics have not yet been studied. Their formation and maintenance mechanism for example is still investigated. In 2019, a modelling study successfully modelled realistic TIWs in the Equatorial Pacific Ocean, by generating them from an unstable mode resulting from the coupling of two Rossby waves (Tanaka & Hibiya, 2019). The TIWs forms as resonance develops between two equatorial Rossby waves when the background currents slowly increase. Two sources of energy for the TIWs have been evidenced, the kinetic energy associated to the barotropic current shear (de Decco et al., 2018; Kelly et al., 1995; Philander, 1976, 1978) and the potential energy through the baroclinic conversion of the density gradient (Cox, 1980; Grodsky et al., 2005; McCreary Jr & Yu, 1992). The importance attributed to these two sources varies greatly, and this is due to the great limitation in studying baroclinic instabilities. Most observation-based studies (Weisberg & Weingartner, 1988) did not consider the effects of salinity because of the scarcity of observations. Grodsky et al. (2005) based on data from a single mooring showed that salinity contributed to the energetics of the TIWs in the mixed layer. Lee et al. (2014) observed for the first time TIWs in salinity, more than 35 years after their first observation in SST, thanks to the development of satellite salinity and the launch of the SMOS and Aquarius satellites. They supported Grodsky et al. (2005) observation and drew a first estimate of the salinity gradient contribution to the wave's potential energy at basin scale based on unprecedented satellite observations. However, the computation of the energy associated with the waves based solely on surface observations implies strong assumptions on the contribution of salinity and temperature to the density gradient at depth.

While the Atlantic is the best studied ocean basin, the equatorial Atlantic is greatly under-sampled. The equatorial Atlantic is often a cloudy region, due to the strong clouds and precipitations associated to the ITCZ, preventing the infrared monitoring of SST and ocean colour. The SST products have still greatly improved our comprehension of these waves, but to accurately represent the surface stratification, sea surface salinity and numerous measurement (temperature, salinity and currents) at depth are necessary. Currently, only the PIRATA (Bourlès et al., 2019) moorings consistently provide these informations. However, the moorings observations are limited because the TIWs are not the same over the equatorial Atlantic basin (Jochum et al., 2004). The equator is a divergence zone, so the number of profiling float is relatively small, but with time Argo help completing the dataset.

Physical variables are easier to acquire than biology and biogeochemistry, so the lack of data in the equatorial Atlantic is even more acute in these areas. Biogeochemical studies of the TIWs mainly rely on satellite chlorophyll (Jochum et al., 2004; Strutton et al., 2001), and until recently the study by Menkes et al. (2002) was the most recent one delving into the special ecosystem sustained by the TIWs and associated vortices. In the last 3-5 years, progress made on the comprehension of the biogeochemistry of the TIWs and will be discussed in chapter 5.

Much remains to be discovered about TIWs, but in this thesis we focus on the role of salinity, and finally couple salinity and temperature to get a realistic representation of surface density and stratification. It is possible thanks to new higher resolution and long term (10 years) satellite salinity data, coupled with a 10-year database of Argo floats, that will allows us to answer some of the many questions raised. We will focus on describing the seasonal variability of the waves, as well as the interannual variability within the limits of the dataset. Then, we will take into account the role of salinity in the calculation of the cross equatorial density gradient, in this region of the globe where temperature and salinity, for once, have the same effect on density and enhance the density gradient. This study is a first step towards a more complete representation of tropical instability waves, which will also allow a better understanding of the biogeochemical dynamics of the waves because in the equatorial Atlantic, biogeochemistry is strongly coupled to salinity.

NBC rings

On the western side of the tropical Atlantic basin propagates another type of mesoscale feature: the North Brazil Current rings. The NBC rings form off the border between French Guiana and Brazil (Figure 1.9), and slowly spread along the continental shelf to the Lesser Antilles arc.

With a mean diameter of 250 km, that can sometimes exceed 400 km, they are the largest rings of the world. As most eddies, they travel west (see section 2.2), the change of direction of the South American coastline opens up a corridor were they can move north-west despite being formed on the western side of a basin. They follow the shape of the South American coastline with a speed of about 8-15 km per day (Johns et al., 1990; Mélice & Arnault, 2017), and reach the Lesser Antilles where most of them strongly interact with the topography and die, after a journey of 3-4 months (Fratantoni & Richardson, 2006; Jochumsen et al., 2010). The number of rings formed per year vary, some studies estimating 3 to 7 rings a year (Aroucha et al., 2020; Fratantoni & Glickson, 2002; Goni & Johns, 2001; Mélice & Arnault, 2017) and other up to 8-9 rings per year (Johns et al., 2003).

The absence of the Coriolis force at the equator acts as a dynamic barrier, separating the Southern Hemisphere from the Northern Hemisphere.

The NBC rings are formed by the instability of the NBC once this current crosses the equator. To conserve its potential vorticity, the NBC abruptly changes its direction from north-west to east, and curls back in a tight loop, in a similar way to the Agulhas current. This 90° turn is called "retroflection" by Bang (1970) by analogy with the anatomy of mammalian intestines. The NBC retroflects twice, first at depth into the EUC, around 2°N (Schott et al., 1998). Then, the rest of the NBC retroflects seasonally (from mid-July to December) into the NECC around 7°N, 48°W. The NBC therefore breaks up into large eddies by "pinching" of the retroflection (Figure 1.5). Other mechanisms were proposed to explain the NBC rings generation even when the surface NBC does not retroflects. Equatorial Rossby waves that propagate westward and reflect on the coast of Brazil could generate these eddies (Jochum & Malanotte-Rizzoli, 2003) It is worth noting that the position of both retroflections is variable. At the surface, the retroflection extend northward up to 9-10°N when shedding a ring, and then retracts to 6-7°N.

The NBC rings are anticyclonic, due to the configuration of the retroflection, whose pinch gives an anticyclonic spin to the eddies (Figure 1.5), but also due to the stability of these structures. Anticyclones intensify when travelling northwestward as they compensate for the increasing planetary vorticity (Jochum & Malanotte-Rizzoli, 2003).

Some NBC rings are formed by the first NBC retroflection at depth around 2°N, while other are formed at the surface around 8°N by a combination of mechanisms. This creates eddies that can vary greatly in thickness. Some of them can extend from the surface to two thousands metres, while others are trapped close to the surface and extend only to two hundred meters. Also, some sub-surface vortices only have been observed, intensified in the thermocline but with no surface signature (Wilson et al., 2002).

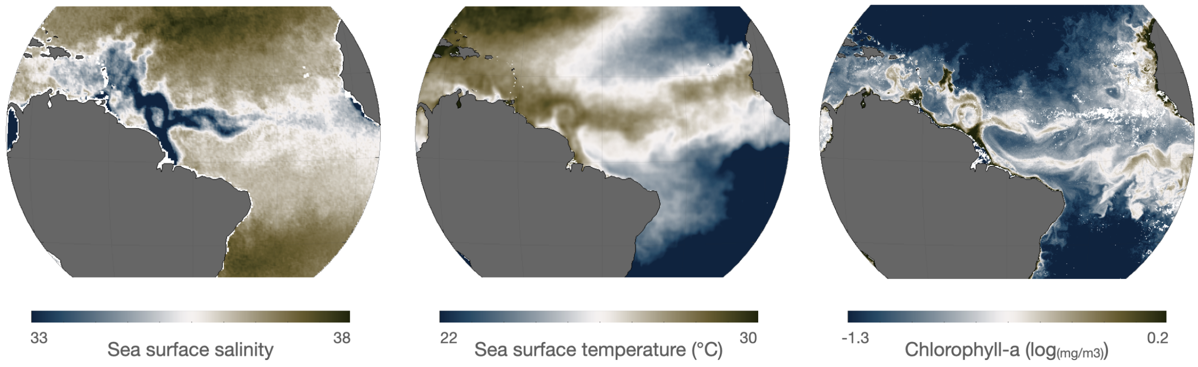

Figure 1.9: From left to right, snapshots of SSS, SST and chlorophyll-a on August 28^{th}, 2015 highlighting the separation of a NBC ring from the NBC retroflection.

Some parallels can be drawn between the NBC rings and the best-known Agulhas rings. The importance on the meridional overturning circulation of the Agulhas rings has been shown repeatedly, by their ability to transport Indian Ocean water masses into the Atlantic Ocean. (eg. Lutjeharms and Gordon, 1987). While the Agulhas Rings provide inter-gyre transport (Indian to Atlantic), the NBC Ring transport is inter-hemispheric, transporting waters from the South Atlantic into the North Atlantic (Johns et al., 1990; Johns et al., 2003). The NBC rings are not necessarily deep, but they are very large. For example a 200-m thick eddy of 400 km diameter approximatively contains a volume of 2.5 10^{13} m^3 of South Atlantic water. It roughly translates into a volume flux per year of 1 Sv per eddy. More detailed and accurate calculation, taking into account the variability in eddy shapes, estimated an average ring induced transport of 1.1 Sv per ring (Johns et al., 2003). For comparison, the annual mean volume flux of South Atlantic waters through the Florida Current a branch of the AMOC located further north, is of 10 to 15 Sv (Schmitz Jr & Richardson, 1991). Five to nice rings are shed every year, which mean they account for 1/3 to 2/3 of the transport of South Atlantic water and are a significant fraction of the MOC (Johns et al., 2003).

One of the things that makes NBC rings so special is that they form and propagate just downstream of the Amazon plume. This fresh, productive water mass can wrap around the edges of the eddies, making them clearly visible in satellite salinity and chlorophyll-a (Figure 1.9 and Fratantoni and Glickson, 2002; Ffield, 2005). It raises the question, do the NBC rings play a role in the transport of Amazon waters ? The salinity and temperature signature of the ring is therefore very plume dependant, as the intensity and direction of the plume varies seasonally. Their temperature signature is not very strong and changes, they have a warm SST anomaly in the first half of the year and a cold one in the second half because the anomaly is relative to the regional SST (Ffield, 2005). Figure 1.9 shows that rather than having a distinct SST signature, it is the waters upwelled locally near French Guiana stirred around the eddy that delineates it.

While NBC rings are one of the most intriguing features of the Atlantic, being among the largest eddies and connected to the world's largest rivers, they are surprisingly not well observed. Indeed, the observation of these rings is limited : usually, the intense rings of the western boundary currents such as the Gulf Stream are often observed in SST due to the strong gradient between the core of the ring and their surrounding (Brown et al., 1986). The NBC develop in the western tropical Atlantic warm pool, so the surface temperature gradients are weak, and this method is ineffective. Altimetry is key in observing eddies, however the NBC retroflection is highly dynamic and the signal associated to near-equator ring is small, which makes the detection by altimetry tricky, in particular their separation from the retroflection. Salinity therefore stands out as one of the key variables to observe the NBC rings, with strong SSS gradients observed almost all year around and no impact of a cloudy sky on the dataset.

Studies have mainly focused in trying to understand the formation, evolution, transport and demise of the rings. However, their interaction with the Amazon plume means that they could modify the air-sea exchanges in a region strongly coupled to the atmosphere and in the path of tropical cyclones. The Amazon river plume is a very important feature of the western tropical Atlantic on many accounts with a significant impact on its biodiversity (Section 1.3.2). The biogeochemistry and biology of the rings is still a mystery, as is their interaction with the Amazon plume's ecosystems.

1.4 Objectives of the thesis

1.4.1 Questions

In this general introduction, I have highlighted the evolution of scientific knowledge on the oceanic mesoscale and to establish a knowledge base on the tropical Atlantic Ocean. Years of research, stemming from pronounced efforts in satellite development and sampling of the tropical Atlantic Ocean, have highlighted the place of the mesoscale in the heart of this ocean. This has led to an understanding of their formation, and some of their impacts, further emphasising their importance.

Many questions remain unanswered on the tropical Atlantic, despite this area being a major ocean hub, with a strong cross equatorial boundary current, and at the limit between the two hemisphere. In this thesis, we examine the mesoscale through the lens of surface salinity. From this perspective, the tropical Atlantic ocean is the ideal place of study. It presents one of the largest variability in salinity, which has an impact on the physics of the ocean through stratification in particular. In this region, the biogeochemistry is also strongly coupled with salinity. The ocean mesoscale is numerous and large in the tropical Atlantic, which makes it easier to observe from satellite products. Moreover, the region has recently been at the heart of oceanographic cruises having for objective to study the ocean mesoscale, bringing to light new and more complete datasets.

In this thesis, we take advantage of these unique properties of the Atlantic ocean to answer some of the many questions revolving around the tropical Atlantic mesoscale:

- What is the role of salinity on Tropical Instability Waves ?

As introduced in section 1.3.4, the observation of TIWs in salinity is relatively recent. Due to the datasets available, most studies focused on their signature in temperature. The few observations that focused on salinity (Grodsky et al., 2005; Lee et al., 2014) showed a strong link between TIWs and salinity, that we continue to explore. We first investigate the surface salinity signature of the TIWs, by looking at its seasonal and interannual variations. Temperature and sea surface height are also used to bring out similarities and peculiarities of the salinity TIWs signature, and how it impacts the TIWs density structure. It is important to better understand the surface stratification, and air-sea exchanges associated to these waves. It then also raises the question: if salinity plays a role in defining the TIWs density gradient, how much does it contribute to the TIWs energetics ? In a second part, we therefore focus on the potential energy associated to the deformation of the density gradient by the waves (perturbation potential energy, PPE). The aim is to see if salinity plays a significative role in the waves potential energy signal. Since most of the studies that looked at the baroclinic sources of energy for TIWs didn't take into account salinity, it could be a important factor to have in mind when discussing the relative importance of barotropic and baroclinic energy sources.

- What drives the Amazon plume pathways, and the export of freshwater to the open ocean ?

On the western side of the basin is located one of the most interesting hub of the region. The strong boundary current of the tropical Atlantic gyre retroflects seasonally and forms large anticyclonic eddies all this right next to the mouth of the world's largest river. The presence of the Amazon is a tool for understanding the dynamics of the region, as the fresh Amazon waters can act as a tracer of ocean circulation. The main variability in the northwestern tropical Atlantic is seasonal. Curiously, this area is very little sampled, which means that while studies have pointed out the large scale variability of the plume (Coles et al., 2013), the small scale one is still not well known. In winter, the Amazon water were thought to remain confined on the shelf. A freshwater plume sampled in February 2020 during the EUREC^{4}A-OA cruise showed the contrary, and challenges our knowledge of the dynamics of the region. We therefore investigate how the NBC rings intervene in the formation mechanism of this plume, its impact on the air-sea fluxes of the region and we try to determine how frequent this situation is, and the importance of this freshwater export pathway to the open ocean.

In summer the dynamics at first glance look straightforward. Before mid July, the NBC does not retroflect and the fresh plume waters are advected toward the Lesser Antilles. Once the NBC sets up, it entrains the plume waters toward Africa. However this large-scale view does not take into account the role of the winds and of the NBC rings, that still propagate toward the northwest in summer. A large freshwater pool translating toward the northwest in September 2021 is observed during the Tara Microbiome mission, showing that even when the NBC retroflects, freshwater transport toward the northwest can happen. We therefore investigate the formation mechanism of this event, and then try to refine our understanding of freshwater transport in late summer. Late summer is also the peak period of the tropical Atlantic cyclone season, meaning that understanding the transport of freshwater lenses is key to characterise the barrier layers of the Northwest tropical Atlantic.

- What is the role of the NBC rings on the western tropical Atlantic carbon budget ?

The Amazon waters are not just a passive tracer, they are the source of a rich biogeochemistry, which has consequences for biological growth and the ocean carbon sink. In winter, little is known of the CO_2 air-sea exchanges of the northwestern tropical Atlantic, due to no cruise sampling the corridor between French Guiana and the Lesser Antilles where the NBC rings travel. As observed previously, the physical properties of the ocean in winter are much more variable than expected, due to the interactions between the NBC rings and the Amazon plume that export fresh water filaments to the open ocean. It also suggest that the air-sea CO_2 fluxes in the region are variable, and that the region is more complex than described in previous large-scale climatology. In climatology, the southern part of the region is described as source of CO_2 to the atmosphere due to the influence of the NBC bringing CO_2-rich waters from the equator. Above 13°N, the region is rather a sink, due to the seasonal cooling of these waters. The observations carried out during EUREC^{4}A 2020 cruise in February 2020 challenges this perspective, and allows us to identify the mechanisms responsible for the air-sea CO_2 fluxes variability and their signature in temperature, salinity and chlorophyll-a. In doing so, it gives us the possibility to reconstruct the air-sea CO_2 fluxes from these three variable, to better take into account the role of mesoscale feature such as the NBC rings, and sub-mesoscale features such as the freshwater filament in the carbon budget of the northwestern tropical Atlantic in winter.

In summer, the Amazon waters dominate a large part of the western tropical Atlantic (up to 15%). This season was therefore more studied, which highlighted the strong carbon sink associated to the export of the fresh and nutrient-rich Amazon waters to the open ocean. The Tara microbiome study revealed that the Amazon plume was not one large structure, but rather the accumulation of small-scale structures. It also gathered CO_2 air-sea fluxes data in NBC rings that strongly interacts with the Amazon plume. To asses the carbon budget of the Northwestern tropical Atlantic, it would be interesting to look at the combination of the large scale, and mesoscale structures, to better understand the mechanisms driving the variability air-sea CO_2 fluxes in summer by using all data collected in the region and combining it with satellite data.

1.4.2 Structure of the thesis

The first three chapter following this introduction describe the methods and datasets we used. Chapter 2 will present the methods used in this thesis, with a focus on the carbonate chemistry and the work done to retrieve the fluxes of CO_2 from the parameters measured commonly by ships. This chapter is not an extensive review of all methods used in the thesis, as some of them, which are specific to one study, are described in the corresponding chapter. Chapter 3 present the in-situ data acquired during the EUREC^{4}A and Tara microbiome cruise and Chapter 4 provides information on the satellite product that completed the in-situ dataset, with a main focus on satellite salinity.

The results will be presented in four chapters, followed by a closing chapter where we will try to discuss the implications of the work conducted across this thesis in a broader context. The first chapter will focus on bringing a new colour to the largest mesoscale structure of our study area, by using new salinity data to study the tropical instability waves. In the following two chapters, we study the role played by the North Brazil Current rings on the Amazon plume in winter, and its biogeochemical consequences. The last chapter of this result section will investigate the complex interactions between the NBC rings and the Amazon plume in summer.

In Chapter 5, we present the seasonality and discuss the interannual variability of the TIWs in temperature, salinity and sea surface height. We then compare the relative impact of salinity and temperature in the energetics of theses waves. This work was published in the Journal of Geophysical research: Oceans in November 2020 (Olivier et al., 2020). Supplementary material to this first paper is included in Appendix A.

In Chapter 6, we move to the western part of the basin to study an event of a large freshwater filament spreading in the open ocean during a period of low Amazon outflow in winter 2020. We follow the plume, understand its dynamics, and study the occurrence of this type of phenomenon. This work was published in the Journal of Geophysical research: Oceans in

November 2021 (Reverdin et al., 2021). The supplementary material of this paper is provided in Appendix B.

In Chapter 7, we continue the work of the previous chapter by conducting the first study looking at the air-sea CO_2 fluxes in winter of the western tropical Atlantic, with a focus on the NBC rings. We developed a method based on in-situ data to reconstruct the CO_2 fluxes from satellite maps of temperature, salinity and chlorophyll at high resolution to understand the mechanisms driving the biogeochemistry in winter. This work was published in the journal Biogeosciences in April 2022 (Olivier et al., 2022a). Supplementary material to this paper is also included in Appendix B.

In Chapter 8, we complete the work previously done by looking at the summer season. The Tara Microbiome cruise revealed a very peculiar mesoscale structure of low salinity, showing an alternative path for the fresh water of the Amazon plume. We therefore investigate the freshwater transports in August, and better defined the Amazon river plume dynamics in a large outflow period. This work has been submitted in September 2022 in the Journal of Geophysical research: oceans, and is currently under review (Olivier et al., 2022b). Supplementary material to this paper is also included in Appendix C. Next, we will present preliminary results on the biogeochemistry of this region in summer. Tara crossed many diverse regions, bringing valuable information on the pCO_2 of the Amazon plume, the NBC and the NBC rings, as well as the river-ocean continuum.

These four chapters are published or almost published papers, so are meant to be understandable independently from one another, which is why there might be some redundancies at times.

We will conclude this work in Chapter **??**, and present some perspectives of future work. We will focus on the western tropical Altanic, taking full advantage of all datasets available summer to draw the most complete biogeochemical picture of the region, and also in the western Weddell sea, where it could be interesting to use the recently acquired data from Tara data to understand the salinity and CO_2 variability in another region of the planet.

Finally, as a result of the current climate crisis, I was involved in a group effort at LOCEAN to quantify the carbon footprint of our research practises and propose alternative low-carbon pathways for the laboratory. Appendix E present the carbon footprint of my PhD, and discusses the carbon footprint of observations in oceanography.

DATA AND METHODS

Sea water CO_2 | 2

2.1 Carbonate biogeochemistry

2.1.1 The essential variables of the carbonate system

Dissolved inorganic carbon

In the ocean, carbon dioxide exists in three different inorganic forms: aqueous carbon dioxide ($CO_{2(a)}$),bicarbonate ion (HCO_3^-) and as carbonate ion (CO_3^{2-}). The carbonate species are related by the following equilibria:

$$CO_{2(g)} \rightleftharpoons CO^*_{2(aq)} \tag{2.1}$$

$$CO^*_{2(aq)} + H_2O_{(l)} \rightleftharpoons H^+_{(aq)} + HCO^-_{3(aq)} \tag{2.2}$$

$$HCO^-_{3(aq)} \rightleftharpoons H^+_{(aq)} + CO^{2-}_{3(aq)} \tag{2.3}$$

The sum of all the dissolved forms of CO_2 , HCO_3^- and CO_3^{2-} is called total dissolved inorganic carbon (DIC):

$$[DIC] = [CO^*_{2(aq)}] + [HCO^-_{3(aq)}] + [CO^{2-}_{3(aq)}]$$

In typical seawater conditions (salinity of 35, pH of 8.1, temperature of 25°C), bicarbonate is the dominant species (86.5%), followed by carbonate ion (13%), whereas dissolved carbon dioxide is present only in small concentrations (0.5 %).

Alkalinity

Another essential quantity for the description of the carbonate system is the alkalinity, which is closely related to the charge balance in sea water. Total alkalinity is defined as the number of moles of hydrogen ions equivalent to the excess of proton acceptors over proton donors in a one kilogram sample of water (Dickson, 1981).

$$TA = [HCO^-_{3(aq)}] + 2[CO^{2-}_{3(aq)}] + [B(OH)^-_4] + [OH^-] - [H^+]$$
$$+ minorcomponents$$

Air-sea CO_2 flux

The exchanges of CO_2 between the different reservoirs are described by the flux of CO_2. In a natural steady-state situation, the net CO_2 flux between the ocean and the atmosphere globally is close to zero. Regionally however, surface water can be undersaturated or supersaturated in $_2$ with respect to the atmosphere concentration, creating local sources and sinks of $_2$. The air-sea CO_2 flux (F) and can be expressed as the difference between the flux entering the ocean ($F_{atm->sw}$) and the outgoing flux ($F_{sw->atm}$)

$$F = F_{atm->sw} - F_{sw->atm} = K_0 \cdot k \cdot \Delta pCO_2 \tag{2.4}$$

where $\Delta f CO_2$ is the difference of CO_2 partial pressure between the atmosphere and the ocean, K_0 the solubility of CO_2 in sea water, accurately known as a function of temperature and salinity (Weiss, 1974) and k is the gas transfer velocity. The gas transfer velocity k expresses the ease with which a molecule of CO_2. can pass from the gaseous to dissolves phase (and vice-versa).

2.1.2 Drivers of the CO_2 flux

The CO_2 flux variability depends on the winds and on the gradient between the atmospheric and oceanic fCO_2. In the northwestern tropical Atlantic, we will show that it is often dominated by the variability of the ocean pCO_2. Variations in pCO_2 are due to both physico-chemical and biological phenomena. In this thesis we try to understand among all the complex processes the dominant ones in our region of interest.

The pCO_2 at the ocean surface is affected by the dissociation constants of the chemical equations mentioned in 4.1 to 4.3, and by the gas solubility. Its is therefore impacted by changes in temperature, salinity, DIC and alkalinity. Takahashi et al., (1993) computed the dependence of fCO_2 one each of these variables. They highlight that at seasonal time scales, the effect of temperature is one of the strongest. For a salinity range of 34 to 36, an increase of 1°C in temperature leads to an increase of pCO_2 of 4.23 μatm. The Amazon River flows into the tropical Atlantic and forms huge salinity gradients. Using solubility of Weiss (1974) and the dissociation constants (of the equilibria presented in equation 2.1.1) of Mehrbach (1973) refit by Dickson and Millero (1987) the pCO_2 increases of 4% by ‰in salinity. The effect of salinity on the pCO_2 is a manifestation of the changes in the solubility of CO_2 associated to the change of the dissociation constants of the carbonic acid. The effect of temperature on the pCO_2 is both due to the changes in the dissociation constants and on the dependence of pCO_2 on temperature when computed from the CO_2 molar fraction.

Many physical processes influence the water temperature, salinity, DIC and alkalinity. Temperature variations are driven by solar energy input, air-sea heat exchanges and the depth of the mixed layer. Salinity varies due to precipitations, evaporation and in our region the main factor is river outflow. Horizontal and vertical advection are processes influencing all four variables. Deeper water masses are usually saltier, colder and enriched in respired CO_2, enhancing the pCO_2 once they are upwelled to the surface.

The variation of DIC and alkalinity brings additional information. The increase of anthropogenic carbon increases the DIC, but not the alkalinity as it does not modify the charge balance. They are influenced by river outflows, as the mean DIC and alkalinity of rivers are much lower than the typical oceanic values, and these values are typical of each river.They are also controlled by biological processes. Photosynthesis reduces the DIC and slightly increases the TA as nutrients and inorganic carbon are taken up by the phytoplankton. In case of calciferous phytoplankton growth, both DIC and TA decreases.

2.2 Computing experimentally the air-sea CO_2 flux from an equilibrator pCO_2 system

The air-sea CO_2 flux (F, mmol $m^{-2}d^{-1}$) can be expressed as:

$$F = \cdot K_0 \cdot k \cdot (fCO_{2sw} - fCO_{2atm}) \tag{2.5}$$

where K_0 is the solubility of CO_2 in seawater, expressed as a function of SSS and SST by Weiss (1974) and k is the gas transfer velocity. k is calculated following the relation from Wanninkhof (2014):

$$k = 0.251 \cdot < U^2 > \cdot (Sc/660)^{-0.5}, \tag{2.6}$$

where Sc is the Schmidt number, and $< U^2 >$ is the averaged squared wind speed at 10 m above sea level. For all the computations, we assume that SST (at the intake) and SSS are the ones measured by the TSG system.

This thesis work is based on the ship based observation of the air-sea CO_2 flux. We used an equilibrator pCO_2 system, so the flux is actually computed from the difference of fugacity in the atmosphere and in an air equilibrated with the surface sea water. The fugacity of CO_2 in the atmosphere (fCO_{2atm}) is derived from the atmospheric mole fraction (xCO_{2atm}) measured at the NOAA observatory in RPB to calculate the partial pressure of CO_2 in the atmosphere (pCO_{2atm}):

$$pCO_{2atm} = xCO_{2RPB} \cdot (P_{atm} - pH_2O); \tag{2.7}$$

and the fCO_{2atm}

$$fCO_{2atm} = pCO_{2atm} \cdot exp \left(P_{atm} \cdot \frac{B + 2\delta}{R \cdot SST} \right) \tag{2.8}$$

The fugacity of CO_2 in sea water (fCO_{2sw}) is computed from the fugacity of CO_2 at the equilibrator temperature (fCO_{2eq}). A correction is then applied to the fCO_{2eq} to compensate for the difference in temperature between the equilibrator and the sea surface:

$$fCO_{2sw} = fCO_{2eq} \cdot exp \left(0.0423 \cdot (SST - T_{eq}) \right) \tag{2.9}$$

fCO_{2eq} is derived from the partial pressure of CO_2 in the equilibrator (pCO_{2eq}):

$$fCO_{2eq} = pCO_{2eq} \cdot exp\left[\left(B + 2 \cdot (1 - xCO_{2eq} \cdot 10^{-6})^2 \cdot \delta\right) \cdot \left(\frac{P_{atm}}{R \cdot T_{eq}}\right)\right] \tag{2.10}$$

with R = 82.0578 $cm^2.atm.mol^{-1}.K^{-1}$, B and δ the virial coefficient for CO_2 (Weiss, 1974). B in cm^3mol^{-1} is given by:

$$B = -1636.75 + 12.0408 \cdot T_{eq} - 3.27957 \cdot 10^{-2} \cdot T_{eq}^2 + 3.16528 \cdot 10^{-5} \cdot T_{eq}^3 \tag{2.11}$$

and δ in cm^3mol^{-1} by

$$\delta = 57.7 - 0.118 \cdot T_{eq} \tag{2.12}$$

The air inside the equilibrator is assumed to be at 100% humidity whereas it is dry when measured inside the LICOR. The CO_2 partial pressure in the equilibrator (pCO_{2eq}) is computed with a correction using the water vapor pressure applied to the dry mole fraction (xCO_{2eq}) measured and is given by

$$pCO_{2eq} = xCO_{2eq} \cdot (P_{atm} - pH_2O) \tag{2.13}$$

with P_{atm} the atmospheric pressure at the sea level and pH_2O is the water vapour pressure at the sea-surface salinity (S) and temperature of the equilibrator (T_{eq}). The water vapour pressure is calculated following Weiss & Price (1980):

$$pH_2O = exp\left(24.4543 - 67.4509 \cdot \left(\frac{100}{T_{eq}}\right) - 4.8489 \cdot \log\left(\frac{T_{eq}}{100}\right) - 0.000544 \cdot S\right) \tag{2.14}$$

Oceanographic cruises & in situ data

3

3.1 EUREC^{4}A

EUREC^{4}A-OA (ElUcidating the RolE of Cloud-Circulation Coupling in ClimAte Ocean-Atmosphere) field campaign took place in January-February 2020. It expressed an ambitious effort to quantify how cloud-properties co-vary with their atmospheric and oceanic environment across the big range of relevant scales (Stevens et al., 2021). It comprised more than four weeks of measurements in the eddy field generated by the North Brazil Current (NBC) along the coast of South America, and in the downstream winter trades of the North Atlantic.

Four research vessels (RV) cruised the northwestern tropical Atlantic as part of the Ocean-Atmosphere component of the (EUREC^{4}A-OA field campaign (Figure 3.1). EUREC^{4}A-OA aims at investigating the heat, momentum and CO$_2$ exchange across the air/sea interface using innovative high-resolution ocean observations and a hierarchy of numerical simulations. This international collaboration involved the French RV Atalante, the German RV Maria S. Merian and RV Meteor, and the American RV Ronald H. Brown. These cruises provided a large number in situ measurements for the study of the meso to sub-mesoscale winter features of the northwestern tropical Atlantic ocean, and their impact on the atmosphere.

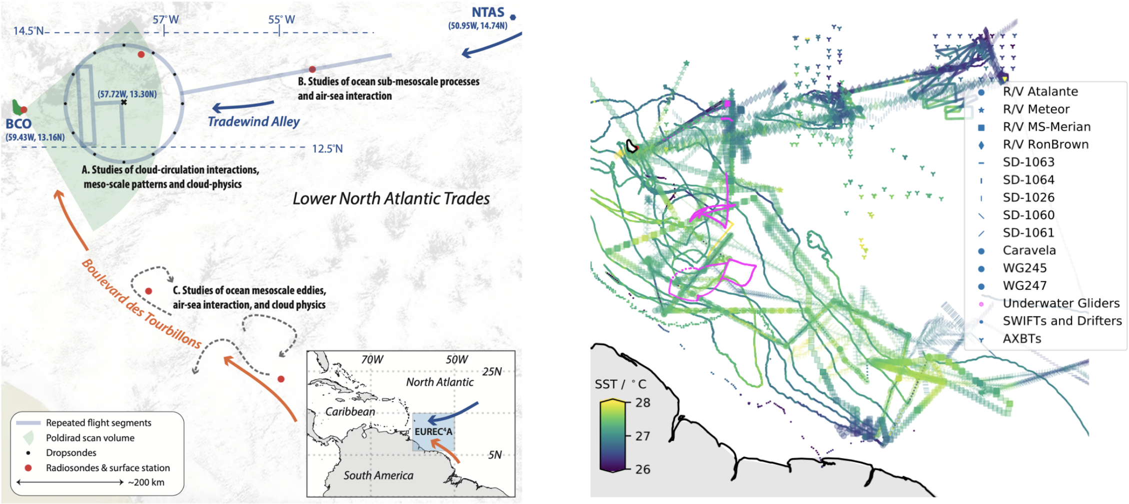

Figure 3.1: Left: The EUREC^{4}A study area in the lower trades of the North Atlantic. The zonally oriented band following the directions of the trades between the Northwest Tropical Atlantic Station (NTAS) and the Barbados Cloud Observatory (BCO) is called Tradewind Alley. The second theatre of play follows the southeast to northwest meanders of the Boulevard des Tourbillons. The background shows a negative of the cloud field taken from the 5 February, 2020 MODIS-Terra overpass. Right: Map showing the location of the measurements by surface and sub-surface platforms, including the journey of the fours ships mobilised for the EUREC^{4}A mission. Both figures are from Steven et al., (2021).

3.1.1 Thermosalinograph

The thermosalinograph (TSG) is an indispensable instrument on any research vessel. Connected to the ship's water intake, it continuously measures the temperature and conductivity of the sea water while the ship is in motion. Salinity is then derived from conductivity and temperature. Its main advantage is its very high temporal resolution, while its spatial resolution is limited to the ship's path.

The TSG consists of a cell equipped with electrodes that determine the conductivity of the seawater. Thermistors measure the temperature of the water in the cell and near the hull. On most vessels, TSGs are SeaBird SBE21 sensors. This sensor provides real-time temperature and conductivity data. Another temperature sensor is mounted near the seawater intake to correct for temperature changes caused by the piping joining the intake to the SBE21 that might warm the water.

On large research vessels like the Atalante, the intake is usually located at around 5-6 m depth. The TSG near-surface measurements are most of the time representative of surface conditions but could be different in very stratified areas.

3.1.2 Underway pCO_2

A system continuously monitoring the near-surface ocean pCO_2 was installed on three out of the four ships (RVs Atalante, Maria S. Merian and Ronald H. Brown). The three systems are different. As I was in charge of the Atalante CO_2 system, this set-up will be presented in more details.

The pCO_2 system on the Atalante (from Lefevre et al., 2009) consisted of four parts, and was refurbish by Matthieu Labaste and Christophe Noisel from the LOCEAN DITM's team. First, an equilibrator is connected to the ship water intake. Seawater from the TSG pumping circuit circulates in the equilibrator at a rate of 2 L min^{-1}. A closed loop of about 100 mL of air flows through the equilibrator designed to avoid bubbles at the air-sea interface. The air in contact with the sea water equilibrates so that the air and sea water CO_2 mole fraction (xCO_2) are the same. To minimize temperature corrections, the equilibrator is thermostated with the same seawater as the one used for xCO_2 measurements. The air is then analysed by a LICOR LI-7000 infrared analyser that will measure the xCO_2. However, the air entering the LICOR must be completely dry in order to have a correct CO_2 reading, since water vapour (the first greenhouse gas) absorbs infrared radiation at the same wavelengths as the CO_2. Therefore, at the exit of the equilibrator, the air goes through several water traps. On the Atalante, the first water trap is physical, with the air passing through a water cooler to condense the water vapour. It then goes into a chemical magnesium perchlorate trap before being sent to the LICOR. The fourth part of the system is for calibration. The LICOR is an instrument that tends to rapidly drift. Therefore, every 8 to 12 hours, the LICOR stops analysing the air coming through the equilibrator and instead analyses standards. The standards are air gases with a known exact concentration of CO_2. Ideally, these known concentrations bracket the likely CO_2 concentration of sea water. A "zero CO_2 concentration" standard (nitrogen gas) is used to calibrate the zero of the LICOR as well as the higher standard (precise but non-zero CO_2 concentration). Calibration of the dataset is done with the 3 different gas standards from zero: low, medium and high standards.

The General Oceanic Inc. 8500 pCO_2 instrument installed on board the Ronald H. Brown follows a similar methodology to the Atalante underway pCO_2 system and is detailed in Pierrot et al (2009).

While the Atalante and the Ronald H. Brown used an instrument with an equilibrator, the Maria S. Merian used a membrane pCO_2 instrument. This OceanPack CUBE FerryBox system from SubCtech is also connected to the TSG, and water is pumped at a rate of 7L/min. Instead of circulating in a thermosted equilibrator, water flows along a membrane through which CO_2 diffuses. Then, as in the Atalante system, on the other side of the membrane the air circulates through a non-dispersive infrared gas analyser (here the LICOR LI-840).

3.1.3 Conductivity Temperature Depth

The conductivity, temperature and depth (CTD) is one of the most common instrument on research vessels. As the ship stops during stations, the rosette carrying the CTD and up to 24 Niskin bottles goes down the water column to usually 2000 m. The CTD sensor measures temperature, conductivity (from which is derived salinity) and pressure all along the profile, while the Niskin bottles are fired at the selected depths to collect water for filling the water samples on deck. Additional sensors such as an oxygen and a fluorimetre were also installed on the rosette to complete the profile.

3.1.4 Samples

On the Atalante, samples for dissolved oxygen, dissolved inorganic carbon (DIC) / total Alkalinity (TA) (the two variables are analysed from the same sample), inorganic nutrients (silicate, phosphate, nitrate and nitrite) and salinity were taken from the rosette. At each station, oxygen, oxygen isotopes, nutrients and salinity were sampled at every depth, while DIC/TA was sampled on at least three chosen depths. DIC/TA and nutrients samples were particularly useful to this thesis. They were additionally collected three times a day on the underway system to provide a better sampling of the surface conditions. DIC/TA samples were also used to check the range of the values reported by the underway-fCO_2 system. The 138 DIC/TA samples were measured at the SNAPO-CO_2 facility by potentiometric titration using a closed cell, following the method of Edmond (1970). The accuracy of the DIC and TA measurements is of 2 μmol.kg-1. Nutrients were conserved by heat pasteurisation and stored in the dark before being analysed on land by colourimetry at the Institut pour la Recherche et le Développement (acrshortIRDLabel) LAMA service in Brest, with an accuracy of 0.2μmolL-1 for nitrate and silicate and 0.03μmolL-1 for phosphate.

3.1.5 Drifters

The RV Atalante deployed five surface velocity program (SVP) drifters instrumented by the company "Pacific Gyre" (Lumpkin & Pazos, 2007) that were used in this thesis. These buoys drift with the currents at 15 m and measure temperature and salinity every 30 minutes at 20-cm, 5-m, and 10-m depths. They also measured surface barometric pressure as well as wind speed and direction 0.5 m above the surface, with regular GPS positioning.

3.2 Tara

Tara is a 36-m long schooner from the Fondation Tara Océan, originally called Antarctica and built in 1989 by the french explorer Jean-Louis Etienne. It has then be refitted to operate oceanographic equipment. On board the sailing boat are six sailors and six scientists, often accompanied by an artist and a journalist. Among the scientists, there is one chief scientist, one engineer in charge of instrument maintenance and data management, two deck scientists preparing and preserving samples for later biogeochemistry and genetic analyses, and two scientists in charge of preparing and preserving samples from nets for morphological analyses and imaging live samples on board. Since its first mission Tara Arctic in 2006, Tara travels the world on missions lasting several years to better understand life in the oceans.

Figure 3.2: Voyage of the Tara during the two-year mission Microbiome. Tara's journey is separated in legs, and I embarked on the ones coloured in orange. The map is a courtesy of the Fondation Tara Océan.

3.2.1 Mission Microbiomes

In each litre of sea water can be found between 10 and 100 billion of planktonic micro-organisms. They represent more than two thirds of marine biomass. They constitute the first link in a huge food chain, the other end of which feeds the greater part of people on earth. These marine algae and photosynthetic bacteria are service providers. However, despite their key importance, our understanding of these micro-organisms is only superficial. The plankton can be separated into five groups, the zooplankton, the phytoplankton, the protist, the bacteria and the viruses (some phytoplankton species are also protists or bacterias). The microbiome represents the four lasts groups, the unicellular organisms. Studying the microbiome, main component of the plankton, in the Atlantic is the key objective of the ATLANTECO program and of the most recent Tara mission.

The mission Microbiomes started in October 2020, when Tara left its home port, Lorient, for a two-years voyage (Figure 3.2). After a long transect until Punta Arenas, the CEODOS Chilean program sampled the coast of Chile on the first four legs of the mission. I joined the ship on July 20^{th} 2021 in Le Marin, Martinique during the refit of the ship to participate in the 1st leg of the ATLANTECO program. This leg focused on the Amazon plume and NBC rings, key subject of this thesis. Due to the deteriorating sanitary conditions in Martinique, and the enormous difficulties in getting missing parts for the CTD winch delivered, the departure of the ship was delayed. This three-week delay was used to install the instruments (including the pCO_2 system) and prepare the first leg of the new program that finally started on August 18^{th} 2021 and arrived in Macápa, Brazil on September 9^{th} 2021. The two following legs, from Macápa to Belém (September 12^{th} - September 16^{th}) and from Belém to Salvador da Bahia (September 24^{th} - October 8^{th}) completed the study of the Amazon region by the schooner. I installed the additional pCO_2 system and the LOCEAN is in charge of Tara's TSG. These two instruments will be described in the following sections.

3.2.2 Thermosalinograph

The main difference between the TSG on traditional research vessel and on Tara is the depth of the intake and the length of the piping. The intake is located much closer to the surface at about 1.5-m depth (Figure 3.3), although it could at times also pump water closer to the surface. Tara's TSG was installed in Lorient by the LOCEAN DITM team, and the data is presented in figure 3.5. In very stratified regions, this shallower depth makes a significant difference on the measured SSS and SST. In the Amazon region, the low-salinity plume was well captured by Tara's TSG, but being as thin as 4 m at times, it could be missed by a traditional research vessel. The length of the piping is also shorter, and a temperature sensor is also installed right at the ship's intake to get an accurate SST measurement.

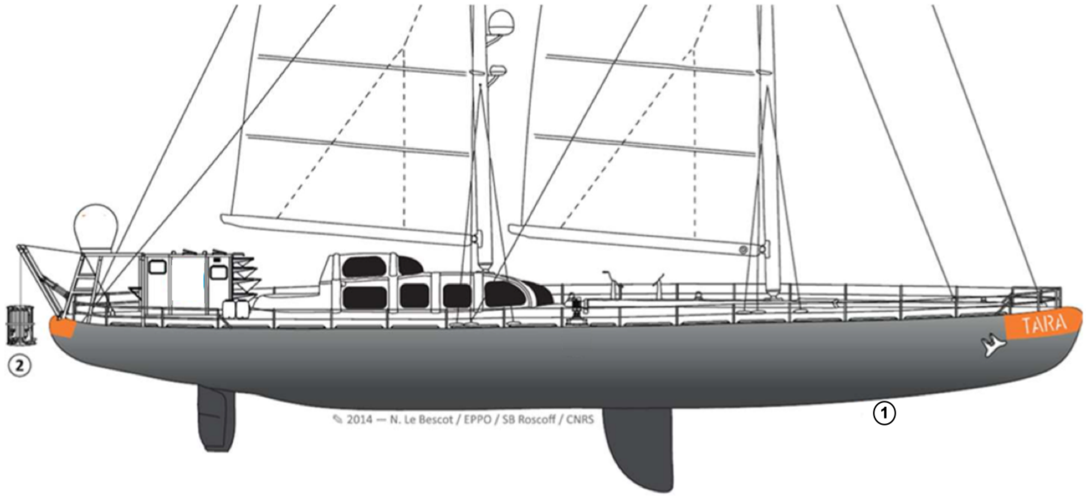

Figure 3.3: Sampling devices on-board SV Tara are shown from the vessel's side-view. [1] Continuous Surface Sampling System (TSG intake); [2] the CTD rosette. Adapted from Pesant et al., (2015).

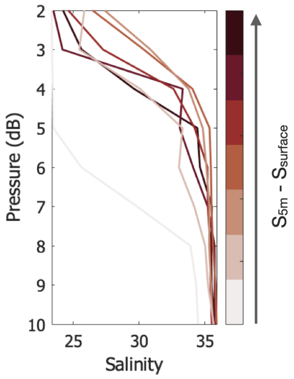

The immersion of the TSG varies from ship to ship. For a research vessel, the measured SST and SSS is between 5 and 8 m, while for Tara, it is 1.5 m. Ho and Schanze (2020) showed how a freshwater lens formed as a result of heavy rainfall in the tropical Pacific could be undetected by the TSG at 5 m, despite a 9 pss and 1°C anomaly at the surface. This resulted in a local 150 μ atm pCO_2 anomaly that is not detected by a system linked to the TSG at 5 m. The Amazon plume is also a good example. During station 38 in the plume (Figure 3.4) the salinity difference between 2 and 5 m can reach 8 pss, and the temperature 0.8°C which could have a significant impact on the fCO_2 (about 107 μatm, using the salinity/fCO_2 relationship of 13.4 μatm.pss^{-1} from Lefevre et al., 2010).

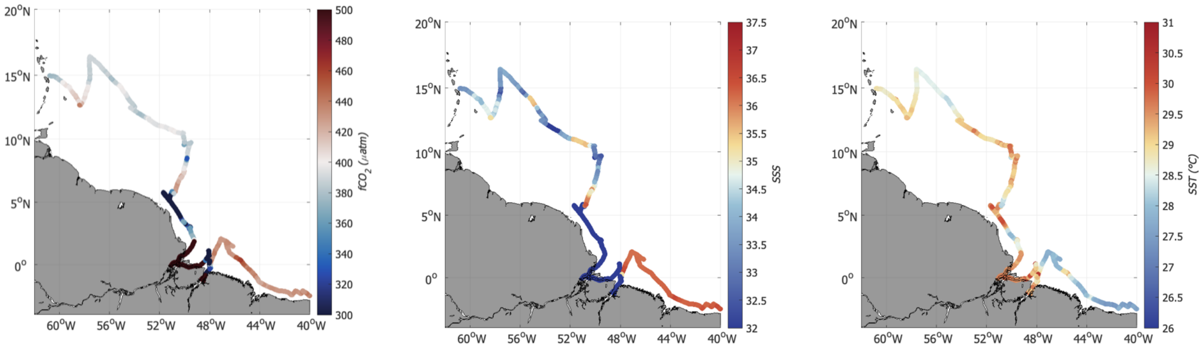

Temperature

Figure 3.5: From left to right, Tara's in-situ near surface measurements of fCO_2, salinity and temperature.

Figure 3.4: CTD salinity (top) and temperature (bottom) profiles for Tara's station 38b in the Amazon plume. The profiles colour are sorted by ascending difference between salinity (temperature) between 2 m and 5 m.

3.2.3 Underway fCO_2

Installing an underway fCO_2 system on Tara was a challenge due to the extremely limited space on the boat. Douglas Vandermark and Christopher Hunt, from the University of New Hampshire, proposed to use one of their underway fCO_2 instrument, that I installed and supervised on board the schooner.

Unlike the Atalante, space is limited on board the schooner. The continuous water line is used by 9 instruments, stored under the boat's floors, and in a small laboratory of a few square metres. The installation of the CO_2 system therefore required a lot of ingenuity and help from the sailors and engineers on board. The body of the system (equilibrator, LICOR analyser and electronics) was installed in the small laboratory, while the gas cylinders were stored on the front deck of the schooner (Figure 3.6). The atmospheric line was installed by the sailors on the first ribbon of the foremast. The gas cylinders and the atmospheric line are connected to the LICOR system by tubes running inside the ship and under the floor, up to 15 m long. Such a long distance is not ideal, but was the best compromise found.

In order to have enough flow (minimum 2 $Lmin^{-1}$) entering the equilibrator, a second pump and water circuit connected to the sea water intake was installed (Figure 3.3). This also limits the sea water heat exchanges, by reducing the length of the circuit and time spent in the tubes.

The weak point of the CO_2 system is the gas cylinders. For an ideal measurement, 3 standards are necessary, one at 0 ppm and two xCO_2 values framing the probable value of the measured xCO_2 (as on the Atalante). As space on Tara is so limited, only two standards have been installed, one at 0, and one at 500 ppm, which were expected to bracket the expected xCO_2 in the open sea. The gas bottles could not be stored vertically inside due to the lack of space and instead they were placed lying down on the front deck outside. We made a wooden mould to hold them in place so that they would not move, and protected them with plastic. Nevertheless, the front deck of the schooner bangs a lot and is often covered by waves. The cylinder regulators are fragile, so they were the first to be damaged. One additional challenge on Tara is that the scientific crew changes almost every month, and there was no operator with fCO_2 training on board when I was not there. The system from the University of New Hampshire is very robust, and engineers that rotated on-board took good care of it.

The CO_2 system was installed in July 2022 in Martinique, and operated until end of February 2022. It was active from August 18^{th} 2021 (beginning of leg 5) to December 10^{th} (end of leg 9), collecting data in the undersampled coastal area, revealing very strong spatial variability and coast-open ocean gradients. Some parts needed to be changed when I re-embarked in Antarctica on January 24^{th},and it run well after that. The CO_2 system finally broke down after the second crossing of the Drake Passage at the end of February, where the rough sea damaged the recently changed regulator and ended up emptying the gas bottles.

Post-processing

Tara's fCO_2 data (figure 3.5 needed considerable post-processing to obtain a clean and ready-to-analyse dataset. The processing of the data is two folds : first cleaning the data, and then calibrating it.

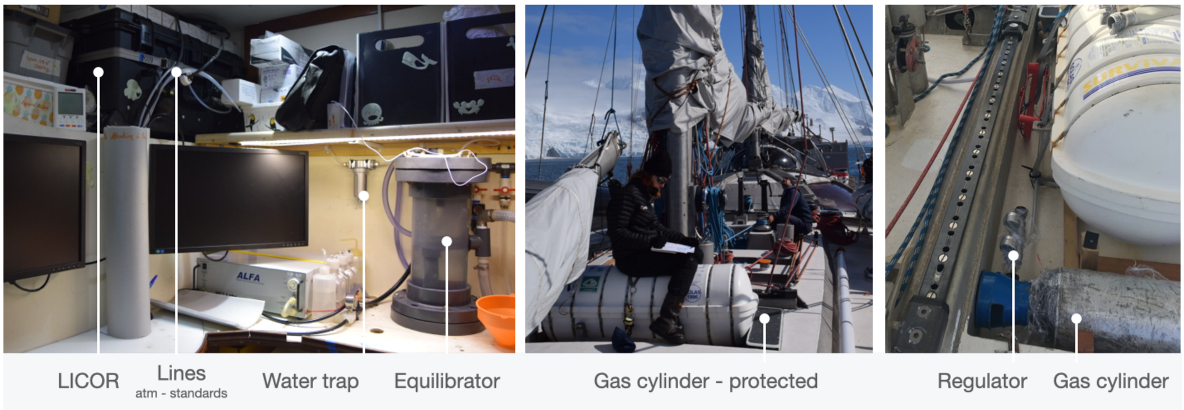

Figure 3.6: fCO_2 sampling devices on-board SV Tara. The picture on the left shows the interior of the underway laboratory, where the equilibrator and the LICOR (inside the black box) are installed. The atmospheric and standards lines connect directly to the black box. The middle picture shows the front deck of the ship, the standards (gas cylinders) are laying on each side of the life raft, protected by an anti-slip plastic support. Right: the support is removed, the gas cylinder, the regulator and the lines are apparent.

The system responds relatively quickly to a change in fCO_2. Pierrot et al.,(2009) showed that an equilibrator pCO_2 system response time is a bit more than two minutes for values on the order of 150 μatm.

When the cycle changes (from sea water to zero for example), the valve switch generates a strong transient spike in the data, that can sometimes be higher than 500 ppm. To remove all wrong data associated to a cycle change and the resulting response time, the first 8 minutes following a valve switch are deleted (Figure 3.7). As the sea water cycle lasted for 6 to 12 hours, most of the measurements remains, and the influence of the valve switch and equilibration is removed. The atmosphere cycle is shorter (15 to 20 minutes), but is used mainly for calibration purposes, so it is not problematic to remove a large part of the cycle.

For the standards (zero and span) as the measurements are only used for calibration, the last minute before the valve change is also removed, and the remaining last minute of good measurements is averaged and retained. The zero and span values are then linearly interpolated for all time steps. At this stage, the data is mostly clean, if some outliers are remaining they can be removed manually.

The calibration is then done following Pierrot et al., (2009). For each sea water or atmospheric measurement, a set of interpolated standard values (zero and span) is obtained. It is then linearly regressed following a least-square analysis detailed below:

$$xCO_{2zerocorr} = xCO_{2mesured} - zero \tag{3.1}$$

$$xCO_{2corr} = \frac{xCO_{2zerocorr} * SpanValue}{(span - zero)} \tag{3.2}$$

where zero and span are the interpolated zero and span data, SpanValue is the theoretical value of the span gas tank measured in the lab and $xCO_{2mesured}$ is the sea water or atmospheric data.

Unfortunately, there is considerable doubt as to the real value of the span. The value requested to the company was 500 ppm. The value reported by

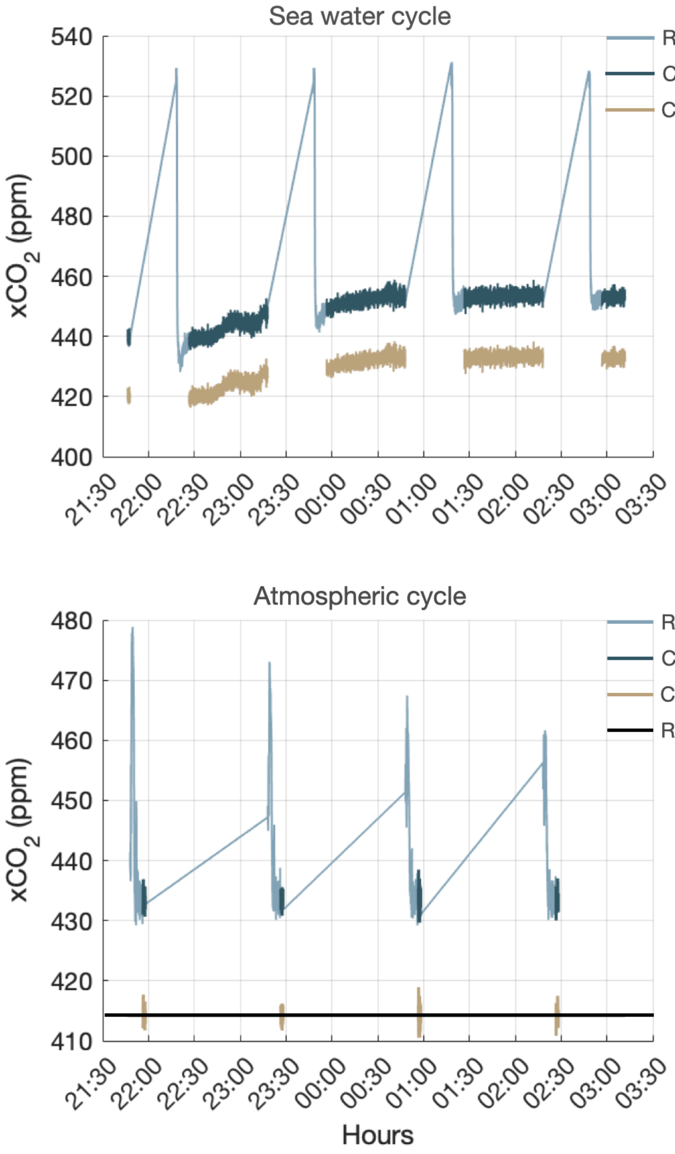

Figure 3.7: Tara xCO_2 extracted near Barbados (night of 18-19 August) of the time series of the seawater cycle (top) and the atmospheric cycle (bottom). The raw data are shown in light blue, the data cleaned of valve change pollution in dark blue and the cleaned and calibrated data in brown. For the atmospheric cycle, the value measured at Ragged Point Barbados (SVP) on 15 August (414.245) is shown in black.

the Airgas company is 507.9 ppm, with an uncertainty of 2%. The value measured in the laboratory before the cruise was 530 ppm. However, the 530 ppm span value gives unrealistic atmospheric (close to 440 ppm) and oceanic (>450 ppm) xCO_2 measurements (blue in Figure 3.7).

The atmospheric xCO_2 near SVP derived from Tara pCO_2 system calibrated with a 530 ppm span was 437.09 ppm during the night from August 19^{th} to 20^{th}, when the schooner was in close vicinity of Barbados. The atmospheric xCO_2 measured at RPB on August 15^{th}, 2021 (closest measure to Tara's passage) was 414.245 ppm. In order for the Tara xCO_2 data near Barbados to match the ones at RPB, the span value should be 502.3 ppm, which is within the uncertainty range given by the Airgas company. I have therefore used this value to calibrate the entire dataset (yellow in Figure 3.7).

This method relies on the stability of the atmospheric CO_2 near Barbados. In between the measurement made at SVP and Tara's passing near

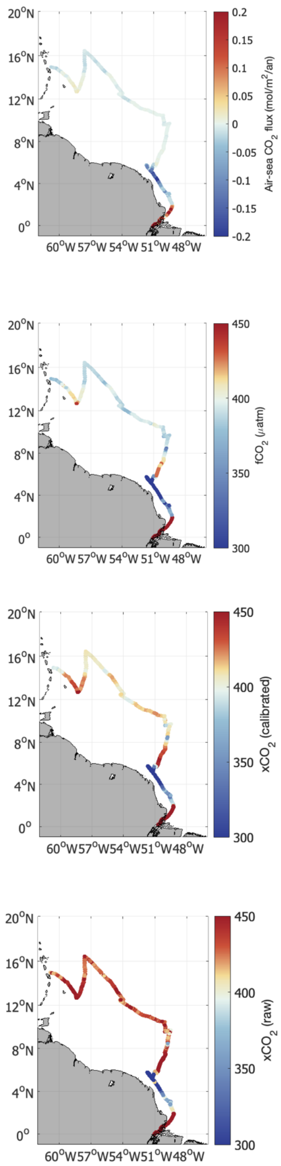

Figure 3.8: From top to bottom, final air-sea CO_2 flux, sea water fugacity of CO_2, calibrated sea water xCO_2, and raw sea water xCO_2 from Tara leg 5.

the island, winds were moderate and blowing from the sea, so the atmospheric xCO_2 is not expected to vary much from day to day (0̃.5 ppm, up to 1 ppm in the worst case). In the worst case, an error of 1 ppm in the calibration value would lead to a +- 0.84 ppm averaged difference over the dataset. Tara crossed highly variable regions during its voyage, that makes us confident that the uncertainty on the dataset is not impacting significantly the results. The Amazon region is one of the most variable areas, with a pCO_2 than can be as low as 70 μatm driven by intense blooms and low salinity plume waters, to the 3000 μ atm of the respiration-dominated river.

The calibrated data are then averaged over one minute.

3.2.4 CTD stations

Since the beginning of the Tara expeditions (such as Tara Ocean), all missions have had a strong biology component. With time, more physical and chemical oceanographic measurements have been included. The Tara stations are therefore not organised in the same way as for a typical physical oceanographic mission (such as EUREC^{4}A). Few stations are done, but they last up to 24 hours in order to well characterise the water column on a physical, chemical and biological basis. In order to get enough water from the rosette to do the 32 protocols required at each depth, there can be up to 12 casts of the CTD for a single station. During a more typical cruise, there is only one (or a few) casts for each station, and the number of station and depth sampled is higher. The availability of multiple CTD profiles during each Tara station brings further information on the daily cycle, and other high frequency variability.

3.2.5 Samples

The main objective of Tara is to collect samples that will be analysed by partners laboratories once on land. During the mission Microbiomes (2020-2022), more than 12000 samples have been collected (at the time of writing, the samples from the last 5 legs (13-18) have not yet been accounted for). We collected 2000 samples during the leg 5 (Martinique - Macápa) and 1300 samples during the leg 11 (Antarctica). The sampling covers three main categories: ocean biogeochemistry, ocean microbiome (short and long read sequencing, metabolomics, proteomics, imaging, cell chemistry), plastic microbiome (short-read sequencing, biogeochemistry, imaging) and aerosol microbiome (short-read sequencing, biogeochemistry, imaging). The protocols forming the ocean biogeochemistry group include DIC/TA, DIC and carbon 13 isotopes of the DIC (DIC13), salinity, oxygen-argon ratios, oxygen isotopes of sea water, oxygen and nitrogen isotopes of nitrates, methylmercury, trace metals (Fe, Mg, Cu ...) and inorganic nutrients (silicate, phosphate, nitrate, nitrite). As for the EUREC^{4}A-OA cruise, the 68 samples for DIC/TA from the Amazon region were analysed at the SNAPO-CO_2 by Jonathan Fin. The 107 (Amazon) DIC13 samples were measured by Coraline Leseurre and Gilles Reverdin at the LOCEAN-CISE by Cavity Ring-Down spectrometry. The 50 surface nutrients samples were pasteurised and analysed by Francois Baurand in Brest as for the EUREC^{4}A cruise. The 16 samples in the

Amazon plume and river were as well analysed for ammonium on top of the more traditional silicate, phosphate, nitrite and nitrate. The nutrients samples taken on the rosette were frozen and analysed at the CNRS LOMIC laboratory in Banyuls by Mireille Pujo-Pay. Freezing the samples can induce an error for silicate as for high values they precipitate. In both cases, the samples were not filtered, they were left to decant and the part without solid residue was analysed. This results in errors when there was high sediment load, and in different ways for pasteurized and frozen samples.

3.2.6 Drifters

On top of five SVP drifters with an SST sensor drogued at 15 m (similar in form to the ones deployed during the EUREC^{4}A campaign), Tara deployed 43 small surface followers in the Amazon plume region. These small SPOT drifters were developed by the Helmholtz-Zentrum Hereon (Callies et al., 2018). They have a small surface tube and are drogued at 50-cm depth, with tracking done by the Spot/Gobalstar satellite system. They were often deployed as triplets, and when possible at the same site as an SVP drifter.

3.3 Other dataset

3.3.1 ERA5

In order to compute the air-sea CO_2 fluxes on large spatial areas, the European Centre for Medium-Range Weather Forecasts (ECMWF) Reanalysis v5 (ERA5) hourly wind speed, SST and mean sea level pressure (P_{atm}) are used. ERA5 covers the period from January 1950 to present and provides hourly data on a 30 km grid.

3.3.2 Argo floats

An Argo float is an autonomous floating robot that alternately dives and ascends through the top 2000 metres of the ocean, collecting temperature and salinity observations as it goes. The Argo Program has collected roughly 1.8 million hydrographic profiles that are freely available to the public. Prior to Argo, there were about 535,000 hydrographic profiles to depths greater than 1,000 m in the World Ocean Database 2009 (Boyer et al., 2009), with large seasonal and geographical sampling biases (Riser et al., 2016). Today, more than 3800 of these drifters drift over the world's ocean collecting precious information. The Argo program regroups more than 30 countries and was named after the mythical ship of Jason and the Argonauts in search of the Golden Fleece. Together with the satellite mission Jason (monitoring ocean topography), the modern day Argo's quest is to shed new light on the ocean.

The float moves vertically thanks to an hydraulic system, which controls the buoyancy of the float by adjusting the amount of oil in an external bladder. When the float descents, it increases its density by withdrawing oil from the bladder into the instrument. After reaching a defined "parking depth" of usually 1000 meters, the float drifts along with the currents for about ten days. Then, the float descends to 2000 meters before inflating with oil its external bladder, rising to the surface. Along the way, the float records a vertical profile of the ocean temperature and salinity. It is then transmitted on-land via satellite (Argos or Iridium system) after the float reaches the surface. The data collected by all Argo floats is made freely available (http://www.argo.ucsd.edu). Recent Bio-Argo floats can also be equipped with additional sensors to measure oxygen content, ocean pH, and other biogeochemical parameters such as nitrates and chlorophyll. The Argo float CTD measures temperature within an accuracy of 0.001 degree C , pressure within 0.1 dbar, and calculate salinity using conductivity, temperature, and pressure within 0.001 pss.

The dataset is composed of different types of floats used and developed over the years, and it is challenging to detect possible biases in the measurements in particular pressure and conductivity biases. Recently, we have observed that the different physical characteristics of each Argo float could mean that not all of them can rise or descent in steep density gradients. In the Amazon plume for example, a strong surface density gradient in the fresh and warm plume waters prevents some Argo floats to reach the surface and transmit the profiles (Reverdin et al., 2023, to be submitted and presented in Appendix D).

In the body of this thesis, argo floats are used to complement satellite data in the central tropical Atlantic (so are not subject to this issue), when studying tropical instability waves in chapter 5. Argo float temperature and salinity (flagged as good) profiles located in the band 0°N-3°N, 10°W-30°W from January 2010 to December 2018 were used.

Satellite data 4

Satellite and in situ data are extremely complementary. While the resolution and accuracy of in situ data is very high, satellite data offer a near-daily global coverage that in situ data cannot achieve. The objective of this Ph.D thesis is to take advantage of the best aspects of both.

4.1 Sea surface salinity

The definition of salinity depends on whether one defines salinity by its nature (absolute salinity, expressed in g.kg^{-1}) or by its effects on conductivity (practical salinity, sometimes expressed in practical salinity scale (pss)). By nature, salinity is the "total amount of dissolved material in grams in one kilogram of sea water" (Sverdrup et al., 1942). Salinity is estimated by measuring conductivity, temperature and pressure. It is defined as the ratio of the conductivity of water at 15°C to the conductivity of "normal water" under the same conditions. The « Normal Water » or « Standard Seawater » have a known composition and its “Absolute Salinity” (SA) (i.e. mass fraction of dissolved material) is 35.1650 g.kg^{-1}, which is different from its Practical Salinity (35 pss). The Practical Salinity Scale, PSS-78, expresses the Practical Salinity of seawater as a function of temperature and pressure. While the TEOS-10 (Thermodynamic Equation of Seawater, 2010) recommends the use of absolute salinity, the difference between absolute and practical salinity is small in the context of this study focusing on large salinity gradients. Moreover, most instruments, including the salinity satellites, measure the conductivity, and therefore practical salinity. We will use the practical salinity, and the associated Pratical Salinity Scale in the following manuscript.

To retrieve SSS from space, satellite missions use passive measurements in the 1.4 GHz protected band. This wavelength penetrates well through the atmosphere, and the instrument is then able to probe the Earth surface sea surface emissivity even in presence of clouds. At that frequency, the dielectric constant of the ocean that determines the ocean emissivity depends on the conductivity of sea water, and therefore on salinity. Satellites retrieve the salinity in the top 1 cm of the surface layer.

Since the sensitivity of the radiometer measurements to the salinity decreases with decreasing temperature, the most accurate SSS are retrieved in warm waters, which make the tropical Atlantic an ideal study area.

4.1.1 SMOS

The Soil Moisture and Ocean Salinity mission (SMOS) (Kerr et al., 2001) launched on the 2nd of November 2009 monitors the SSS over most of the global ocean regions for more than twelve years (Figure 4.1). This mission, developed by the European Space Agency, the Centre National des Etudes Spatiales (CNES) and the CDTI, is part of the Earth Explorer program. It is innovative in many way, as it is the first satellite to infer

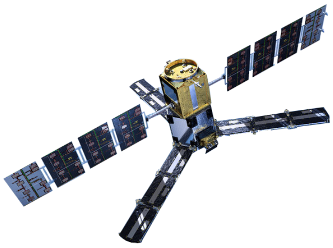

Figure 4.1: The SMOS satellite

SSS. The SMOS satellite carries the Microwave Imaging Radiometer with Aperture Synthesis (MIRAS) instrument, a microwave radiometer using interferometric technique for the first time on-board a satellite. Owing to this novel technique, the spatial resolution of SMOS products is ~45 km, and global coverage can be obtained in three days. However, being the first L band (1.4 GHz) mission has some drawbacks. For SMOS it was to discover the very high and unexpected level of radio frequency emissions in the protected 1400-1427 MHz band which interfere with the signal (radio-frequency interferences, later RFI)(Daganzo-Eusebio et al., 2013).

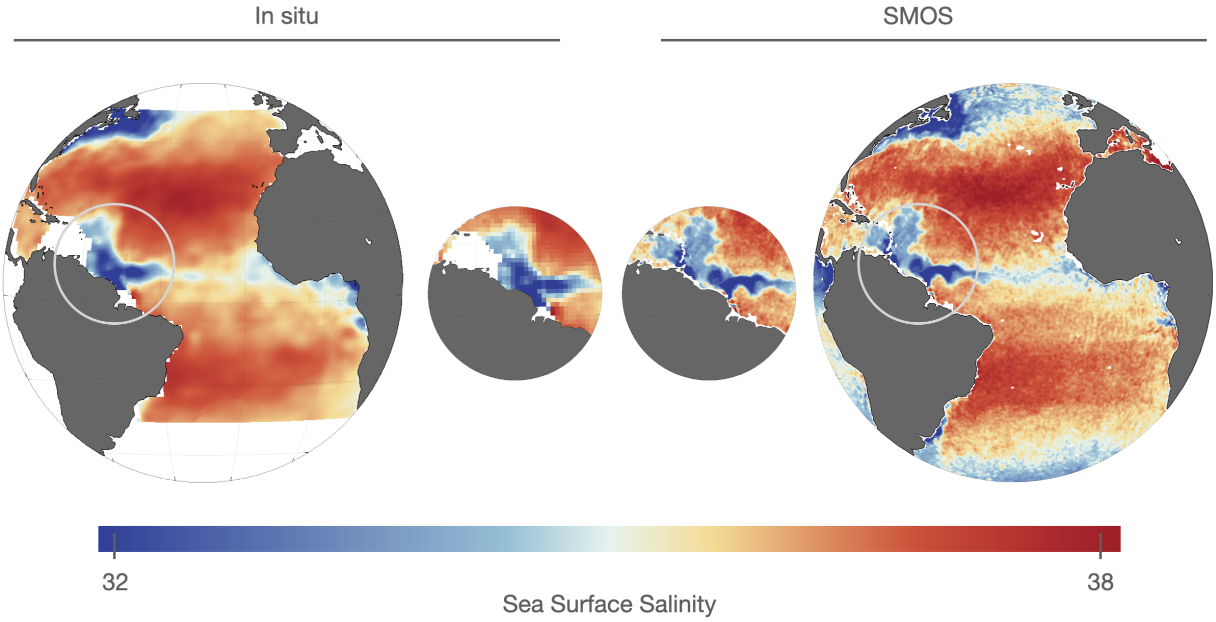

Figure 4.2: The two first figures on the left represent the SSS gridded from ships of opportunity, argo floats and mooring data for August 2010, with a zoom on Amazon river plume in the northwestern tropical Atlantic. The SSS product is an update of the one presented in Reverdin et al., (2007). On the right, the figures represent the same area for a snapshot of SMOS SSS on August 28th, 2010.

The mission characteristics are to cover the globe twice in less than 3 days to capture the quickly varying variables, with a dusk/dawn orbit to minimize the gradients (humidity and temperature) at the land surface atmosphere interface.

As a result of SMOS, for the first time the signature of the oceanic mesoscale circulation on salinity has been highlighted. In 2012, SMOS SSS observations coherently delineated meanders pinching off from the current to form well-identified salty and fresh core Gulf Stream rings (Reul et al., 2014). Figure 4.2 compares the SSS from in-situ data only (only data available before the satellite SSS) and a snapshot from SMOS in August 2010. It highlights the ocean mesoscale, shows well the meandering Gulf Stream as well as the North Brazil Current rings in the Amazon region.

4.1.2 Aquarius

The Aquarius/SAC-D mission (Lagerloef et al., 2008) was developed collaboratively between NASA (National Aeronautics and Space Agency) and Argentina's space agency, Comisión Nacional de Actividades Espaciales (CONAE). Aquarius is a sun-synchronous polar-orbiting radiometer, with a 7 day repeat cycle (Figure 4.3). It provides SSS data from August 2011 to June 2015 and has a spatial resolution on the order of 150 km. In this manuscript, the Remote Sensing System (RSS) version 4 Aquarius data is used.

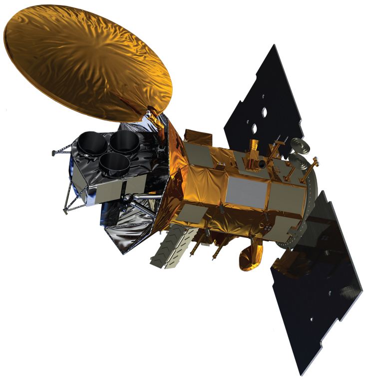

Figure 4.3: The Aquarius satellite

4.1.3 SMAP

The Soil Moisture Active and Passive (SMAP, Piepmeier et al., 2017) had been designed by the Jet Propulsion Laboratory (JPL) and NASA Goddard Space Flight Center for monitoring soil moisture (Figure 4.4). It is a sun-synchronous polar-orbiting satellite mission equipped with a passive radiometer in L-band and an active L-band radar launched on January 31th, 2015. Following the lost of Aquarius, the US teams made a big effort to retrieve SSS from SMAP. Despite the rapid loss of the active radar, the radiometer providing the SSS measurements operates since April 2015. SMAP's orbit covers the entire globe in 3 days, and the measure has a spatial resolution of 40 to 70 km depending on the product, complementing well the SMOS data. Moreover, SMAP has the ability to record time-frequency sub-band data, which provides a way to detect and correct emission contamination caused by man-made sources of RFI.

Figure 4.4: The SMAP satellite

4.1.4 CCI

The Climate Change Initiative sea surface salinity (CCI+SSS) project is an initiative supported by the European Space Agency (ESA) aiming to produce a sea surface salinity Climate Data Record. For the first time, data from all satellites measuring SSS from space are combined, taking each instrument specific features into account. The CCI SSS is based on a temporal optimal interpolation of SMOS (2010-present), Aquarius (mid-2011; mid-2015) and SMAP (2015-present) L-band radiometers measurements (Boutin et al., 2019). The resulting data set enables global SSS to be monitored and studied with unprecedented accuracy over the 2010–2021 period, at a 50 km, weekly or monthly resolution (Boutin et al., 2021). It is smoothed with a 7-day Gaussian filter, and it is sampled on a 25 km grid daily. It reveals large SSS signals related to phenomena affecting climate in various parts of the world ocean, some of which will be discussed in this thesis. The SSS CCI v3.2 is used in this study, the data are freely available and are updated and extended as more satellite data become available.

4.1.5 SMOS + SMAP high resolution

Global CCI SSS products are smoothed over 7 days and one month. In highly variable regions, such as river plumes, variations in surface salinity are expected on much smaller time scales. LOCEAN and ACRI-st in the frame of the Ocean Salinity Center of Expertise for CATDS (CATDS CEC-OS), therefore developed a new temporal interpolation scheme that intends to keep as much as possible high temporal frequency SSS variability (over typically one day or two). Temporal resolution of satellite SSS products is limited by revisit times. The combination of ascending and descending SMOS passes allow revisit times on the order of 1.5 days. The addition of SMAP data consolidates this information. The products are regional, and were made using SMOS SSS only (up to April 2015) and using SMOS and SMAP SSS since May 2015. It uses a local method, that instead of smoothing the data with a 7-day Gaussian correlation kernel such as in the CCI product, it uses an exponential kernel. It gives more weight to the measurements of each individual day and better conserves the temporal variability of the area.

4.1.6 Validation of the SMOS + SMAP high resolution products

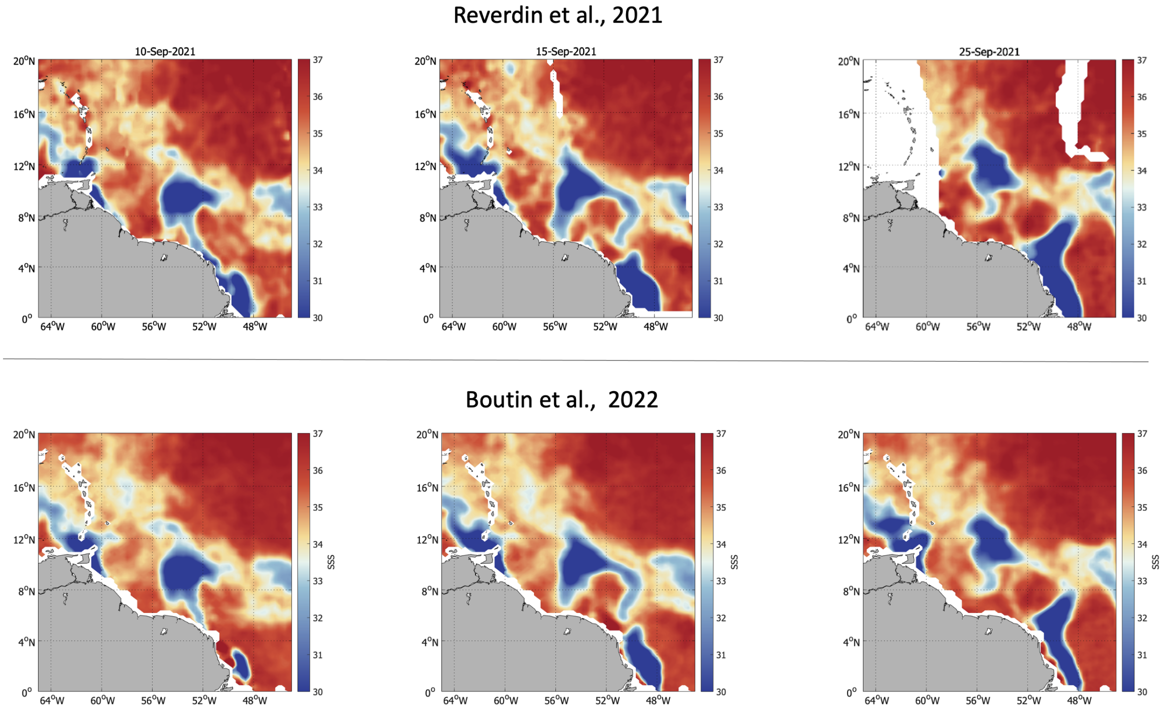

Figure 4.5: Snapshots of satellite SSS along SMOS and SMAP swath for the 10^{th}, 15^{th} and 25^{th} of September, as derived from a superimposition of daily SMOS and SMAP SSS (top, Reverdin et al. 2021) and from a temporal optimal interpolation aiming at keeping high temporal resolution (CATDS High resolution product, Boutin et al, 2022; bottom)

The focus of this study is on medium-scale structures in regions where salinity is highly variable, both spatially and temporally. In order to preserve the temporal variability of salinity as much as possible, we tried not to use salinity products that were too averaged over time. First, we manually combined the ascending and descending orbits of the SMOS and SMAP satellites (work done mainly by Gilles Reverdin and presented in Reverdin et al., 2021). This allows to keep the temporal variability of the Amazon plume, but some days no satellite orbit covers the region of interest. In addition, some errors in the SMOS and SMAP raw swaths had to be removed manually, such as the RFIs.

On this basis, the LOCEAN-ACRI-st CATDS Expertise Center therefore investigated the possibility of producing combined SMAP and SMOS products with higher temporal resolution than the current CCI products. The CCI products are temporally averaged over 7 days using a Gaussian correlation kernel. The aim being to get as close as possible to the products resulting from the combination of raw orbits, several solutions have been considered. The most convincing solution is to use an exponential correlation kernel, which gives a very strong weight to each individual day.

To validate this product, we made several comparisons: with the products from the raw combination of orbits, and with the salinities measured by the TSG of several oceanographic cruises.

The first case study was the Tara Microbiome mission in August-September 2021. We compared the new high-resolution SMOS+SMAP products (Boutin et al., 2022, later called BV) with those from the raw orbit combination (Reverdin et al., 2021, later called RO) and the measurements from the Tara thermosalinograph. The two satellite products are colocalised along Tara's track from August 18^{th} to September 7^{th} 2021. The BV maps are produced daily, while the RO maps are produced on days where there was sufficient coverage by the SMOS and SMAP satellites pour represent the Amazon plume. To compare the three datasets, only the days with RO data are taken into account. Since the SMAP and SMOS spatial resolution is of about 50 km, the Tara data is smoothed over 50 km for a more accurate comparison.

Figure 4.5 shows how the two satellite products compare. The RO product is not smoothed in time at all, so represent the best temporal variability one could expect from the SMOS and SMAP data. In two weeks, the fresh pool presented on figure 4.5 propagates quickly and changes its form. This variability is as well observed on the BV product than on the RO one. Nevertheless, very close to the coast (around 52-50°W) the BV product sometimes present very high salinities. Data close to the coast are often removed in SSS products before the mapping due to higher errors. This, together with inadequate knowledge of the statistical distribution of the monthly SSS over long time period (at the end of the temporal optimal interpolation applied to the CATDS HR product, an absolute adjustment of SSS over the whole time period (>10years) is performed in each pixel by comparing a high quantile of the satellite SSS distribution with the ones of an in situ interpolated SSS product (ISAS) (see Boutin et al. 2021)) implies that the SSS fields are not always consistent with expectation near the coasts. When using this product, these areas (such as those very close to the Amazon estuary) should be handled cautiously.

In Figure 4.6 we introduce the comparison with Tara's along track near-surface salinity data. The RO product seems to better capture the low salinities (15<S<20 pss) sampled by Tara. However, the BV product better represents the medium salinity range (20<S<30). Both product perform well for higher salinities (S>30). The two products have their advantages, but these comparisons show that the BV product performs well, and has the advantage of being gap free and with a daily temporal resolution over 2010-2021. Further comparisons were done in areas of different SSS variability, for different seasons (in winter compared to the EUREC^{4}A data) and different years and are presented in Appendix...

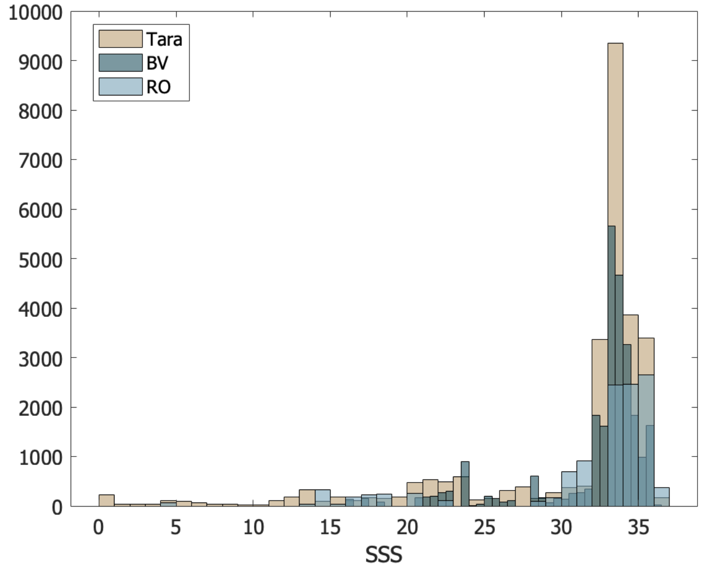

Figure 4.6: Histogram of the SSS distribution for Tara (smoothed over 50 km) and the BV and RO products colocalised along the Tara's track.

4.2 Sea surface temperature

Sea surface temperature (SST) is a key climate and weather measurement obtained from space by satellite microwave and infrared radiometers (Minnett et al., 2019). Space-based infrared instruments are capable of achieving high spatial resolution and are available with a nadir spatial resolution of $\tilde{1}$ km. Infrared SST measurements are obstructed by clouds and contaminated by atmospheric aerosol present in the atmosphere. Fortunately, measurements of SST, at lower resolution, can be made by passive satellite microwave radiometry in all weather conditions except rainfall.

Two products have been used, the Met Office OSTIA SST that provides daily gap-free SST maps, and the high resolution CLS SST maps using only infrared measurements and therefore can have gaps.

4.2.1 OSTIA

The Met Office produces the OSTIA SST analysis daily (Donlon et al., 2012). OSTIA uses satellite SST data provided by international agencies through the Group High Resolution SST Group (GHRSST) regional/global work-share framework. GHRSST products include data from microwave and infrared satellite radiometers. The system also uses in situ SST data available on the Global Telecommunications System. The SST analysis is a multi-scale optimal interpolation that is designed for applications in numerical weather prediction and ocean forecasting systems.

The OSTIA product provides daily map of global sea surface foundation temperature on a 0.05° x 0.05° horizontal grid, using in-situ and satellite data from both infrared and microwave radiometers. The sea surface foundation temperature is the water temperature below the surface that is not influenced by a thermally stratified layer of diurnal temperature variability (either by daytime warming or nocturnal cooling). This product is available from January 2007 to present on the Copernicus Marine Environmental Monitoring Service (CMEMS)

This product is smoother than the CLS one (presented just below) because of the inclusion of microwave data. It will be preferred when dealing with long time series and inter-annual variability, when the need of a gap-free product is essential, such as in Chapter 5.

4.2.2 CLS-SST

The Collecte Localisation Satellite (CLS) SST is derived from satellite infrared radiometers (https://datastore.cls.fr/catalogues/sea-surface-temperature-infra-red-high-resolution-daily). The data of four satellites is averaged daily, and has a high spatial resolution of 0.02° x 0.02°. Since this product only uses data from infrared radiometers, it may have several gaps locally due to the presence of clouds. It is available from May 2007 to present. For the studies presented in chapters 7 and 8 focusing on shorter time periods, this product is preferred. The Northwestern tropical Atlantic during the EUREC^{4}A and Tara cruises was mostly cloud-free or partially clouded ensuring good data coverage.

4.3 Chlorophyll-a

One way the abundance of phytoplankton in the ocean is estimated is by measuring the amount of chlorophyll-a in the water. The chlorophyll-a is a green pigment present in the phytoplankton cells and used for photosynthesis. Chlorophyll-a concentration is a proxy for the surface primary productivity, but represents only the surface concentration. The concentration of chlorophyll a in surface waters can be estimated by measuring the colour of the water (ocean colour) with optical radiometers.

As for CLS SST, the CLS chlorophyll-a product is a daily average (https://data-store.cls.fr/catalogues/chlorophyll-high-resolution-daily) of four satellite sensors, VIIRS (on Suomi-NPP and NOAA-20 US platforms) and OLCI (on Sentinel 3A and 3B Copernicus European platforms). It has a high spatial resolution of 0.02° x 0.02° and is available from May 2007 to present. As for the radiometer SST, it is also limited by the cloud cover. The daily average is nevertheless sufficient most of the time to have an almost complete coverage in the Northwestern tropical Atlantic during our periods of interest. The near-surface concentration of Chla in inland and coastal waters via remote observations, is a challenging task. In near-coastal waters, it can be difficult to separate the chlorophyll-a from the coloured dissolved matter, since detritus and colored dissolved organic matter (CDOM), co-vary with Chla.This issue is particularly present close to the Amazon mouth, as the levels of CDOM are very high, and light can be absorbed by the very large amount of sediment present. Even if algorithm producing the Chla have greatly improved, it is important to note that in coastal region, high levels of Chla can also represent high level of detritus and CDOM, as will be discussed in Chapter 7. Nevertheless, our use of Chla is mainly qualitative and therefore not impacted to much by this issue.

4.4 Altimetry

4.4.1 Absolute Dynamic Topography & Geostrophic currents

An altimeter measures the distance between the satellite and the water surface which, by knowing the altitude of the satellite relative to a reference ellipsoid, can be translated into a measure of sea level. By estimating the difference between the Geoid and this ellipsoid, it is possible to obtain the measurement of the absolute dynamic topography (ADT) and to characterise the variations in sea surface height as a function of an equipotential line of the gravity field. The Sea Level Anomaly (SLA) describes the difference between the actual sea surface height (SSH) and a mean sea surface height over a certain time period. Accurately observing the position of the geoid (thus the ADT) is complicated, but satellite gravity missions and the use of in situ data greatly improved the measurements.

This work uses the products developed by the Segment Sol multimissions d'ALTimétrie, d'Orbitographie et de localisation précise (SSALTO) and Data Unification Altimeter Combination System (DUACS) system thanks to the collaboration between the Centre National d'Etudes Spatiales (CNES) and the CMEMS. This altimetry product delivers the SLA computed with respect to a twenty-year 2012 mean, ADT, and derived geostrophic currents.

Data from all altimeter Copernicus missions (Sentinel-6A, Sentinel-3A/B) and other collaborative or opportunity missions (e.g. :Jason-3, Saral[-DP]/AltiKa, Cryosat-2, OSTM/Jason- 2, Jason-1, Topex/Poseidon, Envisat, GFO, ERS-1/2, Haiyang-2A/B/C) is combined to form daily maps with a resolution of 0.25° x 0.25°. The product optimised with a time lag of several months (delayed-time) is when possible preferred over the operational near-real-time one.

4.4.2 The Ocean Eddy Detection and Tracking Algorithms (TOEddies)

The TOEddies algorithm is an eddy detection algorithm developed by Laxenaire et al., (2018) following an evolution of the method proposed by Chaigneau et al. (2008; 2009). It is based on the key assumption that for geostrophic eddies, the streamlines correspond to the closed contours of Sea Surface Height (SSH). The eddy detection algorithm is a two-step process: it identifies the occurrence of eddies before deriving their trajectories.

The detection method identifies the local maxima (anticyclones) and minima (cyclones) of the ADT as possible eddy centres. It then searches for the outermost closed ADT contour around each extremum. It also defines the contour corresponding to the ADT contour along which the mean azimuthal geostrophic velocity is maximum. This "characteristic contour" tends to be more robust and consistent over time than the outermost contour. Trajectories are computed by associating the eddy with the characteristics (overlap, Rossby number, amplitude) closest to the previous day. Chapters 6 to 8 focus on the interactions of the NBC rings with their surroundings. To define and track the rings, the TOEddies algorithm is used.

RESULTS

Tropical Instability Waves in the Atlantic Ocean

5

5.1 Introduction

The impressive Tropical Instability Waves (TIWs) were the first mesoscale signal observed in the tropical Atlantic in the late 1970s (Duing et al., 1975), and will also be the first studied in this thesis. As introduced in Chapter 1, one of the key characteristic of the equatorial Atlantic is the strong ocean-atmosphere coupling. The intensity of the air-sea exchanges is related through the surface stratification to density. While the temperature signature of the TIWs is well studied, it is not the case of the SSS one. In this first study, we propose to look at both variables in parallel, to study first the signature of TIWs in salinity, but also the respective contribution of these two variables to the surface density.

This study is mainly supported by satellite products of SSS, SST and SSH. In 2009 was launched the first salinity satellite, and since then we have acquired a long term time series, improved by the launched of the Aquarius and SMAP satellites. Their combination provides SSS data at a spatial resolution of 50 km, which is suitable to the study of TIWs whose wavelength is close to 1000 km. This emblematic phenomenon of the tropical Atlantic is the ideal case study to analyse the contribution of surface salinity. First of all, salinity observation from space is easier and more accurate at higher temperatures. Furthermore, these waves have a large spatial scale, which makes them easily observable despite the lower resolution of satellite salinity compared to satellite temperature.

The development of long term time series of satellite sea surface salinity brings new light to this phenomenon. In the first part of this study, we present the seasonal variability of the TIWs signature in SSS, and compare it to their dynamic signature on the SSH and their SST signature. We show that TIWs have a different seasonality depending on the observation variable. The SSS signature is stronger in spring compared to temperature, making it the ideal variable to study TIWs at the beginning of the TIWs season, while temperature is more adapted from June onwards. This result translates on the contribution of salinity and temperature to density. The seasonal cycle of the SSS contribution leads the one of the SST by a month. We show that the contributions of SSS and SST to density have the same magnitude, highlighting the necessity of taking into account salinity when computing surface density. Moreover, in this region, adding salinity makes the density gradient stronger as both contribution enhance each other. Previous studies of the cold tongue dynamics provide clue to understand the one month lag between the two contributions. As the equatorial upwelling starts forming the saline waters of the EUC surfaces, however in July the EUC starts to erode creating to a salinity maximum in June, leading the SST minimum of about a month.

Taking advantage of the 9-year time series, we then delved into the year to year variability of the temperature and salinity signal of the TIWs. We observed than the interannual variability of TIWs in salinity is different from the one in temperature. The temperature signal is closer to the one in SSH, suggesting a dominant role of ocean dynamics. The salinity signal seems to be also strongly driven by the variability of precipitations. The link between the interannual variability of TIWs and the two leading mode of variability in the region, the AMM and the Atlantic Niño is relatively small. While they can explain some individual years or pattern, they do not correlate over the whole time series. Longer time series are need to untangle the relative role of the two modes of variability on the TIWs, while keeping in mind that they may influence salinity and temperature in different ways.

The last part of the paper focuses on the energetics of the TIWs. The study on the seasonality of the TIWs showed that salinity contributes significantly to the surface density gradient. We therefore wonder how including the salinity in the computation of density influenced the potential energy given to the TIWs by the density gradient. Many studies debated the relative importance of kinetic and potential energy as an energy source for the TIWs, however the calculation of potential energy is not complete without the addition of salinity. In order to compute the potential energy induced by the perturbation of the density gradient by the TIWs (PPE, perturbation potential energy), we use all Argo floats profiles available in the equatorial band. The relative contributions of salinity and temperature to the PPE seasonal cycle is the same than the one observed at the surface from satellite. The Argo profiles also show that the TIWs-related perturbation of the salinity gradient penetrates less deep (35 m) in the water column than the temperature one (45 m). The contribution to the integrated PPE over the top 60 m is nearly equally distributed between temperature and salinity. Therefore, not taking into account salinity underestimates the total PPE by almost a factor of two.

This study therefore highlights the strong variability of the TIWs, and that their signature can be different depending on the observation variable. It shows that salinity brings new information to characterise the waves, and that to study their impact on density, either to characterise stratification, or energetics, it is a key variable that enhances the temperature signal. The two variables are complementary, and both bring out different aspect of the waves.

5.2 Article published in *Journal of Geophysical Research: Oceans*: Tropical Instability Waves in the Atlantic Ocean: Investigating the relative role of salinity and temperature from 2010 to 2018

Léa Olivier* • Gilles Reverdin* • Audrey Hasson*† • Jacqueline Boutin*

Received 23 July 2020 – Published 11 November 2020

---

* Sorbonne Université, CNRS, IRD, MNHN, UMR 2159, Laboratoire d'Océanographie et du Climat: Expérimentations et Approches Numériques, LOCEAN-IPSL, Paris, France
† Université de Toulouse, CNES, CNRS, IRD, UPS, Laboratoire d'Etudes en Géophysique et Océanographie Spatiales (LEGOS), Toulouse, France

5.2.1 Abstract

We identify and analyse tropical instability waves (TIWs) in the equatorial Atlantic Ocean during 2010-2018 using satellite derived observations of sea surface salinity (SSS), sea surface temperature (SST), sea level anomaly and Argo profiles. In particular, the weekly 50-km resolution SSS time series from the climate change initiative project provides an unprecedented opportunity to observe the salinity structure at a scale closer to the SST scale. We examine the relative contributions of SSS and SST to the horizontal surface density gradient on seasonal and interannual time scales and how they contribute to the TIW properties and energetics. For the central Atlantic TIWs, the maximum of the SST contribution to the density anomaly lags the SSS one by approximately one month. Argo vertical profiles indicate that temperature and salinity both significantly contribute to TIW-related density anomalies. In May-June, salinity contributes to 50% of the perturbation potential energy (PPE) in the top 60-m, and between 30 and 45 % from July to September. While variations in SST appear to be related to dynamic processes, the interannual variability of SSS is also influenced by precipitations. However, the two leading modes of variability in the region (Atlantic Meridional and Zonal modes) do not well explain at 1°N these interannual variations.

5.2.2 Plain Language Summary

Density is a key variable, influenced by both salinity and temperature and essential to understand the equatorial Atlantic dynamics. Each spring and summer, the horizontal density gradient generated by the equatorial upwelling is subject to undulations associated with tropical instability waves (TIWs). These waves are important features that influence both the ocean dynamics and air-sea interactions. The scarcity of historical salinity observations has been a limiting factor in the study of the relative role of salinity and temperature (and therefore density) in the TIWs dynamics. To do so, we use here an unprecedented 9-year satellite-based sea surface salinity dataset together with sea surface temperature and in situ Argo floats data. We show that the Atlantic TIWs seasonal and interannual variations are different in salinity and temperature. The TIWs surface salinity seasonal cycle leads the temperature one by one month. Concerning the wave energetics, salinity is responsible for almost half of the potential energy generated by the density gradient. Contributions of temperature and salinity are similar in May and June, while temperature dominates in July to September. Further characterization of the seasonal cycle, interannual variations and energetics of TIWs will be necessary to better understand their role in climate.

5.2.3 Introduction

Ocean salinity is one of the key variables governing the density-driven global circulation, which in turn redistributes heat around the globe (Durack et al., 2012). In the tropical Atlantic Ocean, horizontal salinity gradients contribute much to density gradients and therefore to the large scale ocean circulation's baroclinicity (Murtugudde & Busalacchi, 1998; Foltz et al., 2004; Johnson et al., 2012; Lee et al., 2014). Horizontal surface salinity gradients are present in the tropical Atlantic for a large range of scales (Reverdin et al., 2007; Grodsky et al., 2014; Kolodziejczyk et al., 2015). At basin scale, the strongest horizontal salinity gradients are observed between the tropics and the subtropics. This is due to a combination of four main processes: (1) the high evaporation rates of the northern subtropics and south of the equator, (2) the Amazon's outflow which water spreads north of the equator, (3) the tropical rainfall excess north of the equator (Da-Allada et al., 2013; Yu, 2015), as well as (4) advection by a complex current system. The near-surface ocean circulation of the region is indeed dominated by a series of seasonally varying currents and countercurrents bounded by the equatorial edges of the northern and southern subtropical gyres (Lumpkin & Garzoli, 2005; Behera et al., 2013). The tropical Atlantic Ocean is furthermore characterized by a strong mesoscale activity (Chelton et al., 2011) playing a major role in the transport of physical and chemical properties, such as heat, salt and nutrients and presenting strong horizontal gradients.

Close to the equator, horizontal gradients are especially strong because of the presence of the Atlantic cold tongue in spring and summer (Camara et al., 2015; Da-Allada et al., 2017) and the seasonal migration of the Intertropical Convergence Zone (ITCZ). Therefore, salinity does not only vary in space but also with time. In spring and summer this region is subject to strong current shears: between the North Equatorial Counter Current (NECC) and the northern branch of the South Equatorial Current (SEC) at the surface, and between the SEC and the Equatorial Undercurrent (EUC) at subsurface. At the end of the 1970's, Düing et al. (1975) and Legeckis (1977) observed that the meridional position of the temperature front associated with the Atlantic (and Pacific) cold tongue was subject to intraseasonal horizontal fluctuations due to tropical instability waves (TIWs). This discovery fuelled numerous studies based on satellite and in-situ observations, as well as on models. Located within a few degrees of the equator, these waves propagate westward with a time-period of 20-30 days and a wavelength on the order of a thousand kilometres (Legeckis & Reverdin, 1987; Steger & Carton, 1991; Qiao & Weisberg, 1995). They have a marked seasonal variability, peaking in July (Jochum et al., 2004), as well as an interannual variability influenced to a certain extent by the El Niño phenomenon in the Pacific (An, 2008; Im et al., 2012) and Atlantic Niño in the Atlantic (Perez et al., 2012).

TIWs have a strong influence on their environment. Indeed, through air-sea coupling they interact with the winds, clouds and precipitations at local scales (Chelton et al., 2001; Caltabiano et al., 2005; Seo et al., 2007; Wen et al., 2012). Their associated transports contribute to the warming of the mixed layer in the equatorial band (Jochum et al., 2007), as the equatorward heat flux generated by the TIWs in the upper 50-m approximately reaches 100 W.m-2 (Weisberg & Weingartner, 1988) which is comparable to the atmospheric heat flux in the tropics. They also play an important role in the heat exchanges between the surface and the deep ocean (Jochum & Murtugudde, 2006). TIWs are associated with an undulation of the chlorophyll front (Strutton et al., 2001; Jochum et al., 2004) and through their effect on the nutrient distribution (Murray et al., 1994), they impact the development of marine ecosystems (Menkes et al., 2002; Martinez et al., 2018). TIWs hence are important dynamical features that influence the air-sea interactions and biogeochemistry of the tropical Atlantic Ocean. CMIP (Coupled Model Intercomparison Project) models suggest that Atlantic TIWs will be energized under global warming scenarios (Seo & Xie, 2011). Further investigating TIWs from observations would therefore provide useful information to improve their representation in models (Ham & Kang, 2011). Historically, TIWs were first detected from Sea Surface Temperature (SST) and current observations (Düing et al., 1975; Legeckis, 1977). They have then been observed in sea surface height (Musman, 1992; Katz, 1997), and they have also recently been observed in Sea Surface Salinity (SSS) from novel satellite missions, both in the Pacific (Lee et al., 2012; Yin et al., 2014) and in the Atlantic (Lee et al., 2014).

TIWs extract their energy through interactions with the mean background state. Some studies proposed that the undulations of the SST front associated with TIWs originate from barotropic instabilities fuelled by the shear of the tropical currents system: between the NECC and the northern branch of the SEC (Philander, 1976, 1978; Weisberg & Weingartner, 1988; Kelly et al., 1995; de Decco et al., 2018) and between the SEC and the EUC (Jochum et al., 2004; Von Schuckmann et al., 2008). Several studies show nevertheless the importance of baroclinic instabilities in the generation of TIWs (e.g. Cox, 1980; McCreary Jr & Yu, 1992; Grodsky et al., 2005). The baroclinic conversion indeed makes the density gradient contribute to the energetics of the TIWs. It represents the energy conversion between the background available potential energy (APE) and the perturbation potential energy (PPE). The accurate representation of the horizontal density gradient has been a great limitation in studying the importance of baroclinic instabilities in the past. Most observation-based studies (e.g. Weisberg & Weingartner, 1988) did not consider the effects of salinity because of the scarcity of observations. Grodsky et al. (2005) based on data from a single mooring showed that salinity contributed to the energetics of the TIWs in the mixed layer. Lee et al. (2014) supported this observation and drew a first estimate of the salinity gradient contribution to the wave's PPE at basin scale based on unprecedented satellite observations. However, the computation of the energy associated with the waves based solely on surface observations implies strong assumptions on the contribution of salinity and temperature to the density gradient at depth.

The main objective of this study is therefore to investigate the TIWs properties and energetics in the Atlantic Ocean. This study takes advantage of a combination of SSS, SST and sea level anomaly products from remote sensing, as they provide a full dynamical spatial and temporal sampling of the wave surface variability. In particular, the most recent satellite-borne SSS dataset combining the observations of three missions enables us to perform this study over a 9-year period (2010-2018) at a horizontal resolution close to 50 km and at a weekly time scale. The satellite and in-situ data from Argo float profiles are furthermore associated in order to have the most accurate representation of the TIWs' horizontal and vertical structure as well as seasonal variability. This paper is organized as follows. In section 2, the satellite and in situ data products are presented as well as the methodology. Results are reported in the four subsections of section 3. The first subsection presents the analysis of the propagating characteristics and spatial structure of TIWs.

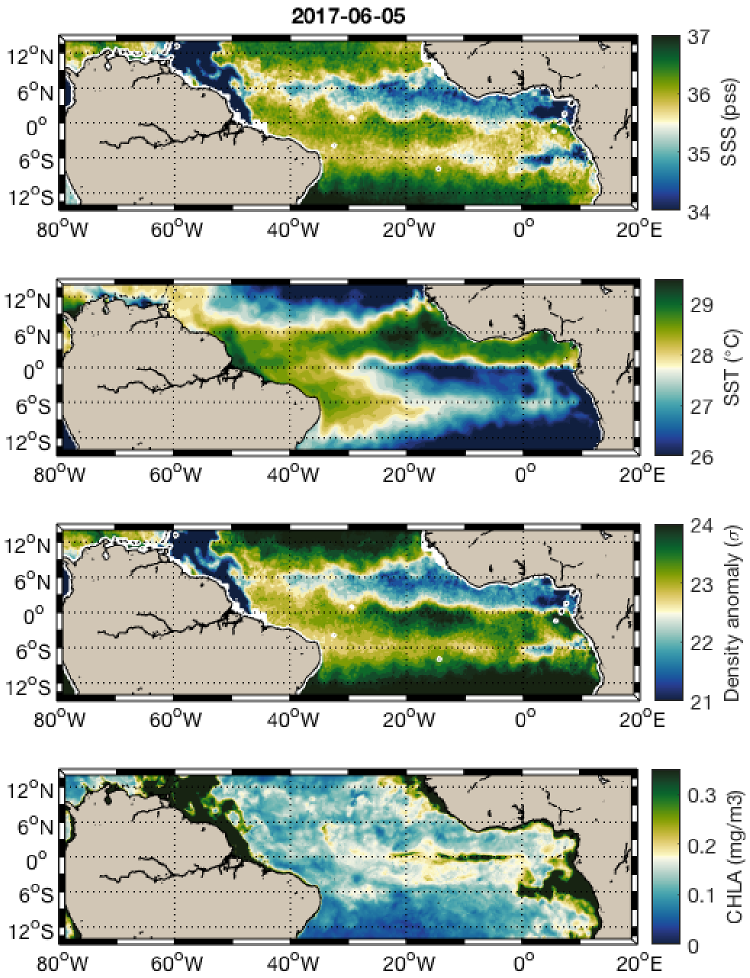

Figure 5.1: 5^{th} June 2017 snapshot of a) sea surface salinity, b) sea surface temperature, c) sea surface density ($\sigma = density - 1000kg.m^{-3}$), d) surface chlorophyll.

The variability on seasonal timescales of TIW signature in SSS and SST and their respective contribution to the density gradient is presented in subsection 3.2, while the interannual variability of TIWs is described in subsection 3.3. The relative contribution of salinity and temperature on the TIW energetics is characterized in subsection 3.4, by estimating the PPE integrated over the upper water column impacted by TIWs. Section 4 discusses the results and section 5 concludes and underlines the limits of this study.

5.2.4 Materials and Methods

Data

We use satellite-derived SSS, SST, chlorophyll (Figure **??**), sea level anomaly and precipitation datasets, as well as in situ data from Argo floats. These datasets are presented below. A core product for this study is the ESA CCI (European Space Agency Climate Change Initiative) version 1.8 Sea Surface Salinity (Sea_ Surface_ Salinity_ cci) available from 2010 to 2018 (Boutin et al., 2019). It provides, at near-global scale, integrated homogenised multi-mission time series of SSS data. It is a long-term multi-mission salinity Climate Data Record based on a temporal optimal interpolation of three L-Band radiometric missions: the Soil Moisture and Ocean Salinity (SMOS, Jan. 2010-present), Aquarius/SAC-D (Aug. 2011; June 2015) and the Soil Moisture Active Passive (SMAP, Apr. 2015-present). Systematic discrepancies between different satellite acquisitions in various geometries are adjusted in a similar way as the adjustments applied to SMOS datasets available at Centre Aval de Traitement des Données SMOS (Boutin et al., 2018). The European SMOS mission consists of a sun-synchronous polar-orbiting satellite (Font et al., 2009; Kerr et al., 2010; Reul et al., 2020). Its orbit covers the entire globe within 3 days and the retrieved SSS has a spatial resolution of 45 km. The Aquarius/SAC-D mission was developed collaboratively between NASA (National Aeronautics and Space Agency) and Argentina's space agency, Comisión Nacional de Actividades Espaciales (CONAE). Aquarius has a 7-day repeat cycle and provides SSS data with a spatial resolution on the order of 150 km (Lagerloef et al., 2008). Developed by NASA, SMAP mission covers the entire globe in 3 days, and has a spatial resolution of 40 km (Entekhabi et al., 2010; Piepmeier et al., 2017). The merged SSS CCI product dataset used in the present study has therefore an effective resolution of nearly 50 km. It is smoothed with a 7-day Gaussian filter and is sampled daily on a 25-km EASE (Equal Area Scalable Earth) grid. The TIWs interannual variability in the CCI dataset is coherent with the one observed by the individual satellites (supplementary Figure S1). The CCI v1.8 used in this study is very similar in our area of interest to the recently available CCI v2.3. Therefore, no significant changes of the results on TIWs and salinity structures are expected. The Operational Sea Surface Temperature and Sea Ice Analysis (OSTIA) SST product, distributed by the Copernicus Marine and Environment Monitoring Service (CMEMS) combines satellite data provided by the Group for High Resolution Sea Surface Temperature (GHRSST) project, together with in-situ observations (Donlon et al., 2012). The analysis is performed using a variant of optimal interpolation described by Martin et al. (2007). Daily maps of SST are produced at a resolution of 1/20° (approx. 5 km). OSTIA SST uses most SST data available for a day, from both infrared and microwave inferred SST. This product is available from 1981 to present. Sea level anomaly maps are produced by Ssalto/Duacs and distributed by CMEMS. Sea level anomaly is mapped using an optimal interpolation method. It is produced daily on a 0.25° x 0.25° grid. The product chosen (SEALEVEL_ GLO_ PHY_ L4_ REP_ OBSERVATIONS_ 008_ 047) combines data from all satellites available for the period 1993 to present. We also use rainfall data from the Global Precipitation Climatology Project (GPCP) in its version 2.3. This product merges data from rain gauge stations, satellites, and sounding observations to estimate monthly rainfall. Precipitations are then available on a 2.5° global grid from 1979 to present, and a monthly climatology over the years 2010-2018 is made. The GPCP data is provided by the NOAA/OAR/ESRL PSD (Adler et al., 2003). Surface chlorophyll data are the GlobColour dataset derived from ocean color at a 1/24° resolution. It is a merged product from multiple satellite missions observations (SeaWiFS, MERIS, MODIS, VIIRS NPP, OLCI-A, VIIRS JPSS-1 and OLCI-B; Maritorena et al., (2010)). GlobColour data is developed, validated, and distributed by ACRI-st.

In addition to the satellite-based data, we use Argo float temperature and salinity (flagged as good) profiles located in the band 0°N-3°N, 10°W-30°W from January 2010 to December 2018 (supplementary Figure S2). All Argo float profiles for the period and area of interest (648 in total) are interpolated with a 1-m resolution. The top 5-m measurements are discarded due to the lack of numerous good quality data close to the surface and the value at 6 m is extrapolated to the surface.

Methods

Various studies have shown that the most energetic TIWs have frequency and wavelength in the equatorial band in the 20-50 day period range and close to 10° zonal wavelength (Legeckis & Reverdin, 1987; Steger & Carton, 1991; Qiao & Weisberg, 1995; Jochum et al., 2004). In order to detect changes due to the TIWs variability (and following the approach proposed by Lee et al. (2014)), SSS, SST and sea level anomaly data are filtered with a 20-50 day 0-phase second order Butterworth band-pass filter. Further very long wavelength zonal variability structures are removed with a 20° high-pass second order 0-phase Butterworth filter. These long wavelength structures are particularly intense in the first half of the year. Special treatment was applied to SSS in order to reduce the noise and enhance the signal of the SSS gradient in the central tropical Atlantic: SSS data are averaged over 5 pixels (5x0.25°) in longitude, on the basis of a comparison with ship-mounted thermosalinograph and satellite data presented in the supplementary information (Figure S3). For all variables the amplitude (envelope) of the wave packet is deduced from the filtered TIW anomalies. We assume that the filtered signal can be approximated by a harmonic wave

$$A(t)\cos(\omega t + \Phi) \tag{5.1}$$

where $A(t)$ is the amplitude, ω the local pulsation, and Φ the local phase. $A(t)$ varies with a time period T longer than the one of the waves. From the cosine function properties, the temporal mean of squared cosine is $\frac{1}{2}$ over one period. Therefore, a low-passed $\tilde{A}(t)$ is estimated as:

$$\tilde{A}(t) = \left(\frac{2}{T}\int_0^T dt A^2(t)\cos^2(\omega t + \Phi)\right)^{\frac{1}{2}} \tag{5.2}$$

the integration over the time period T is achieved through a 50-days, 0-phase second-order low-pass Butterworth filter.

In order to compute the PPE generated by the horizontal density gradient, Argo profiles from 2010-2018 and between 10°W-30°W and 0°N-3°N (black box in Figure 5.2) are sorted into two categories (positive and negative) based on the sign of the filtered density anomalies. These anomalies for the 5th of June 2017 are represented in Figure 5.2. Mean profiles of salinity, temperature and density associated with positive (t_+,s_+,ρ_+) and negative (t_-,s_-,ρ_-) density anomalies are computed for each month (supplementary Figure S4).

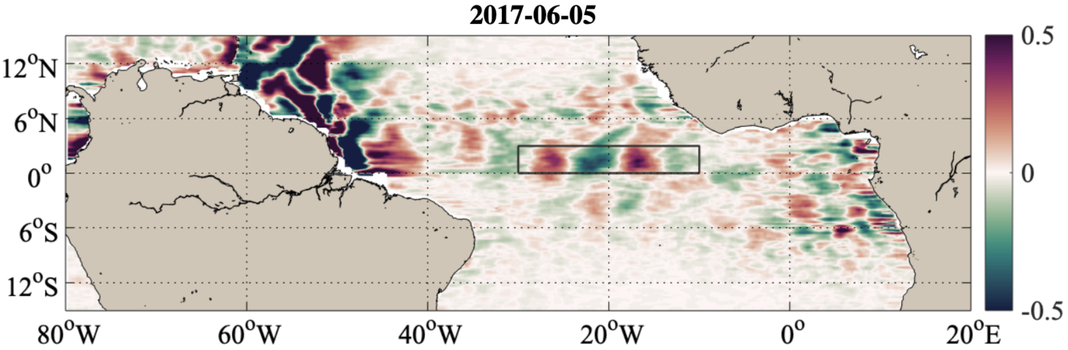

Figure 5.2: Snapshot of the density anomaly on June 5, 2017. The black square corresponds to the region where Argo profiles are selected.

Since Argo float profiles are not evenly distributed, the mean profiles located in positive and negative surface density anomaly for each month are not at the same latitude-longitude. The strong meridional and zonal gradients in spring and summer can bias the results. To avoid this, we divided the large 30°W-10°W longitude band into four smaller bands (30°W-25°W, 25°W-20°W, 20°W-15°W and 15°W-10°W) and neglected the zonal gradients in each band. The mean meridional gradient of temperature and salinity is then estimated from the Argo data set for each couple of months, at each depth and in each band. Mean profiles t_+,s_+,ρ_+ and t_-,s_-,ρ_- are computed for each month, in each band, corrected from the mean meridional gradient and then averaged over the four longitude bands. In the thermocline near the depth of the core of the EUC (near 60 m), the scatter of temperature and salinity between the different profiles becomes large. This results in large uncertainties (supplementary Figure S5) in the composite monthly profile, so we will not interpret the results deeper than 60 m. The results do not change significantly for a small variation of this limit, but would be impacted if the change is on the order of tens of meter as PPE is sensitive to density anomalies at depth. To characterize the density layer directly influenced by salinity anomalies, the top 60 m is divided into two layers: surface to 35 m, and 35 m to 60 m. The 35-m limit is chosen based on the comparison between the positive and negative salinity profiles for the months of May, June, July, August and September. It corresponds on average to the depth where the signal is inferior to 90% of the surface one (the vertical salinity gradient is close to 0) and therefore above which surface anomalies are rather evenly distributed in the water column. A variation of a few meters of this limit does not change significantly the results presented in part 3.4. The PPE of the water column is defined as the vertical integral of the potential energy associated to a small density perturbation (Lorenz, 1955; Kang & Fringer, 2010):

$$PPE = \int_{-60}^{0} \rho' g z dz \tag{5.3}$$

with ρ' the density perturbation computed as $\rho' = \rho_+ - \rho_-$, g the acceleration constant and z the depth in the water column. We are investigating an instability intensified in the upper water column, we therefore integrate from the surface to the EUC depth (60 m). Moreover, below 60 m uncertainties become larger than the difference between the positive and negative profiles (ρ', S' and T' , Figure S5). We separate the contribution of salinity and temperature to the density perturbation as:

$$\rho' = \rho_0 \cdot \beta \cdot S' - \rho_0 \cdot \alpha \cdot T' \tag{5.4}$$

With $S' = S_+ - S-, T' = T_+ - T_-, \rho_0 = 1025 kg/m^3$ the reference density, α the thermal expansion coefficient and β the haline contraction coefficient computed from the mean temperature and salinity profiles for each month. Therefore, the relative contributions of salinity and temperature to the integrated PPE are, for salinity and temperature respectively:

$$\int_{-60}^{0} \rho_0 \beta S' g dz \tag{5.5}$$

$$-\int_{-60}^{0} \rho_0 \alpha T' g dz \tag{5.6}$$

To calculate the available potential energy (APE) generated by the background meridional density gradient, and the contribution of temperature and salinity, we adopt a similar method to the PPE. Instead of calculating the energy associated with the deviation of the mean density profile by a TIW perturbation, we look at the energy associated with the deviation by the meridional gradient of the mean density profile. For each band in longitude we define $\rho'' = \rho_S - \rho_N$ where ρ_S represents the mean density profile in the 0°-1.5°N box and ρ_N the one in the 1.5°-3°N box. We then average over the four longitude bands. By replacing ρ' by ρ'' in equation (3.3) we obtain the APE computed on the top 60 m. The contribution of temperature and salinity to APE are calculated in a similar way by replacing S' and T' by $S'' = S_S - S_N$ and $T'' = T_S - T_N$ in equations (3.5) and (3.6).

5.2.5 Results

Observations and properties of tropical instability waves

Figure **??** represents a typical situation at the end of boreal spring on June 5th 2017 and illustrates the main large-scale and mesoscale horizontal gradients in the tropical Atlantic. The SSS structures reveal the influence of the Amazon's outflow on the western side of the basin. In early June, the just-set North Brazil Current retroflection (8°N-54°W) barely advects any fresh water eastward. The ITCZ, located near 4°N, begins to shift northward and contributes to the band of fresh water between 2°N and 6°N. Around the equator, salty water is brought to the surface by the upwelling system. Mesoscale features such as the cusp-like deformations of the SSS gradient are present around 1°N, with a difference of up to 1 pss between the two sides of the cusp. These features are a trademark of the TIWs and are also observed in both SST (Figure **??**b), with a difference of over 2°C across the cusps, and surface density (Figure **??**c) with a difference of over 2 $\mathrm{kg/m^3}$ across the cusps. The correspondence between SSS and SST features associated with TIWs and surface chlorophyll

(Figure **??**d) corroborates previous studies showing that TIWs play a large role in the biogeochemical processes in the equatorial Atlantic (e.g. Menkes et al., 2002).

Westward propagation along 1°N is found on all data sets, when filtered to retain the 20-50 days periods and 0°-20° wavelengths in order to highlight the TIWs (Figure 5.3). It has been previously shown that TIWs in the Atlantic are particularly intense at 1°N (Chelton et al., 2000; Lee et al., 2014) and it is also the case in the data used for this study. We nevertheless observe a shift of the SST and SSS front toward the equator in the East and away from the equator in the West (supplementary Figures S6, S7 and S8). Between 2010 and 2018, we observe the presence of TIWs at 1°N every year in SST, SSS and sea level anomaly.

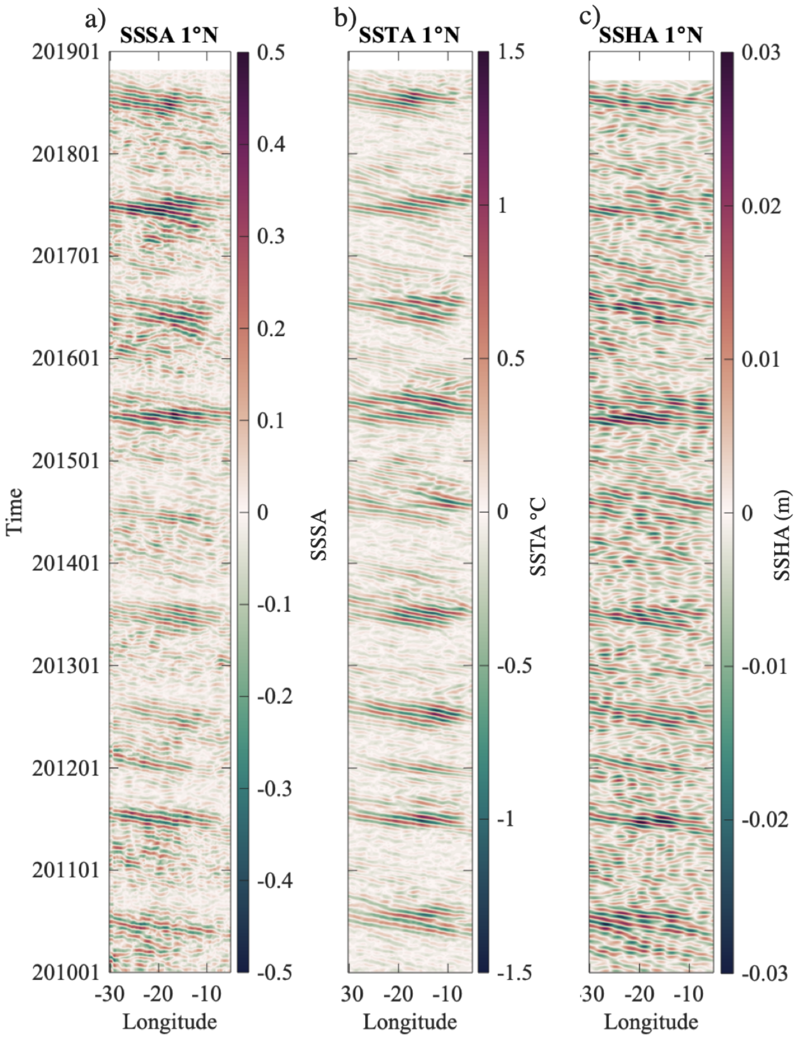

Figure 5.3: 2010-2018 Hovmöller diagrams at 1°N of (a) sea surface salinity anomaly, (b) sea surface temperature anomaly, and (c) sea level anomaly.

Seasonal variability of TIWs signature in SSS and SST and their contribution to the density gradient

The seasonal climatologies of the amplitude of the 9-year SSS, SST and SLA TIW-anomalies (SSSA, SSTA, SLA) are represented in Figure 5.4. The altimeter sea level is a deviation from the local time-mean (hence the notion of sea level anomaly), thereafter we will use SLA to refer to the TIW-anomalies of sea level. TIWs are present in all datasets during the same season (May-September) and are almost non-existent during boreal winter. On average, they reach half of their maximum amplitude on the 5th of May in SSS, 19th of May in SLA and 1st of June in SST. TIWs gradually get more intense (as visible in the amplitude of SLA, Figure 5.4c), and reach a peak in July. Their amplitude then decreases and is significantly dampened (half of the maximum amplitude) by the 1st of August in SSS (a duration of 88 days), 11th of August in SLA (a duration of 84 days) and 21st of August in SST (a duration of 81 days). The SSSA amplitude average is 0.3 pss, with a maximum 0.53 pss in June 2015. The SSTA amplitude average is 0.7°C and reaches 1.3°C in July 2012 (Figure 5.3). The 2011-2012 period stands out as a winter event of TIWs is observed (Figure 5.3, visible on all datasets).

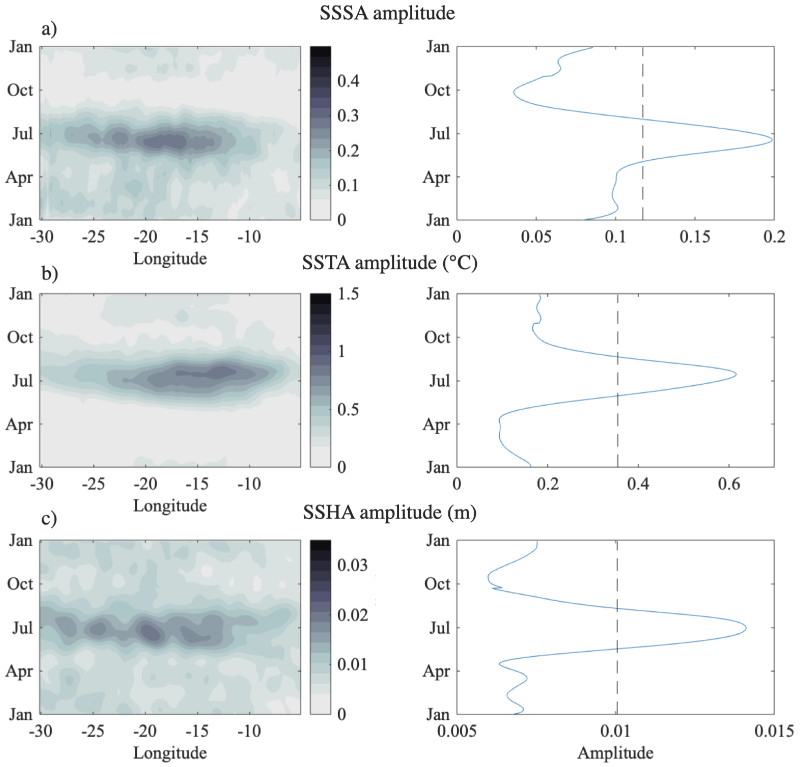

Figure 5.4: Hovmöller diagram of the 2010-2018 (a) SSSA amplitude climatology, (b) SSTA amplitude climatology, (c) SLA amplitude climatology at 1°N (left) and corresponding longitude averaged monthly climatology (right). The dashed line corresponds to half of the maximum amplitude.

We investigate the seasonal variability of both SST and SSS and their relative contribution to surface density (respectively $\rho(SSTA)$ and $\rho(SSSA)$). By linearizing the equation of state for sea water (small variations of the density) at the surface with respect to a mean state, we have the following relation:

$$\rho = \rho_0[1 - \alpha(T - T_0) + \beta(S - S_0)] \tag{5.7}$$

Therefore,

$$\rho(SSSA) = \rho_0 \cdot \beta \cdot SSSA$$

and

$$\rho(SSTA) = -\rho_0 \cdot \alpha \cdot SSTA$$

where α and β are fixed and computed with T_0 and S_0 (35.8 pss) the mean values of SST and SSS for the season and region investigated. Changes in thermal and haline coefficients due to the seasonal and interannual SST changes are neglected as they are relatively small here.

At first order, $\rho(SSTA)$ is only slightly higher than $\rho(SSSA)$ (by 0.05 kg/m^3, Figure 5.5). In 2017, $\rho(SSSA)$ is even higher than $\rho(SSTA)$. The surface density gradient is significantly influenced by salinity in 2012-2013, as observed by Lee et al. (2014). This result is relevant for all years, and the contribution of SSS to the TIW density gradient was even smaller in 2012-2013 than the 9-year average. At the surface, the contribution of salinity to the horizontal density gradient is comparable to the one of temperature and thus not negligible. On average the TIW signal appears 27 days earlier in SSS than in SST (Figure 5.4). The relatively weak SST gradient in spring allows the strong SSS gradient to significantly influence the density gradient. A lag of 26 days is also found between $\rho(SSSA)$ and $\rho(SSTA)$ (Figure 5.5c), considering the appearance date as the date where the amplitude reaches half of its maximum intensity. Until the 11th of June, $\rho(SSSA)$ dominates over $\rho(SSTA)$. During the second part of the year (after August), the signal in SSS is much weaker while the one in SST lingers until the beginning of boreal autumn.

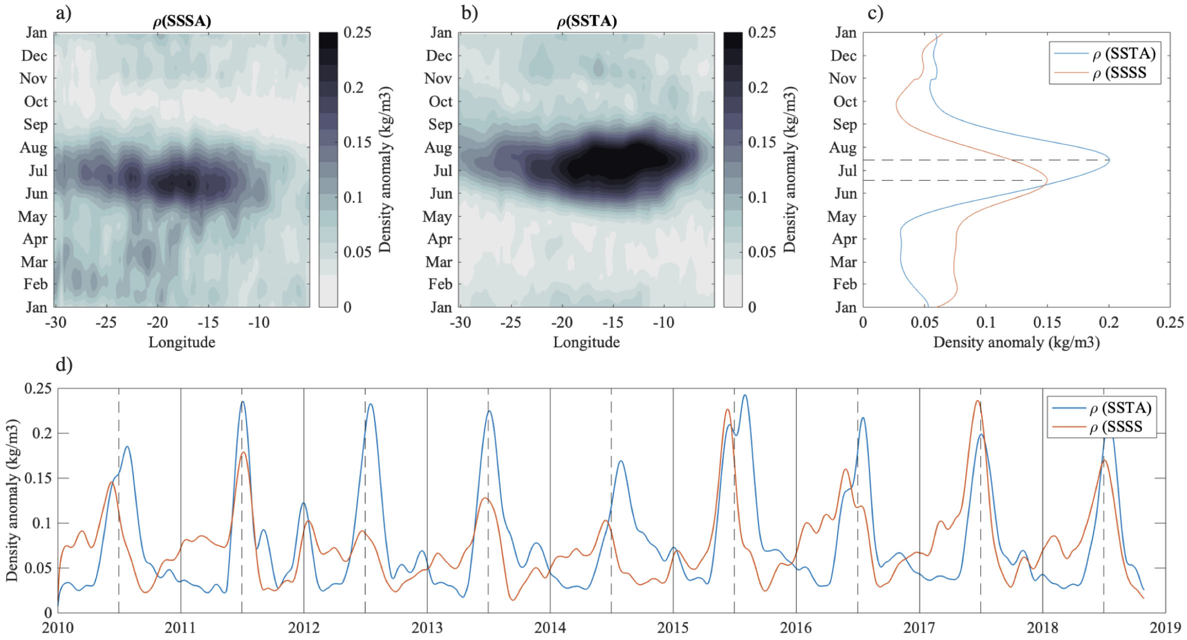

Figure 5.5: Hovmöller diagrams of the 2010-2018 climatological SSSA (a) and SSTA (b) amplitudes contributions to surface density at 1°N. (c) Corresponding 30°W-5°W longitude averaged climatologies for the contribution of SSS (orange) and SST (blue). (d) Nine-year time series of the contribution of SSSA (orange) and SSTA (blue) to density averaged over 30°W-5°W longitude.

Interannual variations of TIW properties and signature in SSS and SST

The relatively short 9-year long SSS and SST time-series provide some preliminary information on the interannual variability of TIWs (Figures 5.5d, 5.6). The Atlantic Ocean presents a large and complex interannual variability. While the SST variability associated with TIWs has been studied before (e.g. Perez et al., 2012), we have the opportunity to study the SSS variability and therefore the relative contribution of salinity to the density gradient and TIWs density anomaly.

Regarding the interannual variability of the amplitudes of SSSA, SSTA and SLA, three time-periods stand out (Figure 6). From 2012 to 2014, TIWs signature in salinity is low. On the opposite, the amplitude of SSSA is the strongest during the 2015-2018 time-period. 2010-2011 is characterized by moderate salinity amplitudes. The variations of the amplitude of SSTA and SLA do not present the same patterns as the one of SSSA. Indeed, in contrast to the amplitude of SSSA, both the ones of SSTA and SLA are weaker than usual from 2016 to 2018. The three datasets are nevertheless concordant in 2011, 2014 and 2015. In 2011 and particularly in 2015 they present stronger amplitude than usual, and the opposite happens in 2014. Overall, the interannual variations of SLA are more correlated with the one in SSTA than in SSSA (SLA is correlated to SSTA with a correlation coefficient of 0.6 and only of 0.25 with SSSA).

Interannual variations of $\rho(SSSA)$ reflect the ones of SSSA particularly well (Figure 5.5d). $\rho(SSSA)$ is lower during the 2012-2014 period, and particularly large in 2011, 2015 and 2017. $\rho(SSTA)$ follows the same variations as the amplitude of SSTA, but its year-to-year variations are less pronounced. Changes in seasonality happen only in 2011, when $\rho(SSSA)$ peaks later than usual and leads to the disappearance of the one-month gap between $\rho(SSSA)$ and $\rho(SSTA)$. Thus, the interannual variability of the TIW signals at 1°N does not follow a unique pattern, with changes in seasonality and intensity that can be different in SSS from SST. The results at this latitude hold for nearby-latitudes (c.f. supplementary Figures S6, S7 and S8 showing high correlation coefficient between the time series at 1°N and the ones at 0.5°N and 1.5°N, as well as slightly smaller standard deviations at these other latitudes). The small interannual latitudinal shifts of the SSS and SST fronts are thus not responsible for the changes between the SST and SSS signals described above.

By a radon transform in the 30°W-5°W longitude range we compute a mean westward velocity (averaged on SLA, SSS and SST for their common period of maximum intensity (6th of June - 20th of July, Figure 5.4, Figure S9)), of 0.4 m/s. The radon transform has been previously used in several studies to compute the phase speed of waves (Cipollini et al., 2001; Caltabiano et al., 2005; Yin et al., 2014) and is detailed in Hill et al. (2000). It gives the variance of the longitude-time plot along a radial line oriented at a specific angle. Phase speed can then be obtained by retrieving the angle of maximum variance. The phase speed of TIWs varies interannually. Such a variability has been suggested by previous studies in the Pacific (Contreras, 2002; Lee et al., 2012; Yin et al., 2014). From 2010 to 2018, the respective wave speeds are : 0.35 (2010), 0.45 (2011), 0.3 (winter 2011-2012), 0.35 (2012), 0.35 (2013), 0.45 (2014), 0.4 (2015), 0.3 (2016), 0.45 (2017), 0.4 (2018), in m/s, reported to the closest 0.05 m/s. These estimations have to be used carefully as the speed of TIWs is also subject to considerable spatial variability, and the time-period over which it is estimated is not very long. It indeed changes with longitude, as phase speeds are usually faster in the east than in the west (Jochum et al., 2004), and with time, as they are faster in June than in September. What stands out is that waves propagate more rapidly in 2011, 2014 and 2017 and are slower in 2016.

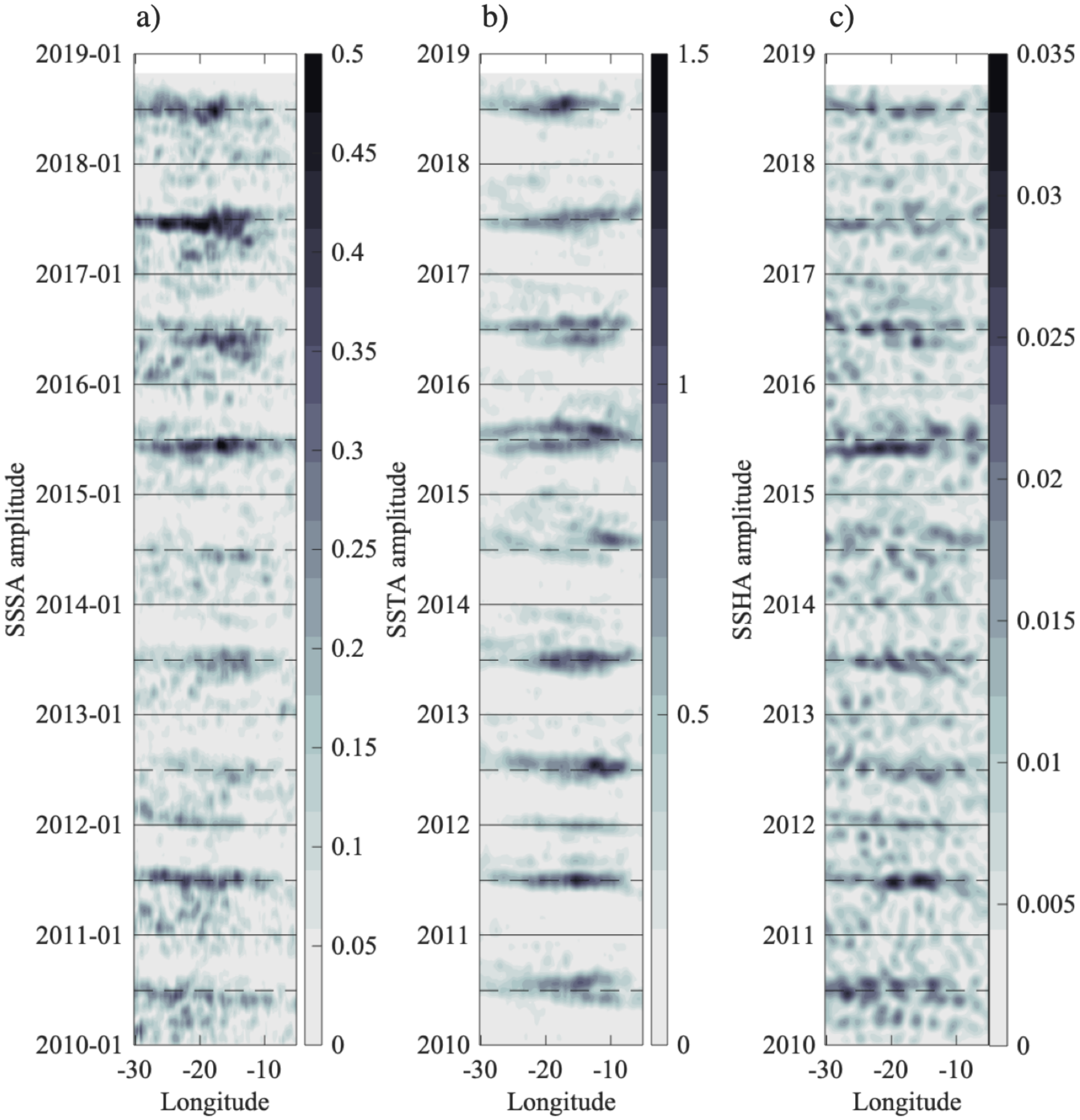

Figure 5.6: 2010-2018 Hovmöller diagrams at 1°N of (a) SSSA amplitude, (b) SSTA amplitude, (c) SLA amplitude. The mean AMM index for the month of April-May- June (orange) and the opposite of the mean ATL3 index for the month of June-July-August (blue) are represented in (d). AMM, Atlantic Meridional Mode.

Energetics of TIWs: PPE

TIW energy is associated with the total perturbation energy, sum of the perturbation kinetic energy and perturbation potential energy (PPE). Baroclinic instability converts energy between the background APE and the PPE. This is modulated by the density gradient. Previous satellite-based papers addressing the question of the energy delivered to the TIWs by the horizontal density gradient were limited by the lack of subsurface data. One approximate way to get around this problem is to use a definition of the PPE similar to the one for vertically-propagating internal waves, as done by Lee et al. (2014). However, with a focus on the energy extracted by TIWs from the horizontal density gradient, one should in particular consider what happens in the near-surface ocean, to which the approximate formula may not be relevant. This study is based on 9 years of data and includes sufficient Argo profiles in each climatological month to assume that our results are representative of the mean monthly situation during these 9 years. The Argo data provide vertical profiles of density anomalies associated with surface TIWs. Without doing any assumption on the vertical density gradient, we compute the PPE at each point of the water column. However, below 60 m the signal becomes too uncertain to be analysed.

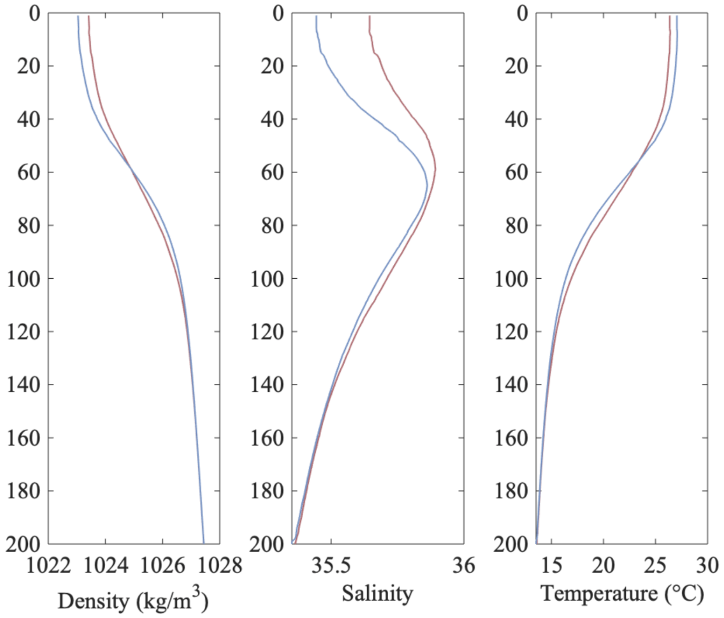

Figure 5.7: Mean density (a), salinity (b), and temperature (c) Argo profiles located in a satellite detected positive (red) and negative (blue) tropical instability wave anomaly for May-June-July-August-September from 2010 to 2018.

Based on the sign of the density anomaly associated with TIWs, profiles were sorted into two categories to create composites. Figure 5.7 presents the mean composites of the density, salinity and temperature profiles averaged in May-June-July-August-September located in a positive and negative TIW-related density anomaly. Near the surface, profiles in a positive density anomaly are saltier, colder and therefore denser than profiles in a negative density anomaly and correspond to characteristic profiles of upwelling conditions. Below 60 m, the sign of the difference in temperature and density changes, but the uncertainty related to the scatter in the dataset is too large, and the results are not significative. Using the density anomaly profiles, we compute the total PPE (Equation 3.3) and the relative contribution of salinity (Equation 3.5) and temperature (Equation 3.6) to PPE. Figure 5.8 shows the integrated PPE on the surface-35 m layer (layer with surface salinity anomalies) and for the 35-60 m layer. In both layers, the contribution to the integrated PPE is nearly equally distributed between temperature and salinity. Therefore, not taking into account salinity underestimates the total PPE by almost a factor of two. These results in the surface layer are similar to the ones deduced by satellite observations from the amplitudes of $\rho(SSSA)$ and $\rho(SSTA)$ (Figure 5.5). In the top layer, salinity and temperature contributions to PPE have the same overall magnitude in May and June (Figure 5.8a). While the contribution of salinity stays almost constant in July, the one of temperature reaches a strong maximum. Temperature contributes to two thirds of the total PPE in July and August. Both contributions then decrease until September. A similar seasonal variability is present at depth (Figure 5.8b). Salinity and temperature contributions are comparable until July, and temperature then contributes slightly more than salinity to the total PPE. Therefore, during the development phase of the TIWs, the salinity contribution to PPE is as important as the temperature one. From July to September, the PPE is dominated by temperature but the salinity signal is not negligible, with salinity contributing 30 to 45% of the total PPE.

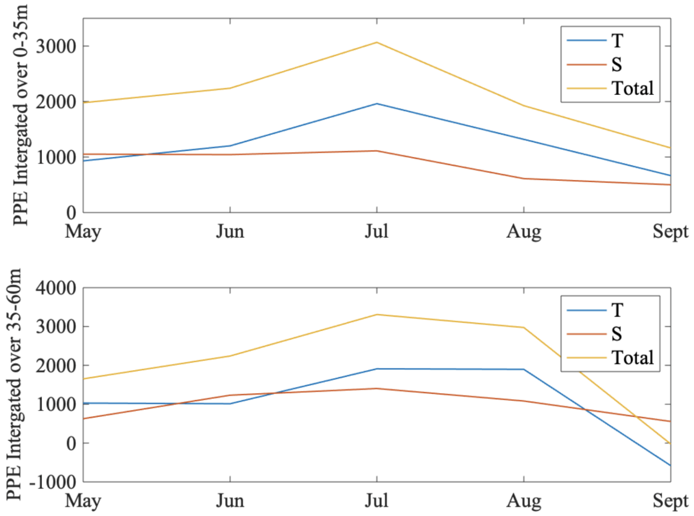

Figure 5.8: Integrated perturbation potential energy on the top 35 m of the water column (a) and on the 35-60 m (b). PPE is represented in yellow; orange and blue describe respectively the contribution of salinity and temperature. PPE, perturbation potential energy.

The background APE, representing the energy available for baroclinic conversion, (supplementary Figure S10) is also subject to seasonal variations. The maximum APE is reached in June (one month earlier than PPE) for both layers, and decreases progressively until September. Temperature contribution the APE is slightly higher than the one of salinity, and is higher in the 35-60 m layer. The APE below 60 m is deeply influenced by the presence of the EUC which goes beyond the scope of this analysis.

5.2.6 Discussion

Mean seasonal cycle

The maximum of $\rho(SSTA)$ lags the one of $\rho(SSSA)$ by approximately one month (Figures 5.4 and 5.5). The maximum amplitude of SSSA is also observed one month before the SSTA one. At large scale, this lag between the maximum of SSS and the minimum of SST in the region of the Atlantic cold tongue has been observed by Schlundt et al., (2014), and studied by Da-Allada et al., (2017). From model data, they analysed the different terms of the salinity budget and found that the vertical mixing between the SEC and the EUC is mainly responsible for the salinification of the area in spring and summer. From further analysis of the EUC they showed that its erosion leads to the disappearance of its associated salinity maximum from July to September, reducing the contribution of vertical mixing and advective salinity flux into the mixed layer. Therefore, the surface signal in salinity starts to decrease in June–July, while the cold temperature signal is maintained up to July by the upwelling. This erosion of the equatorial salinity maximum during boreal summer was also reported by several authors based on observations and models (Gouriou & Reverdin, 1992; Kolodziejczyk et al., 2009; Johns et al., 2014). We suggest here that the large-scale seasonality of temperature and salinity influences the seasonality of mesoscale phenomena such as TIWs. It would induce a time difference of approximately one month between the maximum signals in salinity and in temperature at the surface, which is also the mean lag observed between $\rho(SSTA)$ and $\rho(SSSA)$ (Figure 5.5).This phenomenon can also explain the PPE seasonal cycle, with similar contribution of salinity and temperature in May-June followed by dominance of temperature in July-August.

As observed in part 3.4., the mean seasonal cycle of PPE as derived from Argo profiles (Figure 5.8) has the same shape as the one of $\rho(SSTA)$ and $\rho(SSSA)$ deduced from satellite observations (Figure 5.5c) but with a weaker amplitude. While salinity dominates the satellite surface density signal in May-June, it is indeed less the case using Argo profiles, with temperature and salinity contributing with a similar magnitude. The satellite data products represent SSS integrated over an area of 50x50 km^2 centred at 1°N, whereas we select Argo floats located in the 0°N-3°N latitudinal band. This sampling difference could lead to the observed difference in the respective salinity and temperature contributions. In salinity, TIWs are the most visible at 1°N (see supplementary Figure S6), therefore, even by trying to remove the effect of the meridional gradient on Argo profiles it is still possible that by combining data from this larger latitudinal band the Argo salinity signal is dampened. The temperature signal is also the most visible at 1°N, but is more persistent at higher latitudes than the SSS one (supplementary Figure S7) and could be less affected. Henceforth, it is possible that the influence of salinity is a little underestimated with respect to the one of temperature in the analysis using Argo data. Satellite salinity and temperature are representative of the top surface layer of the ocean (less than 1-cm depth), whereas the Argo profiles uppermost values are at 5-m depth. Even though the near-surface vertical structure of TIWs is not well characterized, it is likely that there might be a slight horizontal shift between the surface and sub-surface structures. This might happen for the signal in temperature as a consequence of surface erosion and of the SST feedback on the air-sea fluxes, and for the signal in SSS as a consequence of rain induced surface stratification under the ITCZ.

Interannual variability

Discussing the interannual variability in the Equatorial Atlantic is challenging. Large scale SST, wind stress divergence and curl, and current shear indices hardly explain the interannual variability of near equatorial TIWs in SST and SLA (Perez et al., 2012). The tropical Atlantic Ocean variability is dominated by two major modes, the Atlantic Meridional Mode (AMM) and the Atlantic zonal mode, commonly referred as the Atlantic Niño mode. We first discuss the interannual variability in the amplitude of the waves, and then of their phase velocity, in light of these modes. We particularly focus on the variability in the TIW-related salinity anomalies, as it has not been studied before.

SSS in the tropical Atlantic is controlled by several seasonally varying processes among which high precipitation under the ITCZ and river discharge (Awo et al., 2018; Grodsky et al., 2020). Both processes are strongly influenced by precipitations, and the leading mode of interannual rainfall variability in the tropical Atlantic is the AMM (e.g. Grodsky & Carton, 2018). It peaks in spring and is related to a cross-equatorial gradient in SST (Ruiz-Barradas et al., 2000; Chiang & Vimont, 2004) that governs anomalous meridional atmospheric pressure differences and related shifts of the ITCZ which in turn affects rainfall. The mean spring (April-May-June) AMM index from NOAA is represented by orange bars in Figure 5.6d. A positive AMM index indicates an anomalous northward shift of the ITCZ. In consequence, precipitations are reduced close to the equator and rainfall enhanced north of the equator. We thus expect more contrasted SSS signals during positive AMM phases. However, the year to year AMM index does not present a strong correlation with the ASSSA. To understand why the relation holds better some years, it is also interesting to look at the AMM trend. Indeed, a decaying phase of the AMM leads to a salinification north of the equator decreasing the salinity gradient at 1°N, whereas this gradient is enhanced during the build-up phase (Grodsky & Carton, 2018). It will therefore enhance the signal resulting from a positive or negative AMM index. During the period of interest here, 2010-2018, AMM goes mainly through two phases: a decaying phase (from positive to negative) from 2012 to 2014 and a build-up phase (negative to positive) after 2014 (Figure 5.6d). These two phases also correspond to the periods of low (before 2012-2014) and high (2015-2018) amplitude of SSSA. Therefore, the decaying phase of the AMM accentuates the decrease of the salinity gradient that we would expect for a negative AMM index, coherent with the low amplitude of SSSA in 2013 and 2014. The opposite mechanism will enhance the salinity gradient, and therefore the amplitude of SSSA as observed in 2016, 2017 and 2018.

The Atlantic Niño is the other main mode of variability in the tropical Atlantic. Several studies have shown the dependency of the Pacific TIW intensity to the El Ni*ñ*o phenomenon (Hashizume et al., 2001; Contreras, 2002; Wang & Fiedler, 2006; An, 2008). During El Niño years, the decrease in SSS and SST gradients associated with weaker-than-usual easterly winds and equatorial upwelling, is believed to generate less energetic TIWs. On the contrary, during la Niña year, TIWs are intensified due to a stronger current shear at the equator and gradients are more pronounced. The SSS and SST TIWs-related anomalies are thus enhanced (Contreras, 2002; Yin et al., 2014). Analogous mechanisms seem to occur in the Atlantic with the Atlantic Niño dynamics, but with a less clear connexion (Perez et al., 2012). The opposite of the ATL3 index (Atlantic counterpart of the Pacific Ni*ñ*o3 index), as defined by Zebiak (1993) and averaged over June-July-August is plotted in Figure 5.6d. The correlation with the amplitude of SSSA, SSTA and SLA is unclear, with some years being in good agreement (2015) and others years not so much (2014). The ATL3 index is in better agreement with SSTA and SLA than SSSA. Even if the intensity of the ATL3 index is not well correlated to the amplitude of the variable studied, 6 years out of 9 we observe an agreement between the sign of ATL3 and the variations of SSTA and SLA. In 2011, 2013 and 2015, Atlantic Niña conditions correspond to stronger amplitudes in SSTA and SLA and the opposite is observed in 2016, 2017 and 2018.

The variations of SSTA are more correlated with SLA than the one of SSSA. This suggests that they are more influenced by dynamical processes (mainly linked to the cold tongue), while SSSA is also impacted by precipitations, river discharge or different dynamics.

From 2010 to 2019, the two indexes tend to work in opposite way. The competition between the two indexes can therefore partly explain the mixed results. A 9-year time series is too short to unravel the parts played by the AMM and Atlantic Ni*ñ*o mode on the interannual variability of SSSA, SSTA and SLA in such a complex environment. We can expect that with longer time series and therefore more meaningful statistics we might be able to shed light on the phenomena driving the interannual variability of TIWs in the tropical Atlantic.

Nevertheless, this study focusing mainly on the variability of the TIW-related salinity anomalies, we will delve deeper into the understanding of two contrasted years that stands out of our time series: 2015 and 2017. 2015 presents strong SSSA, SSTA and SLA (Figure 5.3), whereas 2017 is characterized by strong SSSA but weak SSTA and SLA.

The very intense signature of TIWs on SSTA, SSSA and SLA in 2015 makes this year particularly interesting (Figure 5.3). The good agreement between the three datasets emphasizes the role of dynamical processes. According to the ATL3 index, 2015 is the strongest Atlantic Niña year of the time-series. The observations present multiple characteristics coherent with an Atlantic Niña phenomenon: enhanced SSTA, SSSA and in particular SLA; anomalies extended further east than usual, SSTA and SLA persisting until late summer. Even if the correlation between the TIWs interannual variability and ATL3 index is weak on the 9-year time series, 2015 is a year where Atlantic Niña conditions influence the TIWs for all variables.

In opposition to 2015, the amplitudes of SSTA and SLA are weaker than usual in 2017 whereas strong SSSA amplitude is observed. The horizontal salinity gradient at the surface is strongly enhanced, but not the temperature one. This year, the contribution of SSS to surface density dominates over the SST one during the whole TIW season at 1°N (Figure 5.5d). When considering the SSS anomaly maps for 2017 (supplementary Figure S11a) we observe unusual high SSS in the equatorial band, between 0°W and 20°W which directly contributes to increasing the SSS horizontal gradient. By considering precipitations over the ocean for the months of March-April-May-June 2017 (supplementary Figure S11b), the correlation between the patterns of high salinity - low precipitations and between low salinity - high precipitations is striking. The equatorial salinification is associated with anomalously low precipitations. The high salinity patch is slightly more latitudinally spread out than the precipitation one, probably due to horizontal advection through Ekman transport. Between 16°W and 30°W, north of 3°N, negative salinity anomalies associated with high precipitations anomalies (reaching $2\mathrm{mm.d}^{-1}$) are indeed observed sustaining this stronger than usual meridional SSS gradient. Precipitations as well as dynamical processes may play a role in 2017. From July to September, lower TIW activity in SSTA and SLA at 1°N than averaged over the 2010-2019 period is observed. It is also the period were the upwelling is fully set up, although the cold tongue is weak in 2017 (positive ATL3 index) which reduces the SST contrast, therefore limiting the observation of TIWs in SST. The absence of TIWs observed at 4°N-23°W (Perez et al., 2019) from July to September support the results presented here at 1°N. The observation in salinity therefore deviates from the one in temperature due to the different processes that impact the meridional salinity and density gradient. While in 2017 the salinity gradient seems to be dominated by the precipitations north of the equator, the one in temperature is influenced by the cold tongue dynamics.

The phase speed of TIWs is also subject to interannual variations (Figure S9). On average TIWs propagate at 0.4 m/s which is an intermediate value between the Chelton et al. (2000) speed of 0.3 m/s estimated from microwave SST signals and Lee et al. (2014) speed of 0.5 m/s estimated from SSS, SST and SLA data for 2012-2013, and within the range reported by Jochum et al. (2004) (0.3-0.5 m/s). From 2010 to 2018 the TIW phase speeds vary within these bounds. A certain spread in the phase speed is expected as the waves are generated by an unstable flow field and not by a forcing with a distinct period. Therefore, the TIW properties such as the phase speed range, could result from variations in the properties of the most unstable barotropic or baroclinic modes (Jochum et al., 2004) which depend on the background state (stratification, shear). A change in this background state, seasonal or interannual, would modify the most unstable mode and thus the preferred phase speed. In particular, stronger upwelling and resulting deeper propagation layer (decrease of the stratification due to stronger vertical mixing) and stronger shear should modify the phase speed. Another hypothesis involves the variability of the mean current at 1°N. The absolute pulsation depends on the mean flow. A stronger westward flow at 1°N would hence accelerate the propagation speed of the TIWs. Links with the ATL3 index are however unclear. Enhanced upwelling and surface currents during Atlantic Niña years lead most of the time to high phase speeds (2011, 2014, 2015 but not 2013), whereas the opposite does not hold for Atlantic Niño years.

Satellite data provide a good analysis of the surface TIWs interannual variability, but cannot describe the processes happening at subsurface. Unfortunately, the number of Argo profiles limits the study of the subsurface variability. In order to have a significant number of profiles, we aggregate the data acquired during two distinct periods, each period being characterized by a strong surface salinity anomaly, with TIWs being much less visible in SSS in 2012-2014 than in 2015-2018. It allows us to obtain a significant number of profiles for each period, which makes us confident in the results. By separating the profiles between these two periods, we observe that the PPE in the top 35-m layer is dominated by temperature in 2012-2014 (PPE_T = 545 $J.m^{-2}$ and PPE_S = 231 $J.m^{-2}$) and salinity in 2015-2018 (PPE_T = 613 $J.m^{-2}$ and PPE_S = 736 $J.m^{-2}$). PPE is also larger in the top 35-m for the second period (1318 $J.m^{-2}$ in 2015-2018 and 781 $J.m^{-2}$ in 2012-2014). The high uncertainties linked with the low number of Argo profiles (especially in 2012-2014 where only 146 profiles are used) prevent us from dwelling further into the analysis. Nevertheless, the interannual variability observed at the surface is consistent with the one observed at subsurface, which is promising for further studies on the interannual variability with longer time series and a greater number of profiles.

5.2.7 Conclusions

The SMOS satellite mission provides unprecedented observations of SSS over more than 10 years. By complementing this information with Aquarius and SMAP SSS, the CCI project derives a first combined multi-mission product from 2010 to the end of 2018. The ~50-km resolution of CCI SSS provides a good observation of large scale and mesoscale variability in the tropical Atlantic Ocean. CCI SSS data are able to well capture TIWs and their properties (propagation speed, length scale), in addition to SST and SLA data. In line with previous studies, 1°N is found to be the latitude at which waves are the most energetic. At this latitude, the mean 2010-2018 westward propagation speed is 0.4 m/s. SSS together with satellite-based SST are used to investigate the relative contributions of the two parameters to the meridional gradient of surface density generated by TIWs. Argo profiles are used to investigate the associated subsurface signals. In the top 60 m of the water column, salinity and temperature contributes in almost equal proportions to the PPE. Our study shows that even on a very well documented phenomenon such as the TIWs, the earlier lack of salinity observations of the waves was an issue impeding its full understanding. Not retaining salinity in the computation of PPE would underestimate the PPE by almost a factor 2. This implies that when trying to estimate the respective barotropic and baroclinic energy sources for the TIWs, not taking into account salinity would result in underestimating the baroclinic contribution.

The seasonal variability of TIWs in salinity and temperature differs, as the SSS anomalies generated by the waves peak approximately a month before the SST ones. This lag is also found in the relative contributions of SSS and SST to the density anomaly associated with the TIWs and to the TIW PPE. In May-June the contribution of SSS to PPE has the same magnitude as the temperature one, at surface and at depth and therefore represents ~50% of total PPE. In July-August-September the relative contribution of salinity compared to the one of temperature decreases but still stays relevant and represents 30% to 45 % of the total PPE. An interesting next step in the study of TIW energetics would be to directly consider velocity to draw a more complete vision of the waves dynamics and total energy by including kinetic energy and estimating the baroclinic and barotropic conversion terms.

There is a large interannual variability modulating the seasonal signal, with different variations in SSS, SST and SLA. The Atlantic Meridional and zonal modes contribute to understand these variations for some specific years, such as in 2015, but hardly explain the totality of the interannual variability. Therefore, this 9-year long satellite SSS time series emphasizes the importance of having a long-term time series of satellite salinity. In order to remove the uncertainty concerning the role of the AMM and ATL3 in the interannual variability, a much longer time series (20 to 40 years) is needed. Moreover, the Argo coverage over 9 years is large enough to study the TIWs seasonality, but the analysis is still limited due to uncertainties. It is also too sparse to investigate in detail the interannual variability. Having access to the subsurface structure of TIWs significantly improves the understanding of the seasonal cycle. It also shows that the surface signal can be different from the subsurface one, underlining the complementarity between surface satellite and subsurface in situ data. It would therefore be very enriching to investigate the interannual signal in the same way, for example also including PIRATA mooring data. Furthermore, the SSS satellite product has a one-week temporal resolution. Improving this resolution could lower the smoothing of the wave in the product and better resolve the high frequency variability.

5.2.8 Acknowledgments

This work is a contribution to the Sea Surface Salinity Climate Change Initiative project (contract reference 4000123663/18/I-NB) supported by ESA and to the TOSCA/SMOS-Ocean project supported by CNES (Centre National d'Etudes Spatiales). We benefited from numerous data sets made freely available and listed here : the ESA CCI (European Space Agency Climate Change Initiative) version 1.8 (Sea_ Surface_ Salinity_ cci, https://catalogue.ceda.ac.uk/uuid/9ef0ebf847564c2eabe62cac4899ec41), the OSTIA SST and the SLA produced by Ssalto/Duacs distributed by the CMEMS (https://resources.marine.copernicus.eu), the precipitation climatology project data provided by the NOAA/OAR/ESRL PSD (https://www.esrl.noaa.gov/psd/), the glob colour dataset distributed by ACRI-st (http://globcolour.info) and the Argo data collected and made freely available by the International Argo Program and the national programs that contribute to it (http://doi.org/10.17882/42182). Léa Olivier PhD grant is supported by the Ecole Normale Supérieure and Sorbonne Université. Audrey Hasson is supported by the ESA living planet fellowship. Useful discussions and comments from C. Thouvenin-Masson and A. Supply were appreciated. Helpful discussions with J.L. Vergely about the CCI product are acknowledged. We thank G. Foltz as well as the two reviewers for their interesting comments and suggestions.

5.3 Discussion

This work on tropical instability waves was carried out in 2019-2020. Since then, many studies have advanced our knowledge of these waves, and helped answer some of the questions presented in the introduction. In this discussion part, specific to this chapter, it is also the opportunity to address the biogeochemical impact of these waves. This thesis is based on a physical-biogeochemical coupling, with the aim of understanding the effects of dynamic forcing on biogeochemistry. In the following parts of the thesis, the biogeochemical counterpart of the physical study is performed. This was not the case for this study, so we will present the results of new studies from the literature.

5.3.1 Long term variability

We concluded our study by highlighting the need for long time series in temperature, salinity and currents to study long-term wave behaviour.

Modelling studies have shown that TIWs intensify in response to climate change (Seo & Xie, 2011). Recently, observations have been able to show the long-term intensification of TIWs north of the equator since 1993, in sea surface temperature, sea level anomaly, sea surface salinity and near surface currents (Tuchen et al., 2022). It also highlights the much shorter time-series of SSS and the difficulty to untangle the interannual and decadal variability. Over 2010-2020 the SSS TIWs signal is nevertheless consistent and the TIWs variability in SSS is enhanced during all months. We showed that the TIWs signature in SSS is dominated by the precipitations and the dynamics of the cold tongue and in particular the EUC. There intensification could therefore be linked to these phenomena. Brandt et al. (2021) showed an intensification of the EUC, that could also imply more saline waters brought up by the equatorial upwelling. As climate warms, the global water cycle is expected to intensify (Durack et al., 2012) and the high-precipitations area such as the ITCZ are getting rainier (Yu et al., 2020), decreasing the salinity north of the tropics. These new studies show how all the physical variables of tropical Atlantic are intertwined and how much we can improve our knowledge of this complex system thanks to new and more complete datasets (long term, high resolution, at the surface but also at depth).

5.3.2 Biogeochemistry

The study of the salinity signature of the tropical instability waves is important for the understanding of the biogeochemical and biological impact of the waves. Recently, Shi & Wang (2021) showed that the TIWs-enhanced chlorophyll-a in the tropical Atlantic matched the SSS best, and represented 30% of the mean chlorophyll-a values. They propose that since the phytoplankton blooms is driven by the availability of nutrients, the strong correlation is due to a strong consistency between the change in nutrient concentration and sea surface salinity. Sherman et al., (2022) study in more detail how the phytoplankton reacts to the locally episodic events of enhanced nutrient supply to the euphotic layer by the TIWs. They validate the hypothesis that nitrogen is the limiting factor in the tropical Atlantic (rather than iron for example, that is limiting in the tropical Pacific, Vichi et al., 2008) and that phytoplankton are in a state of balanced growth, waiting for the nutrients which fuel growth and productivity as the TIW passes. Radenac et al., (2020) used a coupled physical-biochemical model to investigate the variability of nitrate in the tropical Atlantic. They show that the main phytoplankton bloom that happens in July-August is driven by as strong vertical supply of nitrate in May-July, the period that we identified as the maximum intensity of the tropical instability waves in salinity. As discussed in section 5.2.6 the EUC surfaces in May-June bringing saline water to the surface, and Radenac et al., (2020) adds that the low-nitrate water also brought up by the EUC are sufficient to enhance the productivity of the cold tongue.

These recent studies highlight the fact that physics and biogeochemistry are coupled, and that in the tropical Atlantic salinity is the variable most related to these phenomena. These studies show the strong link between physics, biology and biogeochemistry and these waves and therefore also suggest consequences for air-sea CO2 fluxes. Unfortunately, due to the lack of in-situ data, this is rather complicated to estimate from observation. In the next parts of this thesis, the presence of new oceanographic campaigns in the western tropical Atlantic, equipped for coupled physical-biogeochemical studies, will allow us to study these phenomena under somewhat different conditions.

Wintertime formation and evolution of a freshwater plume

6

6.1 Introduction

After the study of tropical instability waves in the equatorial Atlantic, we focus in the next parts of this thesis on another type of mesoscale, the North Brazil Current rings. The NBC rings propagate on the western side of the tropical Atlantic, between French Guiana and the Lesser Antilles arc, downstream of the Amazon plume. This next study looks at the interactions between the Amazon plume and the NBC rings in boreal winter 2020. The discharge of the Amazon is minimal in winter, but is still substantial (more than 100 000 m^3/s, so on the same order of magnitude as the maximum discharge of the Orinoco that happens earlier in boreal fall). In this season the strong winds are perpendicular to the coast, and push the water against the shelf (there is little to no Ekman transport and Coriolis force at the Amazon mouth due to its proximity to the equator) and in this region it is thus the wind direction which gives the direction of the momentum transferred to the surface water. It is therefore the period of maximum salinity and minimum productivity in the northwestern tropical Atlantic. The EUREC^{4}A cruise in January-February 2020 challenges this point of view by identifying a plume of freshwater from the Amazon spreading into the open ocean.

At the beginning of February, fresh water reaches the Demerara Rise, a prominent feature of the French Guiana plateau. Instead of staying on the shelf, it gets stirred by the presence of a large NBC ring and spreads out off-shore, reaching up to 12°N. This plume was approximately 120 km wide and lasted for more than 10 days. While the salinity minimum was eroded afterwards the plume was still visible two weeks later. This plume was very stratified, with a freshwater content of 2-3 m of Amazon water distributed down to 40 m. This shallow cap makes the plume driven both by Ekman transport and geostrophic currents.The total area of the freshwater plume reached 100,000 km^2 associated to a transport of 0.15 Sv, approximately the discharge of the Amazon river in February. It therefore represent a very important export of fresh water to the open ocean in winter.

We then looked at the formation mechanism for this plume. First, fresh water from the Amazon needs to arrive on the Guiana plateau. This is possible if the strong easterly wind change slightly its direction. By having a slight northward component, it slightly pushes the water out of the Amazon estuary where it accumulated. We found that on average 3 days of slightly northward wind close to the Amazon estuary favour the transport of freshwater to the Demerara Rise. The second necessary component is the presence of a NBC ring. If no ring is present near the Demerara Rise, the water will stay on the slope until reaching the Lesser Antilles. The Demerara rise is a topographic feature that can momentarily block the progression of NBC rings. When they were discovered, they were even thought to be stationary (Demerara Rise eddies, Bruce 1984; Johns et al., 1990). Not long after leaving the retroflection at the beginning of February, an NBC ring stalled in the Demerara rise region for more than a week. It continuously stirred the freshwater plume toward the open ocean.

We then wondered if this event sampled by the EUREC^{4}A cruise was an exception, or a phenomenon that happened regularly in winter but that was not identified previously due to the lack of observation. By using satellite SSS maps from 2010 to 2020, we were able to demonstrate that this type of phenomena occurs 7 years out of 10. Thus, the winds are the factor determining when the plume will arrive on the plateau while the position of the NBC ring will most likely determine where the plume will detach from the coast.

This study, published in *Journal of Geophysical Research: Oceans* (Reverdin et al., 2021) focuses on the physical properties of this plume and the next chapter will present its biogeochemical properties. I am not the lead author of this study, but I contributed to it significantly. I studied the life of the plume, the mechanisms responsible for the formation of this type of plume (NBC rings and winds) and looked at the occurrence of these plumes from 2010 to 2020.

6.2 Article published in *Journal of Geophysical Research: Oceans*: Formation and Evolution of a Freshwater Plume in the Northwestern Tropical Atlantic in February 2020

Gilles Reverdin[*] • Léa Olivier[*] • Gregory Foltz[†] • Sabrina Speich[‡] • Johannes Karstensen[§] • Jochen Horstmann[¶] • Don Xiao Zhang[‖] • Rémi Laxenaire[**] • Xavier Carton[††] • Hubert Branger[‡‡] • Ruben Carrasco[¶] • Jacqueline Boutin[*]

Received 14 November 2020 – Accepted 17 March 2021

6.2.1 Abstract

In February 2020, a 120-km-wide freshwater plume was documented by satellite and in situ observations near the Demerara Rise (7°N/54°W-56°W). It was initially stratified in the upper 10 m with a freshwater content of 2–3 m of Amazon water distributed down to 40 m. On February

---

[*] Sorbonne Université, CNRS, IRD, MNHN, UMR 2159, Laboratoire d'Océanographie et du Climat: Expérimentations et Approches Numériques, LOCEAN-IPSL, Paris, France
[†] NOAA/Atlantic Oceanographic and Meteorological Laboratory, Miami, FL, USA
[‡] Laboratoire de Météorologie Dynamique, ENS-Ecole Polytechnique-CNRS-Sorbonne Université, Paris, France
[§] GEOMAR Helmholtz Centre for Ocean Research Kiel, Kiel, Germany
[¶] Helmholtz-Zentrum Geesthacht, Geesthacht, Germany
[‖] CICOES/University of Washington and NOAA/Pacific Marine Environmental Laboratory, Seattle, WA, USA
[**] Center for Ocean-Atmospheric Prediction Studies, Florida State University, Tallahassee, FL, USA
[††] Laboratoire d'Océanographie Physique et Spatiale, UBO-CNRS-IFREMER-IRD, Plouzané, France
[‡‡] IRPHE, CNRS-AMU, Luminy, France

2^{nd}, ship transects indicate an inhomogeneous shelf structure with a propagating front in its midst, whereas minimum salinity close to 30 pss was observed close to the shelf break on February 5th. The salinity minimum eroded in time but was still observed 13–16 days later with 33.3 pss minimum value up to 400 km from the shelf break. At this time, the mixed layer depth was close to 20 m. The off-shelf flow lasted 10 days, contributing to a plume area extending over $100000 km^2$ and associated with a 0.15 Sv ($10^6 m^3 s^{-1}$) freshwater transport. The off-shelf plume was steered northward by a North Brazil Current ring up to 12°N and then extended westward toward the Caribbean Sea. Its occurrence followed 3 days of favourable wind direction closer to the Amazon estuary, which contributed to north-westward freshwater transport on the shelf. Other such events of freshwater transport in January–March are documented since 2010 in salinity satellite products in 7 out of 10 years, and in 6 of those years, they were preceded by a change in wind direction between the Amazon estuary and the Guianas favouring the north-westward freshwater transport toward the shelf break.

6.2.2 Plain Language Summary

This study documents how freshwater from the Amazon reaches the deep ocean up to 12°N in the northwest tropical Atlantic in January–March. The classical view is that the water is channeled along the shelf to the Caribbean Sea. Here, we document a freshwater plume from in situ and satellite observations during the EUREC^{4}A-OA/ATOMIC program in 2020. This plume separated from the shelf near 55°W north of French Guiana on February 2–5. This fresher water was stirred by a North Brazil Current ring up to 12°N before mostly spreading westward. The near-surface water was initially very stratified at least until 10-m from the surface. More than 14 days later and 400 km farther north, salinity as low as 33.3 pss with mixing depths on the order of only 20-m was still encountered. The total area of the freshwater plume reached 100,000 km^2 with a flow of freshwater on the order of 0.15 Sv ($10^6 m^3 s^{-1}$) during 10 days. This phenomenon seems to be triggered by changes in the wind direction on the shelf closer to the equator, and has also been observed in satellite products in 7 out of 10 years since 2010.

6.2.3 Introduction

The main topic of this study is the freshwater transport from the Guiana shelves to the Northwest Tropical Atlantic in boreal winter and the processes that control this transport. Fresher surface layers are often relatively thin and induce strong stratification in the upper ocean layers, limiting the turbulent heat and momentum fluxes across the base of the mixed layer. In winter, this condition has the potential to enhance near-surface cooling by sensible and latent surface heat fluxes and the trapping of momentum enabling the development of barrier layers and temperature inversions at the base of the halocline (Mignot et al., 2012). Freshwater originating from the shelves also carries nutrients and organic matter that sustain food webs.

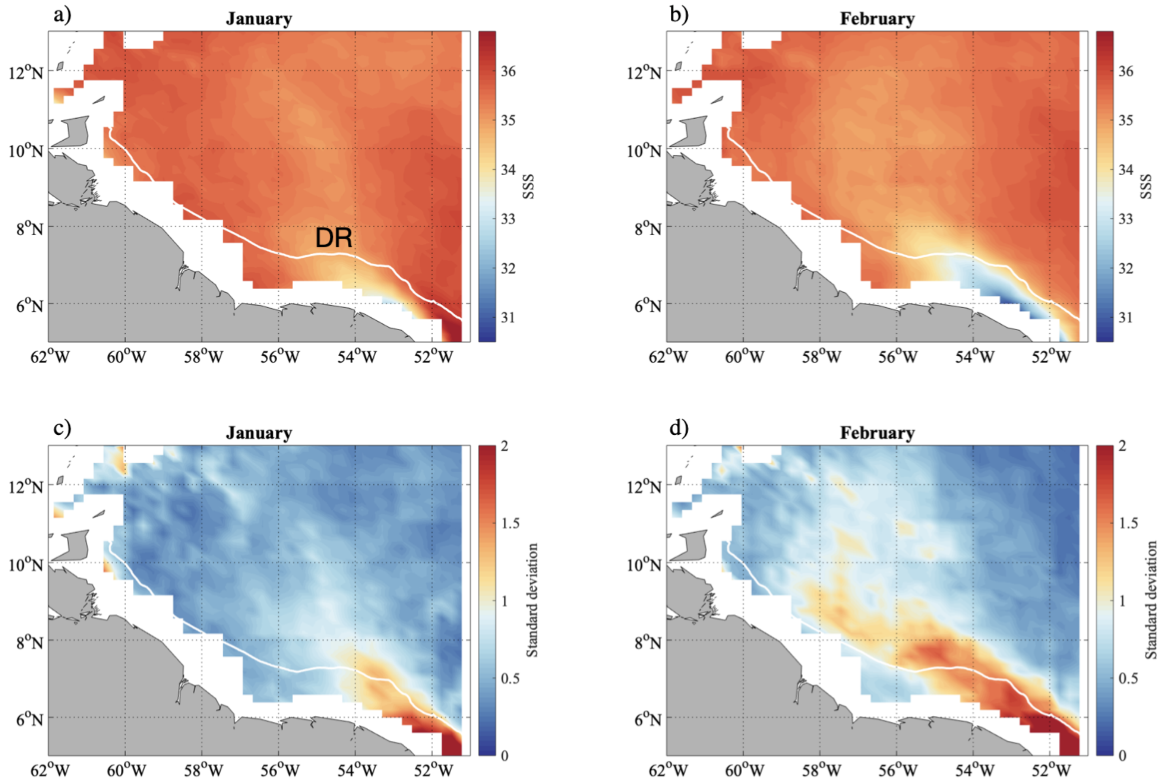

Figure 6.1: Average salinity and its standard deviation based on weekly satellite sea surface salinity (Climate Change Initiative products) in 2010–2019. Upper panels: averages for January and February, and lower panels the corresponding standard deviations. DR indicates Demerara Rise location.

The freshwater input by the Amazon and other northeastern South American rivers is minimal in December and progressively increases from January to May. During this period, the North Brazil Current (NBC) retroflection is either non-existent or weak. As a consequence, January through March is the season of maximum salinity in the northwestern tropical Atlantic west of 45°W, with no offshore transport of freshwater at the NBC retroflection, and with salty water flowing along the continental slope of the Guiana shelves. This is also the season of minimal plume extension (defined by salinity less than 35.5 pss) according to Fournier et al. (2017). However, even in this season, occasional freshwater transport from the shelves, either induced by eddies or the winds (via the Ekman transport), might lead to the development of surface freshened layers, although the associated barrier layers are mostly found north of 10°N (Mignot et al., 2012).

Pathways of freshwater transport have also been documented using data from surface drifters (Muller-Karger et al., 1988) and profiling floats (Hu et al., 2004), which illustrate large seasonal variability of the pathways. It is usually expected that in the early part of the year, the freshwater pathway along the Guiana shelves and into the Caribbean Sea is favoured. This is also documented in the model and data study of Coles et al. (2013) with freshwater mostly trapped on the shelf and no clear evidence from historical CTDs of fresh surface layers offshore of the shelves.

Satellite surface imagery (L-band radiometry) illustrates that this offshore freshwater transport does not happen frequently in January (Figures 6.11a and 6.1b), but that it is often present in February (Figures 6.1c and 6.1d) and later in the year. In February, the weekly sea surface salinity (SSS) product used here for 2010–2019 shows a band of maximum variability near the shelf break between 54°W and 58°W and peaking near 55°W. Though the maximum is within 100 km of the shelf break, the increase in variability compared to January extends all the way to 12°N in the longitude range 54.5°W-58°W, and it is associated with intermittent fresh plumes. This contributes to lowering the average surface salinity in this offshore region.

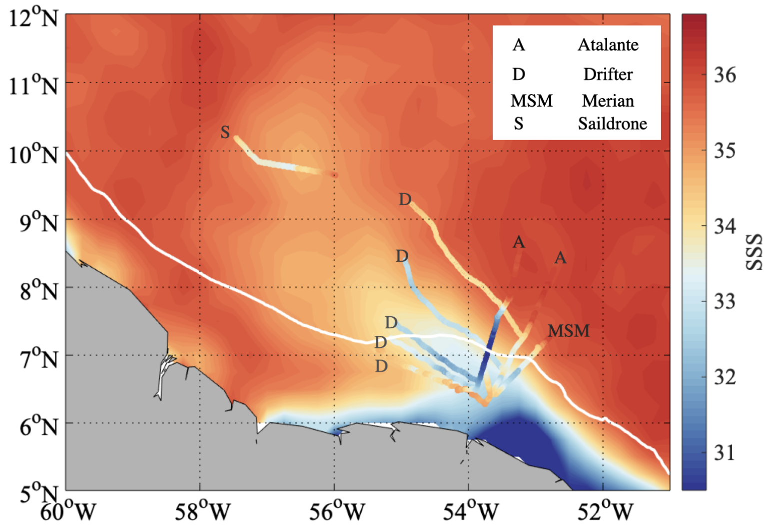

Figure 6.2: Average for February 2–19, 2020 of the daily salinity fields based on SMOS and SMAP satellite data, overlaid with the data collected by the various observing platforms within the fresh plume (A for R/V Atalante on February 2 and 5, Maria S. Merian (MSM) for R/V MSM on February 2; D for drifters on February 2–7 and S for Saildrone during February 16–18). The different tracks/trajectories are color-coded with observed surface salinity.

Pathways of surface freshened layers originating from the shelves and ultimately from the Amazon have been followed in the past using satellite ocean color imagery (Hu et al., 2004; Müller-Karger et al., 1988) and more recently the L-band microwave imagery of surface salinity (Fournier et al., 2015, 2017; Grodsky et al., 2014; Salisbury et al., 2011). The study of Fratantoni and Glickson (2002) illustrates the entrainment of shelf water rich in Chla in the ocean interior around large intense anticyclonic eddies detached from the NBC in February 1999. These eddies were also investigated for hydrography by Johns et al. (2003).

These different studies highlight the importance of eddies in shaping where the transport of fresh shelf water to the deep ocean happens, in particular the role of anticyclonic eddies shed from the NBC retroflection near 8°N close to the Demerara Rise (DR), early in the year. These studies have also pointed out the sensitivity of the freshwater transport to wind magnitude and direction. Winds parallel to the coast and the shelf-break were found to be more favourable for offshore transport than wind perpendicular to the shore. Thus, during the early months of the year, when the atmospheric Inter-tropical Convergence Zone shifts southward, the dominant northeasterly winds are not favourable for this off-shelf transport east of 53°W.

However, quantifying advection and transport of surface freshwater in such analyses is hindered in two ways. First, color imagery is not a direct estimate of salinity (although Salisbury et al. [2011] and Fournier et al. [2015] show how this can be used). Second, the time averaging of the satellite products, in particular from L-Band, is often over one week or more, which is rather long to display the detailed processes involved in the freshwater transport. In this study, we explore the transport of fresh shelf water to the north in this region using novel in situ observations and high frequency satellite products. In early February 2020, during the Elucidating the Role of Clouds-Circulation Coupling in Climate Ocean-Atmosphere (EUREC^{4}A-OA) experiment (Stevens et al., 2021), the RV Atalante and the RV Maria S. Merian (MSM) surveyed an area close to the Guiana shelf just as a plume of freshwater was ejected from the shelf to the deep ocean (Figure 6.2). The period investigated in this study spans from the 2nd to the 21st of February 2020, after which the surface freshened plume was less clear and there were less in situ or remote sensing data available.

6.2.4 Data

The data used include measurements collected by the two research vessels, by five instrumented drifters de- ployed into the freshwater plume, and by Uncrewed Surface Vehicle (USV) Saildrones (Zhang et al., 2019) deployed for the EUREC^{4}A-ATOMIC (Atlantic Tradewind Ocean Mesoscale Interaction Campaign) cruises and equipped to measure sea surface temperature (SST), SSS, and current profiles. The plume was also followed daily using satellite imagery (ocean color and salinity from L-band radiometry), as well as model simulations (Mercator PSY2V4) and satellite altimetry.

In Situ Data

Both RV Atalante and MSM continuously measured temperature (T) and salinity (S) from thermosalinographs pumping water near 5 m below the surface, and they measured wind with dedicated meteorological sensors. During crossings of the fresh plume on the 2nd and 4th–5th of February, either a moving vessel profiler (MVP) or a fast uCTD were deployed from RV Atalante and MSM, providing high resolution T and S vertical profile sections across the plume in the upper 50 m. The RV Atalante was also equipped with a 150 kHz RDI Acoustic Doppler current profiler (ADCP), providing currents 29 m below the sea surface. The MSM 75 kHz ADCP provided calibrated currents starting at 18.5 m below the sea surface (8-m bins).

A coherent-on-receive marine radar (MR) developed at the Helmholtz-Zentrum Geesthacht (Carrasco et al., 2017) was operated on board MSM for monitoring the surface roughness as well as the ocean surface currents in the vicinity of the vessel. The MR operates at X-band (9.4 GHz) with a pulse repetition of 2 kHz with vertical polarization. The pulse length of 50 ns results in a range resolution of 7.5 m and the 7.5′ anten- na array allows an azimuthal resolution of 0.9°. The radar was operated with an antenna rotation frequency of ~0.45 Hz covering a range distance of 3.2 km around the vessel, thus a 6.4 km width along the track of the vessel. The normalized backscatter intensity results from the temporal mean radar backscatter intensity at every point, which is normalized and corrected for range and wind direction dependencies (Dankert & Horstmann, 2007). As the normalized backscatter intensity is strongly dependent on the ocean surface roughness it depicts all structures that affect the surface roughness. In addition, the MR image sequences are utilized to retrieve the near-surface current (in approximately the upper 5 m) maps by analyzing the wave signal (Huang et al., 2016; Lund et al., 2018; Senet et al., 2001). Therefore, the MR image sequences are converted from the spatiotemporal domain to the wavenumber-frequency domain via a 3-D FFT. Within the wavenumber-frequency domain, the wave signal is located on the so-called dispersion shell. In the presence of a current, the Doppler effect leads to a translation and dilation of the dispersion shell. The current is determined using a fit that minimizes the wave signal's distance from the dispersion shell.

Between the two crossings of the plume, the two vessels surveyed a salinity-stratified area on the shelf. During this survey, the free-drifting platform Ocarina (Bourras et al., 2019) was deployed for a little more than 12 h. This platform was equipped with a 1,200 kHz ADCP to measure current profiles at 0.5 m resolution between 0.29 and 17.29 m from the sea surface. These data are combined with temperature and salinity profiles collected from the RV Atalante MVP to estimate the gradient Richardson number (Ri) in this stratified near-surface layer at different times of the day.

The five surface Velocity Program (SVP) drifters deployed in the plume were instrumented by the company "*Pacific Gyre*" to measure temperature and salinity every 30 min at 20-cm, 5-m, and 10-m depths. They also measured surface barometric pressure as well as wind speed and direction 0.5 m above the surface, with regular GPS positioning. Positions were edited for some erroneous data and are less certain for one drifter closer to the coast. Temperature and salinity data retrievals were good at 20-cm depth, with some early loss of data occurring at 5-m and 10-m depth. This was not an issue during the first 10 days of deployment except for one drifter not used here just to the north of the plume. For this investigation, the comparison of the three depth records does not suggest significant salinity biases. A fleet of four USV Saildrones operated in the eddy-rich area north of the Guianas (9°N-12°N) and crossed the freshwater plume during 17th to 18th February. We use the position, temperature, salinity, and wind reported every minute, as well as the ocean velocity profiles (300 kHz RDI ADCP) averaged every 5 min from one NOAA Saildrone. The velocity profiles from 6 m down to a maximum depth of 104 m are provided with a 2-m resolution.

Satellite Data

The satellite data used are daily products of chlorophyll, mapped surface current from near-real time (NRT) DUACS-NRT altimetry products, and daily analyses of surface salinity based on a blend of data from differ- ent L-band radiometry satellite missions. Daily chlorophyll-a (Chla) concentration maps on a spatial grid of 0.02° are provided by CLS (https://data-store.cls.fr/catalogues/chlorophyll-high-resolution-daily). The maps are composites built from four satellite sensors, VIIRS (on Suomi-NPP and NOAA-20 US platforms) and OLCI (on Sentinel 3A and 3B Copernicus European platforms). The VIIRS L1A products are downloaded from the NASA Ocean Color Web, whereas the OLCI L1 products are downloaded from the EUMETSAT Copernicus On-line

Data Access in NRT. As described in Stum et al. (2015), the Polymer software (Steinmetz et al., 2011) is used since 2014 to compute Chla from the top of atmosphere reflectances. During our period of interest, they are usually without many gaps, except on the 13th to 17th of February. We use them qualitatively, so contamination by colored dissolved matter or particles is not an issue for the objectives of this study. Geostrophic current maps are produced by Ssalto/Duacs and distributed by Copernicus-Marine Environment Services (CMEMS). The currents are computed from absolute dynamical topography mapped using an optimal interpolation method (Taburet et al., 2019). The maps (product SEALEVEL_ GLO_-PHY_ L4_ NRT_ OBSERVATIONS_ 008_ 046) are produced daily on a 0.25° × 0.25° grid, based on combined altimetric data of all the satellite missions within the time window from at least 15 days before to 6 days after the date of interest. Mean currents are added to the anomaly as described in Rio et al. (2011). The spatial scales resolved in the currents are usually on the order of 100 km or more, with significant damping at smaller scales (see also Dibarboure et al., 2011, for an earlier product).

The salinity products used are from the Soil Moisture Ocean Salinity (SMOS, January 2010–present), and Soil Moisture Active Passive (SMAP, April 2015–present) missions. The European-led SMOS and the NASA SMAP missions observe the surface by L-band radiometry from sun-synchronous polar-orbiting satellites (Entekhabi et al., 2010; Font et al., 2009; Kerr et al., 2010; Piepmeier et al., 2017; Reul et al., 2020). Both SMOS and SMAP orbits cover the entire globe within 3 days with data provided close to 6 a.m. and 6 p.m. local time. The retrieved SSS has a spatial resolution of ~45 km for SMOS and between ~40 and ~50 km for SMAP. Here, we use the SSS acquired each day on ascending and descending orbits separately, the SMOS L2Q fields (doi: https://doi.org/10.12770/12dba510-cd71-4d4f-9fc1-9cc027d128b0), corrected for systematic errors depending on the geometry of acquisition of the satellite (Boutin et al., 2018), delivered by Centre Aval de Traitement des Données (CATDS) and the SMAP L2 fields delivered by Remote Sensing System (RSS v4 40 km). The SMAP product is a little smoother than SMOS, and it generally has smaller errors also suggesting slightly larger scales resolved. Two SMOS images with evidence of Radio-frequency interference contamination have been removed during the period investigated, and the contamination became worse later in February. We also use SMOS and SMAP combined weekly SSS generated by the Climate Change Initiative Sea Surface Salinity (CCI + SSS) project (doi:https://doi.org/10.5285/4ce685bff631459f- b2a30faa699f3fc5). It provides weekly level-3 SSS data from 2010 to 2019 at a spatial resolution of 50 km, a sampling of 25 km and 1 day, by combining data from the SMOS, Aquarius, and SMAP missions.

We illustrate the different products on the 12th of February, when the fresh plume was fully developed along 56°W (Figure 6.3). Both SMAP and SMOS SSS show a mostly south-to-north structure along 56°W extending from the shelf over to the deep ocean (shelf break in white), although with a slightly different pattern (note that they are taken 12 h apart). The Chla map also shows filaments and regions of higher load, which could be either chlorophyll, remnants of Colour Dissolved Organic Matter or remnants of sediment and detrital matter not fully filtered out of the products. These structures align to some extent with the currents that connect the outer area of the shelf to the deep ocean. They are located on the western side of a large anticyclonic eddy shed by the NBC retroflection (A1). A smaller cyclonic structure (C1) is also visible close to the shelf break, southwest of the northward currents. The Chla map presents finer scales, as expected from the better resolution of the satellite imagery in the visible part of the spectrum compared to L-band radiometry.

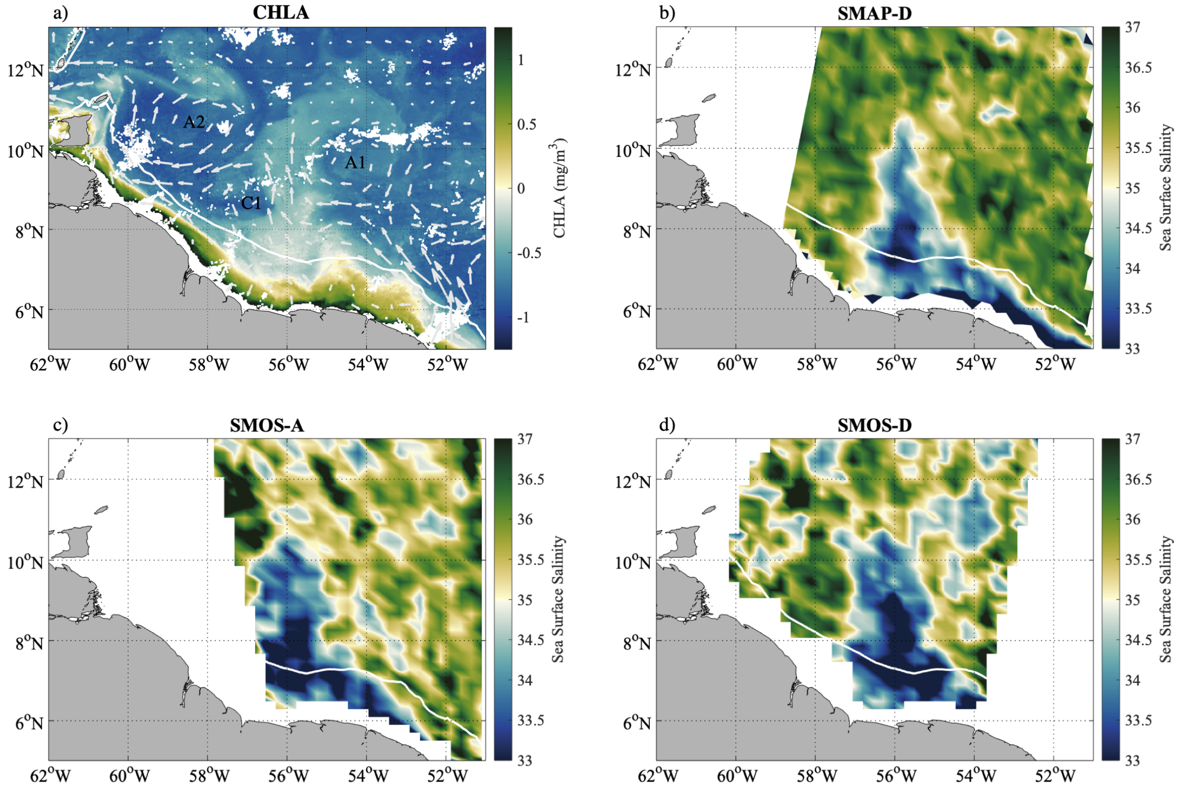

Figure 6.3: Satellite maps on February 12th. Chla and geostrophic currents (white arrows, a), SMAP SSS along its descending track (b), SMOS SSS along its ascending (c), and descending track (d) for the 12th of February. The shelf break is represented by the 100-m bathymetry contour (white line). Two anticyclonic (A1, A2) and one cyclonic (C1) eddy are labeled in (a).

SMAP L2 and SMOS L2Q maps present systematic differences with respect to in situ data that also depend on whether they correspond to descending or ascending tracks. The issue is particularly large for the SMOS product where the systematic differences are also found to vary across the tracks, in particular on the eastern edge of the descending tracks due to a sun-tail contamination not filtered out in the L2Q fields. Part of this contamination is however taken into account in the estimated error provided with the SMOS L2Q products and we eliminated SMOS data for which the estimated error was larger than 1 pss. We attempted to correct the remaining systematic differences on a track by track basis, although the applied adjustment is often uncertain at the 0.1–0.2 pss level, in particular for SMOS. We did not correct island effects on the SMAP maps that are particularly noticeable to the east/north-east of islands (Grodsky et al., 2018) because they are mostly outside of the main area of our study.

In order to provide full salinity fields and reduce errors by averaging enough data, we combined the adjusted SMOS and SMAP L2 gridded fields. As the fresh plume evolves on a roughly daily time scale, as observed for example from Chla maps, it is best to keep a rather short time averaging. For half the days, combining the tracks at 6 a.m. and 6 p.m. (local time) was sufficient to provide full coverage of the fresh water plume. For other days, it was necessary to add data from 6 p.m. of the previous day (thus a total time span exceeding 24 h). This leaves only 2 days with no salinity product, out of the 20 days investigated.

At each grid point, the field value is estimated by a simple weighting of data inversely proportional to the L2Q estimated error, and with a spatial weight decaying as a Gaussian with a radius of 30 km as a function of the distance of the data to the grid point. No data farther than 50 km is incorporated. We also assumed that errors on data closer than 25 km are fully correlated to account for the real footprint of the satellite data which is on the order of 50 km. The resolution of the final daily field is probably close to 70 km. Estimated uncertainties on the daily fields are typically on the order of 0.5 pss, consistent with the comparison to in situ data. The comparisons with in situ data also suggest that the daily fields tend to produce higher salinities in the core of the plume with the freshest observed salinities, and lower salinities on the sides. These are possible effects of the salinity field smoothing, although we could not fully verify it as data coverage was not evenly distributed. The daily fields nevertheless give precious information on the salinity distribution as illustrated in Figure 6.2 for the average over 18 days.

The IFREMER CERSAT Global Blended Mean Wind Fields product, distributed by CMEMS, is used in this study. It provides 6-hourly surface winds in the region of interest on a spatial grid of 0.25° in lat- itude and longitude. From 2010 to 2018, the reprocessed product is used (WIND_-GLO_ WIND_ L4_ REP_ OBSERVATIONS_ 012_ 006), while for 2019 and 2020 we used the near real time one (WIND_ GLO_ WIND_ L4_ NRT_-OBSERVATIONS_ 012_ 004).

Finally, we used ocean velocity and salinity outputs from the Mercator PSY2V4 model, both in analysis and forecast modes. These were made accessible, together with all satellite data, to guide the ships during the field campaign in order to survey the fresh water plumes (Figure 6.4). Since January 30th they consistently suggested a westward (and possibly offshore) extension of the eastern Guiana shelf fresh pool, although they sometimes missed the full extent of the plume's offshore extension.

6.2.5 Results

Life of the Plume

In late January 2020, the region located between 7°N north of the continental shelves of the Guianas and up to 12°N is mostly covered by surface water with a salinity between 35 and 36.5 pss (Figure 6.4), which is typical in this season of low precipitation and low input of freshwater from the Amazon and Orinoco rivers (Figure 6.1). Freshwater is witnessed edging north-westward on the shelf east of French Guiana in late January, both in satellite products and in the Mercator PSY2V4 model simulations. Near 53°W, the shelf break bathymetry changes. Overall, the shallow isobaths tend to be zonally oriented west of 53°W, with a large cone (DR) associated with past sediment transport extending

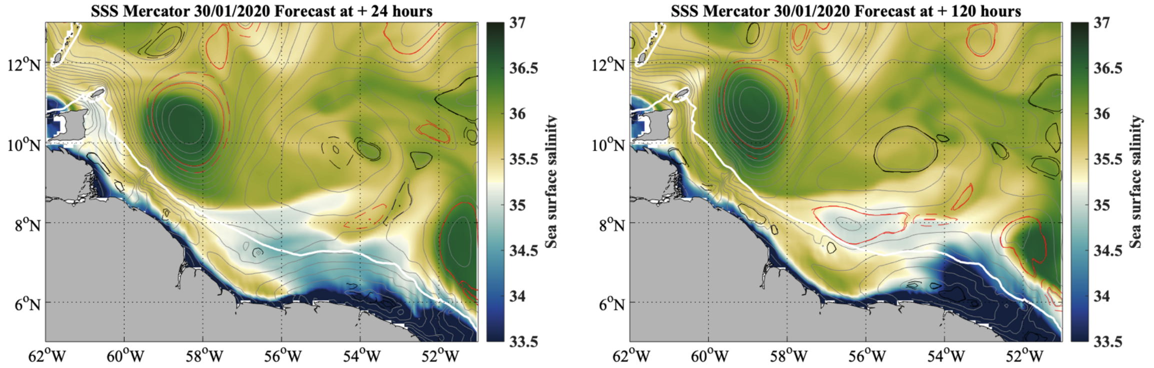

Figure 6.4: Mercator PSY2V4 model SSS (color) and sea level (gray contours) forecast and eddy detection made on the January 30, 2020 for January 31, 2020 (left) and February 4, 2020 (right). The eddy detection is shown by dashed contours (red for anticyclones and black for cyclones; Laxenaire et al., 2018). The shelf break is represented by the 100-m bathymetry contour (white line).

farther offshore and presenting less steep off- shelf topography. Changes in geostrophic currents, often associated with the retroflection of the NBC and formation of anticyclonic eddies to the northeast of the cone, would favor near-surface northward transport. In addition, the wind direction being less orthogonal to bathymetry would also favor off-shelf Ekman transport. Off-shelf transport events are thus expected near that longitude. Indeed, this is what was forecasted from the Mercator PSY2V4 operational model on January 30th with a clear off-shelf extension of the fresh pool indicated on February 4th, even though it did not extend as a full- fledged plume (Figure 6.4). Three SVP drifters were released into this freshened plume on February 2nd, and two additional drifters were deployed during a return section of RV Atalante on the 4th–5th of February a little further north, as the plume extended in that direction (with salinity dropping across this section to close to 30 pss) (Figure 6.2).

To illustrate the plume evolution, we present (Figure 6.5) daily snapshots of Chla and sea surface salinity. The freshwater off-shore event started on February 4th, when the plume began to detach from the shelf, overflowing the shelf break near 53°W-54°W. An anticyclonic NBC ring (A1) northeast of the plume had al- ready entrained relatively fresh water (SSS on the order of 35 pss) since late January all the way up to 10°N. This feature is also seen on the Chla distribution across the shelf break. The northward offshore transport of fresh and productive water continued on the 7th of February, following fairly well the surface geostrophic currents. The anticyclonic eddy (A1) centred around 54.5°W-9.5°N likely participated in advecting water from the plume northward (on its western side) and limited its westward propagation. A small cyclonic eddy (56.5°W-8°N, C1) channeled the northward geostrophic flow and also contributed in steering the plume northward. The situation was quite similar on the 9th and on the 12th with the northernmost part of the plume, rich in chlorophyll, steered by the northern part of the anticyclonic eddy A1. In the meantime, the plume started to be influenced to its west by the eastern side of a second anticyclonic eddy (A2, centred around 58.5°W-11°N). Around the 12th, we observe the first indication (in particular in SSS) suggesting a future separation of the plume from the shelf. This separation started on the 14th of February and was clearly visible on the 15th. The dynamic situation changed quickly as the cyclonic eddy C1 disappeared, with a strong north-westward current near the shelf almost topographically steered, and the two anticyclones north of 9°N. The fresh pool formed by the plume spread horizontally (and probably vertically), with surface salinity on the order of 33.5–34 pss.

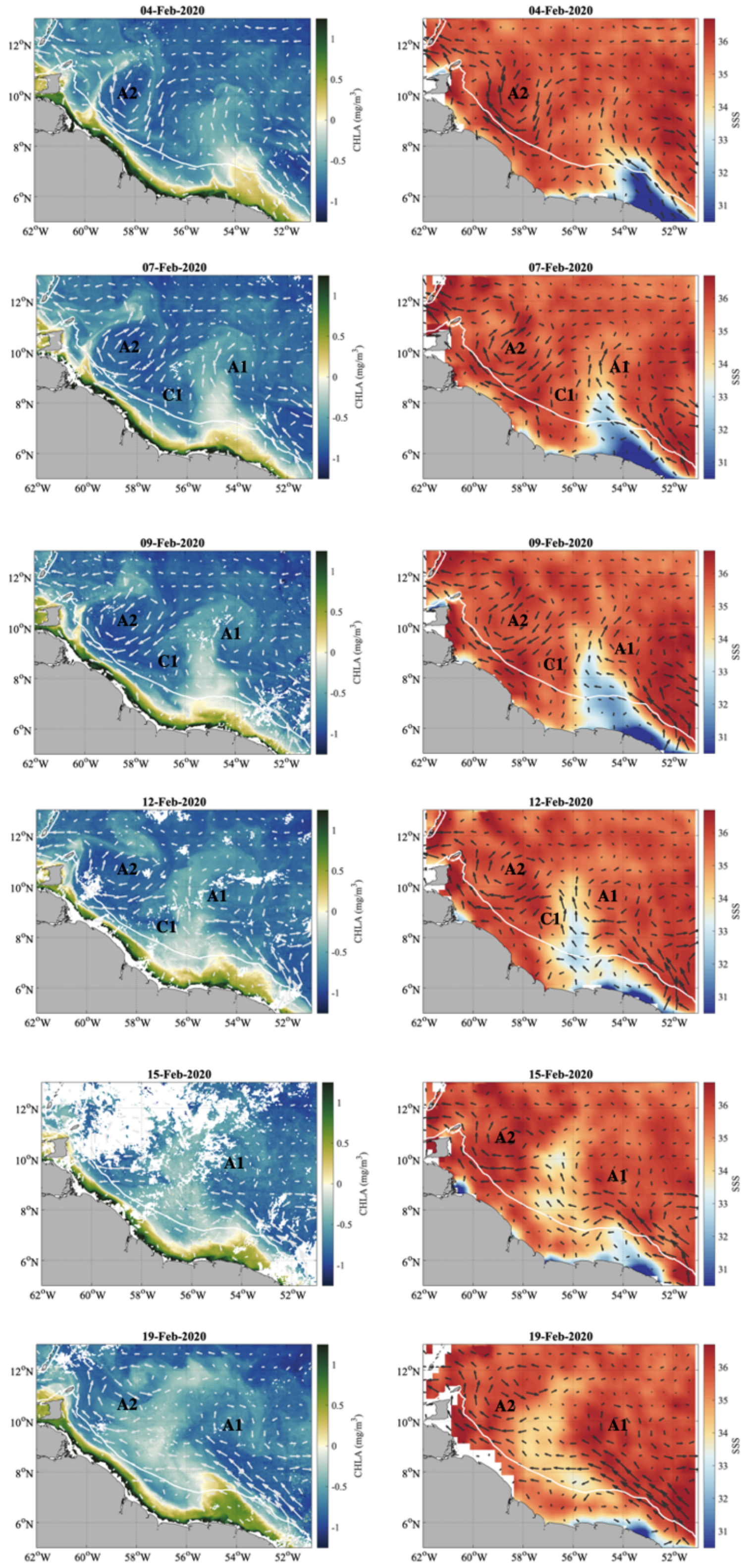

04-Feb-2020

07-Feb-2020

09-Feb-2020

12-Feb-2020

15-Feb-2020

19-Feb-2020

Figure 6.5: Snapshots of daily satellite Chla and SSS maps with overlaid geostrophic currents (arrows) for the 4th, 7th, 9th 12th, 15th, and 19th of February 2020. The shelf break is represented by the 100-m bathymetry contour (white line).

Intrusion of salty water from farther west near 9°N might have contributed to the erosion of the salinity minimum. This is particularly pronounced on the February 15th map. At that date, two drifters close to- gether experienced very large salinity differences (up to 0.5 pss at 3-km distance near 9°N/56.6°W), illus- trating how sharp the gradients were near this wedge of salty and low Chla water. Horizontal mixing with the plume water can be expected from this date, except if the saltier/Chla-free water is entrained under the fresher water. This penetrating saltier water seems to partially separate fresher water to the north from the freshwater closer to the shelves.

On the 17th and 18th of February, the Saildrone crossing the fresh pool still encountered SSS as low as 33.3 pss near 9.8°N/56.5°W, similar to what is suggested by the salinity maps (Figures 6.2 and 6.5). Then, by February 19th, the low salinity pool had become less pronounced (minimum values increase to 34 pss), but had extended further westward in particular just north of the shelf break, nearly reaching the southern edge of eddy A2. Afterward, it was difficult to follow because of uncertainties in the salinity maps that are on the order of 0.5 pss. Another way to investigate the plume evolution is to consider a Lagrangian perspective, based on the time series of the five drifters deployed in the plume (SSS lower than 35 pss) on February 2nd and 4th either on the shelf or near the shelf break. For the first 4–5 days after deployment they drifted north to north-westward and remained coherently separated cross-stream (Figure 6.6a). The drifters are drogued at 15-m depth, which might be within the stratified layer under the freshest surface water, in particular at deployment (see Section 6.2.5). The drifters were deployed in a horizontal gradient of SST (1°C change across the plume), with coldest water closest to the continent. Interestingly, this gradient as observed by the drifters remained fairly consistent over time, although its amplitude gradually diminished (Figure 6.6b). Moreover, large temperature daily cycles are observed, with initial amplitude exceeding 0.5°C. The wind (Figure 6.6d) also illustrates a daily cycle with strongest wind in the early morning and weakest wind in the late afternoon. It was rela- tively weaker at the beginning of the deployment near the shelf break, in line with the corresponding larger temperature daily cycle. For all drifters the wind increased over time during this initial 5-day period and as the drifters moved away from the shelf.

Salinity (Figure 6.6c) variability between the different trajectories is not as regular as temperature variability. The trajectories present some rather fast changes of SSS (by up to 1 pss), which indicate the presence of small-scale gradients/blobs advected relative to the drifters. The red salinity curve, corresponding to one of the middle deployments, remained the lowest. Nevertheless, 7 days after its deployment, it has values very close to the black curve (corresponding to a drifter located to its northeast, in slightly warmer water). It is the drifter farthest east (gray line, always off shelf) that presents the least variability. All together during this period and for all drifters, salinity is very similar at 0.20-m and 5-m depths whereas there are gradients of up to 1 pss between the surface and 10 m for most drifters (Figure 6.6e). This is not found for the drifter that is farthest from the shelf (gray curve). It indicates a deeper fresh layer in this region, even though at times this drifter presents lower salinity than the drifter closest to shore (green curve). The periods of large salinity stratification between the surface and 10 m depth are not found at the same times for the different drifters (Figure 6.6e). They tend to be less common on February 6th and 7th, after a few days of drift away from the shelf and with the stronger winds.

Sections Across the Plume (Extension, Gradients, and Thickness)

On the 2nd of February both RV Atalante and MSM crossed the nascent plume (Figure 6.7a). The overall currents were directed to the northwest, so in general the MSM section is upstream from the Atalante sections. Both vessels were coming from the deep ocean over the outer shelf, with salinity decreasing and reaching a plateau, until a sharp front was encountered by the two ships. This front is located on the shelf near 06.68°N/53.51°W (Atalante) and 06.78°N/53.25°W (MSM), with much fresher (by more than 1.2 pss) and warmer water on the inner-shelf side of the front (Figure 6.7b with the inner-shelf to the left and values on the x-axis increasing offshore). Interestingly, the front was farther away from the coast and with warmer and fresher water on its southwest side for the MSM section compared to the Atalante section (Figure 6.7b). The surface front width is crossed in less than 100 m based on the RV Atalante intake temperature sensor measurements, and is possibly as narrow as 50 m. The respective positions of the front crossings by the two vessels suggest that the front was oriented northeast to southwest. The lower SSS seen by MSM suggests that the front might have been propagating from southeast to northwest, as fresher water was found farther upstream along the shelf break and shelf (i.e., farther southeast) according to the salinity satellite maps and the Mercator PSY2V4 operation model. Indeed, it is probably the same sharp front that was crossed by one drifter (black line in Figure 6.6c with more than 1 pss drop and 0.4 C warming in an hour) less than 4 h after its deployment from RV Atalante. As it is located a little to the north of the position of the front crossed by RV Atalante, it suggests that the drifter was also encountering freshwater coming from its east or southeast.

The combined MVP and uCTD section collected by MSM on February 2nd (note that the MVP started just after crossing the surface front) will be summarized by presenting the thickness of the freshwater plume and equivalent fresh water content (cf. salinity section in supporting information S4). The thickness of the freshwater plume (red curve in Figure 6.7c) is defined here by the depth where salinity reaches $0.5 \cdot (36.4 + SSS)$ corresponding to surface and subsurface waters that have been equally mixed assuming homogeneous salinity profiles above and just below this depth. Here 36.4 pss is a typical value of salinity near 50 m in this survey. The equivalent fresh water content is estimated by vertically integrating the salinity profiles assuming mixing of fresh water with salty water at 36.4 pss. The thickness of the fresh layer and the equivalent freshwater content (referred to 36.4 pss) present strong variability across the section (Figure 6.7c). In particular, there is a large bulge in the freshwater layer thickness just inshore (left on Figure 6.7c) from the front. Indeed, in this bulge, the very fresh surface water presents stratified salinity down from the near-surface to 40-m depth, with water properties at 22 m corresponding to those in the surface water found northeast of the front (cf., supporting information S4). This suggests that

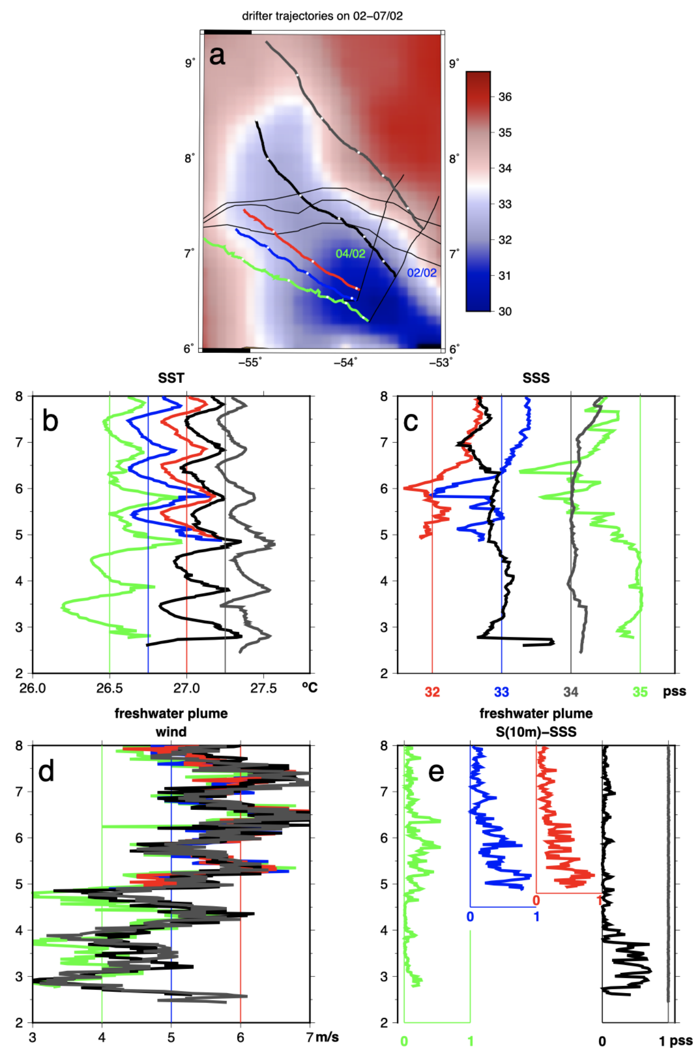

Figure 6.6: The drifter time series from February 2^{nd} to 7^{th}. Top panel, the trajectories (with dots each day at 0 GMT), as well as the SSS map for February 7. Below, four panels as a function of time (vertical axis in February days) for sea surface temperature (b, top left), sea surface salinity (c, top right), measured winds (d, bottom left in m/s), and salinity stratification S (10 m)-S (0.2 m) (e, lower right). The curves are color-coded for the different drifters based on panel (a) (panel (e), the colored vertical straight lines correspond to no-stratification for that drifter).

the freshest surface water had recently overlaid the saltier/warmer water, which had downwelled under the front. Farther to the northeast along that section, there is only a slight decrease of the fresh water content (blue curve on Figure 6.7d) due to deeper surface mixed layer despite higher surface salinity (black curve on Figures 6.7c and 6.7d), especially east of the shelf break (but the number of profiles collected is insufficient to fully apprehend this structure).

On the 4th and 5th of February, RV Atalante crossed the fresh plume on its way from the shelf to the southern side of anticyclonic eddy A1 of Figure 5, a little bit to the west of the earlier crossings (Figure 6.7a). Salinity dropped to nearly 30 pss close to the outer edge of the shelf (Figure 6.7d) and presents very regular and symmetric along-track variability relative to the shelf edge, with no trace of the earlier fronts witnessed on February 2nd. This suggests that at that time the plume was rather broad and at least 120 km across, assuming that the section was at a right angle to it. This assumption about the angle (maybe closer to 70°) is supported by the salinity maps, the drifter trajectories and the ship's vessel mounted ADCP (VM-ADCP), which suggest that the upper ocean currents were nearly at right angles to the cruise track.

On February 5th the MVP (and uCTD) profiles also provide information

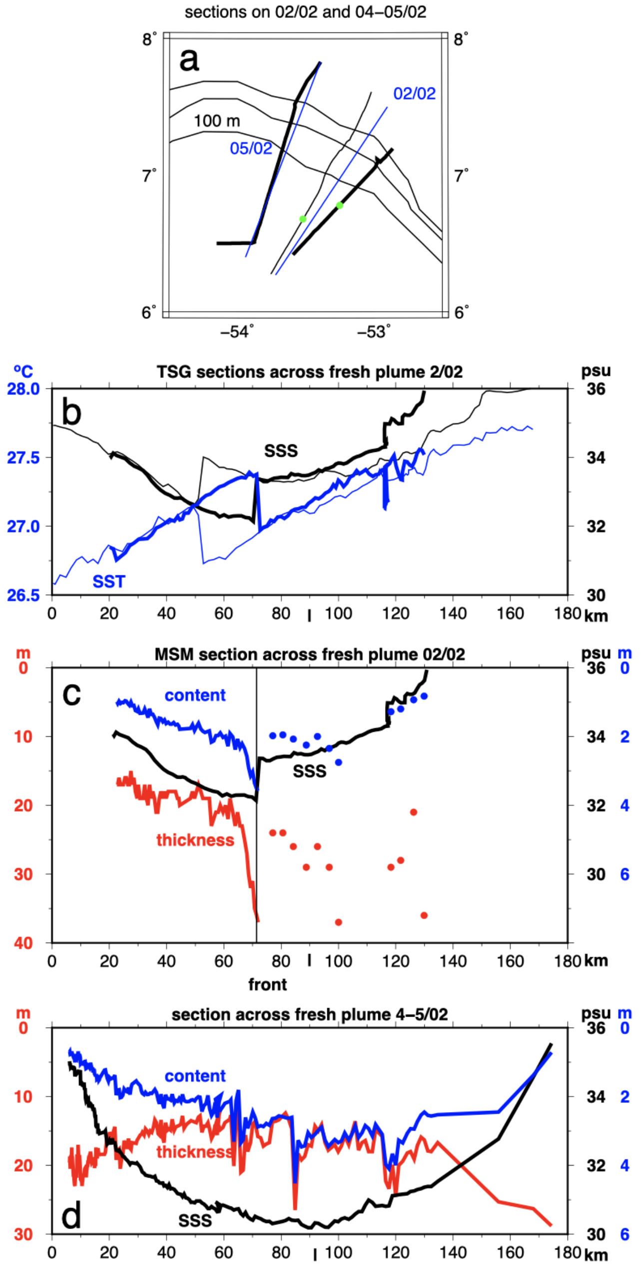

Figure 6.7: Sections across the shelf break near 53°W-54°W. (a) (top panel) Map with the different sections (thin black line for RV Atalante on February 2nd, and thick black line for Maria S. Merian (MSM) on February 2nd and RV Atalante on 4th-5th). The blue lines indicate the axis along which the data are projected for the plots (the 100-, 300-, and 500-m isobaths are plotted), and the green dots the positions of a T/S front. (b) Sea surface temperature (SST) (blue) and SSS (black) sections on 2nd of February from RV Atalante (thin) and MSM (thick) transects. The horizontal axis is distance from the end point on the shelf (53.72°W/6.27°N) and the data of the two ships are projected on the same line median to the two ship tracks. (c and d) Lower panels: the moving vessel profiler (MVP) sections on 2/02 (MSM) and 4–5/02 (RV Atalante) plotted for SSS (black), fresh layer thickness (red) and equivalent freshwater content (blue), with respect to distance from its origin on the shelf (at distances larger than 75 km/134 km on (c)/(d), uCTD profiles instead of MVP data). The vertical bar on bottom axis on both panels indicates the location of the 100-m isobath. For (c), the position of the sharp front in SSS/SST is noted by a vertical line.

on the plume's vertical structure (Figure 6.7d). Based on the salinity criteria for the fresh layer thickness, the section presents thicker fresh layers on the sides of the plume than in between, where it is typically 12–20-m thick (red curve). The fresh layer thickness also presents some very fast variability between successive profiles, for example at 65, 83, and near Figure 6.8. Salty (light gray) and fresh (dark) drifter trajectories are overlaid on the salinity map for February 9 (g, top map). Under it, comparative time series for (left column) the drifter deployed in salty water (on January 31 at 09 GMT) and (right column) the one in fresher water (on February 2 at 22 GMT). Top panels for temperature measurements at 0.2, 5, and 10 m; middle panel for the salinity at these three levels, and bottom panel wind measurements 120 km. This could be indicative of internal waves or solitons, and there are no associated surface salinity or temperature variations. The equivalent freshwater content is on the order of 2-4 m in the central outer parts of the plume, whereas it decreases a little more toward the shelf edge of the plume.

Stratification and shear in the Surface Layer

The MVP sections performed close to the time when the plume separated from the shelf indicate that the fresh layer was rather shallow. We will present evidence of how this stratification constrains vertical mixing and the extent to which off-shore changes in the salinity plume are related to vertical mixing with the deeper saltier water.

The drifters show variable salinity stratification between the surface and 10-m depth in the first 5 days (Figure 6.6e). Such stratification is less common afterward, but some of the drifters also left the core of the fresh plume. Drifters launched in January stayed out of the fresher water re- gion and can be compared with those launched in the plume in order to identify the characteristics of this surface layer. Such an example is presented in Figure 6.8, and although some differences might be related to weather conditions, such as different cloudiness, there are major differences between the drifter data in the plume and outside of the plume that we will describe. First, the temperature diurnal cycle is present in both the salty and fresh regions at the three depth levels but with strikingly different amplitudes (Figure 6.8). The larger diurnal cycle is observed for the buoy located in the freshwater plume despite experiencing winds that were often larger than for the out-of-the-plume drifter. At night in the freshwater plume, temperature remains a little warmer at 10-m depth than at the surface. Ten-meter temperature however usually decreases during night-time, which suggests active night-time vertical mixing near the surface entraining the 10-m subsurface water. Furthermore, surface salinity increases similarly during day and night-time in the salty region, whereas the increase is observed with more diurnal variations in the fresh plume. Except for an event on the second day (Figure 6.8), this seems to confirm the night entrainment of subsurface (salty) water into the near surface layer resulting in a late-night relative surface salinity maximum.

The records of the drifter data in the fresh plume therefore suggest night-time active mixing in the stratified layer near 10-m depth, just below the well-mixed surface layer. We do not have direct information of turbulence activity at that time. However, there is indirect evidence provided by the Ocarina platform deployment over the shelf on February 3rd (supporting information S1). As the local depth was larger than 50 m, interaction of the surface mixed layer with the deep boundary layer should have been small. Nearby MVP profiles collected by RV Atalante (for density profiles) are combined with the simultaneous Ocarina current data (for shear) to estimate a Richardson number (Ri) profile (supporting information S1), with Ri defined as:

$$R_i = -g/\rho \cdot (d\rho/dz)/shear^2 \tag{6.1}$$

Ri has values between 0.2 and 0.8 in the 6-16-m layer. As the profiles were not exactly simultaneous in space and time, we cannot estimate individual Ri profiles and derive precise statistics on the Ri distribution,

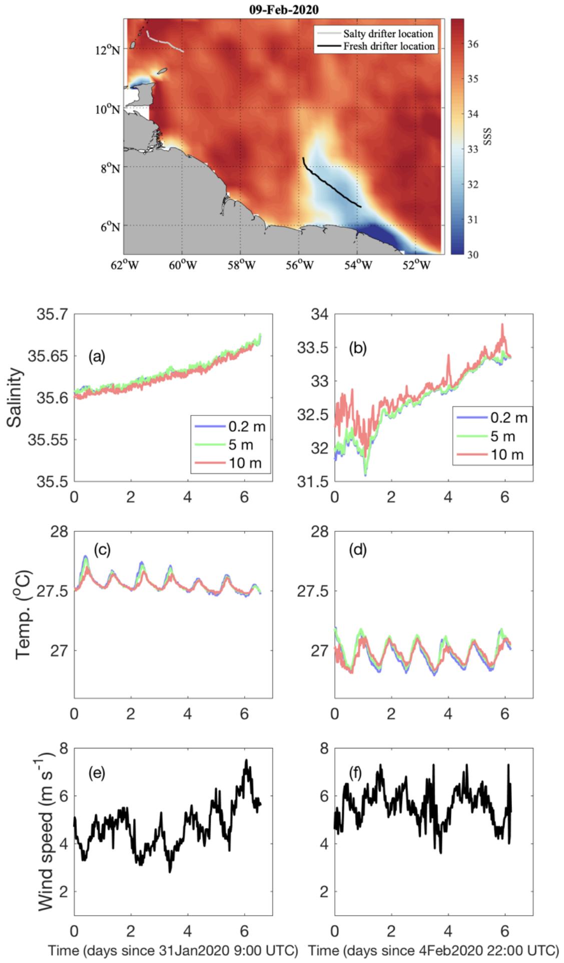

Figure 6.8: Salty (light gray) and fresh (dark) drifter trajectories are overlaid on the salinity map for February 9 (g, top map). Under it, comparative time series for (left column) the drifter deployed in salty water (on January 31 at 09 GMT) and (right column) the one in fresher water (on February 2 at 22 GMT). Top panels for temperature measurements at 0.2, 5, and 10 m; middle panel for the salinity at these three levels, and bottom panel wind measurements.

although the average is on the order of 0.4. These averaged values suggest that the whole layer might have witnessed active turbulent conditions, with values close to the critical Ri for shear-induced instability (Galperin et al., 2007). This happened despite the stratification induced by daily heating, found at least between 6 and 14 m (15 m coincides with the lowest temperature in the profiles).

The Saildrone crossed the fresh pool two weeks later than the ship on the 17th and 18th of February (Figure 6.9a). They did not measure stratification directly, but the ADCP data at 2-m resolution can be used to estimate a mixing depth. This is done by assuming $R_i = 0.4$ in this layer, and then estimating the density profile in the actively mixed layer by vertically integrating $R_i \cdot shear^2 \cdot \frac{\rho}{g}$ down from the surface. The bottom depth of this layer (mixing depth) is reached when the density has increased relatively to the surface by $0.12 kg/m^3$ (Foltz et al., 2018). Alternatively, we use the current profiles to identify the depth of maximum shear. This depth is known to be deeper than the mixing depth, either because of internal waves under the base of the mixed layer or the wind momentum input into the surface layer (Foltz et al., 2020). The two estimates of the mixing depth are quite similar, with the one based on maximum shear being deeper by about 9 m on average. They are weakly correlated (0.42) over the crossing of waters with salinity less than 34 pss (Figures 6.9b and 6.9c). The low correlation results from a small area near 100 km where the maximum shear is found deeper than mixed layer depth MLD based on critical Ri. Both estimates usually illustrate rather shallow mixed layers, often on the order of 20-m thick (averaging 17 m for the density criterion). The estimate is deeper in the eastern part after the sharp salinity frontal increase to 34.05 pss, where the two depths are closer to 30-40 m, which is more typical of what was found during the EUREC^{4}A-OA surveys, at least at night time.

So, overall, MLDs (and presumably the freshwater layer thickness) in the plume are larger, possibly by close to 10 m, than what is observed on the sections 2 weeks earlier and closer to the shelf. There is also no clear diurnal cycle of the MLD within the plume, based on this indirect estimation (the freshest part of the plume was crossed in more than 1 day). This fits with the expectation that density stratification under sustained winds is constrained by the salinity stratification in these shallow and fresh surface layers. Interestingly, the width of the plume did not change much between February 2 (Figure 6.6) and February 18. On the other hand, it expanded northward significantly based on the satellite maps (Figure 6.4), extending to close to 12°N and becoming less linear. Minimum salinities reached in the plume are also larger by February 18.

Advective Budget for the Surface Area

To determine the causes of the freshwater plume's expansion, first we estimate the freshwater pool area from mapped satellite SSS daily products. We define it as the area bounded by the 35 pss isohaline and off- shore of the 100-m isobath. We also estimate an advective area flux based on the currents across the shelf in sectors with salinity less than 35 pss. Currents are estimated by combining AVISO geostrophic currents and Ekman currents estimated with a mixing depth of 20 m and using wind stress estimates from the drift- er closest to the shelf break. Note that 20 m is typical of the fresh layer thickness from the sections on the 2nd, 4th, and 5th of February (Figures 6.7c and 6.7d), but that is larger than the near 10-m MLD found on the southern part of those sections. It is also typical of the MLD observed by the Saildrone section of February 17 (Figure 6.9). The rate of change of the area should equal the area transport, assuming 2-D dynamics, no effect of mixing on this area, and conservation of SSS (no air-sea exchange of water).

The two terms are comparable, although there is often a smaller area increase compared to the flux. The area of the freshwater plume increases rapidly from the 2nd to the 9th of February (Figure 6.10) before increasing more slowly until the 19th and reaching a maximum of close to 100,000 km^2. For the fluxes, the increase is fast until the 14th of February and a bit slower until the 20th. As commented earlier on the plume history (Section 6.2.5), starting on 13th to 14th of February (Figure 6.3), there are some signs of partial separation of the fresh water plume from the shelf (and thus, some plume discontinuity). Interestingly the total area transport was driven almost equally by Ekman and geostrophic advection until the eleventh, and more by Ekman advection afterward.

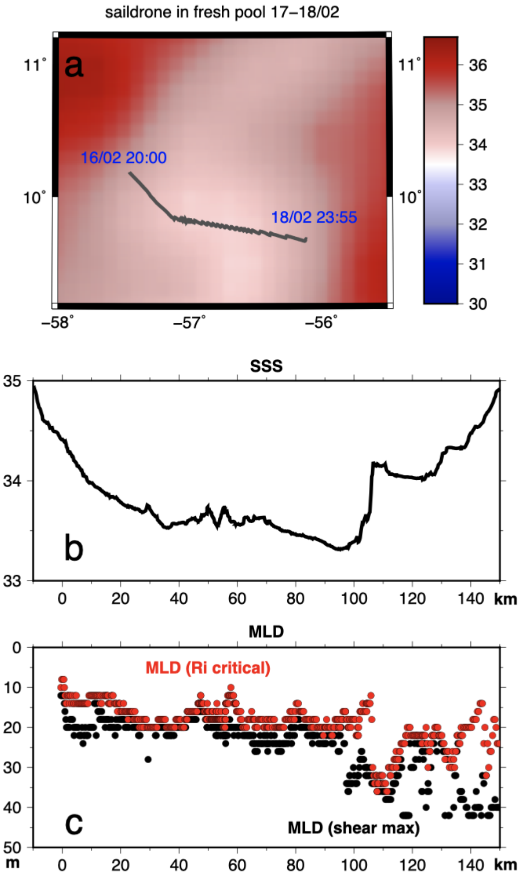

Figure 6.9: Saildrone section (16/02 evening to 18/02) across the fresh plume. (a) Track overlaid on the sea surface salinity (SSS) map for February 17; (b) SSS; (c) different estimates of MLD (maximum shear depth in black and from critical Ri number in red). (b) and (c) Plotted along the section from west to east, as a function of distance from an entrance point in the fresh pool.

We have estimated the total freshwater transport based on ocean currents and the surface salinity maps, though this might be less precise compared to the area transport. We use a constant freshwater layer thickness of 20 m based on the initial sections (Figure 6.7), and mixing with a 36.5 pss deep source. With these assumptions, we find that the transport of fresh-water in this off-shelf plume averaged 0.15 Sv ($10^6 m^3 s^{-1}$) in the 11 days from February 2nd to 11th, and 0.06 Sv from the 11th to the 20th. During the first period, the transport is comparable to the expected outflow of the Amazon River in late January (based on climatology).

Until now, we have not commented on the uncertainties of these estimates. In supporting information S2, we estimate that uncertainties on the cumulative fluxes (blue curve on Figure 6.10) are between 15% and 50% (depending on whether or not the error is random in the daily flux estimates), whereas the error on the total area is likely to be on the order of 10%.

The difference between the two curves in Figure 6.10 is therefore probably within the error bars. Some of the assumptions done for this budget might also break down. Vertical mixing might diminish the area by bringing more salty water and causing mixed layer salinity to rise above

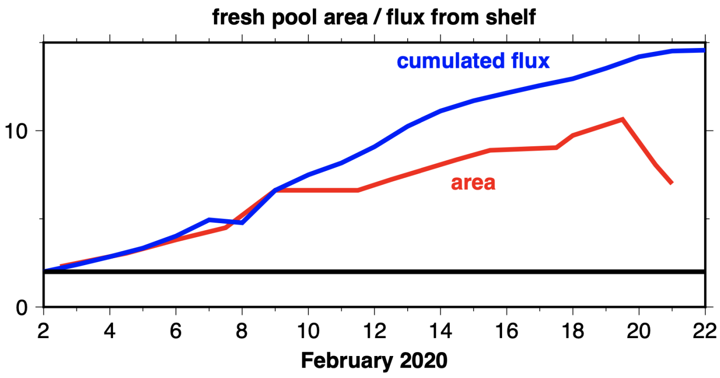

Figure 6.10: The area of the deep ocean sector with S < 35 pss and with depth larger than 100-m (in red; area expressed in 10^4 km^2); the cumulated flux is the horizontal area with S < 35 pss fed by advection from the shelf, estimated assuming horizontal dynamics, no mixing and conservation of surface salinity (in blue).

the threshold in some areas (there is evidence of mixed layer deepening in the Saildrone section on February 17th and 18th). There are also clearly some lateral intrusions/mixing with saltier water, but how this affects the overall area is not straightforward. These issues will be more easily addressed in high resolution numerical simulations and a full three-dimensional budget, as the salinity fields clearly do not have the required resolution for these mesoscale or sub-mesoscale features).

It is even more uncertain to provide an estimate of the total freshwater transport, as the freshwater thickness is not closely correlated with surface salinity, as illustrated in Figure 6.7.

6.2.6 Discussion

Frequency of Such Freshwater Plumes

How often do these freshwater events occur in the winter season during the January to mid-March period, and what drives them? Using the 10 years of weekly CCI SSS products, in each year we find events of fresh- water leaving the shelf and reaching the open ocean. Some events happened farther west, west of 56°W and in some cases the fresh water did not extend north of 10°N. These events (two thirds of the total) were unlikely to have a lasting influence in this sector of the Atlantic, with the freshwater being quickly washed across the Antilles into the Caribbean Sea. Events closer to the one observed in early February 2020 hap- pened in 7 out of 10 years during the winter season (supporting information S3).

An important question is what determines the presence or absence of off-shelf transport of fresher water. A requirement is that freshwater has to be transported from the Amazon estuary near the equator to 7°N/54°W. At this place, the shelf-break direction changes and winds become less perpendicular to bathymetry and thus prone to induce off-shelf transport. Southeast of that, the winds tend to be perpendicular to the shelf break, and even oriented a little farther anti-clockwise in January-February. This, close to the equator, does not favour the north-westward transport of freshwater on the shelf.

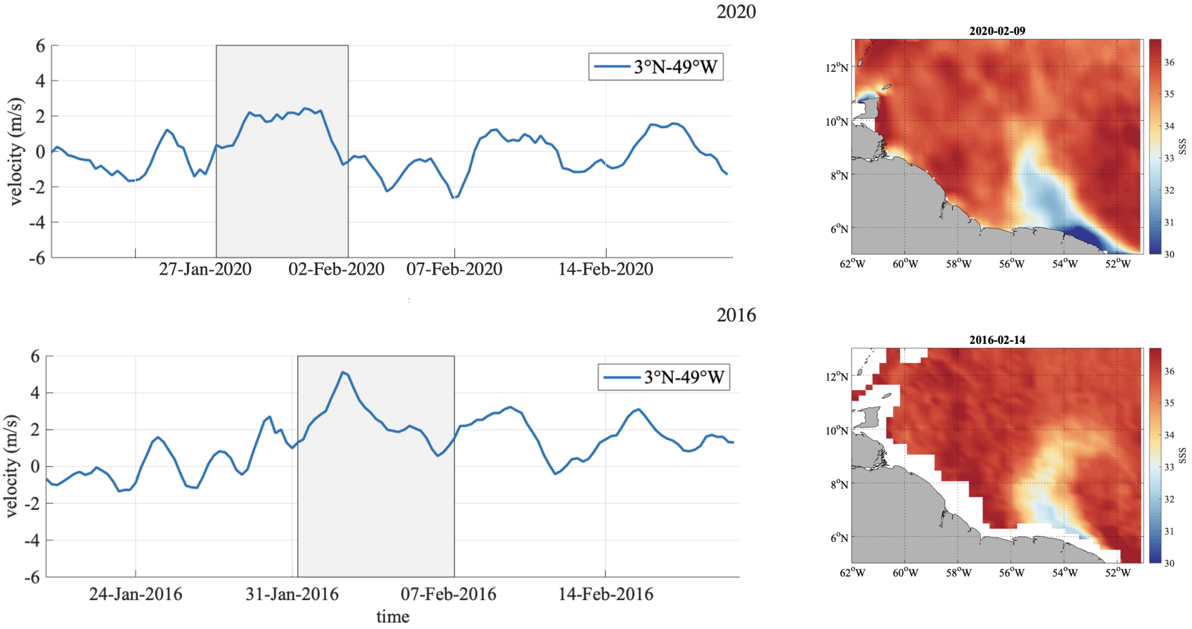

Figure 6.11: Winds at 3°N/49°W in relation to development of freshwater plume events. Only the component of the wind parallel to 100-m isobath is shown on left side for two years (2020, the event we study here; and 2016, a typical other year), with the corresponding developed freshwater plumes presented on the right side (for 2016, from CCI 7-day products). The gray time domain on the wind time series corresponds to the period between the start of the wind event and the start of the freshwater plume separation from the shelf near 54°W-56°W.

Small changes of wind direction are instrumental in inducing northwestward transport of Amazon water on the shelf (Geyer et al., 1991; Lentz, 1995). To estimate when this happens, we define an index based on the wind component parallel to the shelf-break at 3°N, a transition latitude with respect to the Coriolis force. It is halfway along the shelf between the Amazon estuary and French Guiana and is almost always bathed in freshwater. The index is the deviation of the wind component parallel to the shelf break from its average during the months of January and February of that year (positive to the northwest). In 2020, between mid-January to late February, we find only one 4-day period (January 28 to February 1) when the index is positive (Figure 6.11). This change in wind direction is favourable for a north-westward transport of freshwater which, if it flows at 50 cm/s, a typical along-shelf velocity in this season (Geyer et al., 1991; Lentz, 1995) would reach the shelf-break near 53°W-54°W in early February. The timing is thus fairly close to what is observed.

We cannot carry out such a detailed calculation in other years, as we do not know the precise date of appearance of the freshwater plume. However, we find that in 6 out of the 7 years when a freshwater plume developed (the exception being 2018), there was a preceding period with significant positive wind index lasting for a few days. An example is presented in the lower panels of Figure 6.11. The average length of these positive index events is 5.3 days (varying between 2 and 8.5 days), and the duration between the initial date of the wind event and the development of the off-shelf freshwater plume is 6.3 days (varying between 4 and 9 days). These estimates are in the range of what we expect for wind-induced currents. The time scales are long enough that geostrophy and Ekman divergence at the coast might be operating, which would reinforce the north-westward geostrophic current. Of course, other dynamics such as those associated with the shelf- break currents, or the build-up of a pressure head and its evolution near the mouth of the Amazon estuary might also take place.

Another key feature favouring the transport of the plume off the shelf is the anticyclonic eddy (A1) with a core lying slightly east of 54°W. This is an area commonly crossed by NBC rings (Johns et al., 2003). In 2020, the analysis of eddy A1 shows that it did not move very swiftly north-westward before February 21 (Figure 6.12). In particular, between February 7 and 14, the core stalled and only marginally moved to the north, while separating from the shelf-break. This slow motion and the earlier presence of cyclonic feature C1 favors the channeling of the fresh plume by the geostrophic flow from the shelf-break farther north. At the same time, C1 weakens, and A2, another anticyclonic feature farther west moves slowly westward until mid-February, leaving a large area for the plume spreading. Then A1 rapidly moves farther west and intensifies, which would channel a large part of the fresh water closer to the shelf break near Trinidad toward the Antilles (Figure 6.12), as is suggested by the drifters and later weekly salinity maps.

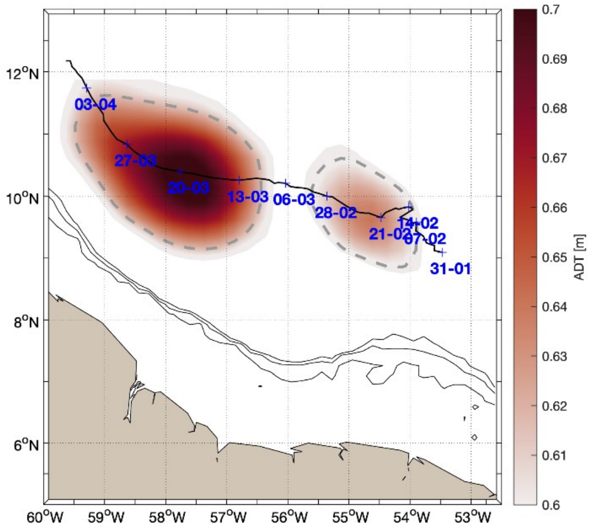

Figure 6.12: Trajectory of anticyclone A1 derived from absolute dynamical topography (ADT) maps by the TOEddies algorithm (Laxenaire et al., 2018). Composite ADT signature of A1 are indicated for February 23 and March 21. The shelf break is represented by the 100-, 300-, and 500-m bathymetry contours (black lines).

Sharp Fronts

The daily salinity composite fields have a resolution on the order of 70 km, whereas the daily composites for Chla have a resolution slightly blurred by the compositing (for example a feature moving at 30 cm/s will be displaced by 26 km in 1 day), and the geostrophic current maps do not resolve structures with diameters smaller than 150 km, implying a large time averaging. Much finer fronts are features common in the surveys (for example in Figures 6.7 and 6.9). Some of these fronts have very large amplitudes, comparable to the mesoscales and are associated with strong surface density changes, and thus are dynamically active. The best resolved structure is the one crossed by two research vessels and one drifter on February 2nd (Figure 6.7). The intake temperature record of

RV Atalante suggests a horizontal scale of the SST and SSS front of less than 100 m and possibly as short as 50 m. According to the VM-ADCP data of the two vessels, this surface front was embedded in a wider and deeper current pointing north-westward. However, data also suggest a rather narrow surface velocity structure just south of the front, with a sharp change of velocity at the sea surface front.

For instance, the RV Atalante absolute velocity presents a westward velocity peak of close to 30 cm/s at the front relative to the velocity before and after the front, despite the ship navigating at a constant speed relative to the sea surface. This peak velocity lasts less than 3 min, thus over a rather small distance of less than 1 km. There is also some indication of a change in the meridional velocity across the front, with the surface velocity directed more northward south of the front than north of the front. On the MSM VM-ADCP shallowest bin at 18-m depth, the velocity vectors also suggest that the structure is converging at least in the direction of the ship's track. There is also a westward narrow velocity peak of 25 cm/s over less than 7 km relative to velocities further away. However, because of the large salinity bulge southwest of the front (Figure 6.7c) under the lowest surface salinity, these velocity structures at 18 m are difficult to interpret, as the uppermost ADCP bin is within the fresher layer close to and southwest of the front, whereas it is in the saltier water under it in other areas. Fortunately, there is also the evidence from the MR radar surface data (Figure 6.13).

As the normalized backscatter intensity is strongly dependent on the ocean surface roughness it depicts all structures that affect the surface roughness, including several internal wave packets along the track, as well as the strong current front close to the northeast corner of the plot. During the 3:39 h track plotted, the surface currents (top 5 m) are pointing northwestward with an increase of velocity along the track toward the northeast, until the velocity front is encountered at the same location as the SST/SSS front. The velocity front at 6.78°N is almost zonal with a slight southward tilt toward the west, and it is associated with a sharp current jump of ~0.5 m/s.

The drifter that crossed the front (farther west and a few hours later) also shows a 50 cm/s westward velocity surge near the front. This surge lasted over 2.5 h, longer than the change in surface temperature and salinity that lasted less than 1 h. It is difficult to translate that into a horizontal scale of the current feature, as it would involve knowing the velocity of the front relative to the drifter. Also, notice that, according to the MSM section, the freshwater layer in the fresher part of the front likely extended past the drogue depth centred at 15-m, so the drifter current represents a mix of the velocity in the freshwater surface layer and below it.

These different velocity estimates are in the same bulk range, and although the width of the associated velocity structure is not the same between MSM and Atalante surface data, these larger velocities in the 25–50 cm/s range close or just south of the front (near the freshwater bulge) are close to the expected velocity of an internal gravity current assuming a Froude number of 1 (with the change in stratification of a little over 1 pss and layer thickness of ~20 m). The velocity data suggest a front/gravity current propagating to the northwest or west with respect to the underlying

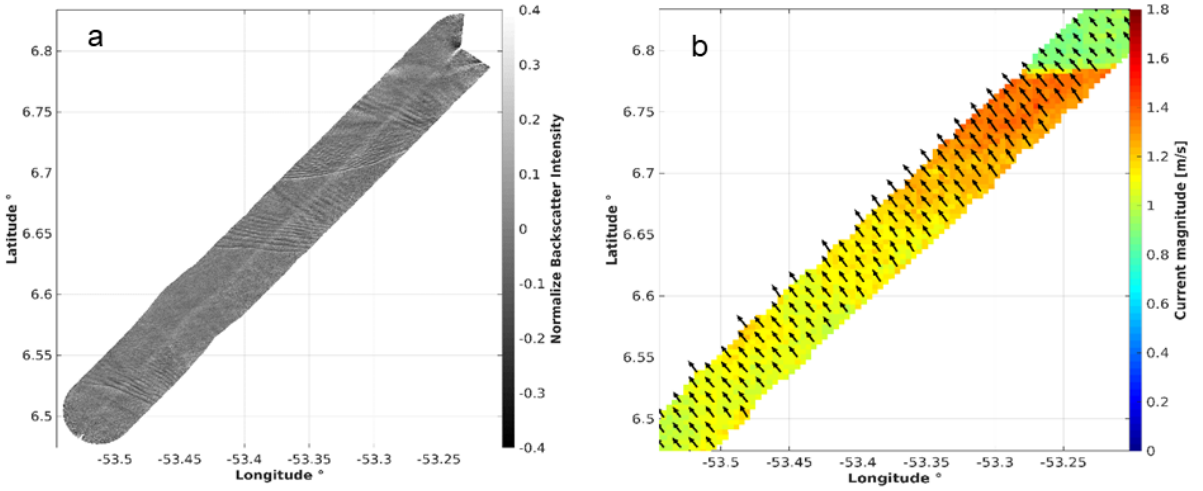

Figure 6.13: Marine radar data between 14:03 and 17:42 on February 2, 2020. Left panel shows backscatter intensity, whereas right panel shows retrieved surface currents, both as arrows and color-coded. The surface front was observed in T-S close to the north-east corner of the plots near -53.25°W/6.78°N.

water at the time it was crossed. Such a propagating front would quickly spread (by 20–40 km/day) the freshest shelf surface waters on top of the less fresh waters found on the other side of the front, contributing to increased stratification of salinity and density. Further investigation is required to better understand what sets this front and its characteristics, and how it sheds internal waves, as is known to happen in freshwater plumes of riverine origin (Nash & Moum, 2005).

Thickness of the Freshwater Layer

The freshwater layers appeared to have a shallow MLD even at night on February 5th, with a stratified layer reaching to within 10 m of the surface. This stratification is also observed on the earlier sections on February 2nd, and in the drifter data during the first 5 days after deployment and as the fresh water starts separating from the shelf. However, the freshwater layer is thicker by 10–15 m or more in the MVP surveys just southwest of the surface front. These different sections were positioned rather close to the north-western edge of the fresh water penetrating from the shelf, based on the daily SSS maps. This is also the case for the drifters, with the salinity map in Figure 6.6 for the last day of the trajectories on February 7th suggesting close proximity of the drifters to the front. MLD is somewhat deeper by February 17th-18th from the indirect estimate of the Saildrone (at least 17 m), though potentially with a large uncertainty as density profiles were not measured. Nevertheless, the difference between the two estimates suggests that there has been some vertical mixing and entrainment of deeper saltier water into the shallow surface fresh water during these 14 days. Thus, this is coherent with the velocity profiles suggesting active turbulence in the fresh plume stratified salinity layer.

Such shallow layers also imply that the drogue of the SVP drifters, which is between 12-m and 20-m depth, is only partially within the surface mixed layer, at least at their deployment in the initial freshwater plume. Their drift might thus differ from the speed of the freshest surface water, possibly explaining why most drifters deployed in the freshwater plume ultimately crossed the salinity fronts to the west of the freshwater plume (near these fronts, Ekman transport tended to be to the right of the drifter trajectories). The observations from Ocarina on the shelf in a salinity stratified layer (although much less stratified than in areas of lowest surface salinity), also indicated strong shear of the current within the top 17 m (close to 40 cm/s shear between depths of 1 and 17 m). Such shear and shallow layer imply a strong slippage of the surface layer relative to the layer just below, which could explain the fast spreading to the north and north-west of the freshwater plume.

6.2.7 Conclusions

In early February 2020, in the core of the saltiest and driest period, a freshwater plume was observed by satellite and in situ data entering the deep north-western tropical Atlantic near 54°W. This changes the perception that during this period, freshwater transport would take place mainly on the shelf and close to the shelf break. This plume was initially very surface trapped with stratification up to 10-m depth and with a width on the order of 120 km. Its freshwater content corresponded to 2–3 m of Amazon water and was distributed down to 40 m, although most of its water was found in the top 20 m. The off-shelf transport lasted for at least 10 days with freshwater transport comparable to the Amazon outflow in January. The plume was still quite well defined 16 days after it started spreading off the shelf break to reach a maximum area of 100,000 km^2, and up to 400 km further north. At this time, the mixed layer had not deepened to more than 20 m as indicated by current profiler data during a Saildrone transect. Although this is difficult to put into context from the limited in situ data, the mixed layer in the plume was shallower than night-time mixed layers found nearby in saltier waters.

A slight change in wind direction along the shelf between the Amazon estuary and 6°N for more than 3 days in late January seems to have triggered the north-westward flow of Amazon freshwater along the shelf and toward the shelf break. The low salinities might also have been sustained by fairly large Amazon outflow in late January compared to other years, estimated from the high river levels reported by altimetry on hydroweb.theia-land.fr. The off-shelf freshwater plume was steered by eddies, and in particular by a nearly stationary anti-cyclonic NBC ring up to 12°N. It also spread toward the Caribbean, due to the evolution of the different mesoscale eddies and to the Ekman transport. This fits with the freshwater pathway (a) in Coles et al. (2013) that they suggest is common from February to May.

The presence of such events of freshwater transport in February is documented since 2010 in 7 out of 10 years, where changes in wind direction closer to the equator concomitant to the presence of anticyclonic eddies to the east of the plume separation from the shelf seems to have contributed to their development and evolution. Such events should contribute largely to a freshening of the surface salinity in February/ March north of the Guiana shelves and south of 12°N. It seems that the mechanism at work here is rather different than what was commented for anomalies later in the year leading to boreal summer, where both current anomalies and wind anomalies, as well as the interannual anomalies of Amazon outflow, or conditions upstream (south of the equator) seem to play important roles.

The position of the 2020 plume's first offshore extension near 54°W is eastward compared to the other plumes detected in CCI products for the other years (Figure S3). We found that such freshwater plumes in February are not rare, and are also commonly associated with the NBC rings such as A1 that was nearly stationary during the plume development and retract water from shelf region into the open ocean. The stationarity is likely linked to the bathymetry of the Demerara Rise to its west that might act to trap/slow down eddies. Clearly more research on the frequency of this phenomenon and how it is modulated seasonally and interannually will be interesting. Inspecting CCI weekly salinity maps suggested that this process also seems to happen in March, and maybe early April, though this will require further investigation. Afterwards in the spring season, with the seasonal wind changes and an increase in Amazon outflow, it is however likely that other processes involved in the development of interannual salinity anomalies in this region east of the lesser Antilles and north of the Guiana shelves might dominate, as suggested by Coles et al. (2013).

6.2.8 Data Availablility Statement

We benefited from numerous data sets made freely available and listed here: the SLA and currents produced by Ssalto/Duacs distributed by the CMEMS (https://resources.marine.copernicus.eu), the Chla maps produced by CLS (also provided at https://observations.ipsl.fr/aeris/eurec4a/#/), the SMOS maps produced by CATDS (CATDS, 2019) (https://10.12770/12dba510-cd71-4d4f-9fc1-9cc027d128b0), and the SMAP maps produced by Remote Sensing System (also at https://observations.ipsl.fr/aeris/eurec4a/#/), as well as CCI+SSS maps produced in the frame of ESA CCI+SSS project (https://10.5285/4ce685bff631459fb2a30faa699f3fc5). Among in situ data, Ocarina data are at https:// www.seanoe.org/data/00663/77479/. All saildrone and salinity drifter data are available here: https://psl.noaa.gov/thredds/cata
and other oceanographic data collected on the research vessels (TSG, uCTD, MVP profiles) are on site https://observations.ipsl.fr/aeris/eurec4a/#/

6.2.9 Acknowldegements

This work is a contribution to the LEFE/IMAGO-GMMC project EUREC4A-OA, to the JPI-Climate and JPI Oceans project EUREC^{4}A-OA, and to the TOSCA SMOS-Ocean project supported by CNES (Centre National d'Etudes Spatiales). Support was also obtained from IFREMER, the French Research Fleet, the French Research Infrastructures AERIS and ODATIS, IPSL, the "Chaire Chanel" of the Geosciences Department at ENS and the European Union's Horizon 2020 research and innovation program under grant agreement no. 817578 TRIATLAS. L. Olivier was supported by a scholarship from ENS and Sorbonne Université. Support for the salinity drifters was provided by the Climate Variability and Predictability Program of NOAA's Climate Program Office. MSM observations benefit from MOSES observational infrastructure. G. R. Foltz was supported by base funds to NOAA/AOML's Physical Oceanography Division. D. Zhang was supported by NOAA's Climate Program Office, Climate Variability and Predictability Program, and the Joint Institute for the Study of the Atmosphere and Ocean (JISAO) under NOAA Cooperative Agreement NA15OAR4320063.

Wintertime biogeochemical process study of the North Brazil Current rings

7

7.1 Introduction

After delving in the physical parameters of the plume, we worked on gathering all the physical and biogeochemical knowledge at the surface to better characterize the impact of the NBC rings on the air-sea fluxes of CO_2 in winter 2020. The plume is put in a winder context, as it is the biogeochemistry of all the northwestern tropical Atlantic that is poorly known in boreal winter. The objective of this study is two folds: understanding the mechanisms responsible for the variability of the air-sea CO_2 exchanges in winter and how the mesoscale and submesocale feature of the northwestern tropical Atlantic modifies the carbon budget of the region.

The first part of this work consisted in identifying the relevant surface water masses, using the in-situ underway SSS, SST and fCO_2 collected during the EUREC^{4}A-OA campaign. In an effort to understand how biogeochemistry is forced by physical processes in the ocean, we used surface chlorophyll-a to complement SST and SSS data in defining surface water masses.We identified six different water masses, that help us look at the fCO_2 signature of the main dynamic features of the area. The NBC brings warm, saline, and high in fCO_2 waters that get transmitted to the NBC rings. As the NBC ring separates from the retroflection, it looses its supply in this water mass, and its surface signature can get eroded due to surface mixing. Out of the two NBC rings studied, one kept the NBC water mass in its centre even four months after its separation from the NBC, while the surface signature of the NBC water is almost gone for the second ring, even after only a few weeks of life. This second NBC rings is the one that strongly interacted with the Amazon fresh plume. These waters constitute a second water mass, which differs in every respect from the NBC water mass, and is characterised by low salinity, low fCO_2 and high chlorophyll-a. On the shelf is also found another water mass that is relatively saline, rich in chlorophyll-a and associated to high fCO_2. This water mass is most probably rich in detrital material, and can sometimes get stirred by eddies away from the shelf, in thin filaments. North of Barbados, away from the influence of the NBC rings, the water is less variable. It is relatively saline, poor in chlorophyll-a and cold due to the seasonal cooling of this subtropical water, the low temperature translates into a low fCO_2. This first part shows that the dynamics dominating the CO_2 variability are mainly the NBC retroflection and the NBC rings, the Amazon plume and the seasonal cooling. It also shows that for this period, three variables, SSS, SST and chlorophyll-a, are enough to explain the CO_2 variability during that season.

Building on this idea that there is a unique fCO_2 for each combination of SSS, SST and chlorophyll-a, we develop a relationship between this four variable based on the in-situ data. This relationship is then interpolated between these four variables for a wide range of values realistic for the region and the winter period. We then are able to use satellite maps of

SSS, SST and chlorophyll-a to retrieve the fCO_2 and then the air-sea CO_2 fluxes. The high resolution of these products resolves the mesoscale and submesoscale phenomena that the first part showed to be key for the carbon budget of the region : the NBC rings and the Amazon plume.

When considering the averaged CO_2 air-sea fluxes over the month of February 2020, we can compute the contribution of each of the water mass to the integrated air-sea CO_2 flux of the region. This allows to identify the regional carbon sinks and sources for the region, and reveals marked differences compared to state-of-the-art climatology in the region from Landschützer et al., (2020) that includes the coastal region. One of the main difference is the presence of the Amazon river's influence. The freshplume is a small feature but accounts for 20% of the total CO_2 sink of the region. It also changes the biogeochemistry of the region where the NBC rings propagate. Instead of being dominated by the NBC water mass that is a source of CO_2 to the atmosphere, this water mass is only present in the retroflection and in the core of some eddies. We also observed that the CO_2 sink associated to the cold and less variable waters in the north of the domain was underestimated in the climatology. In total, the region is a strong CO_2 sink in winter, underestimated by a factor 10 in the climatology.

7.2 Article published in *Biogeosciences*: Wintertime process study of North Brazil Current rings reveals the region as a larger sink for CO_2 than expected

Léa Olivier* • Jacqueline Boutin* • Gilles Reverdin* • Nathalie Lefèvre* • Peter Landschützer† • Sabrina Speich‡ • Johannes Karstensen§ • Matthieu Labaste* • Christophe Noisel* • Markus Ritschel† • Tobias Steinhoff§ • Rik Wanninkhof¶

Received 19 October 2021 – Revised 11 May 2022 – Accepted 16 May 2022

7.2.1 Abstract

The key processes driving the air–sea CO_2 fluxes in the western tropical Atlantic (WTA) in winter are poorly known. WTA is a highly dynamic oceanic region, expected to have a dominant role in the variability in CO_2 air–sea fluxes. In early 2020 (February), this region was the site of a large in situ survey and studied in wider context through satellite measurements. The North Brazil Current (NBC) flows north-ward along the coast of South America, retroflects close to 8°N and pinches off the world's largest eddies, the NBC rings. The rings are formed to the north of

---

* Sorbonne Université, CNRS, IRD, MNHN, UMR 2159, Laboratoire d'Océanographie et du Climat: Expérimentations et Approches Numériques, LOCEAN-IPSL, Paris, France
† Max Planck Institute for Meteorology, Hamburg, Germany
‡ Laboratoire de Météorologie Dynamique, ENS-Ecole Polytechnique-CNRS-Sorbonne Université, Paris, France
§ GEOMAR Helmholtz Centre for Ocean Research Kiel, Kiel, Germany
¶ Atlantic Oceanographic & Meteorological Laboratory of NOAA, Miami, USA

the Amazon River mouth when freshwater discharge is still significant in winter (a time period of relatively low run-off). We show that in February 2020, the region (5–16 °N, 50–59 °W) is a CO_2 sink from the atmosphere to the ocean (-1.7 Tg C per month), a factor of 10 greater than previously estimated. The spatial distribution of CO_2 fugacity is strongly influenced by eddies south of 12°N. During the campaign, a nutrient-rich freshwater plume from the Amazon River is entrained by a ring from the shelf up to 12°N leading to high phytoplankton concentration and significant carbon drawdown (~ 20 % of the total sink). In trapping equatorial waters, NBC rings are a small source of CO_2. The less variable North Atlantic subtropical water extends from 12°N northward and represents ~ 60 % of the total sink due to the lower temperature associated with winter cooling and strong winds. Our results, in identifying the key processes influencing the air-sea CO_2 flux in the WTA, highlight the role of eddy interactions with the Amazon River plume. It sheds light on how a lack of data impeded a correct assessment of the flux in the past, as well as on the necessity of taking into account features at meso and small scales.

7.2.2 Introduction

The North Brazil Current (NBC) is one of the dominant features of the tropical Atlantic circulation. In a region dominated by zonal jets, it flows northward along the coast of South America and separates from the coast around 6-8°N. The NBC seasonally turns back on itself in a tight loop, called the NBC retroflection, and feeds the North Equatorial Counter Current, closing off the equatorial wind-driven gyre (Fig. 7.1). This retroflection occasionally pinches off some of the world's largest eddies, the North Brazil Current rings (Johns et al., 1990; Richardson et al., 1994). After their separation from the NBC retroflection region, the rings travel northwestward toward the Lesser Antilles in a course parallel to the coast of South America. These eddies have been extensively studied using modelling and both in situ (e.g. 1998-2001 NBC Ring experiment; Wilson et al., 2002) and satellite observations (e.g. Goni and Johns, 2001; Fratantoni and Glickson, 2002; Aroucha et al., 2020). They have a mean radius of 200 km, and their diameter can exceed 450 km. Vertically, some of them extend down to more than 1000 m (Fratantoni and Glickson, 2002; Fratantoni and Richardson, 2006; Johns et al., 2003). The NBC rings swirl clockwise and travel with an average northwestward translation speed of 8-15 $km.d^{-1}$ (Johns et al., 1990; Mélice and Arnault, 2017). Most of the anticyclonic eddies detectable by altimetry are rather shallow, extending from the surface to 200-300 m (Garraffo et al., 2003; Wilson et al., 2002). When they reach the Lesser Antilles, they start to coalesce and disintegrate partly due to interactions with the topography (Fratantoni and Richardson, 2006; Jochumsen et al., 2010). There is substantial variability in the number of rings shed per year, ranging from five (Aroucha et al., 2020; Fratantoni and Glickson, 2002; Mélice and Arnault, 2017; Goni and Johns, 2001) to nine (Johns et al., 2003). NBC rings play a crucial role in the inter-hemispheric transport of salt and heat in the Atlantic Ocean and are an important part of the meridional overturning circulation (Johns et al., 2003). The NBC rings disrupt an already complex region located in the vicinity of the Amazon River mouth and at the transition between equatorial and subtropical waters. While most of the studies on rings focused on their physical properties, little is known about their biogeochemical properties and how they affect the air-sea CO_2 flux of the western tropical Atlantic.

The global ocean acts as an atmospheric CO_2 sink, taking up 23 % of total anthropogenic CO_2 emissions (Friedlingstein et al., 2020) and leading to ocean acidification (Masson-Delmotte et al., 2021; Pörtner et al., 2019). The concentration of atmospheric CO_2 is increasing due to human activities (IPCC, 2019, 2021), and characterizing the role of the ocean in mitigating climate change through CO_2 uptake is thus a key investigation. The equatorial Atlantic Ocean is the second-largest source of CO_2 to the atmosphere after the equatorial Pacific (Landschützer et al., 2014; Takahashi et al., 2009). Previous works in this region examined the influence of the equatorial upwelling and of the Amazon plume on the CO_2 flux. CO_2-rich equatorial waters, originating from the equatorial upwelling (Andrié et al., 1986), strongly contrast with the CO_2-undersaturated Amazon River plume waters.

The magnitude of the Amazon River discharge is unique in the global ocean. It represents as much freshwater as the next seven largest rivers in the world combined and contributes to almost 20 % of global river freshwater input to the ocean (Dai and Trenberth, 2002). It therefore strongly impacts the physical, biogeochemical and biological properties of the coastal and the open ocean. Often overlooked, the Amazon River plume is an atmospheric CO_2 sink of global importance (Ibánhez et al., 2016). The plume carries water rich in silicate, nitrogen and phosphate into the tropical oceanic waters that are strongly depleted in nutrients. As water mixes and turbidity decreases, the primary producer's growth and associated biological drawdown are stimulated (Chen et al., 2012). Nitrogen is rapidly consumed, and nitrogen fixation by diazotrophs becomes the main pathway of carbon sequestration in the plume (Subramaniam et al., 2008). This strong carbon drawdown leads to a significant sink of atmospheric CO_2 (Körtzinger, 2003; Lefèvre et al., 2010). Not taking into account the Amazon plume would result in overestimating the tropical Atlantic air-sea CO_2 flux by 10 % (Ibánhez et al., 2016).

The Amazon River's discharge reaches a minimum in December and progressively increases from January onwards. The plume extension is minimum from January to March (Fournier et al., 2015), and as a result, it is the period of maximum salinity in the northwestern tropical Atlantic. The Amazon outflow region is particularly hard to reconstruct due to its strong variability and a severe lack of data. Waters located in the southeasternmost part of the domain act as a strong source of CO_2 to the atmosphere. The source gradually turns into a sink north of 10°N as waters become colder due to seasonal winter cooling. This situation is typical of a transition zone between equatorial and subtropical waters in winter (Landschützer et al., 2020; Fig. 7.1b). The northwestern tropical Atlantic is commonly divided into two parts: the northern much less variable part (also called "Trade wind region") and the southern part, also referred to as Eddy Boulevard (Stevens et al., 2021). The freshwater of the Amazon remains mainly confined to the continental shelf due to winds perpendicular to the coast as it travels northwestward into the Caribbean Sea (Coles et al., 2013). However, it has recently been documented that offshore freshwater transport is often present in February and significantly alters the physical properties of the region (Reverdin et al., 2021). This is partly due to the interaction of the NBC rings with the Amazon plume

(Fig. 7.1a). The ocean colour signature of the Amazon (Muller-Karger et al., 1988) has been used as a tracer to delineate the rings and better understand their generation, evolution and characteristics (Johns et al., 1990; Fratantoni and Glickson, 2002). The Amazon River also influences the surface temperature and salinity of the rings. For example, Fig. 7.1a shows a freshwater plume stirred by a large ring. They are considered warm-core rings but have a warm sea surface temperature (SST) anomaly in the first half of the year and a cold one in the second half because the anomaly is relative to the regional SST, with an extensive warm pool in late summer and autumn (Ffield, 2005). Their signature in salinity is therefore plume-dependent as well. Ffield (2005) reported that three out of four rings were surrounded by lower-salinity water. Salinity and chlorophyll a are therefore critical to understand the surface physical and biogeochemical properties of the region, as well as the air-sea fluxes of CO_2.

The northwestern tropical Atlantic is a dynamically active region, with eddies several hundred kilometres in diameter and connected to the world's largest river. There are surprisingly few biogeochemical observations available for winter months during low outflow of the Amazon River. Few tropical Atlantic measurements of biogeochemical tracers are available, with one transect in winter in the Surface Ocean CO_2 Atlas (SOCAT; Bakker et al., 2016) database south of 10°N crossing the region. This scarcity is a major impediment in understanding the biological and physical processes underlying the oceanic carbon and nutrient cycles in the region. Satellite salinity shows a contrasted spatial structure with eddies and filaments (Fig. 7.1a). In this study, we take advantage of the physical and biogeochemical data collected during the EUREC^{4}A-OA/ATOMIC (Elucidating the Role of Clouds-Circulation Coupling in Climate Ocean-Atmosphere and Atlantic Tradewind Ocean-Atmosphere Mesoscale Interaction Campaign) experiment in January-February 2020, combined with satellite data, to understand how the NBC rings and their related structures impact the air-sea CO_2 flux in winter. The paper is organized as follows. We present the in situ observational data from the EUREC^{4}A-OA/ATOMIC experiment, as well as the satellite data, in Sect. 2. We identify the water masses observed in the region and their physical and biogeochemical properties and estimate the CO_2 fluxes at regional scale using empirical relationships in Sect. 3. In Sect. 4, we compare the results with climatologies of air-sea CO_2 fluxes to evaluate the added knowledge brought by the intensive surveys of February 2020. We discuss the results and the inter-annual variability in Sect. 4, and we conclude in Sect. 5.

7.2.3 Data and Methods

In situ data

The EUREC^{4}A-OA/ATOMIC (Stevens et al., 2021) campaign took place in January and February 2020 and involved research vessels (RVs) from France (RV *Atalante*; Speich and The Embarked Science Team, 2021), Germany (RV *Maria S. Merian*, hereby designated as *Merian*; Karstensen et al., 2020; and RV *Meteor*, not considered in this study since no CO_2 measurements were taken on board) and the United States (RV *Ronald*

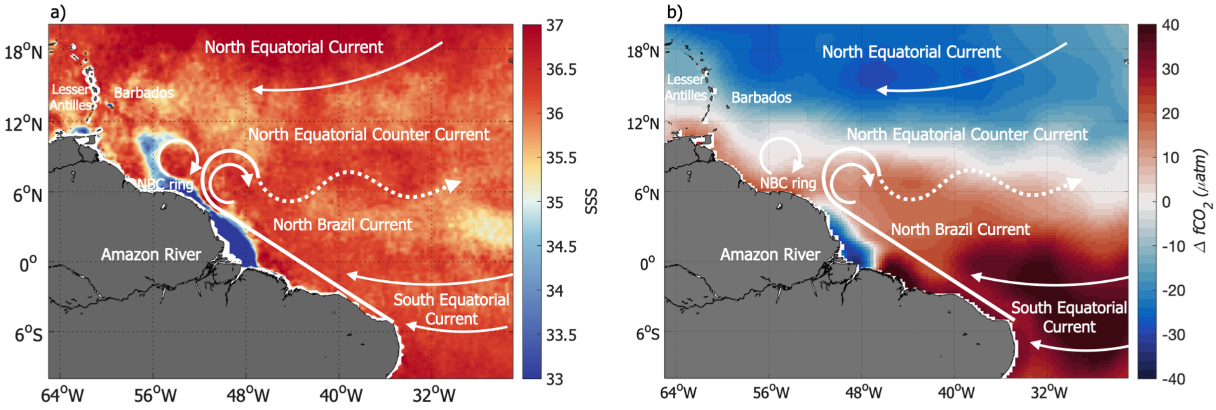

Figure 7.1: Schematic of the main ocean currents in the western tropical Atlantic superimposed over the SSS field of Feb. 7th 2017 (a) and over the February $\Delta f\mathrm{CO}_2$ climatology from Landschützer et al., 2020 (b).

H. Brown, hereby designated as *Ron Brown*; Quinn et al., 2021). These cruises provided numerous in situ measurements, and, in this study, we will focus on the continuous near-surface measurements of temperature, salinity and $f\mathrm{CO}_2$.

Temperature and salinity from thermosalinographs (TSGs), as well as $f\mathrm{CO}_2$ were measured from water pumped ~ 5 m below the surface. For each ship, the resulting CO_2 data are corrected (Lefèvre et al., 2010; Pierrot et al., 2009) from the temperature difference between the water at the ship's water intake and the one analysed by the instrument. RV *Atalante* $f\mathrm{CO}_2$ measurements started on 30 January and ended on 18 February 2020 (Olivier et al., 2020). The underway oceanic and atmospheric $f\mathrm{CO}_2$ were detected by infrared detection using a LI-COR LI-7000 (Takahashi et al., 1993). The $f\mathrm{CO}_2$ system was the same as in Lefèvre et al. (2010). It uses a shower air-sea equilibrator described by Poisson et al. (1993). Seawater from the TSG pumping circuit circulates in the equilibrator at a rate of 2 L min^{-1} . A closed loop of about 100 mL of air flows through the equilibrator designed to avoid bubbles at the air-sea interface. To minimize temperature corrections, the equilibrator is thermostated with the same seawater as the one used for CO_2 measurements. The temperature difference between the equilibrator and the sea was on the order of 0.5°C.

Furthermore, 138 samples for dissolved inorganic carbon (DIC) and total alkalinity (TA) analysis were collected on board RV *Atalante,* as well as inorganic nutrients (silicate, phosphate, nitrate and nitrite). DIC and TA were measured at the SNAPO-CO_2 (French National Facility for Analysis of Carbonate System Parameter) facility by potentiometric titration using a closed cell, following the method of Edmond (1970). Nutrients were conserved by heat pasteurization and analysed by colourimetry at IRD LAMA service in Brest.

An OceanPack CUBE FerryBox system from SubCtech was installed on RV *Merian* measuring continuously the oceanic $f\mathrm{CO}_2$ from 23 January to 19 February 2020. Water is pumped at a rate of ~ 7 L min^{-1} through a debubbler unit subsequently followed by a SeaBird SBE 45 thermosalinograph before it circulates along a membrane through which CO_2 diffuses. On the other side of the membrane, the air loop is circulated at a rate of 0.5 L min^{-1} through a LI-COR LI-840 non-dispersive infrared gas analyser (e.g. Arruda et al., 2020). RV *Ron Brown* completed two legs, from 10 to 25 January and from 29 January to 13 February 2020. The General Oceanic Inc. 8500 pCO$_2$ instrument installed on board follows a similar methodology to the underway fCO$_2$ system deployed on the *Atalante* and is detailed in Pierrot et al. (2009).

An inter-comparison of the fCO$_2$ measured by RVs *Atalante* and *Merian* is attempted when the ships were navigating together at a distance of less than 5 km (Fig. 7.2). On average, the fCO$_2$ measured by RV *Merian* is 6.4 μatm higher than the one measured on RV *Atalante*, with a standard deviation of 4.8 μatm. RVs *Merian* and *Ron Brown* crossed the same water mass at 13–14°N, 57°W on 12 February. On average, RV *Merian* fCO$_2$ is 6 μatm higher than RV *Ron Brown* fCO$_2$. In part we link these differences to the slower response time of the membrane system; however, differences also lie within the uncertainties of the fCO$_2$ observing systems ($\sim$ 5 μatm for the membrane system installed on RV *Merian* , see Arruda et al., 2020, and $\sim$ 2 μatm for the equilibrator systems installed on RVs *Atalante* and *Ron Brown*). The region where RV *Merian* and RV *Atalante* were close is very variable (standard deviation of 20 μatm), and RV *Merian* and RV *Ron Brown* were never in the same place at the same time, so the observed differences could also be due to the natural variability in fCO$_2$ sampled differently by the various ships. Hence, we did not apply any correction, and we checked that the effect of a 6 μatm systematic bias in RV *Merian* fCO$_2$ had a minor effect on our resulting interpolations. A comparison between the reconstructed flux with and without a correction for the 6 μatm systematic bias suggests that such a systematic bias would lead to less than 2 μatm difference in our mean interpolated fCO$_2$ and less than 0.1 mmol.m^{-2}.d^{-1} in the mean derived air-sea CO$_2$ flux.

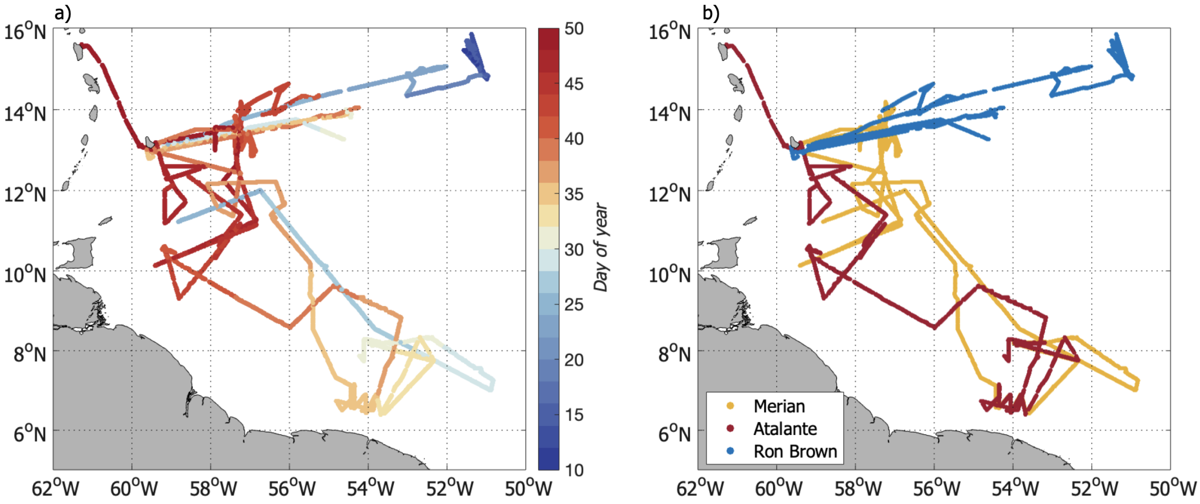

Figure 7.2: Ship tracks colour-coded by day of year (a) and by ship name (b).

Satellite and atmosphere reanalysis data

Daily satellite maps of chlorophyll-a (chl a) and SST, as well as absolute dynamic topography (ADT) and sea surface salinity (SSS), are used in this study.

The salinity maps are a blend of the Soil Moisture Ocean Salinity (SMOS, January 2010–present) and Soil Moisture Active Passive (SMAP, April 2015–present) measurements developed by Reverdin et al. (2021). The European SMOS and US SMAP missions observe the sea surface by L-band radiometry from sun-synchronous polar-orbiting satellites (Entekhabi et al., 2010; Font et al., 2009; Kerr et al., 2010; Piepmeier et al., 2017). Combining 06:00 and 18:00 local time measurements of both missions provides an almost complete coverage each day. When the coverage was not complete over our region, the 06:00 track of the following day was also included. This daily field is available for the first 20 d of February and leaves out only 2 days without sufficient coverage to retrieve salinity data. It has a spatial resolution close to 70 km and an uncertainty on the order of 0.5. This product is optimized for the northwestern tropical Atlantic in February 2020 and has an almost daily resolution. It is an experimental daily product built to have the best representation possible of the Amazon plume variability. The product, its uncertainties and the comparison between the TSG salinity and the satellite SSS are detailed in Reverdin et al. (2021).

Daily chl a concentration maps and SST maps are produced by CLS (Stum et al., 2016) on a spatial grid of 0.02°. The chl a concentration maps are composites built from VIIRS (Visible Infrared Imaging Radiometer Suite; on Suomi NPP (Suomi National Polar-orbiting Partnership) and NOAA-20 US platforms) and OLCI (Ocean and Land Colour Instrument; on Sentinel 3A and 3B Copernicus European platforms) satellite sensors. The SST product is a 1 day average of infrared radiometer satellite data. Both datasets are sensitive to the cloud cover, but during our period of interest, they are usually without many gaps except at the end of February. The comparison between the TSG SST and the satellite SST product is detailed in RV *Atalante*'s cruise report (Speich and The Embarked Science Team, 2021).

Daily ADT maps at a 1/4° resolution combine data from all satellites available for the period 1993 to present. From these ADT fields, the TOEddies algorithm, developed by Laxenaire et al. (2018), identifies eddies and their trajectories. The eddy detection is based on the closed contours of ADT, as well as the maximum geostrophic velocity associated with the eddy.

In order to compute the air-sea CO_2 fluxes, the European Centre for Medium-Range Weather Forecasts (ECMWF) Reanalysis v5 (ERA5) hourly wind speed and mean sea level pressure, P_atm, are used. ERA5 covers the period from January 1950 to present and provides hourly data on a 30 km grid. In addition, the monthly wind speed and SST fields over the period 1998–2015 are used, and a climatology over this period is computed. The wind speed in the region in winter is on average between 6 and 8 m. s^{-1} , and its variability is low.

We compare the EUREC^{4}A-OA / ATOMIC observations with the observation-based CO_2 partial pressure (pCO_2) climatology developed by Landschützer et al. (2020), created using a two-step neural network method (Landschützer et al., 2016) and combining open and coastal ocean datasets. The associated ΔpCO_2 and air-sea CO_2 flux monthly field climatologies over the 1998-2015 period are computed using the ERA5 climatological wind, SST and P_{atm} fields, as well as the atmospheric CO_2 from the Ragged Point, Barbados, station.

Methods

Air-sea CO_2 flux We compute the air-sea flux (F; mmol.m−2.d^{-1}) as follows:

$$F = k \cdot K_0(fCO_2 - fCO_{2atm}), \tag{7.1}$$

where K_0 is the solubility of CO_2 in seawater, expressed as a function of SSS and SST by Weiss (1974); $f\mathrm{CO}_{2atm}$ is the atmospheric CO_2 fugacity; and k is the gas transfer velocity. k is calculated following the relation from Wanninkhof (2014):

$$k = 0.251 \cdot < U^2 > \cdot (Sc/660)^{-0.5}, \tag{7.2}$$

where Sc is the Schmidt number, and U is the wind speed at 10 m above sea level derived from ERA5 wind speed. The ERA5 wind speed is used for the satellite-based analysis and the air-sea CO_2 flux climatology. The measured winds from the ships are adjusted to 10 m following a logarithmic profile (Tennekes, 1973) and used to compute the along-track flux for visualization purposes.

In order to compute $f\mathrm{CO}_{2atm}$ over that period, we first derived the saturation vapour pressure (P_{H2O}) from SSS and SST and then the atmospheric $p\mathrm{CO}_2$ using the monthly averaged CO_2 mole fraction ($x\mathrm{CO}_{2atm}$) measured at the NOAA/Earth System Research Laboratory (ESRL) station in Ragged Point, Barbados (13.17°N, 59.43°W):

$$fCO_{2atm} = xCO_{2atm} \cdot (P_{atm} - P_{H2O}) \cdot C_f, \tag{7.3}$$

where C_f is the fugacity coefficient, a function of the atmospheric pressure and SST (Weiss, 1974).

Reconstruction of $f\mathrm{CO}_2$ from satellite maps Our approach is to derive from the large EUREC^{4}A-OA dataset a relationship linking $f\mathrm{CO}_2$ to SST, SSS and chl a in order to provide maps of $f\mathrm{CO}_2$ based on the satellite maps of SST, SSS and chl a. Chl a was not measured on board; thus, we use satellite surface chl a co-located along the ship track. This set of parameters is used as proxy to describe the influence of ocean dynamics, chemistry and also marine biology on $f\mathrm{CO}_2$. The biological carbon pump is one of the major components of the oceanic and global carbon cycles as the photosynthetic production of organic carbon by marine phytoplankton accounts for about half of the carbon fixation associated with global primary production (Arrigo,2007; Behrenfeld et al., 2006; Field et al., 1998). However, while chl a is an indicator of biological activity, it is also a very good tracer of ocean circulation, so, depending on the water masses origin, $f\mathrm{CO}_2$ and chl a are not expected to be systematically negatively correlated. Waters rich in detrital material tend to limit the phytoplankton growth, and microbial respiration of riverine material on the continental shelf likely dominates (Aller and Blair, 2006; Medeiros et al., 2015; Mu et al., 2021). Even considering the extent of the EUREC^{4}A-OA atomic cruise, the dataset is still sparse and cannot fully represent the small-scale variability it highlights. In order to understand the fluxes at regional scale the need for a good spatial resolution arises. For that, the surface T (temperature), S (salinity) and chl a diagram computed from the ship measurements (and co-located satellite chl a) is interpolated using a linear 3D interpolation on a grid of SST, SSS and chl a. The grid has a resolution of 0.01 °C in SST, 0.1 in SSS and 0.01 in log(chl a (mg m^{-3})). Using a 3D linear inter- polation to map the fCO_2 data over a grid is a simple yet effective solution for a dataset that is still relatively sparse. The method is presented in more details in the Supplement (Text S1 in the Supplement). Using a linear fit prevents oscillations between two data points and yields good results. Along the ship track, the standard deviation between the measured and reconstructed fCO_2 is ~ 4 μatm. Each triplet of surface T , S and log(chl a) in the range of the values measured by the ship is therefore associated with a value of fCO_2 based on the 3D linear interpolation of the in situ values. In order to cover the whole range of T-S-log(chl a) present in the region, we extrapolate to lower temperatures and lower salinities than the ones measured by the ship. In order to do so, we add four points to the T-S-chl a diagram at lower salinities and lower temperatures based on previous knowledge of the region. For the low-salinity domain (SSS < 30), fCO_2 is strongly dominated by salinity, and the influence of temperature is weak (Lefèvre et al., 2010). The SSS–fCO_2 relation developed by Lefèvre et al. (2010) is in good agreement with the SSS–fCO_2 relationship computed from this study data (Fig. S1 in the Supplement) in the common range, and we therefore use it to compute fCO_2 at a salinity of 26 ($fCO_2(S = 26) =$ 251.4 μatm). The lower temperature is mostly located in the northern part of the domain, which is the least variable and where the variations in fCO_2 are dom- inated by the ones in temperature. From this dataset we compute a variation of 15 μatm $°C^{-1}$, which is consistent with the 4.23 % ° C^{-1} expected variation in fCO_2 with temperature due to the temperature sensitivity of the carbonate dissociation constants and CO_2 solubility (Takahashi et al., 2002; Wanninkhof et al., 1999). We use this dependency to compute the fCO_2 at a temperature of 24°C to cover the whole range of temperature in the region.

We combine the interpolated fCO_2 with satellite maps of SST, SSS and chl a to obtain daily high-resolution maps of fCO_2. Some days, either the presence of clouds altering the chl a and SST or the lack of salinity coverage prevents the retrieval of fCO_2 . In order to limit the error in fCO_2 , we only keep 9 days out of the first 20 days of February (2, 4, 6, 7, 9, 11, 12, 17 and 19 February) when the coverage is sufficient. Then, daily mean sea level pressure maps and wind fields are used to compute the air–sea CO_2 flux over the region in a similar way as described in Sect. 2.3.1. The salinity maps present major errors near islands because no correction of the island effect was applied on the SMAP maps (Grodsky et al., 2018). Therefore, the reconstructed flux will be studied over a region excluding the close vicinity of the islands (5-16°N, 59-50°W).

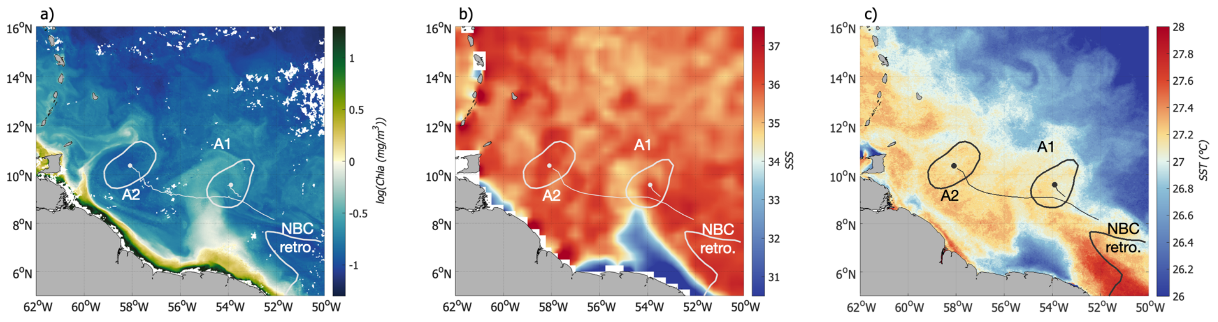

Figure 7.3: a) Chlorophyll-a, b) SSS and c) SST on Feb 6th 2020 with the contours of NBC rings A1 and A2, their centre and their trajectory. The NBC retroflection is identified from the 0.51 m contour of the satellite derived ADT.

7.2.4 Results

A transition region presenting strong mesoscale activity

Figure 7.3 shows how in February 2020 the ocean currents of the western tropical Atlantic (WTA) strongly influenced the variability in SSS, SST and chl a at many scales, with an NBC ring stirring a plume of fresher water rich in chlorophyll a toward the open ocean. This is also supported by the measurements done during the EUREC^{4}A-OA/ATOMIC campaign in January–February 2020 (Fig. 7.4). They show a complex environment - for example $\Delta f\mathrm{CO_2}$ presents similar large-scale features as the climatology - but it also reveals numerous smaller-scale structures (Fig. 7.4a). Among the latter, two stand out. These are the very low $f\mathrm{CO_2}$ in the south-eastern part of the domain and the high $f\mathrm{CO_2}$ around 11°N. In early 2020, the NBC retroflection was very variable and shed two large anticyclonic rings (Fig. 7.3). They are long-lived 250 km large eddies travelling northwestward toward the Lesser Antilles in the Eddy Boulevard region. The ring detection algorithm TOEddies based on ADT indicates that NBC ring A2 separated from the retroflection in late December, was fairly stationary during the cruise period (February 2020) and was located around 11°N, 58°W. NBC ring A1 separated from the retroflection in early February 2020 and then stayed around 10°N, 54°W for 10 d before translating northwestward toward the Lesser Antilles after 20 February. These eddies contribute to the variability in the region in two ways. As they travel, they transport the water trapped in their core during their formation (eddy trapping), but they also stir the surrounding waters (eddy stirring).

Surface water mass identification

In an effort to understand how biogeochemistry is forced by physical processes in the ocean, we used surface chl a to complement SST and SSS data in defining surface water masses. We observed that in the northwestern tropical Atlantic in winter in situ $f\mathrm{CO_2}$ strongly depends on these three variables (Figs. 7.4 and 7.5). There is a strong positive dependence of $f\mathrm{CO_2}$ on SSS, with low $f\mathrm{CO_2}$ for low SSS (Fig. 7.5c and d). Across the whole EUREC^{4}A-OA/ATOMIC region, SST did not vary much (mean SST of 27 °C and standard deviation of 0.5°C), but warmer waters present higher $f\mathrm{CO_2}$. The dependence on chl a allows

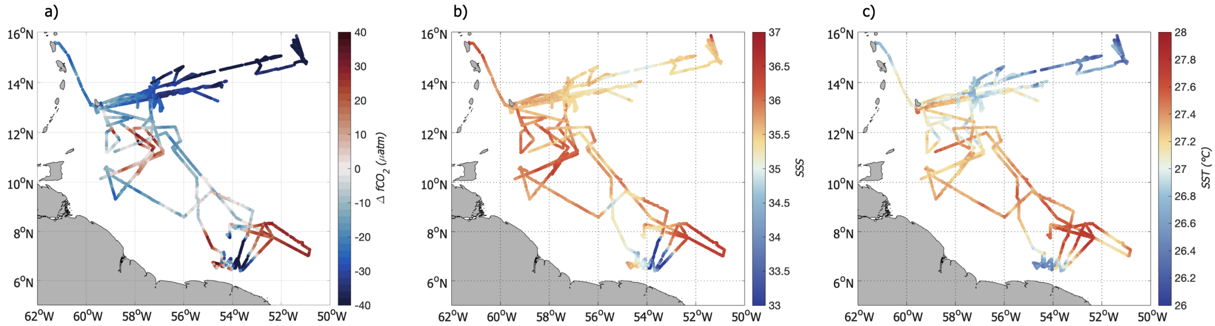

Figure 7.4: a) In-situ measurements of (a) $\Delta f\mathrm{CO}_2$, (b) salinity, (c) temperature.

for the discrimination of water masses with the same surface T and S properties but not the same $f\mathrm{CO}_2$ (Fig. 7.5). Satellite-based chl a is hard to discriminate from detrital material using ocean colour where both are present as they have close spectral characteristics. Figure 7.5 shows that waters with an SST of 26.5 °C and SSS between 35-36 can either be rich in chl a and have a high $f\mathrm{CO}_2$ or below in chla and have a low $f\mathrm{CO}_2$. By combining SST and SSS with chl a and using information from the dynamical structures of the region, we identified six upper-ocean water masses (Fig. 7.5a and b). The along-track $\Delta f\mathrm{CO}_2$ for each ship is presented in Fig. 7.6, colour-coded with the identified water mass, highlighting the link between the surface T-S-chl a relation and $\Delta f\mathrm{CO}_2$. The way we defined water masses, considering time-varying boundaries, is relatively similar to the one used by Longhurst (2010) and some of the surface water masses compare well with Longhurst's (2010) biogeochemical provinces. He identified three provinces in the northwestern tropical Atlantic: the North Atlantic Tropical Gyre province (NATR), the Western Tropical Atlantic province (WTRA) and the Guiana Coastal province. In this first part, we will present two surface water masses that are usually identified in the region (e.g. Longhurst et al., 1995, 2010) and their physical properties.

North of Barbados, the domain is mostly dominated by North Atlantic Subtropical Waters (NASW), similar to Longhurst's NATR. They have a SSS in the range of 35 to 36 and are relatively cold (Table 1). Their SST diminishes over time towards the end of February. These waters are less in- fluenced by coastal dynamics and therefore are not very productive at the surface (chl a levels inferior to 0.14mg.m^{-3}) due to low nutrient levels. They are mainly located north of 13°N and get progressively colder toward the northeast. RV Ron Brown stayed in that Trade Wind region for almost a month (Fig. 7.5). The observations collected from this ship show lower $f\mathrm{CO}_2$ in NASW with respect to the atmosphere ($\Delta f\mathrm{CO}_2$ $\sim$ -40 μatm). Similar results are found on one of RV Merian's transects, with $\Delta f\mathrm{CO}_2 <$ -30 μatm. The NBC is surface-intensified and fed by the central branch of the South Equatorial Current (SEC; Schott et al., 1998). As the cold and saline water from the upwelling region is transported westward by the SEC, it warms up (SST > 27 °C) but retains its saline characteristic (SSS > 36, Table 1) as it reaches the NBC retroflection region (Fig. 7.4). This NBC water mass is oligotrophic (Fig. 7.3b) and therefore in our area of interest distinguished itself by its low level of surface chl a (chla<0.14mgm^{-3}). These waters are found in the retroflection area

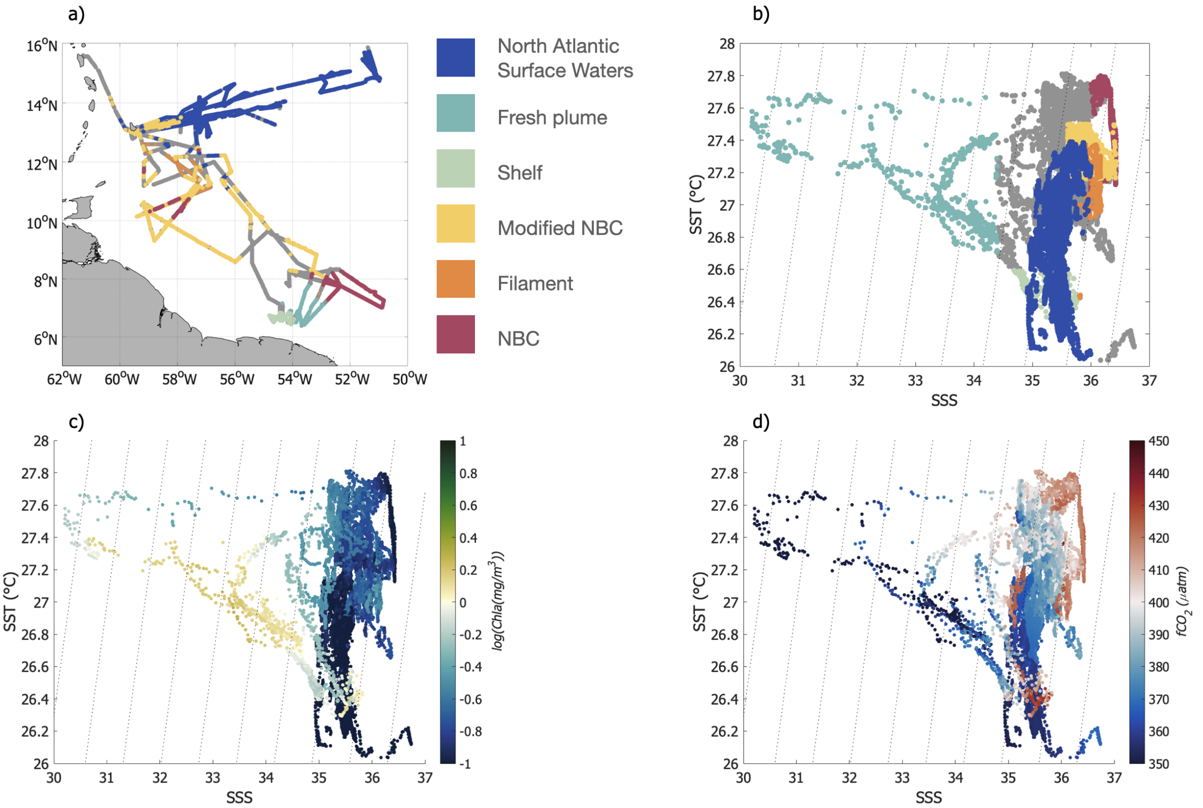

Figure 7.5: a) Map representing the RVs Atalante, Merian and Ron Brown ship tracks colour-coded with the identified water masses. b) T-S diagram colour-coded with the water masses; the grey colour corresponds to points that do not fit into the definition of the identified water masses.

and were sampled by both RVs *Merian* and *Atalante* at the beginning of February (Fig. 7.5). The NBC water mass is in some way similar to the WTRA but does not extend beyond the retroflection, therefore representing a more limited part of the WTRA. We will introduce four new water masses in the following parts, as well as their associated dynamical structures. They can be considered as subsets of the WTRA and Guiana Coastal provinces, these two provinces being too large and not well suited to represent small-scale processes.

North Brazil Current Rings

The extension of the NBC retroflection varies depending on the state of eddy formation. It moves northwestward up until 9°N as an eddy is forming and then retracts to the south-eastern part of the region. During our period of interest, the retroflection shed anticyclone A1 at the beginning of February. It is difficult to estimate the date of shedding as the area is highly dynamic, and detecting the first closed contour of ADT is complicated and may be inaccurate. It is however interesting that the two ships sampled the retroflection when it was expanding to generate A1, and this northwestward expansion is well observed on several physical and biogeochemical parameters (Fig. 7.7a). RV *Merian* crossed the retroflection on 27 January and stayed in the area until 2 February (Fig. 7.6). Chl a present on the shelf is advected by the strong currents on the periphery of the retroflection and delineates well its

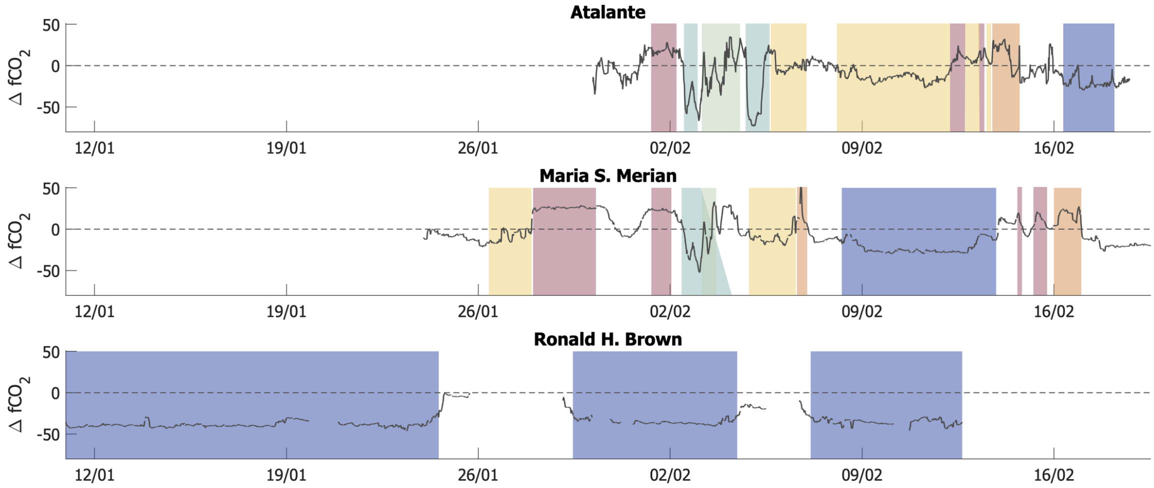

Figure 7.6: RVs Atalante (top), Merian (middle) and Ron Brown (bottom) $\Delta f\mathrm{CO}_2$ time-series. The background color indicates the crossed water mass domains (see definition in legend of Fig 5).

southwestern side (Fig. 7.7a). The NBC waters stand out on the surface T-S diagram as they are the most saline waters observed in the region (Fig. 7.7b). They are also high in $f\mathrm{CO}_2$ which reflects their equatorial origin. Their SST is relatively warm, varying from 27.8°C at the crossing of the first retroflection front to 27.2 °C. The region is rather homogeneous, with an almost constant SSS of 36.3 and $\Delta f\mathrm{CO}_2$ along the multiple crossings, as observed on the Merian and Atalante transects (Fig. 7.6). On average along those transects, the NBC $f\mathrm{CO}_2$ is higher than $f\mathrm{CO}_{2atm}$ by 20 μatm.

Anticyclone A1 is further crossed by RV Atalante on 6 February, just a few days after its separation from the retroflection (Fig. 7.7c). The surface signal is almost lost, both in SST and in $f\mathrm{CO}_2$ (Fig. 7.7c and d). It is mainly composed of modified NBC water, whose properties are close to the NBC water (high SSS, high SST, low chl a) but not as pronounced. This water mass covers a larger area, which mainly encompasses the Eddy Boulevard region. It is defined here as SSS > 35.6, 27.16°C < SST < 27.6°C and 0.11mg.m^{-3} < chl a < 0.25 mg.m^{-3} (Table 1). While the high chl a water delimits well the retroflection area, it partly covers eddy A1.

NBC ring A2 presents a different situation. Detached from the retroflection in early December 2019 (as defined from altimetry detection), it travelled northwestward while retaining an intense coherent core. Coastal waters identified by their high chl a content were less present and mostly entrained at the northwestward edge of the eddy. After 2 months, A2 almost reached Trinidad and Tobago and was located around 11°N, 58°W when it was sampled by the two ships (Fig. 7.7e). The SST signal is eroded, and most of the eddy is mostly made of modified NBC water with relatively low $f\mathrm{CO}_2$. However, high SSS (36.5) and $f\mathrm{CO}_2$ (415 μatm) are still visible near the eddy centre on the two crossings made by RV *Atalante* on 12 and 13 February. This is confirmed by the two sections of the *Merian* that crossed the altimetric eddy centre and measured SSS at 0.5 higher in the 50 km radius around the centre and above 36. The NBC water mass is therefore found close to the centre of eddy A2, as well as its associated high $f\mathrm{CO}_2$.

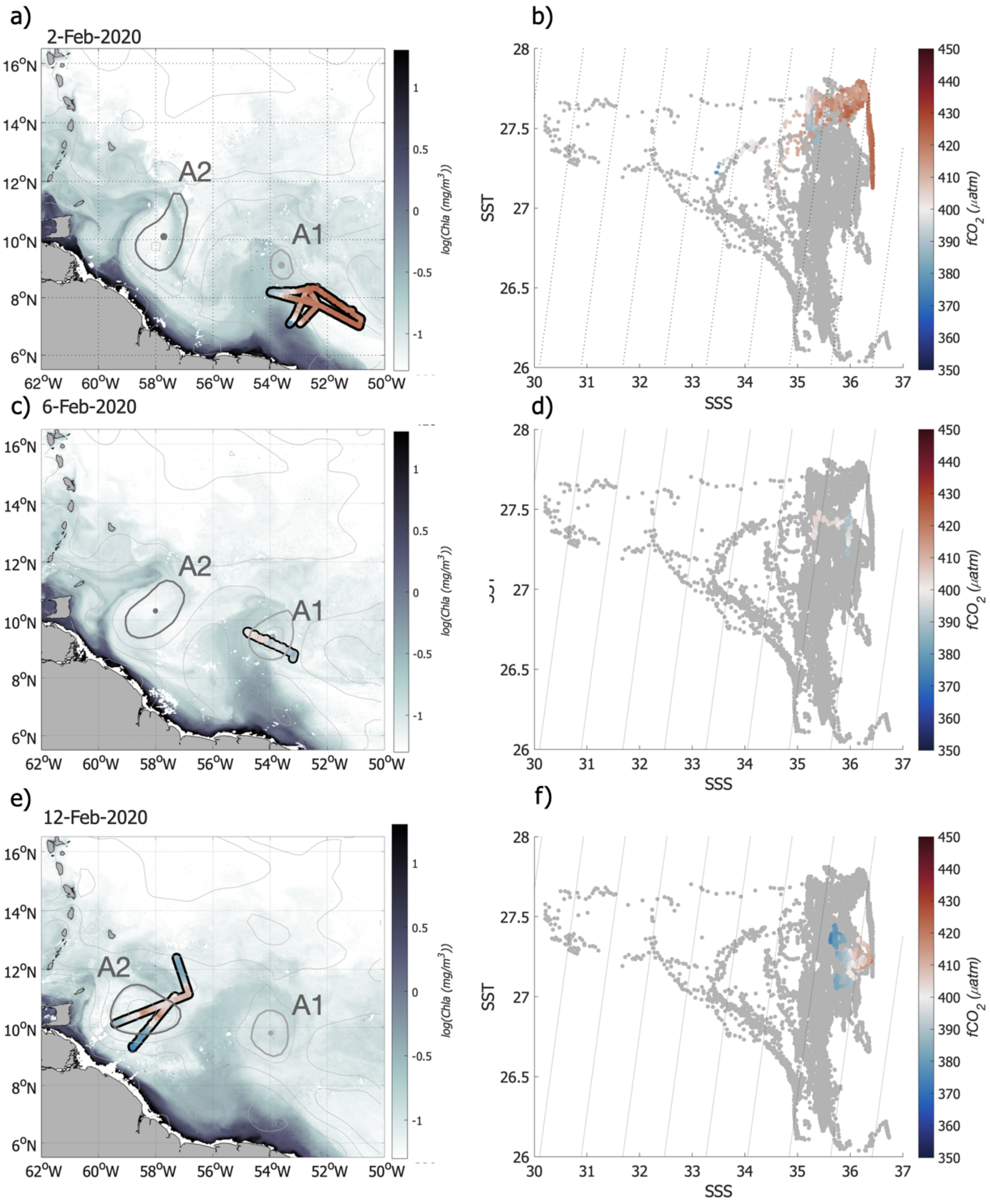

Figure 7.7: a) RVs Atalante and Merian ship track in the NBC retroflection (Merian: Jan. 27th to Feb. 2nd, Atalante: Feb 2nd), c) in NBC ring A1 (Atalante: Feb 6th) and e) in NBC ring A2 (Atalante: Feb 12th-13th, Merian: Feb 13th-14th) colour-coded with fCO_2. The background represents the Chla on Feb 2nd (a), Feb 6th (c) and Feb 12th (e), and the contours of NBC rings A1 and A2 are indicated. b),d),f) Corresponding T-S diagrams colour-coded with fCO_2.

From the collected observations, it appears that the surface signature of NBC rings is relatively variable and complex. It is well marked in their formation area in the NBC retroflection, where waters brought north by the NBC are warmer, saltier and higher in fCO_2 than the water of the northwestern tropical Atlantic. As the eddies travel northwestward, further away from the retroflection, they may be subject to various processes that modify the surface signal. Unfortunately, the data collected are not sufficient to shed light on which processes are involved in this situation. South of Barbados, away from the retroflection, the modified NBC is therefore the most common water mass. Nevertheless, the NBC water is still sometimes observed months after the separation from the retroflection in the eddy centre.

Freshplume

The NBC rings form and evolve in an area highly influenced by the Amazon River plume. Even if February is a period of low Amazon River outflow (Dai and Trenberth, 2002), freshwater events are relatively common. In February 2020, a freshwater plume detached from the Guiana plateau and spread out into the northwestern tropical Atlantic. The off-shelf plume was steered northward by the retroflection and NBC ring A1 up to 12°N and then extended westward toward the Caribbean Sea. Waters carried by the plume strongly contrast with the saline waters of the retroflection. They include water from the Amazon and present low SSS (SSS < 34.5), low $f\mathrm{CO}_2$ ($f\mathrm{CO}_2 < 380\ \mu\mathrm{atm}$) and high chl a (Table 1). The plume was crossed three times: twice on 2 February and once on 5 February (Fig. 7.6). Freshwater from the Amazon arrived on the plateau on 1-2 February and was then entrained northwestward by Ekman transport and geostrophic currents (Reverdin et al., 2021). On 2 February RVs Atalante and Merian left the retroflection area to cross the adjacent nascent plume. SSS rapidly decreased, reaching 33, which is associated with a strong decrease in $f\mathrm{CO}_2$ (Fig. 7.8). From 2 to 5 February, the plume formed, and on 5 February the plume was approximately 100 km wide, with the lowest salinities around 30. Based on satellite SSS data of the following days, the plume appears to have reached even lower salinities and then spread out over the north- western tropical Atlantic. It first spread northward, steered by A1, and then northwestward, channelled between A1 and A2 and reaching all the way up to 12°N and extending over more than 100 000 km^2 (Reverdin et al., 2021). The plume can be followed by satellite SSS and chl a maps (Fig. 7.7a, c and e). Indeed, the low SSS is also accompanied by high chl a as water from the Amazon is considered highly productive. The northwestern tropical Atlantic is in general nutrient-limited, but the nutrients brought by the Amazon can support the occurrence of a bloom. The plume is also characterized by high silicate (between 4 and 10 μmol kg^{-1} in the plume, almost 0 elsewhere), while nitrate and phosphate are rapidly consumed. Traces of inorganic phosphorus were observed in the plume, while nitrates were absent from surface waters (Fig. S2 in the Supplement). Low salinity combined with high biological productivity led to low $f\mathrm{CO}_2$ and a strong carbon drawdown in the plume as the $\Delta f\mathrm{CO}_2$ reached -73 μatm on 5 February (Fig. 7.6). In an area highly influenced by the NBC waters, through rings or the retroflection, the plume stands out and modifies the biogeochemical dynamics of the region.

Shelf water and filaments

The freshwater plume is not the only water stirred by the NBC rings travelling from the NBC retroflection towards the Lesser Antilles. The

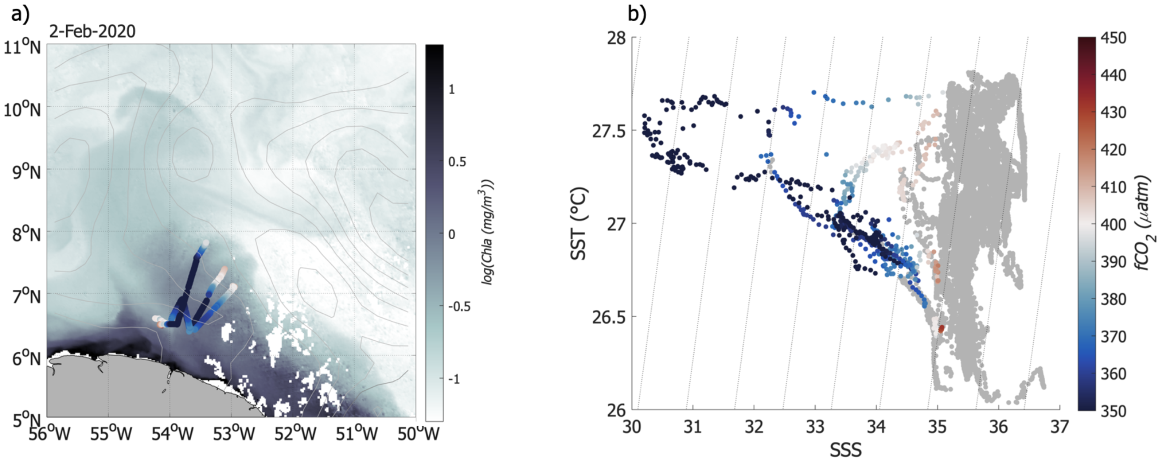

Figure 7.8: a) RVs *Atalante* and *Merian* ship track in the freshwater plume (*Atalante*: Feb 2nd, Feb 5th, *Merian*: Feb 2nd) colour-coded with $f\mathrm{CO_2}$. The background represents the Chla on Feb 2nd. b) Corresponding T-S diagram colour-coded with $f\mathrm{CO_2}$.

shelf water is very different from the plume water and was only sampled sparsely on the way in and out of the plume (Figs. 7.4 and 7.5). On the Guiana plateau water is very rich in chl a and detrital material, rather saline (SSS ~ 35.5), and relatively cold (SST ~ 26.5 °C) (Fig. 7.5 and Table 1). Since the water sampled on the edge of the plume was cold due to a local upwelling event (and/or vertical mixing event) detailed in the Supplement (Fig. S3 in the Supplement), temperature is not homogenous on the shelf. Further north, a filament is stirred on the western side of NBC ring A2 (Fig. 7.9a). It is a small-scale structure, approximately 10 km wide and easily identifiable due to its high chl a. The filament is continuously stirred by A2 and so is already visible on chl a maps on 2 February (Fig. 7.7). It followed A2's westward translation and was crossed on 6 and 17 February by RV Merian and on 14 February by RV Atalante (Fig. 7.6). It has a SSS close to 36 and an SST between 27 and 27.5 °C; thus, it is slightly colder and more saline than its surrounding waters (Fig. 7.9b and Table 1). It stands out because of its high chl a content (chla>0.25mgm^{-3}) even if this is lower than close to the coast or in the freshwater plume. The strongest signal is observed on the ocean carbon parameters. In contrast to the freshwater plume, this filament presents very high $f\mathrm{CO_2}$ (> 430 μatm), highlighting different origins. It stands out from the ship track time series by also having a larger positive $\Delta f\mathrm{CO_2}$ (50 μatm). Whereas the freshwater plume observed more southeastward carries water recently arrived on the plateau from the Amazon, the northwestward filament contains shelf waters.

Air-sea $\mathrm{CO_2}$ flux

In order to better characterize the impact of each structure on the regional flux, we computed air-sea $\mathrm{CO_2}$ flux maps from satellite data, at a resolution of 2.5 km (Fig. 7.10), averaged over the period of the cruise (2-19 February). The along-track flux represented in Fig. 7.10a and the reconstructed regional field (Fig. 7.10b) show the importance of the small-scale dynamical structures and highlight two strong regimes that are found on the reconstructed map. The air-sea $\mathrm{CO_2}$ flux in the northeastern

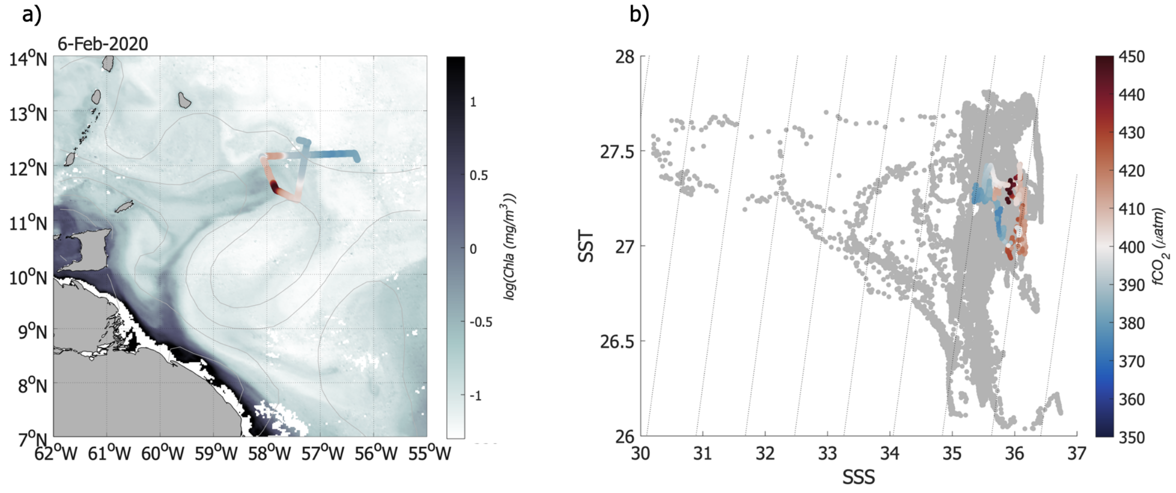

Figure 7.9: a) RV Merian ship track in the shelf water filament (Feb 6th) colour-coded with $f\mathrm{CO}_2$. The background represents the Chla on Feb 6th. b) Corresponding T-S diagram colour-coded with $f\mathrm{CO}_2$.

part of the domain, characterized by the NASW, is mainly dominated by temperature effects, while further south the presence of NBC rings and their interactions with coastal waters create a strong dependence of the CO_2 flux on SSS and on the biological and biogeochemical processes highlighted by the chl a.

We evaluate the integrated air-sea CO_2 flux over the region. In February, waters are the coldest, and the region is a strong CO_2 sink of -1.7 Tg C per month (Fig. 7.11). Three biogeochemical domains mainly contribute to the air-sea CO_2 flux: the NASW, the freshwater plume and the NBC retroflection. The impact on the flux of the small-scale coastal filament is evident along the ship tracks (Fig. 7.10b). However, its contribution to the total flux is weak as the signal is smoothed when averaging over 2-19 February as the filament moves following the A2 ring's northwestward translation. Each of the main three regions is identified based on its averaged SST, SSS and chl a properties in February, and the region-specific flux is determined (Fig. 7.11).

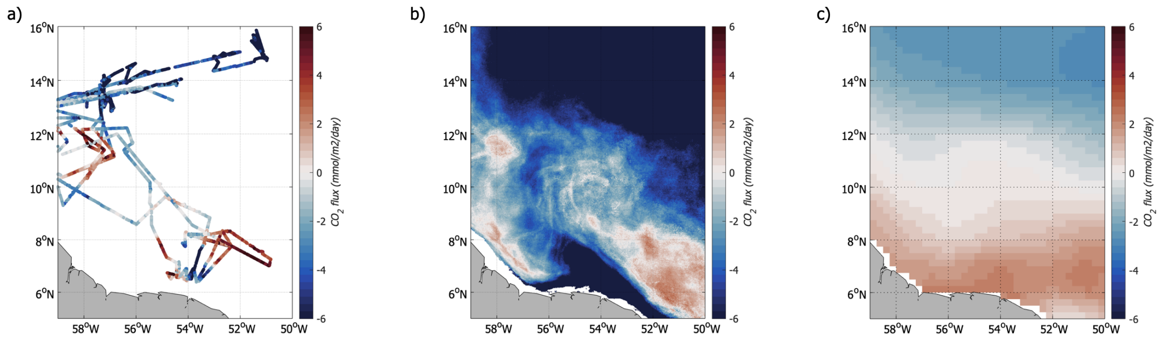

Figure 7.10: a) Air-sea CO_2 flux measured in Jan-Feb 2020 during the EUREC^{4}A-OA/ATOMIC cruise. b) Air-sea CO_2 flux reconstructed over February 2020. c) February climatology of the air-sea CO_2 flux over 1998-2015 (Landschützer et al., 2020).

NASW contributes about 60 % of the total sink due to the relatively cold temperature and to strong winds that enhance the air-sea exchanges.

These waters extend from Barbados northward and eastward, cover more than one third of the domain, and show a weak variability over 2-19 February.

The NBC retroflection is a source of CO_2 to the atmosphere. In February, the strongest signal is observed in the southeastern part of the domain up to 8°N, 53°W. The retroflection nevertheless impacts the region as far as 10°N, 54°W as it is spatially variable, reaching up to 10°N when shedding an eddy. The two NBC rings present a small positive February air-sea CO_2 flux average. Eddy A1 is almost stationary from its formation date (around 6 February) until 20 February, and its neutral to slightly positive CO_2 flux is centred around 10°N, 54.5°W (Fig. 7.10). Eddy A2 translates rapidly westward at the beginning of February and then northward from 15 February. Its signal is therefore not as visible as on the ship tracks as it is averaged over 19 d. The retroflection is the main region with a positive air-sea CO_2 flux; even if the region is too small to have a big global impact, understanding small-scale features may be significant for the total flux. The NBC rings carry part of the signal, which is heavily modified as they travel northwestward. As a result, on average in early to late February only the retroflection maintains a positive flux, while a large part of the domain dominated by modified NBC waters (not influenced by the plume) behaves as a small sink.

The freshwater plume with Amazon water is nascent when crossed by the ships (Fig. 7.10b) but is already the strongest signal of the time series. As the plume develops, it is en- trained by NBC ring A1, then A2, and spreads out into the open ocean, as observed on SSS and chl a maps. The plume generates a strong CO_2 sink that is amplified by strong winds and reaches up to 12°N (Fig. 7.10). The freshwater plume covers only 10 % of the total area but contributes to almost 20 % of the sink. In winter, this region either is not characterized in previous studies or is considered as dominated by high fCO_2 waters brought by the NBC to the climatology. We observe here that the trapping of CO_2-rich water by the NBC ring effect is relatively weak in winter, and the main signal is associated with the filaments they stir. The northwestern tropical Atlantic therefore behaves as a sink of CO_2 in early to mid-February, driven by the cold North Atlantic subtropical waters and the Amazon freshwater plume stirred by NBC rings.

7.2.5 Discussion

Integrated air-sea CO_2 flux

The northwestern tropical Atlantic presents a strong sea- sonal variability in air-sea CO_2 fluxes (Landschützer et al., 2016). In February, waters are the coldest, and we estimate the 5-16° N, 59-50°W domain to be a strong CO_2 sink of -1.7 Tg C per month (Fig. 7.11). This region, located at tropi- cal latitudes but combining characteristics of subtropical waters and river outflow, is difficult to represent in large-scale climatologies. Indeed, the sink for the month of February is smaller by a factor of 10 in Landschützer et al. (2020) and is also considerably smaller in Takahashi et al. (2009), but the low spatial resolution of this last product does not allow for a good quantitative comparison. This region has been rarely observed, and the inter-annual variability described in Landschützer et

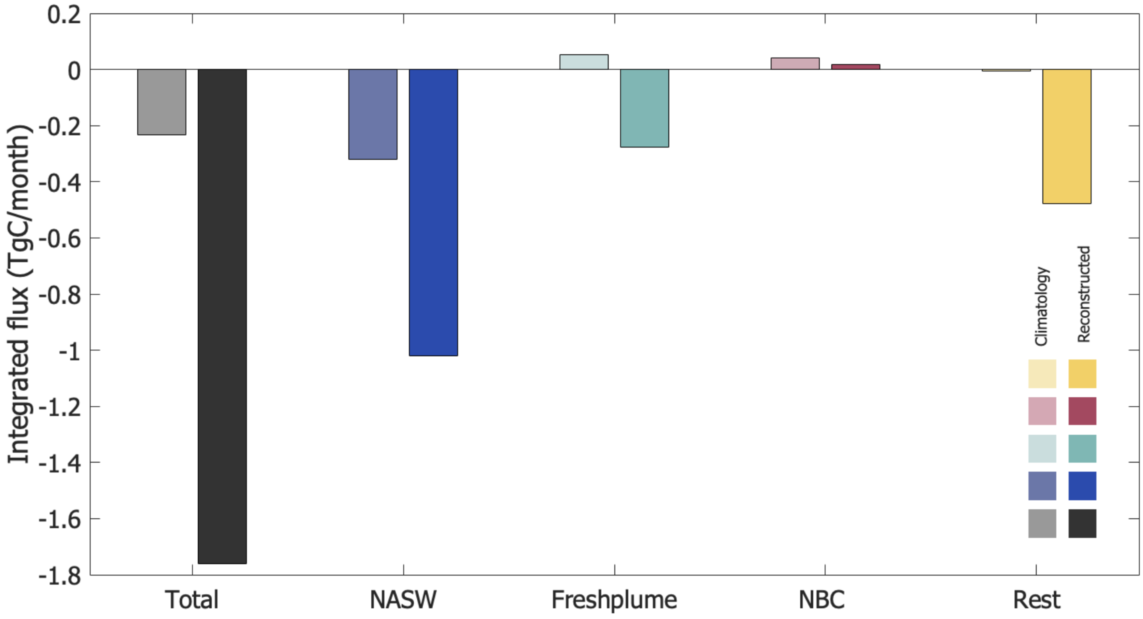

Figure 7.11: Integrated flux for the [5°-16°N, 59-50°W] domain, and for 3 water masses. For each bar duet, the one on the left in faded colours represents the integrated flux from Landschützer et al., (2020) February climatology, while the one on the right is computed from the reconstructed flux. Same colour code as in Figure 7.5.

al.'s (2020) climatology is therefore rather uncertain. The compensating effect of different years cannot explain entirely the difference of signal observed in February 2020 with respect to the two climatologies.

Three water masses mainly contribute to the air-sea CO_2 flux: the NASW, the fresh plume and the NBC retroflection. The NASW contributes about 60 % of the total sink and is not well captured in climatologies, with noticeable differences of more than 20 μatm between the measured ΔfCO_2 in 2020 and the one computed from Landschützer et al. (2020) and Takahashi et al. (2009) (the closest grid point is considered for this comparison). The retroflection is the main region with a positive air–sea CO_2 flux. Its influence is observed up to 10°N, 55°W, but its area is small, so its impact on the regional flux is weak. The positive flux of the retroflection is slightly overestimated in the climatologies, but it could also be due to the difficulty to detect the retroflection at the beginning of February. The main difference is that the NBC waters rich in CO_2 are localized in the retroflection area and are heavily modified when spreading into the Eddy Boulevard.

The freshwater plume is a feature previously not well described for this region in winter, and we found a contribution of almost 20 % to the sink. The impact of the Amazon River has been overlooked so far in winter, but it accounts for a large part of the salinity and biogeochemical variabil- ity. Freshwater from the Amazon is not just located on the shelf, but it can spread northward, advected by the strong current variability associated with the NBC rings (Reverdin et al., 2021). These rings are the largest, faster rotating and the most energetic during boreal winter compared to other seasons (Aroucha et al., 2020). Combined with a seasonal increase in the Amazon's outflow, it induces a large variability in SSS, chl a and fCO_2 The occurrence of freshwater export from the shelf to the open ocean has a strong influence on the salinity and therefore on the mixed layer depth and air-sea heat exchanges (Reverdin et al., 2021). It also strongly impacts the biogeochemistry of the region as the low fCO_2 is due both to the low salinity of the plume waters and to the biological activity. The plume stirred into the open ocean by the NBC rings brings nutrients in a region strongly nutrient-limited and generates a local winter bloom. This in turn plays an important role in the air-sea CO_2 flux and is a crucial feature of the southern part of the northwestern tropical Atlantic.

Extension to other years and inter-annual variability

Few tropical Atlantic measurements of biogeochemical tracers are available, in particular in the northwestern tropical Atlantic. The EUREC^{4}A-OA/ATOMIC campaign provides the first in situ comprehensive measurements of fCO_2 in this region for the boreal winter season. The reconstruction of fCO_2 maps likely provides a good understanding of the spa- tial evolution of fCO_2 and air-sea CO_2 fluxes and is fitted for the months of January-February 2020. Although the processes described here are specific to winter and thus cannot be extended to other seasons, they will be useful to understand the winter variability in other years.

Only a few cruises crossed the region according to the SOCAT database between 2010 and 2019 (period with satellite SSS data), and investigating inter-annual variability is not possible. However, we can test the relation developed for 2020 for other years by using selected cruises from the SOCAT database. We thus first use the relationship to reconstruct fCO_2 along the ship tracks (using in situ SSS and SST and colocalized chl a) and then over the whole region based on satellite products (OSTIA (Operational Sea Surface Temperature and Sea Ice Analysis) SST, GlobColour chl a, CCI+SSS (Climate Change Initiative Sea Surface Salinity), detailed in Appendix A). A comparison between the measured and reconstructed fCO_2 for the water masses sampled by the SOCAT cruises (NASW, fresh plume, NBC retroflection, modified NBC) is presented in the appendix (Table A1). Good agreement is found between the fCO_2 from the SOCAT database and the one reconstructed from the in situ temperature and salinity, as well as co-localized chl a for the four water masses (averaged difference of 5.5 μatm). When comparing reconstructed fCO_2 maps with fCO_2 on ship tracks (Fig. A1), the agreement between fCO_2 in various water masses is very clear even though the spatial structures are sometimes a bit misplaced. This is attributable to the slightly coarser resolution of satellite products not designed specifically for each campaign, to the high spatio-temporal variability in fCO_2, and to missing chl a and SST observations in cloudy areas. February 2020 was mainly cloud free, so we were able to use high-resolution daily SST and chl a. The SSS product used in 2020 is also a daily product. However, for the other years, the satellite chl a (if clouds) and SSS products have a weekly temporal resolution which smears the fast-moving structures. The gradients between water masses are therefore not always well represented, but we find a good agreement between the fCO_2 of each structure, which is encouraging for future studies on inter-annual variability in winter.

By identifying the main processes responsible for the variability in the air-sea CO_2 flux in 2020, we can better understand the inter-annual

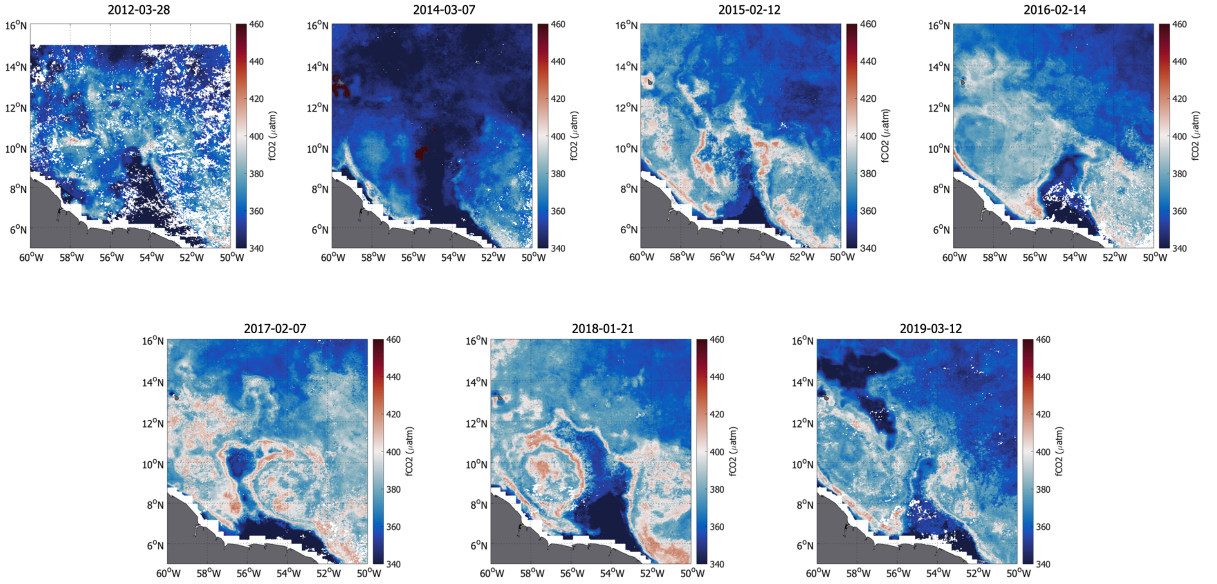

Figure 7.12: Snapshot of reconstructed $f\mathrm{CO_2}$ for all occurrences of fresh plumes extending at least to 10°N and east of 56°W in January-March 2010-2019 (2010, 2011 and 2013 do not present this type of event).

variability in the region. Indeed, each of the main water masses has its own inter-annual variability that shapes the $\mathrm{CO_2}$ variability. The northern part of the domain is dominated by the variation in temperature, and therefore its inter-annual variability is mainly linked to the one of SST. From 32 years of monthly mean SST data, the SST standard deviation in the area is relatively weak and does not exceed 0.5 °C. The northern sink of $\mathrm{CO_2}$ is therefore rather similar from year to year, coherent with the low standard deviation of the air-sea $\mathrm{CO_2}$ flux computed from Landschützer et al. (2020). Some variability is still observed in the snapshot of the reconstructed $f\mathrm{CO_2}$ (Fig. 7.12) but to a much smaller extent than south of Barbados. For example, the strong sink observed in March 2014 is caused by cold SST anomalies over the whole domain. Some small-scale variability in the northern part of the domain is sometimes correlated to SSS anomalies, as in 2019.

The freshwater plume sampled during EUREC^{4}A-OA is a common feature in February. During the 2010-2019 period, events of freshwater reaching the open ocean were observed each year, and freshwater plumes similar to the one described in this paper were observed during 7 out of 10 years of satellite salinity data (Reverdin et al., 2021). Two of the main mechanisms driving the occurrence of the plume are the winds near the Amazon estuary that can induce along-shelf transport to the Guyana plateau and the presence of NBC rings. Most of the plume events similar to the one in this study suggest the presence of an anticyclone to its east. This region is commonly crossed by several NBC rings during winter (Jochumsen et al., 2010; Johns et al., 2003; Mélice and Arnault, 2017), but it also is subject to a strong year-to-year variability that has linkages with the variability in the Amazon River outflow (Aroucha et al., 2020). Therefore, identifying and understanding the processes happening in 2020 should contribute to the better assessment of the inter-annual variability in $f\mathrm{CO_2}$, as well as air-sea $\mathrm{CO_2}$ fluxes, in the northwestern tropical Atlantic during winter. Using a combination of SSS, SST and chl a brings information on the biogeochemistry of the area in winter and represents well the mesoscale structure.

7.2.6 Conclusions

The EUREC^{4}A-OA/ATOMIC campaign provides for the first time synoptic measurements related to the air-sea fluxes of CO_2 in the northwestern tropical Atlantic in winter. Six main surface water masses are identified, one of them north of Barbados (North Atlantic Subtropical Water) and the other five (the NBC retroflection, modified NBC waters, the freshwater plume, the shelf water and the shelf filament) south of Barbados. The investigation highlights the two different regimes of the region. In the northern part, the variability in the CO_2 flux is low, and the area is covered by relatively cold, saline and low-chlorophyll NASW. The southern part is highly variable due to the presence of large mesoscale anticyclonic eddies. In January and February 2020, two NBC rings influence the physical and biogeochemical properties of the region. The NBC retroflection is characterized by waters with equatorial origins that are relatively warm, saline and high in fCO_2. As the rings separate from the retroflection, they interact with the surrounding waters, and the initial signal in fCO_2 is dampened. The main impact of the rings is therefore not necessarily on the surface water they transport in their core (eddy trapping) but rather on the filaments they stir off the coast (eddy stirring). A fresh plume from the Amazon River is transported by the coastal current up to the French Guiana shelf in the beginning of February. The NBC rings entrain the plume of freshwater up to 12°N. This plume is fresh, rich in chl a, and low in fCO_2, strongly contrasts with the surrounding waters, and spreads over $\sim$ 100000 km^2.On the shelf not influenced by the plume, water is relatively saline and high in fCO_2 and chl a probably due to a high concentration of detrital material. As ring A2 propagates westward, it continuously stirs a thin (10 km wide) filament of high fCO_2 shelf water up to 12°N.

Based on the ship observations we identify distinct regimes in fCO_2 linked to certain combinations of SST, SSS and chl a properties. We use this information to construct high-resolution maps of fCO_2 and air-sea CO_2 flux using satellite maps of SSS, SST and chl a. On average over early to mid-February, the region acts as a strong sink of CO_2 (-1.7 Tg C per month), the sink being 10 times smaller in air-sea CO_2 flux climatologies. The NASW is responsible for most of the flux (60 %) due to low temperatures associated with winter cooling and strong winds. South of Barbados, the region also acts as a sink of CO_2. The influence of equatorial water is localized in the retroflection region that acts as a small source of CO_2. The main feature in this part of the domain is the fresh plume that contributes almost 20 % of the total sink.

The processes described here highlight the high variability in air-sea CO_2 fluxes in winter that are quite different from he ones in summer. These features are relatively common in winter and can be used to better understand the inter-annual variability in air-sea CO_2 fluxes. The northern part of the domain is driven by the variability in SST, while the southern one is a combination of the inter-annual variability in temperature, salinity and chlorophyll. It is therefore linked to the year-to-year variability in the NBC rings and the Amazon outflow.

This study is limited by the paucity of data in the region and for this time period. More fCO_2 data closer to the coast would help us to better quantify the influence of shelf water on the flux. The signature of the NBC rings has been described for only two rings that had different signatures. In order to reach more robust conclusions on the transport of surface NBC water by the rings, more eddies should be observed. The variability in fCO_2 occurs at large and small scales. Salinity is one of the most valuable predictors of fCO_2 south of 10°N, but the satellite salinity resolution is much lower than those of temperature and chlorophyll. To have a more accurate prediction of the fCO_2, a high-resolution SSS product would also be very useful.

7.2.7 Appendix A

Due their long time series, the following SST, chl a and SSS products are used to reconstruct fCO_2 maps in winter in the northwestern tropical Atlantic for years other than 2020. Results are shown in Figs. A1 and 12. They are different than the satellite products used in the main study that were only available for a short period.

	Fresh plume	NBC waters	Modified NBC	N
SOCAT fCO2	316.2	413.4	385.8	
fCO2 reconstructed from SOCAT SST and SSS	310.7	410.7	392.9	2
Transect date	2016/01/05	2016/01/08	2015/12/23	2013
Ship name	*Colibri* (France)	*Colibri* (France)	*MSC Marianna* (Panama)	*Bengu* (the Ne
Expocode	35MJ20151229	35MJ20160107	642B20151209	33RO

The OSTIA SST product, distributed by the Copernicus Marine Service (CMEMS) is used here. Daily maps of SST are produced at a resolution of 1/20° and are available from 1981 to present. OSTIA SST uses most SST data available for a day from both infrared and microwave inferred SST. Surface chl a from GlobColour dataset derived from ocean colour at a 1/24° resolution is used. It is a merged product from multiple satellite missions' observations (SeaWiFS, MERIS, MODIS, VIIRS NPP, OLCI-A, VIIRS JPSS-1 and OLCI-B). GlobColour data are developed and validated by ACRI-ST and distributed by the CMEMS. We also use SMOS and SMAP combined weekly SSS generated by the Climate Change Initiative Sea Surface Salinity (CCI+SSS) project (Boutin et al., 2021, https://doi.org/10.5285/5920a2c77e3c45339477acd31ce62c3c). It provides weekly level-3 SSS data from 2010 to 2019 at a spatial resolution of 50 km, sampled daily on a 25 km × 25 km grid, by combining data from the SMOS, Aquarius and SMAP missions.

Code availability. Code used in this study can be made available upon reasonable request to the corresponding author.

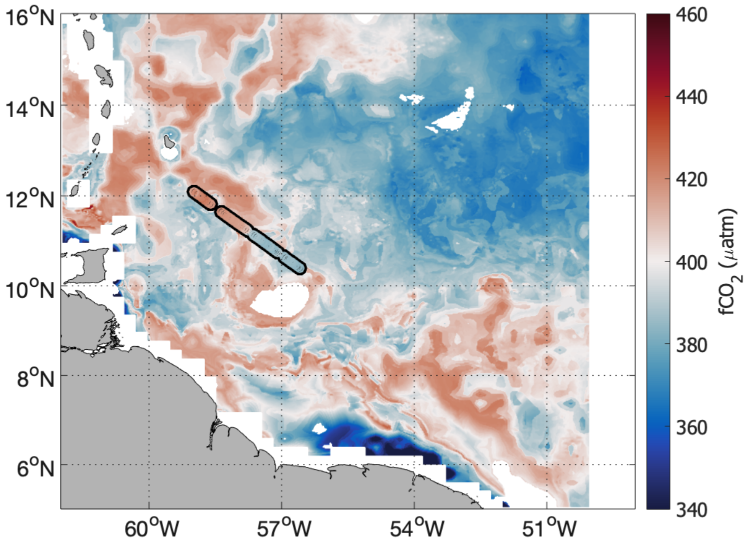

Figure 7.13: $f\mathrm{CO}_2$ reconstructed from OSTIA SST, CCI+SSS and Globcolour Chla for the 23/12/2015 superimposed with the $f\mathrm{CO}_2$ from cruise 642B20151209.

Data availability. We benefited from numerous data sets made freely available and listed here: the ADT produced by Ssalto/Duacs distributed by CMEMS (https://resources.marine.copernicus.eu), the chl a and SST maps produced by CLS (https: //datastore.cls.fr/catalogues/chlorophyll-high-resolution-daily urlhttps://datastore.cls.fr/catalogues/chlorophyll-high-resolution-daily and https://datastore.cls.fr/catalogues/ sea-surface-temperature-infra-red-high-resolution-daily), the SMOS L2Q field produced by CATDS (CATDS, 2019) (https://doi.org/10.12770/12dba510-cd71-4d4f-9fc1-9cc027d128b0), the SMAP maps produced by Remote Sensing System (RSS v4 40km), the CCI+SSS maps produced in the frame of the ESA CCI+SSS project (https://doi.org/10.5285/5920a2c77e3c45339477acd31ce62c3c), and the OSTIA SST and Copernicus GlobColour chl a distributed by the CMEMS (SST_ GLO_ SST_ L4_ REP_ OBSERVATIONS_ 010_ 011 and OCEANCOLOUR_ GLO_ CHL_ L4_ REP_ OBSERVATIONS_ 009_-082).

RV *Atalante* $f\mathrm{CO}_2$ data are available on the SEANOE website: https://doi.org/10.17882/83578. RV *Ron Brown* and RV *Merian* $f\mathrm{CO}_2$ data can be found on the SOCAT database (expocodes 33RO20200106 and 06M220200117 respectively). The Surface Ocean CO_2 Atlas (SOCAT) is an international effort, endorsed by the International Ocean Carbon Coordination Project (IOCCP), the Surface Ocean Lower Atmosphere Study (SOLAS) and the Integrated Marine Biosphere Research programme, to deliver a uniformly quality-controlled surface ocean CO_2 database. The many researchers and funding agencies responsible for the collection of data and quality control are thanked for their contributions to SOCAT.

Supplement The supplement related to this article is available on- line at: https://doi.org/10.5194/bg-19-1-2022-supplement.

Author contributions. LO, JB, GR and NL conceptualized the project. LO carried out the measurements and data analysis. LO, JB, GR, NL and PL contributed to result interpretation. PL, MR and RW provided the crucial datasets. LO, MR, SS, JK, ML, TS and CN conducted field work. LO wrote the manuscript with input from all co-authors.

Competing interests. At least one of the (co-)authors is a member of the editorial board of Biogeosciences. The peer-review process was guided by an independent editor, and the authors also have no other competing interests to declare.

Acknowledgements. This research has been supported by the European Research Council (ERC) advanced grant EUREC^{4}A (grant agreement no. 694768) under the European Union's Horizon 2020 research and innovation programme (H2020), with additional support from CNES (the French National Centre for Space Studies) through the TOSCA SMOS-Ocean, TOEddies, and EUREC^{4}A-OA proposals, the French national programme LEFE INSU, IFREMER, the French research fleet, the French research infrastructures AERIS and ODATIS, IPSL, the Chaire Chanel programme of the Geosciences Department at ENS, and the EUREC4A-OA JPI Ocean and Climate programme. Léa Olivier was supported by a scholarship from ENS and Sorbonne Université. We thank Jonathan Fin at the Service National d'Analyse des paramètres Océaniques du CO_2 (SNAPO-CO_2) at LOCEAN for the analysis of DIC and TA samples, as well as François Baurand at the US IMAGO for the nutrient analysis. Kevin Sullivan performed the data reduction and quality control of data on the *Ronald H. Brown*. We also warmly thank the captain and crew of RVs *Atalante*, *Maria S. Merian* and *Ronald H. Brown*. The measurements on the *Ronald H. Brown* were supported by the Global Ocean Monitoring and Observation (GOMO) programme (fund Ref. 100007298).

Review statement. This paper was edited by Manmohan Sarin and reviewed by Peter Land and three anonymous referees.

Physical and biogeochemical impacts of NBC rings on the late summer Amazon plume

8

8.1 Introduction

The western tropical Atlantic ocean presents a very strong seasonal variability, linked both to the migration of the ITCZ, that modifies the ocean currents and surface salinity though precipitations, and to the Amazon discharge. The boreal summer season is therefore very different from the winter one. In this chapter we investigate the western tropical Atlantic in opposite conditions than in Chapters 6 and 7. In late summer (August, September) the discharge of the Amazon and Pará-Tocantin rivers is decreasing, but still strong. The NBC retroflection is well established and joins the NECC, entraining the fresh Amazon plume eastward (Muller-Karger et al. 1988, Molleri et al., 2010, Coles et al., 2013). Model and drifters studies suggest indeed that the plume is mostly advected in the retroflection during this period, and not much freshwater transport toward the Lesser Antilles arc is expected to take place. However, the NBC rings have been suggested as a mechanism to transport freshwater from the Amazon toward the northwest (Fratantoni & Glickson, 2002, Ffield 2005).

In August and September 2021 the Tara Microbiome mission suggested that there was northwestward freshwater transport during this period through a mesoscale patch of fresh water. Combining in-situ and satellite data, we observed that this fresh water patch is formed by the interaction between the Amazon plume and an NBC ring. After separating from the retroflection, the NBC ring collides with the Demerara rise (a bathymetric feature of the Guiana plateau) and cuts off the freshwater supply that was bringing the Amazon plume stirred around the ring. This creates a large fresh water patch northwest of the ring, of about 200,000 km^2 transporting 0.5 Sv of freshwater toward the Lesser Antilles. This patch, formed in the beginning of September, is observed until late October, when it reached the Martinique and Guadeloupe islands. It is mainly driven by Ekman currents once detached from the NBC ring influence. Its salinity remains below 33.5 for two months, it is shallow and very stratified for a long time, suggesting it could significantly impact the air-sea exchanges of the region. The patch creates a strong anticyclonic circulation due to its strong positive steric anomaly that is detected from satellite altimetry.

Using satellite data to study the entire summer 2021, we observe that the interactions between the Amazon plume, the NBC rings and the NBC retroflection are always present. The Amazon plume is not continuous, as it is the sum of many mesoscale freshwater features. This example on 2021 shows that the freshwater transport from the Amazon alternates between two directions: toward the east and the northwest even when the NBC retroflects. We computed the freshwater transport toward these two directions from 2010 to 2021, and we observe that in late summer on average the fresh-water is advected almost equally toward the east and toward the northwest (figure 8.11). A strong variability is superimposed to this result, 2021 being a year with a stronger transport toward the northwest, while in 2010 the Amazon plume is advected estward.

Knowing the Amazon plume pathways is key for accurately representing the air-sea interactions in the northwestern tropical Atlantic as these fresh waters contributes to the formation of the strong barrier layers of the tropical Atlantic ocean. It is even more crucial when these barrier layers are formed during the peak of the tropical Atlantic cyclone season, and the Lesser Antilles region is on the path of about 60% of tropical cyclones. By the influence of BL on air-sea fluxes, they can contribute to the intensifications of cyclones (Reul et al., 2014, Balaguru, 2012,2020). The spreading of the Amazon River plume also affects the distribution of nutrients and the biological activity. We will preliminary explore this impact, as well as the one on the CO_2 gas exchange in the extended plume in section 8.3.

8.2 Article under review in *Journal of Geophysical Research: Oceans*: Late summer northwestward Amazon plume pathway under the action of the North Brazil Current rings

Léa Olivier[*] • Gilles Reverdin[*] • Jacqueline Boutin[*] • Rémi Laxenaire[‡] • Daniele Iudicone[*] • Stephane Pesant[†] • Paulo H.R. Calil[¶] • Douglas Couet[‡] [§] • Josep M. Herta[¶] • Paula Huber[‖] • Hugo Sarmento[‖] • Andrea Freire[**] • Ariane Koch-Larrouy[??] • Jean-Luc Vergely[††] • Pierre Rousselot[‡‡] • Sabrina Speich[‡]

Received 4 September 2022 –

8.2.1 Abstract

In summer, the Amazon River plume (ARP) extends over much of the western tropical Atlantic Ocean. The Amazon fresh waters repartition is often associated to the dynamics of the North Brazil Current (NBC). The NBC passes off the mouth of the Amazon River and seasonally retroflects toward Africa. In doing so, it forms large anticyclonic rings (NBC rings) propagating northwestward. The Tara Mission Microbiome cruise in

---

[*] Stazione Zoologica Anton Dohrn, Villa Comunale, 80121 Naples, Italy
[†] European Molecular Biology Laboratory, European Bioinformatics Institute, Wellcome Genome Campus, Hinxton, Cambridge CB10 1SD, United Kingdom
[‡] CNRS, Research Federation for the study of Global Ocean Systems Ecology & Evolution, FR2022 - GOSEE, Paris, France
[§] Station Biologique de Roscoff, UMR7144, ECOMAP, Roscoff, France
[¶] EMS, SLU, C/Teodora Lamadrid 40, E-08022 – Barcelona, Spain
[‖] Universidade Federal de São Carlos (UFSCar). Departamento de Hydrobiologia. Rodovia Washington Luiz S/N.São Carlos, S.P., Brazil
[**] Laboratório de Crustáceos e Plâncton, Departamentode Ecologia e Zoologia, Universidade Federal de Santa Catarina, Florianópolis, Santa Catarina, Brasil
[††] ACRI-st, Biot, France
[‡‡] IRD, UAR IMAGO, Délégation Régionale Ouest, Technopole Pointe du Diable, CS 10070, 29280 PLOUZANE

July-September 2021 reveals a new summer freshwater pathway not well documented in earlier studies. Combining in situ and satellite data, we better characterise the summer ARP pathways. In 2021, the ARP was a succession of freshwater patches cut off from the main plume by the NBC rings. September 2021 presented a fresh patch of about 200000km^2, bringing 0.5 Sv of Amazon water northwestward in a period where the main ocean currents suggest eastward transport. This patch was shallow, very stratified, and once separated from the NBC retroflection, it was mainly driven by sheared Ekman currents. It created a surface steric-height anomaly large enough to be identified as an anticyclonic feature in altimetric sea level products. Other similar situations were observed during the summer 2021, leading to a strong intermittency of the ARP transport. Looking back to the 2010-2021 time-period, 2021 was one of the summers where the ARP is the most fractioned, leading to anomalously high northwestward freshwater transport in late summer. This freshwater transport pathway is important for all plume-related phenomenon, from tropical cyclone intensification to distribution of nutrients in the tropical Atlantic.

8.2.2 Plain Language Summary

In boreal summer, the Amazon River plume reaches its maximum extension, bringing fresh and nutrient-rich water to the whole western tropical Atlantic Ocean. The pathways of the plume are driven by the local dynamics, mainly by the North Brazil Current. It flows along the coast of south America, and retroflects in summer toward Africa generating large anticyclonic rings. In July-September 2021, the Tara mission Microbiome highlighted a new plume pathway. Once the NBC retroflection is settled, it carries the freshwater eastward. However, the plume interacts with the retroflection and the rings, cutting off the plume. It creates an alternative path, were some of this water, once separated from the main currents, is pushed by the wind toward the northwest. The freshwater patch observed in 2021 was 200,000 km^2 and very shallow. We show that from 2010 to 2021, in late summer the plume was very discontinuous, and the freshwater transport switched between the east and the northwest due to a combination of winds, presence of rings and position of the retroflection. Characterizing the pathways of the Amazon plume is important for understanding many phenomena, from tropical cyclone intensification to the distribution of nutrients in the tropical Atlantic.

8.2.3 Introduction

The magnitude of the Amazon River discharge and nearby river discharges, such as Pará-Tocantins is unique in the global ocean. It represents as much freshwater as the next 7 largest rivers in the world combined and contributes to 20% of global river freshwater input to the ocean (Dai & Trenberth, 2002). It also contributes much more freshwater to the northwest tropical Atlantic than the local precipitation minus evaporation budget (Ferry & Reverdin, 2004). The resulting Amazon River plume (ARP) spreads out in the Western Tropical Atlantic (WTA) Ocean over up to 1.3 million of km^2 (Subramaniam et al., 2008).

The ARP is a very important feature of the WTA on many accounts with a significative impact on its biodiversity. It is a barrier to animal dispersion, it isolates the Caribbean Sea and tropical Brazil ecoregion and spatially structures animal species diversity (Giachini Tosetto et al., 2022). The ARP brings nutrients in a highly oligotrophic region, maintaining a large phytoplankton bloom (Smith & Demaster, 1996). The nutrients delivered by the Amazon enhance the NPP in the western tropical Atlantic of almost 10 % (Louchard et al., 2021). The plume creates a large ocean carbon sink during the period of maximum discharge (May-June) of the Amazon (Ibánhez et al., 2015; Lefévre et al., 2010), but also in winter, where combined with the local dynamics it maintains a strong CO_2 sink (Olivier et al., 2022).

The Amazon discharges at the equator, in-shore of the North Brazil Current (NBC, Figure 1). The NBC, one of the dominant features of the tropical Atlantic circulation, flows north-westward along the shelves of South America and separates from the shelves around 6-8°N, often to the east of the Demerara Rise. It seasonally retroflects to feed the North Equatorial Counter Current and thus closes the equatorial wind-driven gyre. This retroflection occasionally pinches off large anticyclonic eddies, the North Brazil Current rings (NBC rings, Johns et al., 1990; Richardson et al., 1994). With a mean radius of 200 km and a diameter than can exceed 450 km, they are some of the largest rings in the world. There is a large variability in the number of rings shed per year, ranging from 5 (Aroucha et al., 2020; Fratantoni & Glickson, 2002; Mélice & Arnault, 2017, Goni & Johns, 2001) to 9 (Johns et al., 2003). The NBC rings are an essential part of the WTA system and have been shown to contribute to half of the northward mass transport of the warm limb of the Atlantic meridional overturning circulation (Johns et al., 2003). At the surface, the NBC rings strongly interact with the fresh and light waters from the ARP. In particular, near the Demerara rise (Figure 1), they have often been associated with plumes of Amazon freshwater penetrating from the shelf over to the open ocean (Olivier et al., 2022; Reverdin et al., 2021).

Via the formation and maintenance of barrier layers (BL), the river plumes can have a significant influence on the air-sea exchanges. As a surface shallow layer, the BL enhances the trapping of solar radiation that seasonally can elevate the SST by up to 1°C in the northwestern tropical Atlantic (Foltz & McPhaden, 2009), and up to 4°C in the vicinity of the Amazon mouth (Ffield, 2005). The BL-induced stratification also modifies the trapping of the momentum exchanged between the ocean and the atmosphere. Several studies suggest that BLs created by the Amazon plume weaken the mixing induced by tropical cyclones as well as the entrainment of colder water to the surface, thus contributing to tropical cyclone intensification (Balaguru et al., 2012, 2020; Ffield, 2007; Grodsky et al., 2012; Reul et al., 2014). The tropical cyclone season in the Atlantic spans from June to November and peaks in August-September. It is therefore interesting to investigate how the plume evolves and what controls the advection of its fresh water in the northwestern tropical Atlantic in late summer, a region frequently crossed by tropical cyclones.

The Amazon and Pará Rivers discharge reaches a minimum in December and progressively increases from January onwards. The plume extension is minimum in that time-period (Fournier et al., 2015) and, as a result, it is the season of maximum salinity in the northwestern tropical Atlantic.

During this season, the freshwater of the Amazon was expected to mainly remain confined to the continental shelf due to winds perpendicular to the coast as it travels northwestward towards the Caribbean Sea (Coles et al., 2013). The peak discharge commonly happens in May-June (Dai et al., 2009), and is associated with strong northwestward transport of plume water at 5°N, as the NBC retroflection is either weak or non-existent during this period (Coles et al., 2013). It is followed in August by the largest extension of the plume east of the lesser Antilles in the Northwest tropical Atlantic, often extending northward of 20°N (Fournier et al., 2015; Salisbury et al., 2011). In July-August however, the NBC retroflection settles, and model studies as well as drifters do not suggest direct feeding of the plume water toward the northwest, but instead a large feeding of the North Equatorial Counter Current (NECC) further east (Coles et al., 2013; Molleri et al., 2010; Muller-Karger et al., 1988).

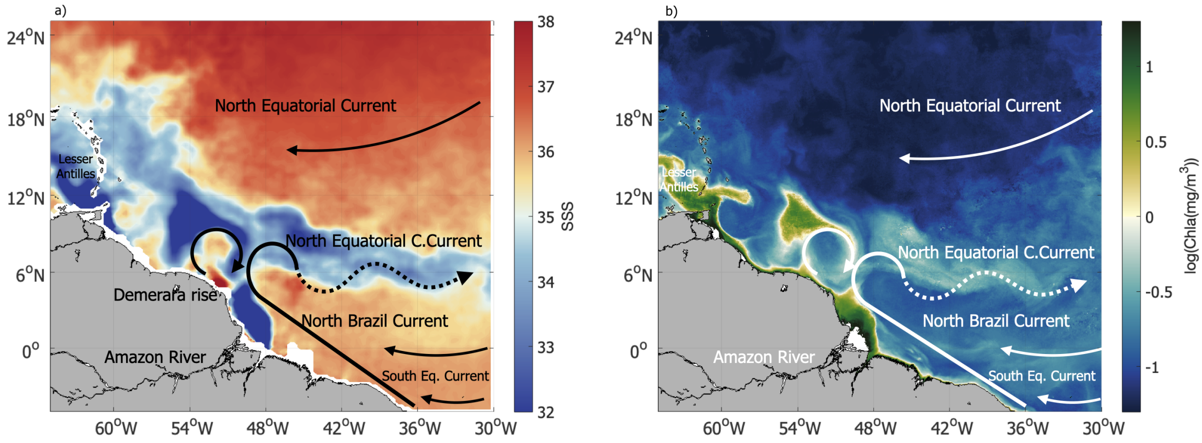

Figure 8.1: Main currents and locations over a) sea surface salinity and b) chlorophyll-a on the 15th of September 2021

On the other hand, different results have been suggested by investigating ocean colour used as a tracer to delineate the NBC rings to better understand their generation, evolution and characteristics (Johns et al., 1990; Fratantoni & Glickson, 2002, Ffield 2005). These earlier analyses suggested that rings could be a way to transport Amazon-origin freshwater northwest of the NBC retroflection, which is compatible with mapped Sea Surface Salinity (SSS) based on the relation between SSS and coloured detrital matter associated with the plume (Salisbury et al., 2011; Fournier et al., 2015). Ffield (2005, 2007) also reported the presence in summer and fall of Amazon freshwater to the west and north of the NBC retroflection. She also presented in situ data from other seasons indicating that newly formed rings are usually surrounded by freshwater or covered by it, and thus that they contribute to the freshwater transport to the northwest of the retroflection. Coles et al., (2013) also mention the possibility of transport by the rings in their modelling study.

In this paper, we revisited the issue of freshwater transport to the northwestern tropical Atlantic during summer, based on data gathered during the Tara Microbiomes expedition in August-September 2021, as well as on daily satellite data. We investigated the interactions between the ARP and the NBC rings to better understand the meso-scale transport of freshwater in 2021. Conclusions reached for this specific summer were extended to the 2010-2021 period based on satellite salinity maps, as well as surface winds and geostrophic currents.

8.2.4 Data

Ship data

The sailing vessel (SV) Tara collected numerous valuable datasets during the AtlantECO mission Microbiome cruise legs 5, 6 and 7 in August-September 2021 (Figure 2). Leg 5 started on August the 18th, 2021 from Fort-de-France, Martinique and finished in Macapá, Brazil on the 9th of September 2021. The following Leg 6 from Macapá to Belém (Brazil) started on September 12th until September 16th 2021. Leg 7 linked Belém to Salvador da Bahia (Brazil) from September 24th to October 8th. The in-line continuous near surface data comprised a Sea Bird SBE45 and SBE38 measuring sea surface temperature (SST) and salinity (SSS), from water pumped at 2 m (or less) from the surface. Although salinity has no unit, in this paper we consider the measured salinity variable, or practical salinity, of symbol pss (practical salinity scale) in agreement with international oceanographic commission recommendation on in situ salinity data (IAPSO Working Group on Symbols, 1985). A few long stations (14 to 24 hours) with repeated conductivity, temperature and depth (CTD) profiles were done from SV Tara in this region. The profiles have the advantage compared to larger research vessels to start close to the sea surface with little near-surface mixing induced by the ship's structure below 2-m depth. Four to twelve casts were usually repeated in the same site over a whole day. During station 38 close to the northern edge of an Amazon freshwater plume, conditions changed considerably between successive casts, providing statistics on variability across the plume's outer front.

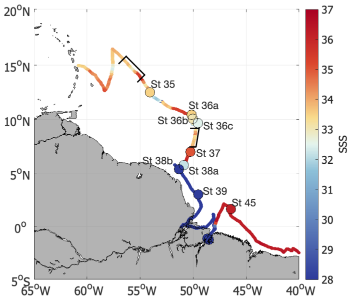

Figure 8.2: SV Tara's journey coloured by the SSS from the TSG. CTD stations are represented by circles, coloured by the minimum salinity of the profile. The black frame highlights the two sections of the route where the TIA has been deployed.

A towed instrument array (TIA) from the Helmholtz-Zentrum Hereon was deployed three times from SV Tara during the leg from Martinique to Macápá. Ten CTD48M from Sea&Sun Technologies attached to a dyneema rope are deployed while the ship is sailing for about 36 hours. Depending on the ship's speed, the deepest CTD can reach down to 55 m. Five of them were equipped with an additional oxygen sensor, while the other five were equipped with fluorescence sensors. Two of these transects (Figure 2) crossed fresh water patches and will be used in this paper. To characterize the density stratification, we computed the mixed layer depth in this paper as the maximum of the vertical density gradient. It compares well with the method looking at a fixed density change from the surface. The surface reference can change a lot between the CTD profiles (some being able to reach closer to the surface than other), therefore the density gradient method was preferred in this study.

Drifters

Five surface velocity profilers (SVP) drifters drogued at 15 m depth (Lumpkin & Pazos, 2007) were deployed from SV Tara and five more from RV Antea during its Amazomix mission (Bertrand et al., 2021) in late August and early September with a focus on the NBC and the Amazon plume. Two SVP drifters were picked up by other vessels less than 10 days after deployment, but all the other ones were still in good working order after a month. In addition, SV Tara deployed 43 small surface followers developed by the Helmholtz-Zentrum Hereon. These will be referred to as Spot drifters. They have a small surface tube and are drogued at 50-cm depth, with tracking done by the Spot/Gobalstar satellite system. Here, we focus on the Spot drifters deployed south of 12°N and away from the Amazon estuary, often as triplets at the same site as an SVP drifter.

The drift characteristics of surface drifters rather similar to the Spot drifters were compared to the SVPs ones (in the absence of non-wind related vertical shears) in the Mediterranean Sea by Poulain et al. (2022). They showed that the difference can be interpreted there as a downwind component on the order of 0.5 to 1% of the wind. With typical winds in the Amazon plume area on the order of 6 m/s, this is equivalent to 3-6 cm/s downwind component. When comparing pairs of close-by drifters (at a distance less than 10 km, and after averaging velocities over 3 hours), we found much larger differences of the zonal velocity component, often exceeding 30 cm/s. The winds were mostly easterlies and in the zonal direction, so these differences correspond to a down-wind drift at a speed 3.5% of the 10-m wind. This is much larger than the expected Stokes drift or other direct wind effect on the small surface element (see Poulain et al., 2022). During EUREC^{4}A-OA (Speich et al., 2021; Stevens et al., 2021), a large downwind vertical shear of 25 cm/s from the top meters to 15 m was observed over the Guyana shelf near 6.80°N/54.24°W (Reverdin et al., 2021) averaged over 11 hours and with a moderate haline stratification (0.4 over that depth range). In the meridional direction, the results are much more variable. Meridional winds were usually smaller, and 8 pairs of drifters (out of 51) show very large differences in meridional velocity exceeding 32 cm/s (3 with a difference larger than 75 cm/s). In all these cases, it corresponds to Spot drifters going faster northward. This is not unexpected as all these instances were in the fresh plume between 4 and 7.5°N, either on the shelf or close to the shelf break, with the plume mostly oriented south-north (or southeast-northwest). The large differences could thus be either associated with horizontal shear (the Spot drifters often being a little bit to the west of the SVP drifters; large horizontal shears were observed near fronts into the plume in February 2020, Reverdin et al., 2021), or possibly with strong localized vertical shears in areas where the plume was fairly shallow and experiencing large acceleration. Large vertical shears are indeed also commented by Coles et al., (2013) during the Anaconda cruises. However, for those cruises, the ADCP did not measure above 11-m depth, and so only the deeper shear could be assessed.

Satellite products

Salinity Sea surface salinity daily maps were produced following Reverdin et al. (2021), for most of August and September 2022. They are a blend of the Soil Moisture Ocean Salinity (SMOS, Jan. 2010-present), and Soil Moisture Active Passive (SMAP, Apr. 2015-present) measurements with an effective resolution of 70 km. The European SMOS and US SMAP missions observe the sea surface by L-band radiometry from sun-synchronous polar-orbiting satellites (Entekhabi et al., 2010; Font et al., 2009; Kerr et al., 2010; Piepmeier et al., 2017). Combining measurements of both missions near 6 a.m. and 6 p.m. local time, provides an almost complete coverage of this region for some days with uncertainties on the order of 0.5 pss or less. We first removed some SMOS tracks strongly influenced by radio-frequency interferences (RFI) in this region, mostly in early September, as well as occasional fresh patches on SMAP maps that were also likely due to RFIs. This together with the actual available tracks implies that we could produce a fairly gap-free field only every two to three days. In addition, a new product was developed following a similar approach to the Climate Change Initiative (CCI) V3 weekly products (Boutin et al., 2021) but with a different temporal smoothing. In order to reduce the temporal smoothing, an exponential time correlation kernel was used instead of a Gaussian time correlation kernel. This high-resolution SSS product available in area of high variability was produced for the whole period of 2010 to 2021 and combines SMOS and SMAP (after April 2015) data (Boutin et al., 2022). Preliminary analysis suggests that this new product provides a satisfactory removal of the worse RFI signals. Away from some South American coastal areas, it allows reproducing well the structures present in the daily product. Some RFI nevertheless persist close to Barbados from 2011 to 2015. For this product, data close to the coast were often removed before the mapping. This, together with inadequate climatological fields, implies that the SSS fields are not always consistent with expectation near the coasts. When using this product, these areas (such as those very close to the Amazon estuary) will not be considered. The consistency of the products with in situ data is illustrated on August 25th with a 3-day track of Tara SSS data superposed (Supplementary Figure S1 and section 3.5). The two high salinity cusps are seen both in Tara track and the SSS products in the right place. On the other hand, selecting the SSS product two or three days before or after (not shown) Tara crossed those cusps results in a position mismatch. It is difficult to go much further in the validation, although there seems to be a tendency for these products to be saltier than observed for the freshest salinity plume areas.

Chlorophyll-a, temperature and altimetry Daily chlorophyll-a (Chla) concentration maps and SST maps are produced by CLS (Stum et al., 2016) on a spatial grid of 0.02°. The Chla concentration maps are composites built from VIIRS (on Suomi-NPP and NOAA-20 US platforms) and OLCI (on Sentinel 3A and 3B Copernicus European platforms) satellite sensors. The SST product is a 1-day average of 4 infrared radiometer satellite data. Both datasets are sensitive to the cloud cover. A comparison with in situ SST during the EUREC4A-OA cruise in January-February 2020 in the northwestern tropical Atlantic of this product is presented in Speich et al., (2021).

In addition, large scale and low frequency geostrophic currents will be used based on daily ADT maps (CMEMS DT-2018) at a $\frac{1}{4}$ resolution which combine data from all altimetric satellites available for the period 1993 to present. These delayed-time maps typically smooth in time the structures over more than a week to 10 days, and resolve current structures down to 100 km scale.

The products of Chla and SSS show the presence of coherent structures in the area of the NBC retroflection or to its east. This is, for example, illustrated on Figure 1 (September 15th) which presents a triangular shaped feature of freshwater (54°W/10°N) as well as a NBC ring to the west of the NBC retroflection. The advantage of the Chla product is its higher resolution which resolves various filaments and small-scale structures that are smoothed out on the SSS map. In this season, the Chla product also presents very little areas without data due to cloud cover. Earlier studies (e.g., Fournier et al., 2015) suggest that it would be more appropriate to use ocean colour products indicative of coloured dissolved organic matter as a proxi for salinity. However, the products that were available presented a much larger percentage of data loss on a daily basis and could not be used in a similar way.

8.2.5 Results

Mixed layer depths

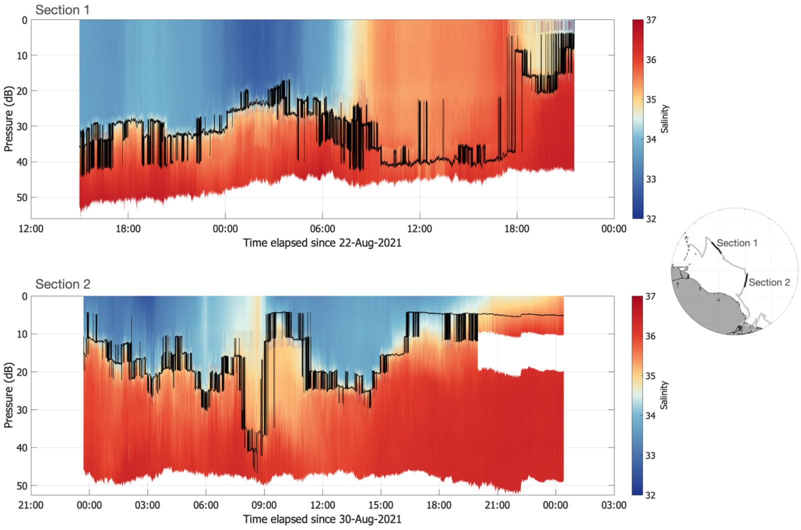

Figure 8.3: Salinity along the two TIA sections. The mixed layer depth is overlayed in black. The map on the right is a reminder of Figure 2, showing Tara's track and the position of the two TIA sections.

The CTD profiles repeated up to twelve times for each Tara station indicate a large range of mixed layer depths (MLD), with often low values in the freshest waters on the shelf (Table 1). Large time variability is observed at each site, in particular for station 38 in the Amazon plume. The surface salinity there varies by more than 6 pss in one day, and over 20 pss in two days (Table 1 and Supplementary Figure S2). The CTD stations closest to the plume on the shelf indicates rather shallow MLD and fresh layer thickness usually less than 6-m thick. Even a little further north near 10°N (Station 36c, August 30th) and near 12.5°N (Station 36b, August 28th) in surface water close to or less than 33.5 pss, the average depth of the fresh layer was only 15 m. The two TIA sections support these results, and show how the MLD and the intensity of the salinity structures crossed by Tara varies (Figure 3). The second section, measured when leaving station 36c, shows similar results than the CTD profiles for low salinity. The MLD varies from 10 to 20 m, with an averaged MLD of 15 m for salinities below 33.5. The first section is the further away from the plume, and for low salinities the MLD is about 30 m data, showing the deepening of the MLD with time and latitude. Thus, strong haline stratification is always observed for surface water with SSS less than 33.5 pss. The MLD thickens as the plume evolves after separating from the shelf, probably due to lateral and vertical mixing conditions induced by the wind and submesoscale instabilities.

We commented that there were a few outliers from the distribution of velocity difference between close-by SVP and Spot drifters. The CTD statistics in this region in the plume suggest that it is very likely that the stratification between the surface and 15m depth was important at the time of these large drifter velocity differences. The intense shallow stratification due to the advection of freshwater likely traps the momentum of the plume layer above the drogue depth of the SVP drifters at this time. We also expect that steric effects associated with the freshwater layer induce an acceleration pressure head near the leading northward edge of the plume, on the shelf, at low latitudes where the Coriolis component is still weak. Both effects might contribute to the large velocity differences observed between drifters advected in the plume surface layer and those advected at 15m depth. Further offshore, as the mixing layer deepens SVP and Spot drifters should both be drifting at comparable velocities, within a deepened mixing layer, but with the large identified downwind shear between the two drift levels (surface and 15m). Thus, with the exception of the Amazon plume upstream region, we expect that drifters of the two types can be used to map the currents in the mixed layer, provided that a downwind shear between the two drift levels is taken into account. Their velocity is plotted together on Figure 4 with Spot drifter velocities adjusted by a downwind shear adjustment to be directly comparable with the SVP drifter velocities.

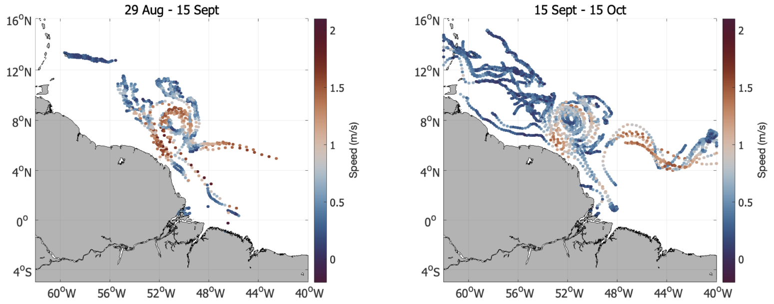

Figure 8.4: SVP and Spot drifters' velocity from August 29th to September 15th (a) and from September 15th to October 15th (b).

The largest velocities from the SVP drifters are observed in the NBC, offshore of the shelf break, with more than 1.8 m/s until 5°N, and again near 7°N southwest of the NBC retroflection. The Spot drifters' high velocities for the same period are also seen southwest of the retroflection, but also on the shelf with very large velocities observed between 5°N and 6.5°N where the drifters crossed the shelf break into the deep ocean (and for one further northwest until close to 8°N). Maximum 3-hour velocities exceed 2.1 m/s for the Spot drifters. All these high velocity trajectories correspond to areas of rather fresh surface water, based on satellite imagery (next section). There are other instances of very strong 3-hour currents closer to the equator on the shelf that are associated with internal tides (Figure 4b).

NBC ring and retroflection impact on the ARP and drifters' trajectories

One of the most striking features of the summer 2021 is the Amazon freshwater plume expansion starting from September 1st. The NBC retroflection is at its northernmost position, around 9°N, as it just formed a well-defined NBC ring. The ring nevertheless initially was quasi-stationary near the retroflection (Figure 5). The plume of freshwater rapidly expanded northward, stirred anticlockwise by the NBC ring on September 4th-8th, as evidenced by the drifters deployed in the plume. As seen on the snapshots of SSS and Chla (Figure 6), the propagation and evolution of this structure was very fast, with velocities diminishing after September 8th as the patch of freshwater spread, leading to its separation from the NBC ring on September 10th. We will refer to this structure as the freshwater pool B.

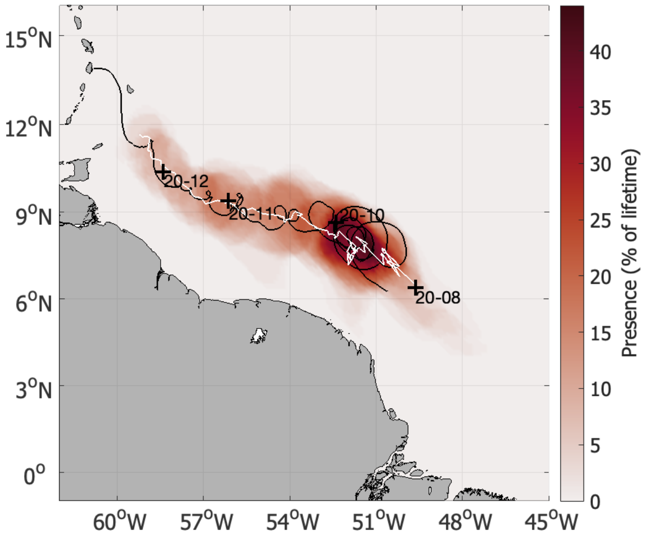

Figure 8.5: NBC ring presence (% of its lifetime), its trajectory as detected from altimetry from TOEddies algorithm (white line, Laxenaire et al., 2018) and trajectory Spot drifter 34 trapped in the ring (black line).

Interestingly, the anticyclonic NBC ring tracked by altimetry and the drifters remained for more than a month close to the NBC retroflection, despite forming a close recirculation (as detected by altimetry) since August 20th (Figure 5). The surface core of the ring moved slowly and remained salty. The ring spent 50% of its lifetime (4.5 months long) in the retroflection region (even after its detachment around September 15th), around 52°W-8°N until late October. 18 Spot and two SVP drifters circled around the ring, with 4 drifters staying its core until its demise 100 days later. At times, the ring stands out in salinity data, as it entrained freshwater almost all around the structure. Part of the freshwater pool B is advected to its northwest on September 10th, and circulate around it until September 20th (Figure 6). By September 22nd, a new tongue of Amazon freshwater extended northward near 50°W to the east of this ring, around a newly reinforced NBC retroflection. One SVP drifter entrained in it from the NBC near the slope shows how it connected to the NECC further east. However, the northward, then eastward transport of freshwater into the NECC did not last very long, and by September 29th and until at least October 3rd the freshwater from the shelf was mostly recirculating further west around the NBC ring, as also illustrated by other drifters either deployed initially closer to the equator or advected around the NBC ring core from its northern side. What was left of the freshwater to the northeast of the NBC ring formed another isolated freshwater pool which moved northward through October (analysed in Section 3.5).

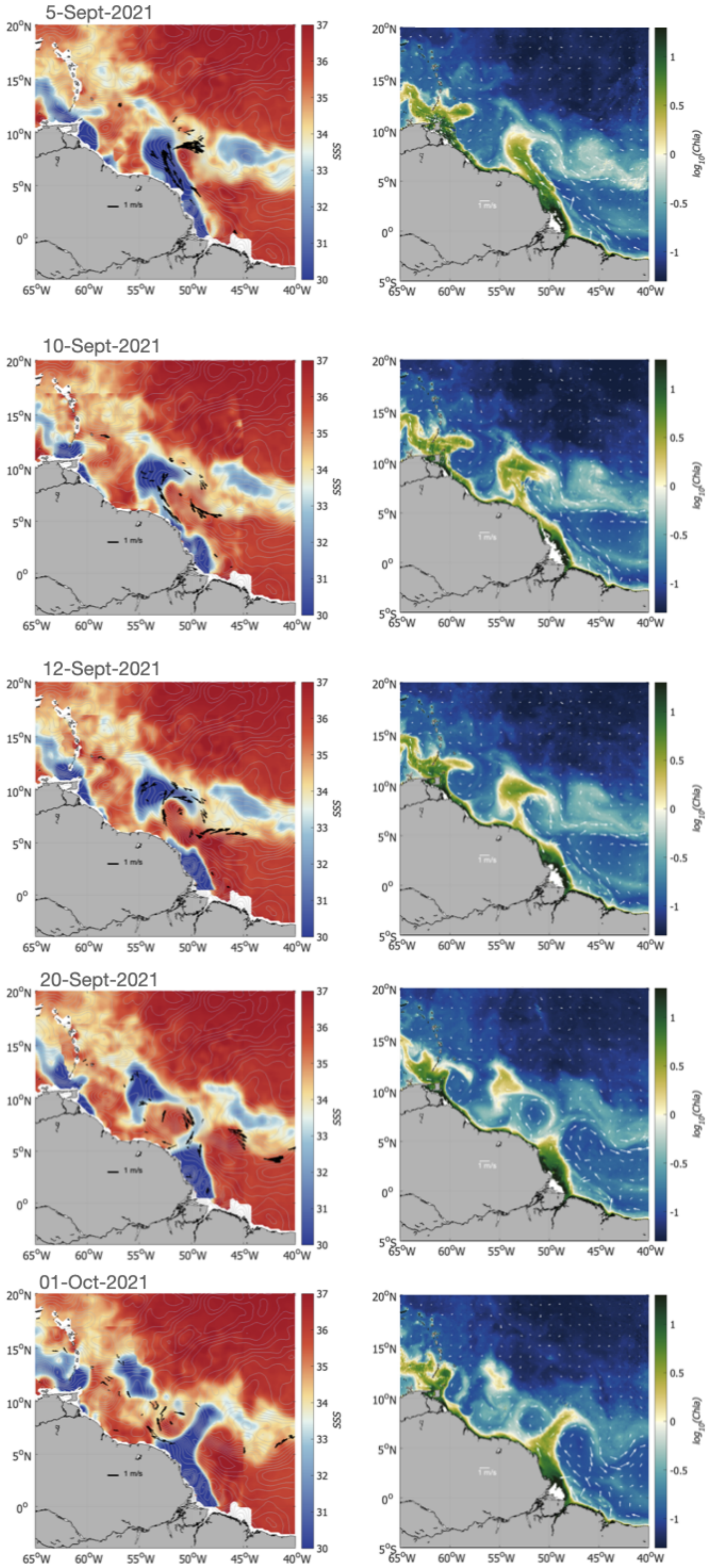

Figure 8.6: Snapshots of SSS (right) and Chla (left) following the evolution of the fresh patch. The black arrows on top of the SSS represent the drifters' velocities while the white arrows on top of the Chla delineate the altimetric geostrophic currents.

Drift characteristics and evolution of the freshwater patch

The newly formed freshwater pool B started rather mushroom-like on September 8th. It then evolved first in interaction with the NBC ring until September 10th-12th, when the ring collided against the plateau cutting off the fresh water supply from the Amazon (Figure 6). Part of the eastward side of the patch was nevertheless still being stretched by the ring circulation until September 15th. This fresh filament shedding resulted in freshwater loss from the patch (Figure 7). There were then other suspected events of filament formation evicting freshwater from the patch such as after September 15th to its southwest, at a time when the fresh patch was nearly triangular shaped. We can clearly observe a north to northwestward drift of the patch over the months of September and October in the daily satellite snap shots (zonal/meridional displacement velocity on the order of -0.15/0.25 cm.s-1), as well as during October. The structure in early October became more elongated, with a minimum salinity higher than 30 pss in a core still detectable on salinity imagery until late October near 16°N/57°W.

This displacement presents fluctuations that are coherent with changes in the wind stress and expected Ekman response a day or two later (Figure 8). The Ekman current explains a large part of the variability, coherent with MLD which are initially on the order of 10 m, but might extend to more than 20 m in October. In addition, there is certainly some influence of the interaction with the underlying current structures, even after the initial period of interaction with the NBC ring.

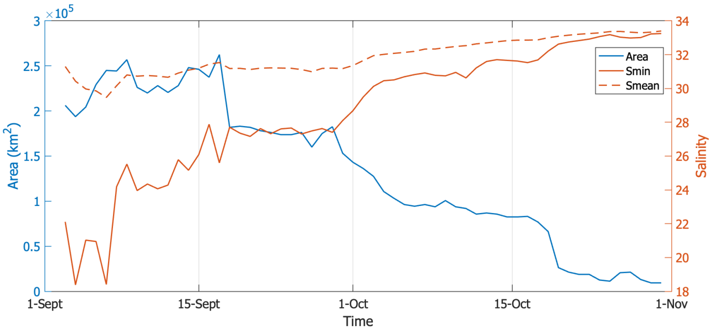

Figure 8.7: Area, minimum and mean salinity of the freshwater pool B defined from SSS maps by the 33.5 pss salinity contour, from September 1^{st} to November 1^{st}.

An indicator of the freshwater pool core area is reported here by the area contained within the 33.5 pss salinity contour. Following a strong initial area increase to close to 200 000 km2 during the formation phase of the patch, there is a decrease associated with the expulsion of the filament around the NBC ring. A slower decrease, in particular in early October, was observed during high winds when saltier water was entrained from below. This was also the case at the end of October, when the salinity in the core became close to the threshold salinity. The average salinity (Smean) as well as the lowest salinity (Smin) indicated a marked evolution in time towards higher salinity (Figure 7). The periods of strong change corresponded to days of larger wind stress (Figure 8), further indicative of entrainment of salty water from below. The change in Smin from September 10th to October 3rd (close to 7 pss, compared to an initial contrast of about 14 pss with underlying water) suggests a doubling of MLD or fresh-layer thickness. If the initial freshwater thickness on September 10th was on the order of 10 m, this is coherent with an evolution to 20 m by October 3rd. These values are similar to the estimates of Ekman velocities (Figure 8). On the other hand, other processes such as lateral mixing or air-sea fluxes would also contribute to the changes in Smin, and this freshwater thickness increase should be thought as an upper estimate. Because the structure became more elongated afterwards, it is possible that the spatial resolution then smears out the minimum salinity evolution, which we will not comment upon.

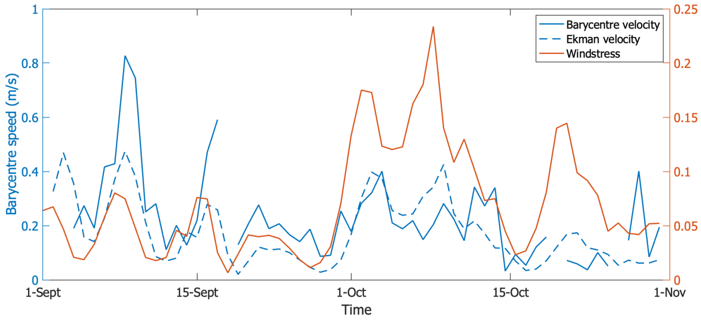

Figure 8.8: Velocity of the barycentre of freshwater pool B compared to the Ekman velocity and windstress at the nearest point from the barycentre from September 1^{st} to November 1^{st} 2021.

Anticyclonic geostrophic circulation around the patch

There are often hints in the drifter trajectories of an anticyclonic circulation around the structure, after it separates from the NBC ring influence (Figure 6). This is also clearly highlighted in the geostrophic currents derived from altimetry (Figure 9). Altimetry does not have the same temporal resolution as the daily products from SSS or Chla, and should probably be thought as 5 to 7-day averages, but resolves the large scales of the fresh patch. Integrating the orthogonal currents across lines from the boundary (33.5 pss salinity contour) towards the structure centre yields an estimate of the sea level increase at its centre compared with the outer area. This estimate is rather uncertain, but its estimated magnitude (integrating from its north or its west) suggests a higher sea level at the centre by 14 cm on September 12th (as seen on the sea level maps). If this was uniquely associated with the steric effect of the fresh layer, the steric effect at the centre would be roughly equivalent to a vertically integrated negative salinity anomaly of 140 pss*m at the centre. Based on Smin at this date and assuming that the anomaly is relative to 36 pss, the S anomaly is 12 pss, so that this steric effect would correspond to a fresh layer thickness of 12 m, which is close to the assumed fresh layer thickness of 10 m. This anti-cyclonic surface circulation in the geostrophic current altimetric maps is thus likely created by the fresh patch formation on September 10th to 15th, and has probably no counterpart below it.

Situation in summer 2021

This well documented sequence illustrates the alternance of the freshwater path either to the NECC or to the northwestern Atlantic, during a season where we mostly expected freshwater transport towards the NECC. We will now extend this period documented by the drifters to the whole summer season of 2021.

2021 presents a very interesting situation, with many interactions between the Amazon Plume and the NBC rings from June to November (Figure 10).

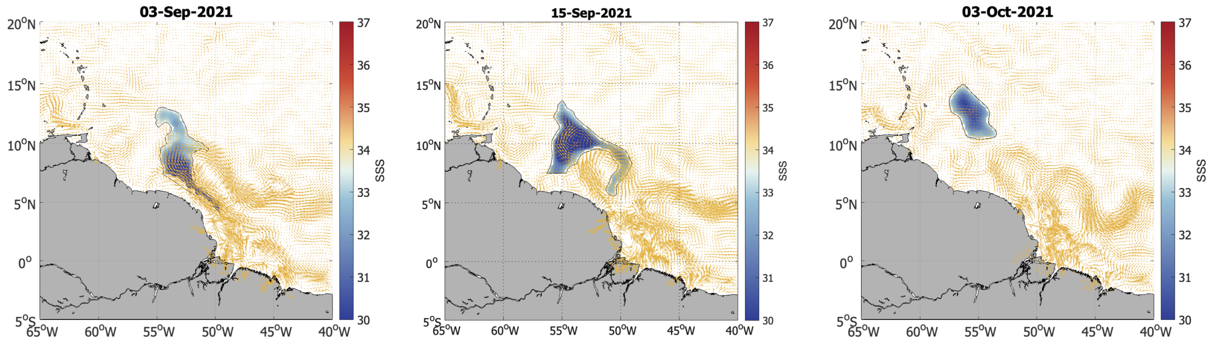

Figure 8.9: Freshwater pool B identified by the 33.5 salinity contour for the 3^{rd}, 15^{th} of September and 3^{rd} of October 2021. Background colours inside the contours indicate the surface salinity of the pool and the yellow arrows represent the geostrophic currents.

Fresh water pool B is one of the most striking examples, but the pathway of the Amazon plume was regularly interrupted and modulated by the rings. Tara crossed one of these freshwater patches on the 22nd-23rd of August with surface salinities down to 32.5. Although there were rain showers during this crossing, this patch seems mostly advective and not locally created, and can be tracked back to the NBC retroflection at the beginning of July, so more than 1.5 month earlier. It was separated from the plume in late July following an interaction between the forming NBC ring we just described and the one detached earlier from the retroflection. Even when the NBC retroflection is not in place, the presence of rings creates freshwater recirculation around the rings. They bring the freshwater northward quickly, and therefore modifies the ARP path. Starting on July 11th, the main pathway of freshwater did not follow the bathymetry and the shelf break near the Demerara Rise. It was directly expulsed in the open ocean by the NBC rings, therefore the coastal area west of the retroflection between 5 to 10°N was rather salty, while the plume expanded north of 11°N.

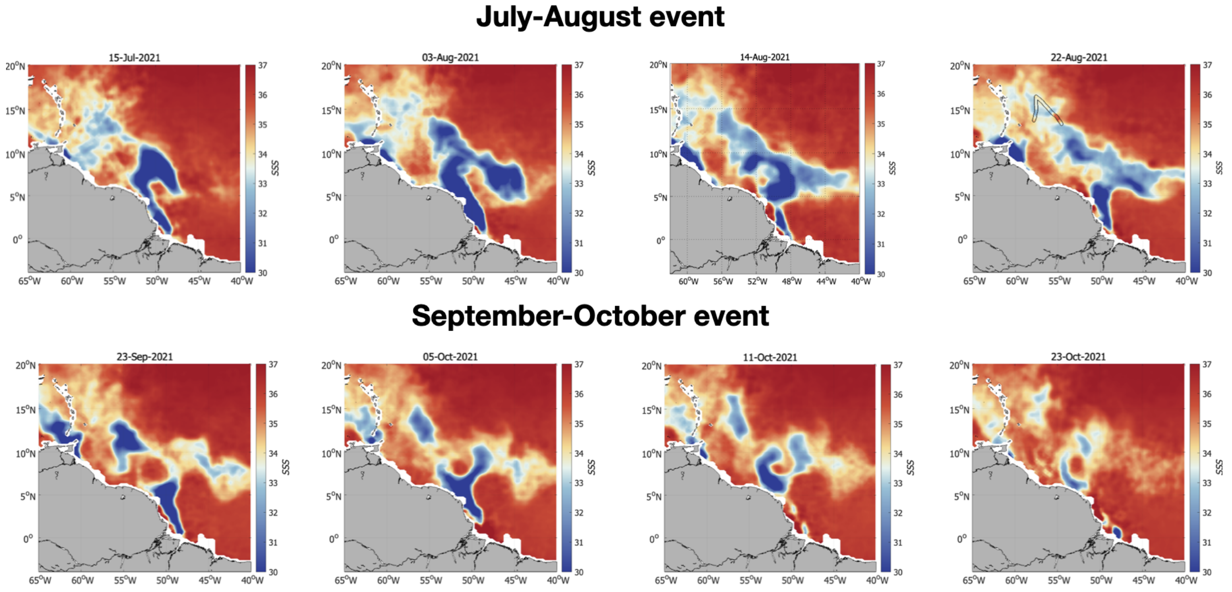

Figure 8.10: SSS snapshots showing the evolution of the Amazon River plume in late July-August (top) and in late September-October(bottom). On the August 22^{nd} map, Tara's track is colour-coded with the salinity from the ship's TSG.

At the end of September, after the fresh patch event, the retroflection was again energetic and started to direct the new ARP towards the NECC. However, the interaction with the ring was still very complex as part of the ARP started to recirculate around the ring around October 1st (Figure 10). Both the ring recirculation and the first NECC pools merged around October 23rd, traveling northwestward and surprisingly not re-joining the NECC.

Interannual variability

Summertime ARP – NBC rings interaction are common in the northwestern tropical Atlantic from 2010 to 2021, inducing an alternating freshwater transport between a northwestward and an eastward direction. However, in this record, each transport event is unique, and none was as striking and well defined as the fresh patch studied in this paper. To investigate the interannual variability of these phenomena, we computed the transports toward the east (NECC) as well as towards the northwest (Caribbean islands), based on satellite SSS, geostrophic and Ekman velocities. The eastward transport is computed across a 45°W section between 4°N and 10°N. The northwestward transport is evaluated through a diagonal section presented on Figure 11b, which is to the northwest of where eddies usually form and separate from the NBC retroflection. The velocity is decomposed as the sum of the Ekman and geostrophic velocities. We assumed a 14 m freshwater thickness (based on Tara' stations 35 and 36a out of the plume, the TIA sections and from Argo profiles located in this region in summer – not shown). The freshwater transport is defined as:

$$\frac{1}{\rho_{ref} \cdot S_{ref}} \int \int \rho \cdot (S_{ref} - SSS) \cdot V \cdot dxdz \tag{8.1}$$

where ρ_{ref} is the reference density for sea water (1025 kg.m-3), ρ is taken as 1020 kg.m-3 to represent the density of the freshwater (average density of water of salinities between 28 and 33.5 from the TSG), and S is the salinity without the freshwater influence taken as 36.

Figure 11 highlights 2021 as a unique year for northwestward freshwater transport in late summer, due to the two strong events analysed above. Some smaller similar events can be observed in 2014, 2018 and 2019. The September patch contributes to 25% of the northwesward transport over the July-November period. Most years the northward transport in late summer happens during short-lived and intense events as in 2011, 2014, 2016, 2018 and even 2019. For those years, eastward transport in the NECC is also more intermittent. There is an episodic switching between northward and eastward transport as supported by the strong anti-correlation (-0.85) between the mean low-frequency (30-days moving average) eastward and northwestward transport for the months of August-September-October (Figure 11c).

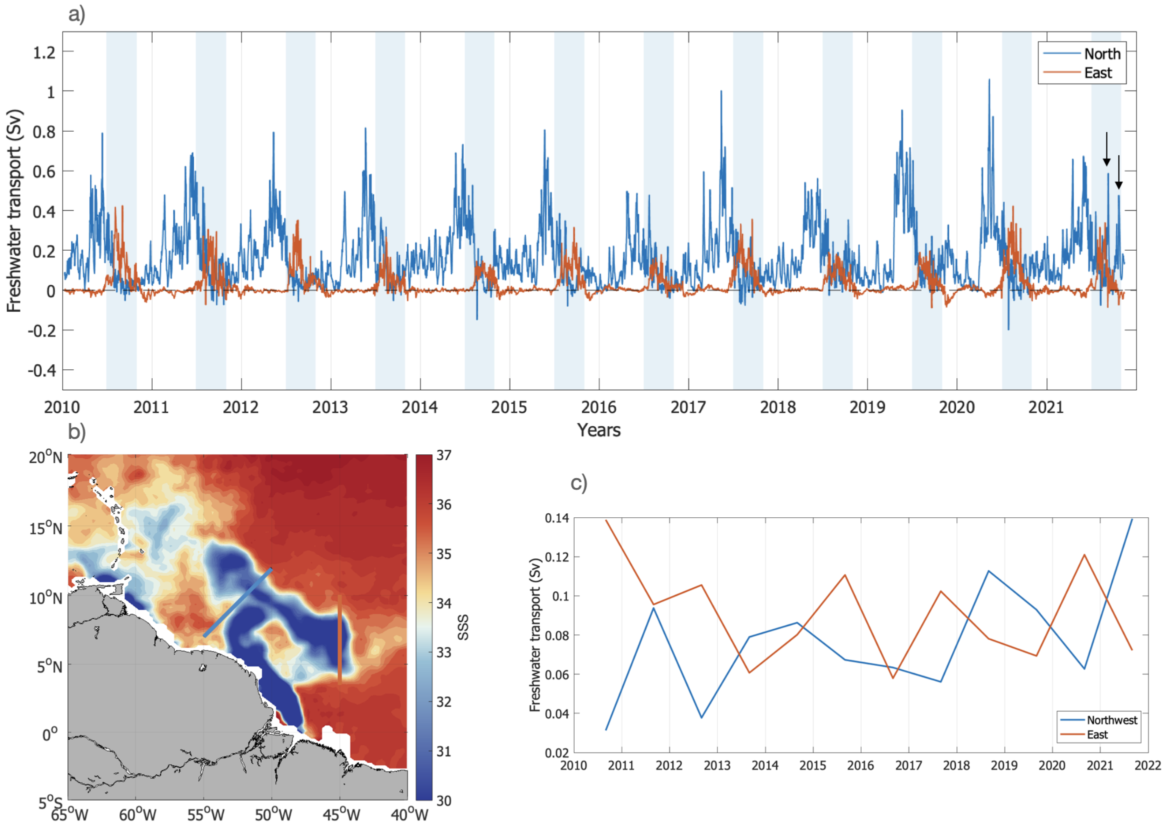

Figure 8.11: a) freshwater transport along the two sections defined on map. The faded bands highlight the July 1st- November 1st period and the two black arrows mark the freshwater events of September and October. (b). Eastward transport is computed over the 45°W section, while the nortwesthward transport is computed over the south-west/north-east section. c) Mean low frequency eastward and northwestward transport for the months of August-September-October.

8.2.6 Discussion

A new summer ARP pathway

This study shows that the plume cannot be treated as a coherent structure, in agreement with Coles et al., (2013) conclusions. The ARP strongly interacts with its environment, and in particular with the NBC retroflection, the NBC rings and the local winds. From satellite ocean colour observation, Molleri et al., (2010) identified three plume pathways, the dominating pathway from August to November being east toward the NECC. From a model, Coles et al., (2013) identified four. Among those four pathways, only the "interior gyre pathway" mentions a prevailing Ekman transport. The "direct northwestward pathway" is described as trajectories advected rapidly northwestward, either through the Guyana coastal Current or further away from the coast. It is marked by less looping behaviour, the transport by the NBC rings being associated to the "indirect northwestward pathway" (Coles et al., 2013).

From observations we show that this 'indirect northwestward' pathway is not only present in winter, but all year-around. In summer, it is even one of the dominant pathway. It is also strongly driven by Ekman transport when the geostrophic currents do not favour this pathway (once the retroflection is settled), explaining the rapid transport of waters. It is mainly discontinuous and is one of the main pathways bringing freshwater to the Northwestern tropical Atlantic in summer and autumn. Water is not directly transported by the rings, but the NBC retroflection and rings play an important part in cutting off these fresh water patches and entraining them out of the main geostrophic currents. Without the presence of the rings, the plume likely would either follow the coast through NBC then the Guyana coastal current, or follow NBC retroflection and join the NECC. The NBC rings strong geostrophic circulation entrains the plume out of the main currents of the region. In doing so, they create the alternative pathway from the Demerara rise toward the northwest, that can either be semi-continuous or completely patchy. The presence of one or two rings near 55°W is key in setting the initial plume shape and direction.

This study highlights the strong role of Ekman velocities in the total northwestward transport of freshwater. The transport estimates present large uncertainties, due to the hypothesis that the salinity is homogeneous over the Ekman layer and that the Ekman and geostrophic currents transport the surface salinity anomaly. The Ekman transport at 90° of the wind direction is an integration of the currents of the Ekman spiral over the Ekman layer. However, the Ekman layer could extend deeper than the low salinity layer, through the vertical salinity gradient. This could change the direction of the transport, with lower surface salinities advected in a direction closer to the wind direction. This transport could also reach deeper layers, which are saltier, and might thus less contribute to the freshwater transport. Geostrophic currents are also subject to large uncertainties, due to the smoothing of the altimetric product both in time and space. The non-linear contributions and thus deviation from geostrophy are also large with the intense currents often present in this region, especially close to the shelf break and where the plume separates from the shelf. The salinity products have also a smoothing in time or space involved and do not resolve structures smaller than 50 or even 70 km, such as some of the filaments observed in the chlorophyll maps.

Interannual variability

Over the last 11 years, a strong interannual variability of the eastward and northwestward freshwater transport is observed (Figure 11). At least four processes generate variability on the transport. First, the upper geostrophic circulation, that has been shown to be one of the main sources of interannual variability in the western tropical Atlantic (Da & Foltz, 2022; Jouanno et al., 2017; Masson & Delecluse, 2001). Here we show the prominent role of the NBC retroflection and of the NBC rings in shaping the ARP.

Once the intertropical convergence zone reaches latitudes higher than 9°N in July, it drives the retroflection of the NBC to feed the invigorated NECC. There is however interannual variation in the intensity of the NECC, and in the establishment of the retroflection, that strongly influences the ARP extension (Da & Foltz, 2022). In 2011, 2014 and 2016, the NBC starts retroflecting later than usual. It leads to longer period of northwestward transport, and weaker total export toward the NECC. On the other hand, an early onset of the NBC retroflection such as in 2017, 2020 and 2021 favours the development of eastward-extending freshwater patches.

However, the detachment of patches from the main ARP is often driven by NBC rings. July 2021 illustrates the example of an interaction between the ARP and two NBC rings, while the September fresh pool B is due to one ring only. The rings are slower in summer (Aroucha et al., 2020) and stay longer in the Demerara rise region as observed in 2021, but with some variability from year to year. The number of rings is also changing (Aroucha et al., 2020), modifying the ARP-ring interactions and therefore the shape of the plume.

The presence of a ring modifies the shape of the retroflection. As a ring forms, the retroflection extends northward (up to 10°N), a position that might favour northwestward transport, especially if the ring circulation is intense. On the opposite, once the ring is shed, the retraction of the retroflection to its southeasternmost position (5°N) favours direct eastward transport.

Then, as the fresh layer is particularly shallow, winds play a strong role in driving its spatial distribution. We show here the prominent role of Ekman currents over the northwestward spreading of ARP and associated freshwater transport in summer. This supports the observation of Fournier et al., (2017) that highlighted how the overall shape of the plume strongly varies under the influence of winds between 2012 and 2014. It is also in agreement with Da & Foltz (2022) showing that the interannual variability of the Amazon and Orinoco River plume is mainly driven by changes in horizontal advection linked to the North Atlantic Oscillation influence on ocean circulation. When investigating the variability of the freshwater transport in the NECC, Grodsky et al., (2022) also points out the strong correlation between SSS anomalies propagating in the NECC and winds.

The Amazon outflow variability modulates the low-frequency (1-year moving average) total fresh water transport (correlation of 0.75, Supplementary Figure S3). The most visible impact is seen in 2016, where the very low flow of the Amazon following the powerful El Niño of 2015 is clearly resulting in both weak northwestward and eastward transports. Gévaudan et al. (2022) indeed highlights the stronger impacts of extreme floods and drought of the Amazon river on SSS variability.

Several mechanisms determine the direction of freshwater transport in late summer. Isolating the effect of a single process is complicated, as they are all intrinsically linked. However, the interaction with an eddy (totally separated or not) from the retroflection is a strong condition to allow a northward transport in this late summer period. The winds then affect directly the freshwater extension through Ekman transport, and also indirectly by shaping the intensity and set off of the NBC retroflection.

On the path of tropical cyclones

From 1960 to 2000, 65% of the category five hurricanes passed over the historical Amazon-Orinoco plume area (Ffield, 2007). It raises the question: are the most destructive hurricanes impacted by the air-sea interactions in this region? The air-sea interactions are strongly influenced by the vertical stratification, and in particular the haline stratification, leading to the formation of barrier layers. From 2010 to 2021, by colocalising the tropical cyclones (TC) tracks (Atlantic Tropical Storm and Hurricane

Tracks, from the National Hurricane Center) and satellite salinity, we observe that 22% of all trajectories passed over waters with salinities below 35 pss. 82% of these occurrences happen in August, September and October, peak of the Atlantic TC season. Understanding the mechanisms driving the SSS variability in this region is therefore important. Reul et al. (2021) insist on the fact that pre-storm vertical salinity gradient in the MLD is a key driver of the strong variability of SSS and SST response to TC. Balaguru et al. (2012, 2020), Grodsky et al., (2012) and Reul et al., (2014), highlighted the role of BL on tropical cyclone intensification. However, TC activity in 2021 was relatively weak, with only 4 TC crossing low salinity areas. Two tropical depressions, Grace and Peter (Figure 12), crossed parts of the freshwater event of July sampled by Tara, and went from the tropical depression to tropical storm category over these fresh waters (in mid-August for Grace and late September for Peter). Tara northernmost CTD station 35 shows the presence a BL on the order of 5 m. On the other hand, 2017 was a year with a strong TC activity, with 6 TCs, most of them evolving to category 5 hurricanes, crossing water with salinity below 35. Cyclone Irma was the strongest of the year 2017, and has been intensively studied by Balaguru et al., (2020) and Reul et al., (2021). The cyclone went through a phase of rapid intensification when crossing a patch of fresh salinity (S<34.5). This fresh salinity patch is the most intense event of freshwater transport in 2017 (Figure 11) and was formed with a similar mechanism as the one of July 2021, with an NBC ring cutting off the ARP and stirring the freshwater away from the coast. 2017 is a year with a strong northward transport of freshwater, despite an early set off of the NBC retroflection. Most of the 2017 freshwater transport happens during the early summer (May-June-early July), but the more recent summer event probably brings more stratified water. The disparate nature of the ARP proposed in this paper offers a means of explaining perhaps smaller but more intense areas of low salinity. It also shows an alternative path for freshwater to the northwest Atlantic in

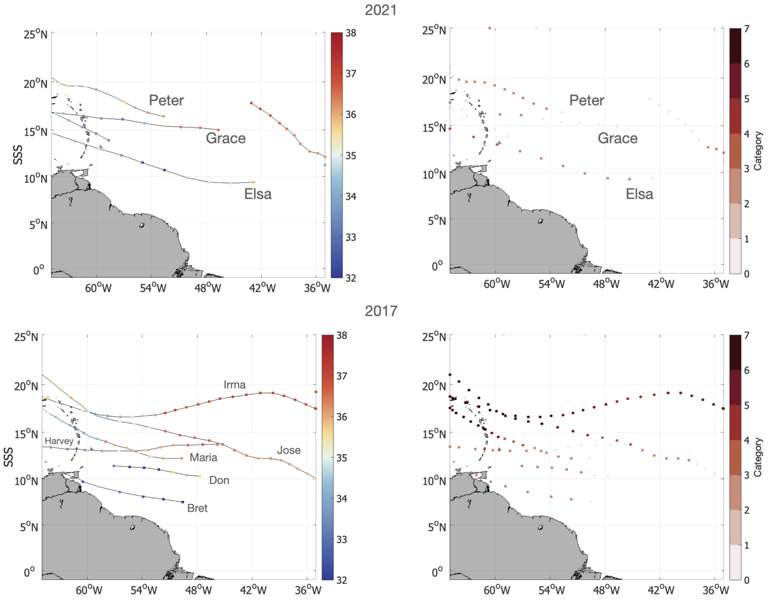

Figure 8.12: Trajectories of tropical cyclones that crossed salinities below 35 for 2021 (top) and 2017 (bottom). The TC tracks are colour-coded with SSS (left) and TC intensity (right, from tropical depression (1) to category five hurricane (7)).

8.2.7 Conclusion

The Tara microbiome mission in the late summer of 2021 highlights a very discontinuous Amazon plume. The layer with a strong surface freshening from the Amazon outflow is very stratified even at a 1000 km from the mouth (pycnocline at 15 m) and is often associated with intense surface currents. The maximum currents are observed in the NBC, the retroflection, the rings but also on the shelf break. Here, we attempted combining in-situ and satellite data to interpret the ARP dynamics.

The drifters highlight the important role of the NBC retroflection and of a newly formed NBC ring in driving the ARP. This ring was stationary and remained in the retroflection region until the end of October. At the beginning of September, the plume expanded rapidly and was entrained on the western periphery of the ring. The ring collided with the shelf and cut off the freshwater source, creating a 200 000 km2 freshwater patch northwest of the ring. Under the action of the winds and therefore of the Ekman currents, this patch did not completely recirculate around the ring but moved to the northwest toward the lesser Antilles. It was identifiable by salinities lower than 33.5 pss until early November. This structure is very stratified, and once detached from the influence of the ring, mainly driven by sheared Ekman currents. The strong steric anomaly associated with the freshwater patch generates an anticyclonic circulation around the patch, well identified by altimetry.

This type of phenomenon demonstrates an alternative to the transport of freshwater towards the NECC, which is favoured when the retroflection of the NBC is in place. By observing the whole summer of 2021, the event described above is a particularly strong case, but is not isolated. As early as in July, we observe a fragmentation of the plume due to interactions with the rings. This is also the case at the end of the Amazon flood period in October-November. The calculation of freshwater transport towards the northwest (Caribbean) and towards the east (NECC) showed a succession of distinct events of varying intensity, and an alternation between the two directions of transport. 2021 presented a larger than average northwestward transport in late summer, linked to these events dominated by Ekman transport. Over the period 2010-2021, it can be seen that for each summer most of the transport is in the form of distinct events, but few are as well defined as the one sampled by Tara in September 2021.

In conclusion, the Amazon plume is not only driven by the large-scale currents prevailing in the region. The Guiana Current and the retroflection-NECC system certainly carry a lot of fresh water, but the almost unavoidable interaction with the NBC rings around 55°W generates alternative paths. These events are intermittent, but intense, and help to explain the spatial distribution of salinity and barrier layers in the tropical Atlantic.

The waters of the Amazon are rich in nutrients, generate high primary production and are associated with a rich biodiversity (Neumann-Leitão et al., 2018; Smith & Demaster, 1996). Better defining the dispersal pathways of these waters therefore has strong consequences for the supply of nutrients to the tropical Atlantic, with either a preference for the central or northwestern Atlantic. Knowing their spreading history is also important for the study of tropical cyclones that often cross low salinity areas near the Caribbean. A larger freshwater input in this area intensifies the barrier layer phenomenon and thus modifies the air-sea exchanges in the region, associated in particular with the intensification of tropical cyclones.

The oceanic mesoscale plays therefore a key role in the export of freshwater from river plumes. The smaller scales revealed by the high-resolution chlorophyll-a also suggest many finer scale phenomena that would be interesting to study, highlighting the need for high resolution satellite salinity products.

8.2.8 Data availability statement

We benefited from numerous data sets made freely available and listed here: the currents produced by Ssalto/Duacs distributed by the CMEMS (https://resources.marine.copernicus.eu), the Chla maps produced by CLS, the SMOS maps produced by CATDS (CATDS, 2019) (https://10.12770/12dba510-cd71-4d4f-9fc1-9cc027d128b0), and the SMAP maps produced by Remote Sensing System. The SMOS SMAP High resolution SSS maps in region of high variability are generated by the CATDS CEC and available on SEANOE (doi: 10.17882/90082, https://www.seanoe.org/data/00789/90082/).

8.2.9 Acknowledgments

This publication has received funding from the European Union's Horizon 2020 research and innovation project AtlantECO under grant agreement No 862923, with additional support from CNES (the French National Centre for Space Studies) through the TOSCA SMOS-Ocean and TOEddies proposals. We warmly thank M. Heineke, Thomas Kock and Rolf Riethmüller (Hereon) for processing the TIA data. LO was supported by a scholarship from the Ecole Normale Supérieure and Sorbonne Université. We thank the Fondation Tara Ocean and in particular R. Troublé, C. Moulin and A. Bourdais for making the Mission Microbiome happen. Thank you to all the Tara leg 5 crew members, M. Hertau, N. Bin, L. Caudan, S. Bin, F. Aurat and A. Prieur for their precious help in conducting the science onboard. Thank you to M. Labaste for analysing the Tara salinity samples, and to C. Guillerm and Météo-France for having provided the 10 SVP drifters.

8.3 Summer biogeochemistry of the western tropical Atlantic ocean

8.3.1 Introduction

In summer, the western tropical Atlantic water warms up, and the invigorated NECC advects CO_2-rich water transported by the NBC toward the east. Taking only into account the large scale properties of the region, summer ocean dynamics therefore favour a strong CO_2 outgassing in this region. This is also what is present in the summertime air-sea CO_2 flux climatologies (Landschutzer et al., 2014, figure 1.7).

However, multiple studies have shown that the carbon budget of the western tropical Atlantic is incomplete without the representation of the Amazon plume. The Amazon brings fresh and nutrient-rich waters that sustain an important phytoplankton bloom (Smith & Demaster, 1996). This water is strongly undersaturated in CO_2 (Körtzinger, 2003, Lefèvre et al., 2010). Modelling studies show that taking account of the Amazon plume reduces the strong outgassing of the western tropical Atlantic (0.5°S-24°N; 30°-70°W) by more than 50% (Louchard et al., 2020), while observations-based study shows that the tropical Atlantic sea-air CO_2 flux could be overestimated by 10% by neglecting the CO_2 sink associated to the Amazon plume (Ibanhez et al., 2015).

Recent studies have highlighted the strong seasonal and interannual variability of the CO_2 sink (Ibanhez et al., 2017; Mu et al., 2021). However, this region, despite of being of global importance, is not well sampled. Ibanhez et al., (2017) studied the seasonal and interannual variability of the CO_2 sink along a ship-line between Europe and Cayenne. While it shows how variable the region is, this dataset do not represent a synoptic view of the western tropical Atlantic. Mu et al., (2021) took advantage of three cruises that happened in May-June 2010, July-August 2012 and September-October 2011. They show the variability of the region in the period of strong Amazon outflow, and highlights that the plume size and salinity affect the magnitude of the regional sink. Despite the importance of the western tropical Atlantic for the carbon budget and the biology of the region, not many data are available. From 2010 to 2021, very few cruises sampling the western tropical Atlantic and the Amazon estuary during the summer months are available in the SOCAT database (Bakker et al., 2016). The ANACONDAS cruises used in Mu et al., (2021) bring valuable information on this region, as does the recent Tara Microbiome cruise in August-September 2021.

The Tara-Microbiome cruise sampled numerous environments, from old plume waters in the northwestern tropical Atlantic, to freshwater lenses, the core of the Amazon river plume and the Amazon river (figure 8.2). It brings new light on the exchanges between the river and the open ocean, but also on what happens to the Amazon water once it leaves the river mouth and spreads out in the tropical Atlantic.

While the Amazon plume is a sink of CO_2, the opposite happens in the Amazon river. The Amazon river outgasses nearly as much CO_2 as the rainforest sequesters on an annual basis. The main source of CO_2 in the Amazon River is the breakdown of young terrestrially-derived organic carbon by microbes (Mayorga et al., 2005; Ward et al., 2013, 2016). Plant respiration and organic carbon decomposition also contribute to the CO_2 supersaturation (Abril et al., 2014). The lower Amazon river (from Obidos to the river mouth) releases an amount of CO_2 of the same magnitude (even higher) as the uptake by the Amazon River plume in the Atlantic Ocean (Sawakushi et al., 2017; Kortzinger, 2003). Following these results, Sawakushi et al., (2017) argue that there is a pressing need to perform measurements of fCO_2 along lower rivers and near-shore plume waters, which are currently large missing gaps in our coverage of regional and global scale carbon budgets. Indeed the region where freshwater extends offshore is not included in the studies that focus on the Amazon river plume, because there was no available data in this region. However, the Tara dataset crosses the river-ocean continuum three times, providing information inside the Amazon and Pará-Tocantin estuary as well as in the Amazon plume.

8.3.2 Results

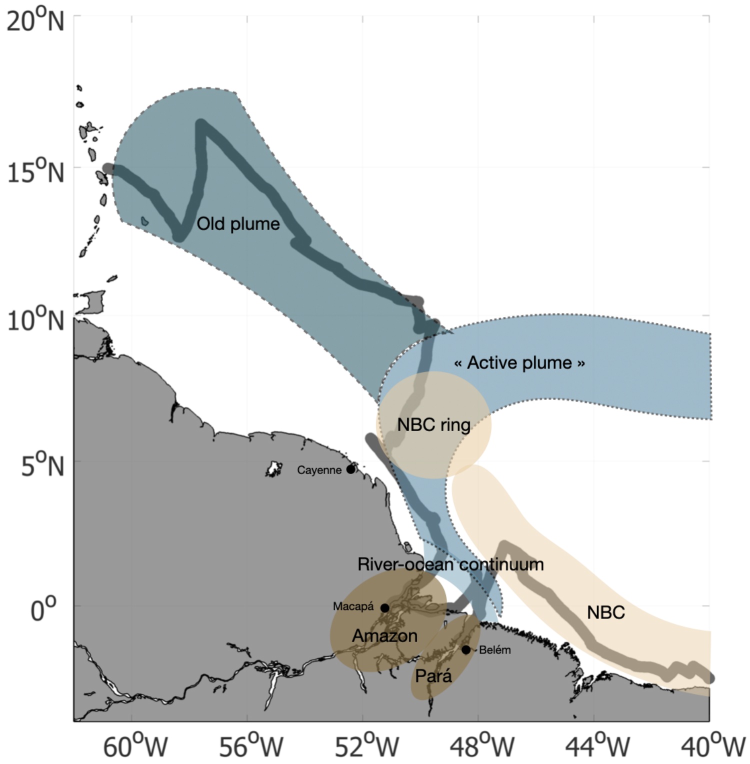

Figure 8.13: Areas of interest crossed by Tara, with a distinctive biogeochemical signature.

Figure 8.13 presents Tara's journey, and shows the many different features it crossed, on a dynamic and biogeochemical point of view. Tara left Martinique in mid-August, and travelled in the northwestern tropical Atlantic waters that are strongly influenced by the remaining of the May-June plume flowing directly into the Caribbean Sea. This area is heterogeneous, also showing more recent freshwater lenses (July). Tara then crossed the NBC retroflection, before sampling a NBC ring and joining the heart of the plume. It finally reached Macapá, in the Amazon River. After staying in the river for a few days, it returned to the Amazon plume, before entering the Pará River to reach Belém. After the stopover in Belém, it followed the NBC on its way to Salvador da Bahia.

We identified six main regions of interest on this transect, presented in Figure 8.13. The NBC is a very important dynamic structure of the region, carrying water from the South and Equatorial Atlantic, and at this time of year retroflects to join the NECC, forming the large NBC rings in doing so. NBC waters are warm, saline, and CO_2-rich. The Amazon plume has been sampled multiple times, and show a strong variability. First the retroflection of the Brazilian current was traversed, then the part of the plume located on the plateau, directly fed by the river. The dataset also provides information about the little known continuum between the ocean and the river. Four river-ocean crossings were made, two in the Amazon and two in the Pará River.

The following sections present preliminary results focusing on one of the regions or aspects identified in the dataset. In the first instance, we will focus on how the Amazon plume carries the biogeochemical properties of the river. After studying the air-sea fluxes of CO_2 and nutrients, we will try to characterise the river-ocean continuum.

Biogeochemistry of the freshwater patch

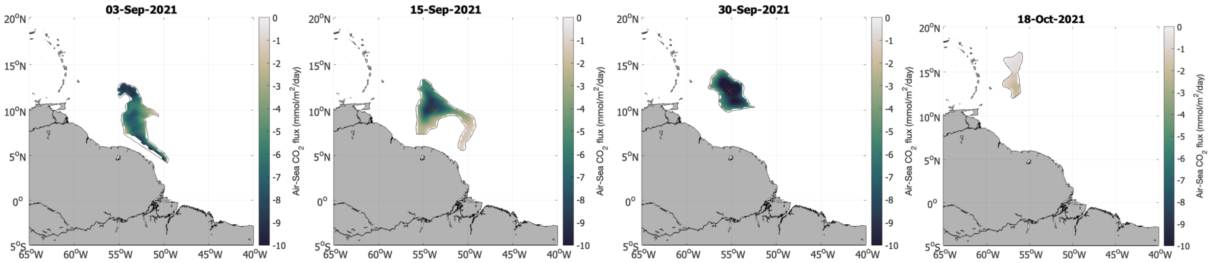

Figure 8.14: Freshwater patch B identified by the 33.5 salinity contour for the 3^{rd}, 15^{th}, 30^{th} of September and 18^{th} of October 2021. Background colours inside the contours indicate the air-sea CO_2 flux of the patch.

We have highlighted the strong interactions between the Amazon plume and the NBC retroflection NBC ring. In September 2021, this led to the formation of a mesoscale freshwater patch, which propagated northwestward. The patch is defined by the 33.5 salinity contour, and during its lifetime includes Amazon waters of salinity between 18 and 33.5. This salinity range is the one most studied in earlier campaigns, which showed a strong relationship between fCO_2 and surface salinity. The relationship of Lefèvre et al (2010) for this salinity range is close to the one that can be derived from Tara data. We therefore use this relationship to determine the oceanic fCO_2 of the freshwater patch. This empiric relationship most likely include the effect on fCO_2 of the air-sea CO_2 and the change in biology during the life of the patch. Using satellite maps of SSS, combined with winds, SST and atmospheric pressure, we reconstructed the ΔfCO_2 and air-sea CO_2 flux of the patch (Figures 8.14 and 8.15).

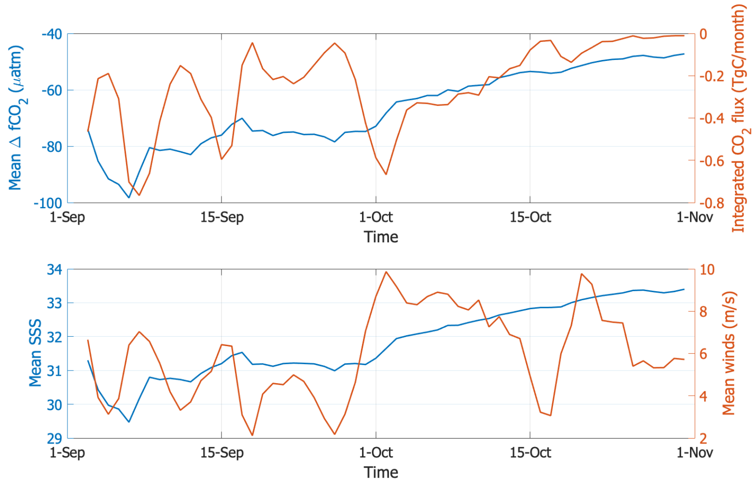

Figure 8.15: Top: Mean Δ fCO_2 of the freshwater patch and air-sea CO_2 flux spatially integrated over the patch. Bottom: Mean SSS and mean winds of the freshwater patch.

The patch is a strong sink of CO_2 with respect to the atmosphere. The variability of the flux integrated over the patch is dependent on both the winds and the water characteristics. The $\Delta f CO_2$ variability during the life of the patch follows the one of the mean salinity while the variability of the CO_2 flux is dependant also on the winds. An increase in winds generates mixing, that increases the mean salinity and reduces the mean $\Delta f CO_2$ of the patch, the effect on the air-sea CO_2 flux is compensated by the strong enhancement of the flux for strong winds (figure 8.15). It is well observed when the winds pick up at the beginning of October, so the CO_2 sink is strongly enhanced despite the fact the winds also increase the mixing of the patch with the surrounding waters. The CO_2 flux spatially integrated On average over the life of the patch (September-October 2021) the CO_2 flux spatially integrated over the patch is higher than the CO_2 flux spatially integrated over the whole Amazon plume from September to March 2010, 2011, 2013 and 2014 (Ibanhez et al., 2017). It shows that the mesoscale features of the plume are of great importance to observe the variability of the carbon sink generated by the Amazon plume.

Nutrients associated to the Amazon plume

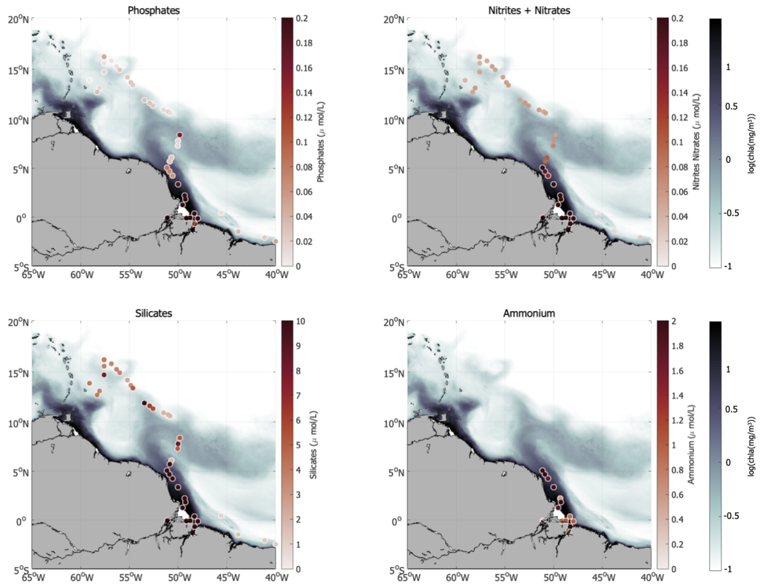

Figure 8.16: Surface concentrations of phosphates, nitrates and nitrites, silicates and ammonium. Background colours represent the mean chlorophyll-a over the sampling period (August 18th to September 7th).

Figure 8.16 shows the nutrients level along Tara's journey. The Amazon waters are very rich in all inorganic nutrients, and sustain a pronounced phytoplankton bloom. We observed on chlorophyll maps that this bloom is not limited to the region close to the Amazon estuary. High levels of chlorophyll are observed around 15°N, east of the Lesser Antilles, and also in the NECC near 7°N-45°W. Nitrogen and phosphates are strongly limiting in the Atlantic ocean, and are almost immediately consumed. While most previous studies focused on the plume waters, Figure 8.16 presents the nutrients concentration measured in an area in the northwestern tropical Atlantic where the plume is older (salinities above 34). We observe in this region that even if the level of nitrites and nitrates is low, they are not entirely consumed (0.04 -0.06 μ mol/L). The phosphate levels however are very low (0-0.02 μ mol/L). Phosphate is the limiting nutrient in this region, suggesting that the phytoplankton organisms have found ways to extract nitrogen in other ways than directly from nitrates. Subramaniam et al. (2008) showed the strong diazotrophy that takes place close to the Amazon estuary Figure 8.16 shows that diazotrophs organisms may also prevail far away from the plume in the northwestern part of the domain. From models, Louchard et al., (2020) show that the nutrient input from the Amazon river is indeed supported by an increase in nitrogen-fixation that doubles the amount of nitrogen brought by the river and available for phytoplankton growth. This also raises the following question, if the phosphates are entirely consumed, how is the bloom maintained? There could be significant re-mineralization of dissolved and particulate organic matter in this region as well as recycling of phosphorus.

The river-ocean continuum

Tara sailed all the way from Martinique to Macapá, inside the Amazon estuary, measuring continuously the underway fCO_2. It then went to Belém, in the Pará river, before joining Salvador da Bahia. It therefore crossed twice the Amazon river-ocean continuum and twice the Pará river-ocean continuum.

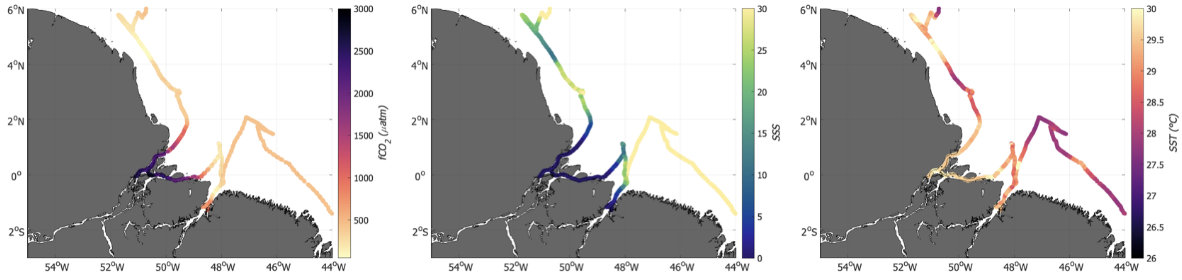

Figure 8.17: Tara's near surface fCO_2, SSS, SST in the vicinity of the Amazon river.

Figure 8.17 shows that the salinity gradient is sharp, the 0 salinity being even reached before entering the river. The CO_2 sink associated to the Amazon plume rapidly transitions in a strong source of CO_2 to the atmosphere as the waters are so turbid that the phytoplankton do not bloom. The transition region is extremely dynamic and variable, it is influenced by very strong coastal currents and strong tides. The two crossings of the Amazon river-ocean continuum are very different (figures 8.17 and **??**). First, we observe that the salinity at which the fCO_2 stops decreasing and starts increasing varies, it happens at 25.1 pss toward the Amazon, and at 11.1 pss on the way out of the river. The salinity at which the sink turns into a source is also different, it happens at 10 pss on the way in and at 4 pss on the way out of the Amazon (figure **??**). The schooner did not take the same path in and out of the river which shows how the Amazon river do not spread evenly over the open ocean. The turbid high fCO_2 waters are encountered much further away from the coast during the first crossing of the continuum that was located on the northwestern side of the river. On the eastern side of the river, the CO_2 sink plume is located closer to the coast, and the plume is probably a combination of both the Amazon and Pará river plumes. Indeed the main currents in the region are from the southeast and toward the northwest. The waters in the core of the Amazon plume in the open ocean follow well the $f\mathrm{CO_2}$/SSS relationship from Lefèvre et al., (2010) that was established from merchant ship from Europe going over to Cayenne. The relationship breaks down in the river-ocean continuum, in the Para plume and in the waters coloured in light blue in figure **??**, left. These waters are located on the plateau, before entering the river, and present peculiar temperature and salinity characteristics. Indeed, Tara arrived from the north and crossed the active Amazon plume (dark blue in figure **??**) with salinities around 15, high temperature (>30°C) and the lowest $f\mathrm{CO_2}$ of the dataset (50 μ atm, figure 8.17). As Tara sailed toward the river, the conditions changed, salinity increased, temperature decreased and $f\mathrm{CO_2}$ increased. I could be due to a local upwelling event due to increased winds (figure 8.15), or horizontal advection of saltier, colder and $\mathrm{CO_2}$-rich water from the NBC ring. At the time of the measurements (S̃ept 5) the ring started to collide with the plateau, forming the fresh water patch described previously (figure 8.6). The transition in and out the Pará river (figure 8.18) is different from the one in the Amazon river and is more homogeneous. This transition is also really sharp, the $f\mathrm{CO_2}$ starts increasing when the salinity decreases below 5 pss, and the sink turns into a source for salinity lower than 3̃-4 pss. Some variability is observed for salinities lower than two pss, possibly linked to a weak discharge of the Pará river.

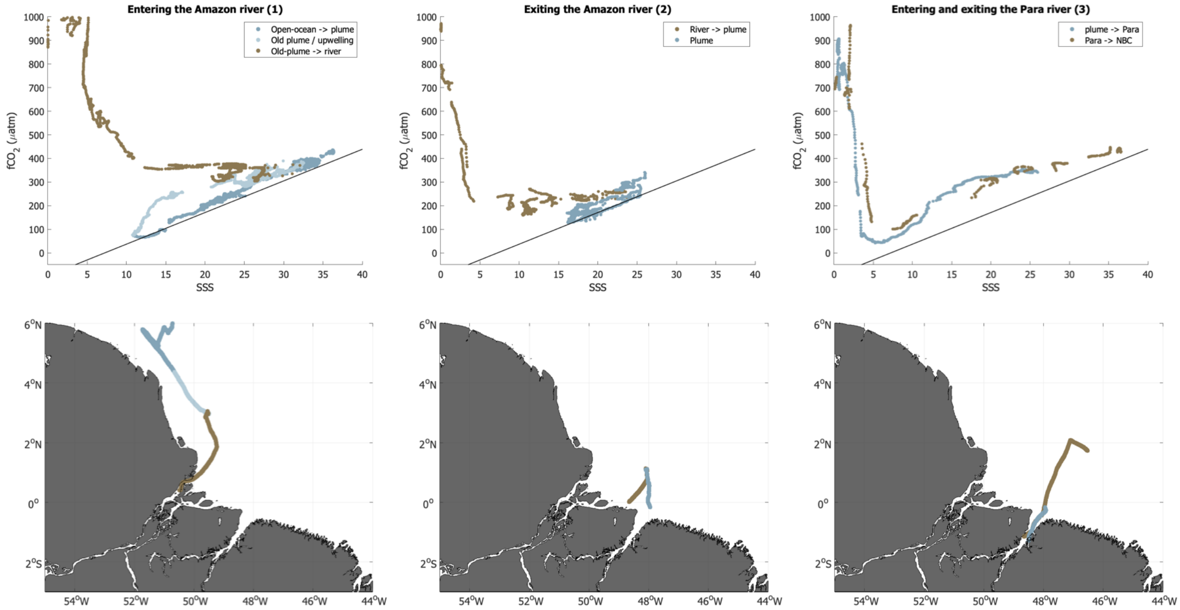

Figure 8.18: $f\mathrm{CO_2}$/SSS diagrams for the different times Tara sampled the river-ocean continuum. The black line indicates the $f\mathrm{CO_2}$/SSS relationship from Lefèvre et al., (2010).

This dataset is one of the first sampling the river-ocean continuum, and the mechanisms responsible for the variability observed are still unknown. This area is key to the understanding of the carbon budget of the Amazon river, but also of the tropical Atlantic. It is also a way to better understand the biology of the region, and the conditions allowing the phytoplankton to bloom. These results are preliminary, but are encouraging for future studies.

CONCLUSIONS AND PERSPECTIVES

Conclusions & Perspectives 9

Context

The oceanic mesoscale is at the heart of ocean circulation. It participates in the transport of water masses, of their physical and biogeochemical properties, and hence it also modifies air-sea exchanges. The mesoscale is present everywhere on the globe. In this thesis I focus on the tropical Atlantic. It is a key region for inter-hemispheric water mass transport and atmosphere-ocean coupling. It is also one of the most variable regions of the globe in terms of salinity, and in combination with ocean dynamics, salinity act as a tracer of the biogeochemistry of the region. The objective of this thesis is to characterize the role of the mesoscale on the temporal and spatial variability of surface salinity and air-sea CO_2 fluxes in the tropical Atlantic Ocean. We focused on two types of mesoscale phenomena: tropical instability waves and North Brazil Current rings. Both phenomena are strongly coupled to salinity, which is highly variable in both regions. The rings propagate downstream of the Amazon plume, we therefore studied extensively how the dynamics of the region impact the propagation of the low-salinity waters of the Amazon plume and the resulting air-sea CO_2 fluxes.

Approach taken

To answer this question, I have chosen an observation-based approach. Although the Atlantic Ocean is historically the most observed ocean, this is not the case for the tropical part, where there is a lack of observations, especially for characterising fine scales. To meet this challenge, this thesis is based on the combination of satellite and in-situ data. Satellite SST and chlorophyll data at fine scales have been developed for decades. Satellite SSS is newer, at a coarser resolution, but allow to observe the oceanic mesoscale in a new way and bring out important information in a region as influenced by salinity as the tropical Atlantic. For the first study on the equatorial Atlantic, the Argo profiles filled the gap of at-sea campaigns. We have exploited the entire SSS time series, using a salinity product that combines data from all suitable satellites. SSS was combined with SST and SSH to get a better vision of the ocean dynamics and variability.

The studies in Chapter 6 to 8 on the Amazon plume and the NBC rings were guided by two at-sea campaigns that combined physical and biogeochemical measurements: the EUREC^{4}A and Tara-microbiome campaigns. I embarked on these two missions and installed a pCO_2 system. I collected, cleaned and calibrated the data before interpreting them. At the surface of the ocean, the measurements acquired (from TSG, drifters, saildrones, pCO_2 system) have a great temporal resolution but a limited spatial one. They were therefore combine to daily maps of satellite SSS, SST and chlorophyll-a. The regular weekly SSS product did not allow to follow the hight temporal variability of SSS in the region.

We therefore used a new product designed for our study which better represent the variability at small time scales.

Results

Scientific results

- What is the role of salinity on Tropical Instability Waves ?

The equatorial upwelling develops in May, bringing up cold and saline water from the equatorial undercurrent. The upwelled waters contrast strongly with the warmer and fresher waters located further north and still influenced by the ITCZ precipitations. The tropical instability waves develop in this context and deform the temperature and salinity gradient in cusp like features. We show, by analysing the SSS and SST signature of the TIWs over 9 years, that the surface salinity gradient is more pronounced in the early TIWs period, so the TIWs signature in salinity is more present in May-June, while in temperature the signal is stronger in June-July. It has consequences on the seasonality of the density signature of the TIWs, the SSS and SST contribution to density reinforce each other, and the TIWs signal in density is strong during the whole season and the largest in June. Since salinity plays a significant role in defining the TIWs density gradient, how much does it contribute to the TIWs energetics ? We first define the potential energy associated to deformation of the density gradient by the passing of a TIW. We then show that the contribution of the top 60-m salinity to this potential energy is far from being negligible, it is on the same order of magnitude as the contribution of temperature. We observe a seasonal cycle similar to the one at the surface. In May-June salinity and temperature contribute each to 50% of the potential perturbation energy, and from July the temperature contribution is slightly higher than the salinity one. It shows that previous studies which did not include salinity in their computation of the potential energy associated to the density gradient, the potential energy was underestimated roughly by a factor two. Therefore, salinity brings information to understand the TIWs intensification in May-June, its interannual variability and its density structure, and salinity provides energy for the maintenance of the TIWs. It also provides information on the impact of the TIWs on biogeochemical and biological parameters. By shedding light on the mechanisms driving the variability of the salinity, it provides insights on the ones responsible for the variability of the parameters strongly coupled to salinity in the region such as nutrients and chlorophyll-a.

- What drives the Amazon plume pathways, and the export of freshwater to the open ocean ?

The Amazon plume pathways are driven by the ocean dynamics and by the winds. In winter, the Amazon outflow is low, but the Amazon plume is not confined to the shelf. The passage of the NBC rings all year around following the continental plateau from the Guiana plateau (close to the Amazon mouth) to the Lesser Antilles creates alternative pathways. The rotation of the rings stir the Amazon plume away from the plateau and into the open ocean. Once in the open ocean, the Amazon plume is advected by the geostrophic currents but also by the Ekman currents.

The role of the winds in advecting the plume is all the more important that the plume is very stratified and shallow.

The seasonality is so strong in the western tropical Atlantic that the conditions in February and September are almost entirely reversed. The Amazon outflow in boreal summer is decreasing but strong, and the dynamics are also very different since the NBC retroflects toward Africa. We nevertheless find similarities between the two regions through the NBC rings in particular. We find that in summer as well there are strong interactions between the plume and the rings, that are admittedly different depending on the season, but also favour an offshelf transport of freshwater toward the northwest. The interactions are more complex and involve the NBC rings, the NBC retroflection and the winds. In this season where the plume is expected to be advected by the NBC retroflection and the NECC, we show that the plume is very intermittent, and that the three phenomena indicated above favour either transport to the NECC or direct transport to the Caribbean. This alternative pathway is possible when an NBC ring stirs the plume away from the geostrophic currents of the retroflection and the NECC. If the winds are favourable, the Ekman currents then carry the feather towards the northwest. In late summer, the two pathways are used in almost equal proportions on average, but with high variability from year to year.

- What is the role of the NBC rings on the western tropical Atlantic carbon budget ?

The tropical Atlantic is a large source of CO_2 to the atmosphere that is mitigated by the presence of the Amazon inflow on the western side of the basin. We observed a strong role in both winter and summer of the small scale features of the plume generated by the NBC rings. By assessing the mechanisms driving the CO_2 flux, we show that in winter the northwestern tropical Atlantic sink is underestimated by a factor ten. The three main reasons that make the region a sink are (1) the drop in temperatures associated with winter, that mainly influence the northern part of the region, (2) the low salinity, low DIC, highly productive waters of the Amazon and (3) the limited influence of the warm, saline and high DIC equatorial waters transported by the NBC. The NBC rings are involved for the last two effects. The NBC rings trap the water from the NBC, but we observe that the surface signature is significant dampened as the eddy travels, and so the ring in itself is not as strong of a source as the NBC. They do not transport significantly the NBC surface signal further west. Moreover, the stirring effect of the NBC rings is very strong in this region, because they stir very contrasting waters over a large area. The low fCO_2 waters of the plume stirred by the ring contributes to 20% of the total sink of the region. It also contributes in the mixing of the surface waters trapped by the rings, dampening the signal of the NBC waters, for a total contribution of about 40% of the total sink. Therefore, the variability at large scale can differ from the one at smaller scale. The interactions between the Amazon plume and the physical forcing of the western tropical Atlantic play a great role in the air-sea CO_2 flux in winter and in summer, where fresh water patches create a regional strong sink.

Methodological results

In order to answer of the last question presented above, I have developed a method to reconstruct the air-sea CO_2 flux based on satellite maps of SSS, SST and chlorophyll. This method is relatively simple, and is based on the relationship between fCO_2 and these three parameters established from the in-situ data. This method is fitted for the needs of this study in winter, as it resolves all the processes and mechanisms we identified as key to assess correctly the air-sea CO_2 fluxes (such as the freshwater filament and the NBC rings). The relationships between fCO_2, SSS, SST and chlorophyll-a this method is based on are specific to the winter season. So it allows for the reconstruction of the CO_2 flux in winter for all years, with a good accuracy, but we expect that for the other seasons the dynamics of the region changes, and so does these relationships.

I also established a collaboration with the University of New Hampshire to installed a pCO_2 system on the schooner Tara for the purpose of this thesis. I took responsibility for the instrument, I installed it at the beginning of the mission Microbiome with the help of the crew. I monitored it from August 2021 to the end of February 2022, when I was onboard (August-September 2021, January-February 2022) but also when I was on land. In this thesis I focused on the tropical Atlantic part of the dataset, but pCO_2 measurements where collected all along the coast of Brazil and Argentina, and then in the Weddell Sea.

Perspectives

The western tropical Atlantic

This thesis opens many perspectives. The section 8.3 of chapter 8 begins to address one of these possibilities. I showed that the interactions between the NBC rings and the Amazon plume are strong and impact the spatial distribution of the low-salinity plume. This first study is based on the analysis of the physical parameters (salinity, currents) of the western tropical Atlantic. The spatial distribution of the plume water strongly impacts the biogeochemistry, from the nutrients distribution to the air-sea CO_2 fluxes. In section 8.3 we showed the potential of the biogeochemical dataset collected during the Tara-Microbiome cruise, to contribute to the many questions remaining to understand this complex region.

Air-sea CO_2 flux

Estimating the air-sea CO_2 flux of the western tropical Atlantic is complex due to the strong variability linked to the Amazon river plume. As we have pointed out on several occasions during this thesis there is a lack of data. Nevertheless, we currently have more data during the summer season than ever, with both ANACONDAS cruises (2010, 2011, 2012) and the Tara-Microbiome cruise which explore regions not sampled by regular lines of ships of opportunity. By combining these datasets, we could improve our understanding of the mechanisms driving the CO_2 sink associated to the river plume. Moreover, satellite salinity over 13 years and at high temporal resolution is now available, and we observed on the example of the September 2021 fresh patch that the resolution is sufficient to observe the mesoscale variability of the region. It shows that the CO_2 sink at mesoscale can be as strong as the large scale flux observed in previous studies (Ibanhez et al., 2015, Louchard et al., 2020). By analysing the main physical and biogeochemical spatial features of the region, we have a better understanding on what drives the fCO_2. In winter we showed the strong influence of the mixing of water masses, and identified the dominating factor (among SSS dilution, temperature, biology effect) in each water mass (or biogeochemical provinces). In summer the dominating factors are different, the nutrients input drives a very strong bloom and the ocean dynamics arrange the water masses differently. The results presented in chapter 8 could be continued to characterised the CO_2 flux of the western tropical Atlantic, and not only the Amazon river plumes.

Moreover, the biological samples from the Mission Microbiome will soon be analysed. In parallel, physical data from the Amazomix cruise (Bertrand et al., 2021) which took place in the same region and had a different focus will also be available. It could be very interesting to couple physical, biogeochemical and biologal parameters sampled during these cruises to study the processes controlling the ocean carbon sink. The biological samples could bring information on the ecological communities responsible for the carbon drawdown for the different phase in the life of the plume.

Nutrients

Important questions remain on the nutrients in the western tropical Atlantic. Satellites show strong levels of chlorophyll-a very far away from the plume. However, most modelling studies and even in-situ studies suggest that in these regions the levels of nutrients are very low. What sustains the phytoplankton bloom ? There are not many inorganic nutrients samples in the region, and most of them are located south of Barbados, in particular in the core of the Amazon plume. The new Tara dataset brings out a larger spatial range of nutrients value, and show that the ensemble nitrates-nitrites are not entirely consumed, even far away from the plume. Louchard et al., (2020) showed from model the importance of the nutrients brought by the Amazon to sustain the net primary productivity. Combining all nutrients data available from previous and the most recent cruises could be interesting to complement this model study and better understand the mechanisms driving the nutrients availability even far away from the "main" plume. More nutrients samples not only at the surface but also at depth have been acquired during the Tara cruise and are now analysed. The detailed study about the micro-organisms developing in these conditions could help understand the role of diazotrophy in the northwestern Atlantic, but also how phosphate is utilised. It is the limiting nutrient in regions where diazotrophy prevails, so how did communities adapt to the low phosphate levels ?

NBC rings

Despite their very large size, the NBC rings are not very well known or studied. In chapter 1 we discussed on the many ways eddies could influence their environment. Regarding the air-sea CO_2 fluxes, we showed that the stirring effect of the rings is very strong, and is dominating over the trapping of waters. Data acquired during the Tara mission microbiome could also be used to assess the mixing induced by the ring, thanks to many vertical microstructure profiles inside and at the periphery of the sampled ring. From CTD profiles, we observed that the ring was relatively shallow (250 m) and had very homogeneous physical and biogeochemical (alkalinity, DIC) properties. The trapping effect might not be dominant for the air-sea CO_2 fluxes, but what influences the biology in such an environment ? During the ring sampling, we observed more marine life, especially medium to large organisms (zooplankton, fishes) than at any other station of the journey. The NBC water is known not to be very productive, but what drives the life inside the ring ? The results of the rigorous biological sampling coupled to the physical measurement could shed light on the transport of ecosystems by eddies, or help understand how the rings participate in the spreading of the Amazon river plume ecosystems. Moreover, in the framework of the JPI-Ocean and ATLANTECO projects,linked to the EUREC^{4}A-OA and Microbiome missions respectively, modelling studies are being carried out to build on the results of observation-based studies such as the ones presented in this thesis.

River-ocean continuum

The river-ocean continuum is a region of key importance in the carbon budget of the Amazon river but is one of the least studied area (Sawkuchi et al., 2017). It is due in particular to the absence of fCO_2 data.The region is difficult to access, it is located in the territorial waters of Brazil. It is very hard for non-Brazilian research missions to get the authorisations needed to navigate and in particular to sample in the territorial waters and in particular in the river until Macápa. Strong currents and tides do not allow any kind of vessel to navigate these waters, and so most of the local Brazilian studies focused on the interior of the Amazon. The Tara dataset crossed four times the river-ocean continuum, twice in the Amazon and twice in the Para river and showed significant differences with each crossing. This dataset is unique, and combined with tides and currents could bring light into the mechanisms driving the variability of this continuum, as well as the position of the transition between the source and sink of CO_2. Moreover, this dataset is coupled with particulate biogeochemistry (particulate organic carbon) and with a full set of biological data. Genomics and environmental DNA can shed light on the communities dominating each part of this gradient, from the microbial activity of the river part to the dominant phytoplankton type in the plume.

The Weddell Sea

The pCO_2 system installed on Tara in Martinique in July 2021 worked for several more months after the Amazon legs described earlier. In January 2022, I joined the sailing boat again in King George Island to participate in the Antarctic leg of the mission (leg 11). With the ambitious goal to characterize the region's microbiome and interaction with its surroundings, this mission objective was two-fold: (1) Sample across well-established physical and biogeochemical gradients, from the Weddell gyre onto the shelf toward Joinville Island, (2) Conduct a multi-day process study around an iceberg and sample the sea ice edge.

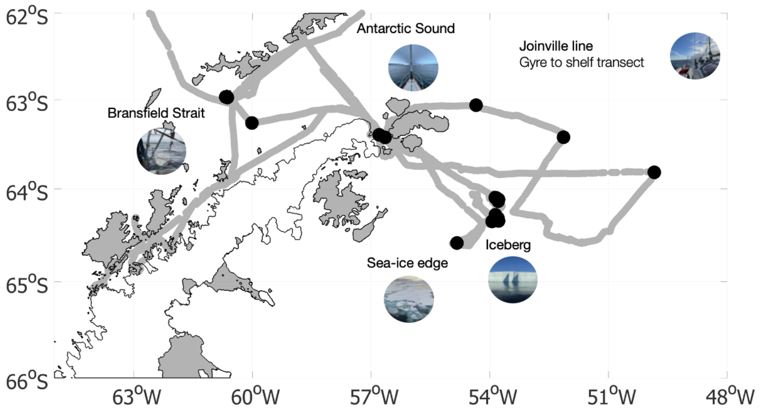

Figure 9.1: Ship tracks and positions of the station carried out during Tara's leg 11 in Antarctica

The western Weddell sea is also a region with a strong variability of SSS. The sources of variability are different than in the tropical Atlantic ocean. In the Weddell sea surface salinity is driven by sea-ice melt or formation, precipitations, iceberg melt and ocean circulation. All of these processes also influence the biogeochemistry of the region and in particular the air-sea CO_2 fluxes. The role of the Weddell sea on the ocean carbon sink is debated, due to the strong lack of observations in the region, in particular during the Antarctic winter (Vernet et al., . The Tara dataset has the advantage of being cross-disciplinary, with physical and biogeochemical measurements are coupled with many biological data. Moreover the Polarstern sampled the same area three weeks later, and Commandant Charcot was in the same area (Antarctic peninsula) at the same time as Tara. Both vessels were equipped with a pCO_2 system and can complete the CO_2 dataset acquired by Tara.

Some of the questions that would be interesting to answer thanks to this new dataset are:

- How does the microbiome respond to variability in the seascape introduced by topography, frontal system and freshwater ?
- How do iceberg impacts the local physics, biogeochemistry and biology? In particular, what is the impact of an iceberg on the air-sea CO_2 flux ?

The advantage of a sailing boat in studying the impact of iceberg is the proximity from the iceberg at which it can operate. While large research vessels need to stay one mile away from the iceberg, Tara can do station tens of meters away from the iceberg. Therefore, the underway data are

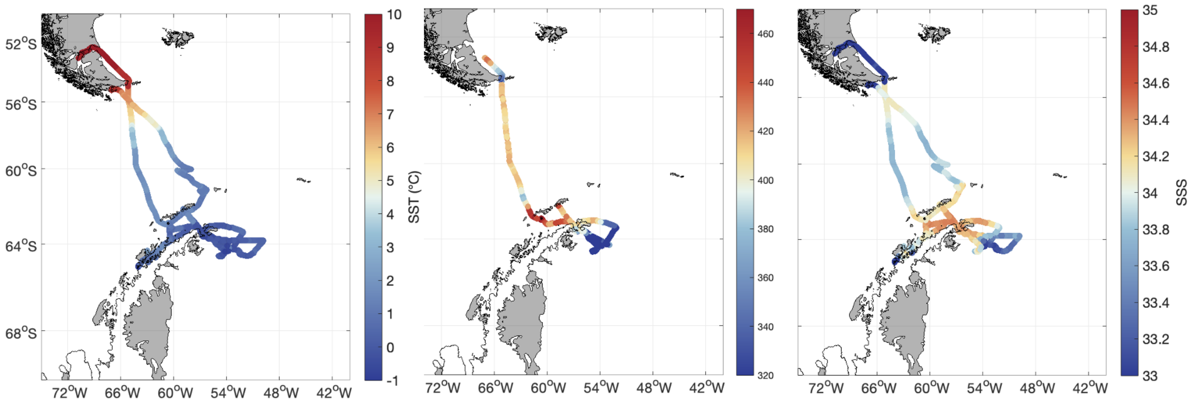

Figure 9.2: Underway SSS, xCO_2 and SST in the Southern ocean

located close to the iceberg, but also all the biogeochemistry, biology and physical dataset collected on the CTD rosette.

The iceberg study was designed with this hypothesis in mind : "Are the iceberg a source of iron significant enough to drive a phytoplankton bloom " ? It is very interesting from a CO_2 flux point of view because thanks to the many data collected we could assess the signature of the iceberg on the flux, but also the mechanisms driving it. Is the dilution linked to the melting iceberg the dominant factor ? What is the part of the carbon drawdown played by the biological activity ?

The physical, biogeochemical and biological dataset acquired during the Antarctic leg of the Tara Microbiome mission is bursting with possibilities. Observations are key to identify the processes happening in the ocean, to better model them and understand their consequences on the biology, biodiversity and climate.

APPENDIX

A

Supplementary material to the first paper

Journal of Geophysical Research: Oceans

Supporting Information for

Tropical Instability Waves in the Atlantic Ocean: investigating the relative role of sea surface salinity and temperature from 2010 to 2018

L. Olivier[1], G. Reverdin[1], A. Hasson[1,2] and J. Boutin[1]

[1]Sorbonne Université, CNRS, IRD, MNHN, UMR 7159, Laboratoire d'Océanographie et du Climat : Experimentations et Approches Numériques, LOCEAN-IPSL F-75005, Paris, France

[2]Université de Toulouse, CNES, CNRS, IRD, UPS, Laboratoire d'Etudes en Géophysique et Océanographie Spatiales (LEGOS), Toulouse, France

Contents of this file

Figures S1 to S11

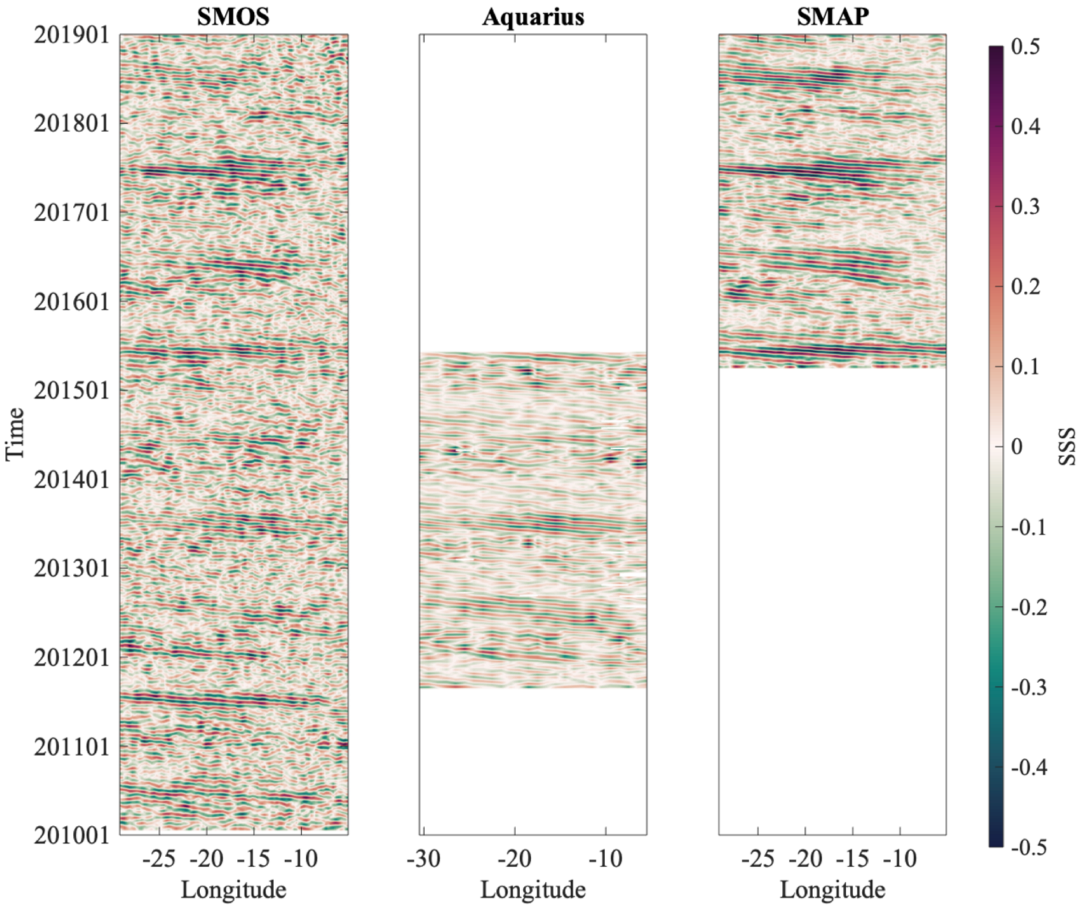

Figure S1. January 2010 to December 2018 Hovmöller diagrams at 1°N of SMOS, Aquarius and SMAP SSSA.

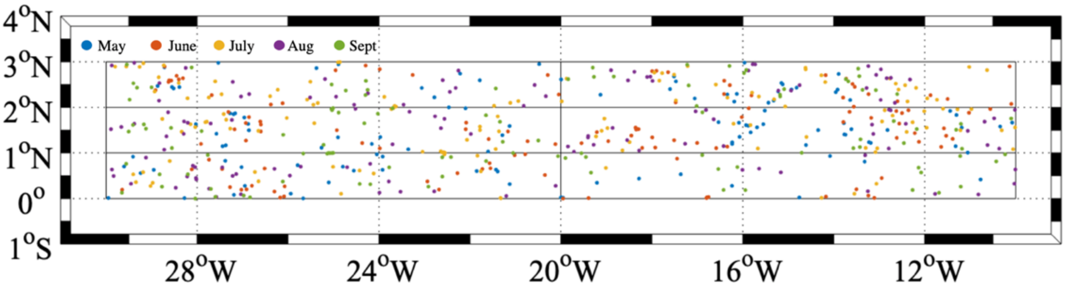

Figure S2. Repartitions of the Argo profiles used in this study, color-coded with the month of the year.

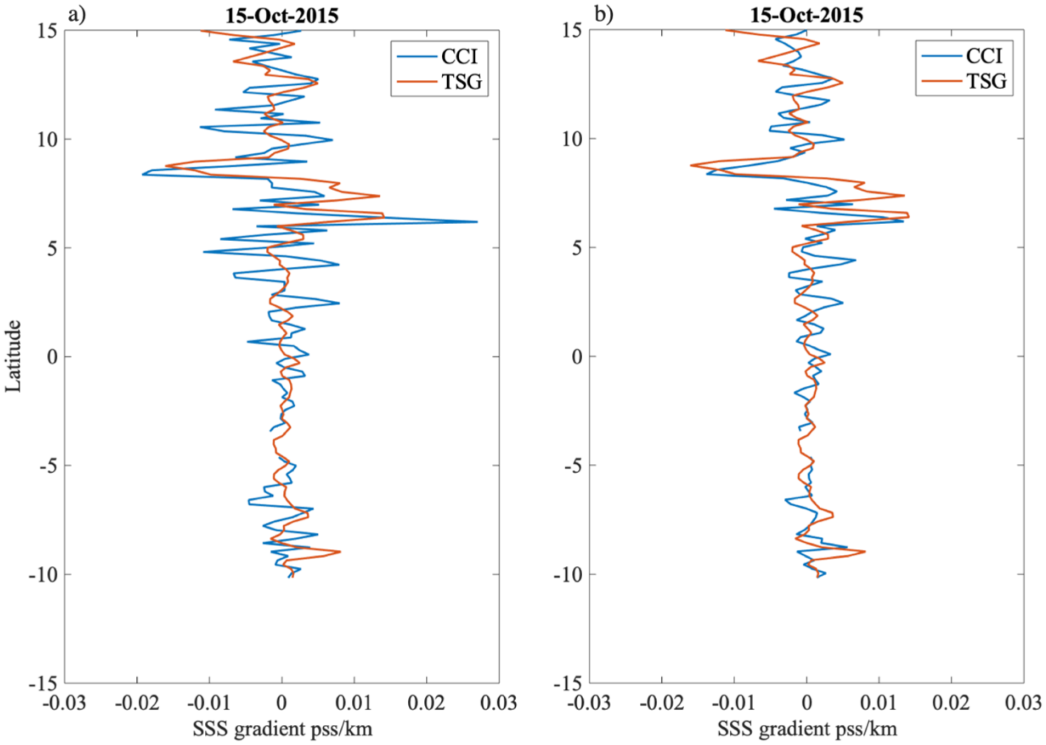

Figure S3. a) In blue are represented the satellite CCI salinity gradient and in orange the thermosalinograph salinity gradient for the 15th of October 2015. b) Same as a) but the satellite CCI data is averaged on 5 pixels in longitude (125 km).

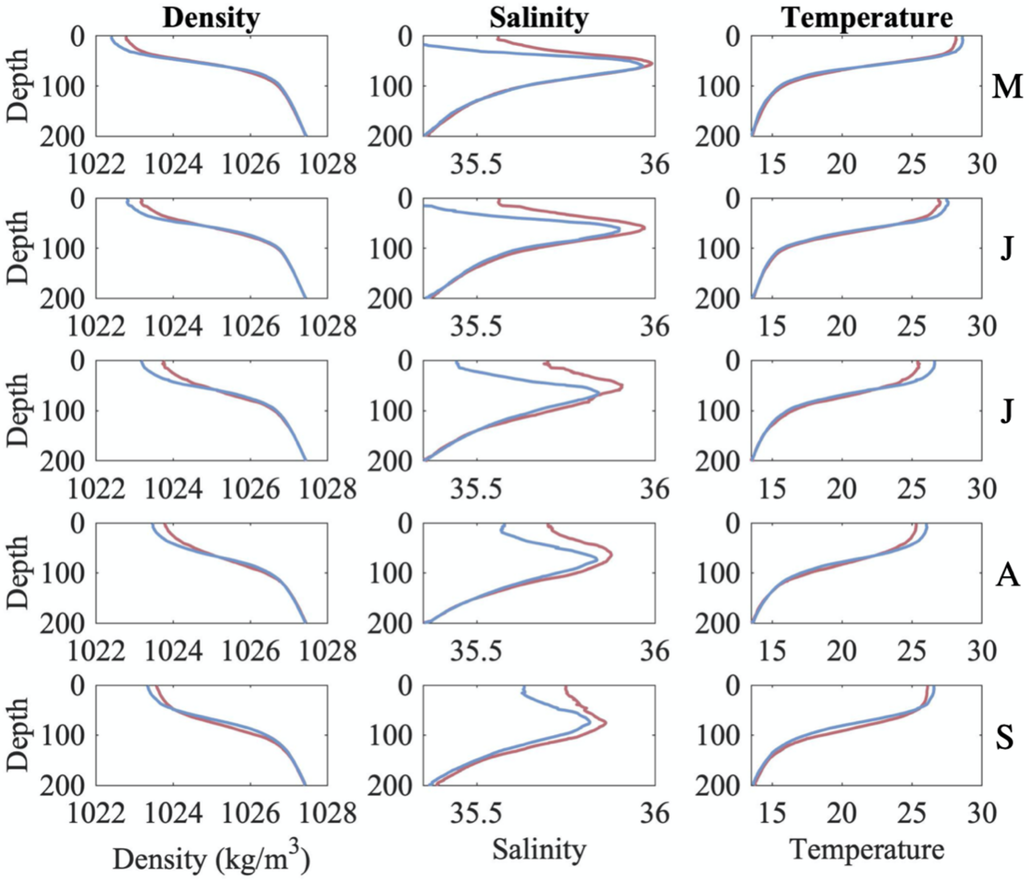

Figure S4. Mean density (left), salinity (middle), and temperature (right) Argo profiles located into positive (red) and negative (blue) tropical instability waves-related sea surface density anomalies determined by satellite from May (top) to September (bottom).

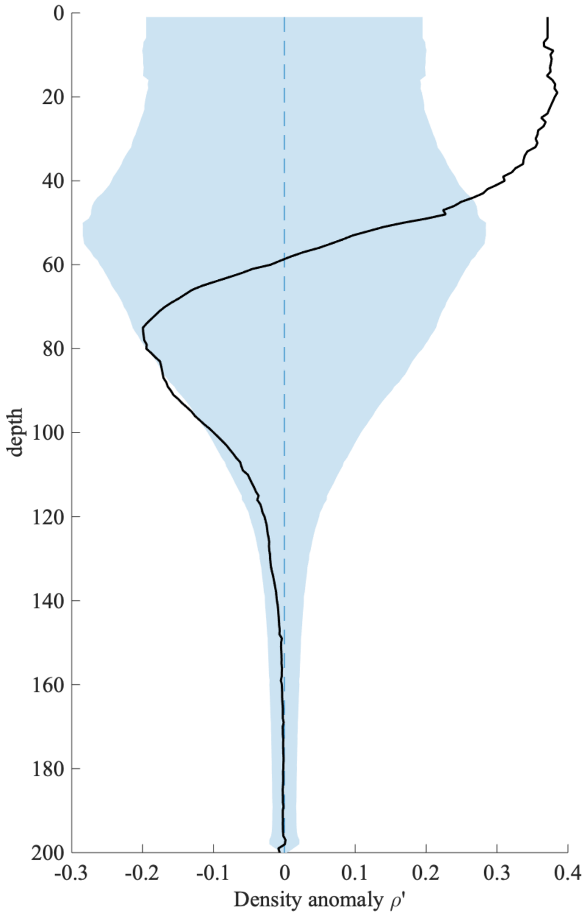

Figure S5. Mean density anomaly computed as the difference between the averaged profiles located in a positive and negative anomaly of surface density for May to September.
+- 1 standard deviation of the uncertainty is represented in shaded blue and estimated with a test of the null hypothesis.

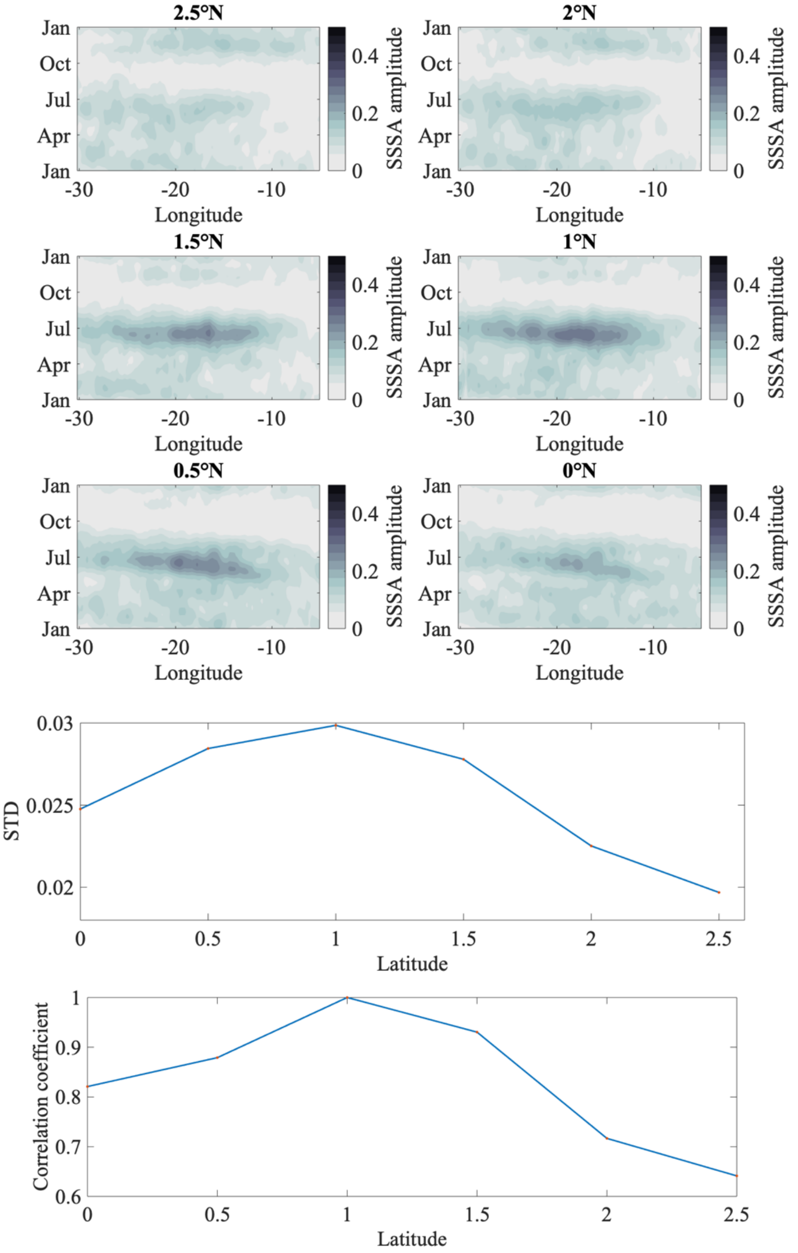

Figure S6. Hovmöller diagram of 2010-2018 climatological mean SSS anomalies amplitudes at 2.5°N, 2°N, 1.5°N, 1°N, 0.5°N and 0° (top). Standard deviation of the longitude averaged SSSA amplitudes for the different latitudes (middle). Correlation coefficient of longitude averaged SSSA amplitudes at each latitude with the one at 1°N (bottom).

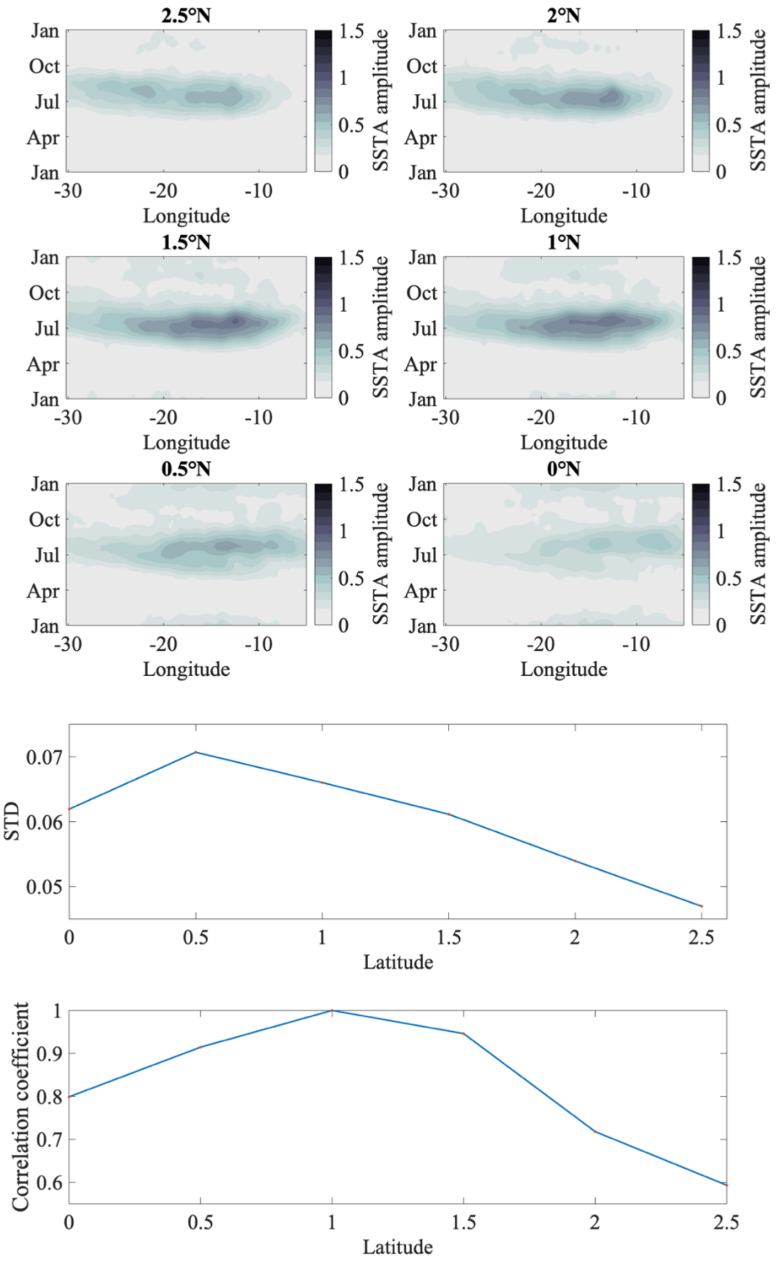

Figure S7. Hovmöller diagram of 2010-2018 climatological mean SST anomalies amplitudes at 2.5°N, 2°N, 1.5°N, 1°N, 0.5°N and 0° (top). Standard deviation of the longitude averaged SSTA amplitudes for the different latitudes (middle). Correlation coefficient of longitude averaged SSTA amplitudes at each latitude with the one at 1°N (bottom).

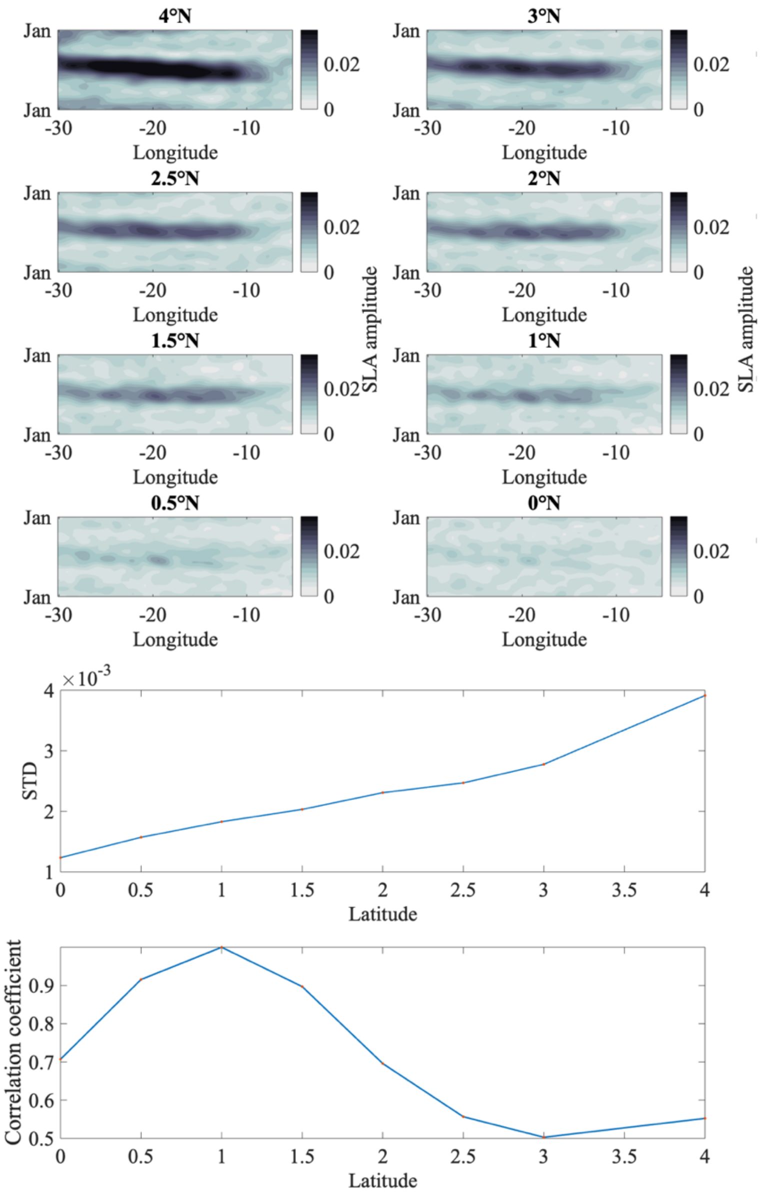

Figure S8. Hovmöller diagram of 2010-2018 climatological mean SLA amplitudes at 2.5°N, 2°N, 1.5°N, 1°N, 0.5°N and 0° (top). Standard deviation of the longitude averaged SLA amplitudes for the different latitudes (middle). Correlation coefficient of longitude averaged SLA amplitudes at each latitude with the one at 1°N (bottom).

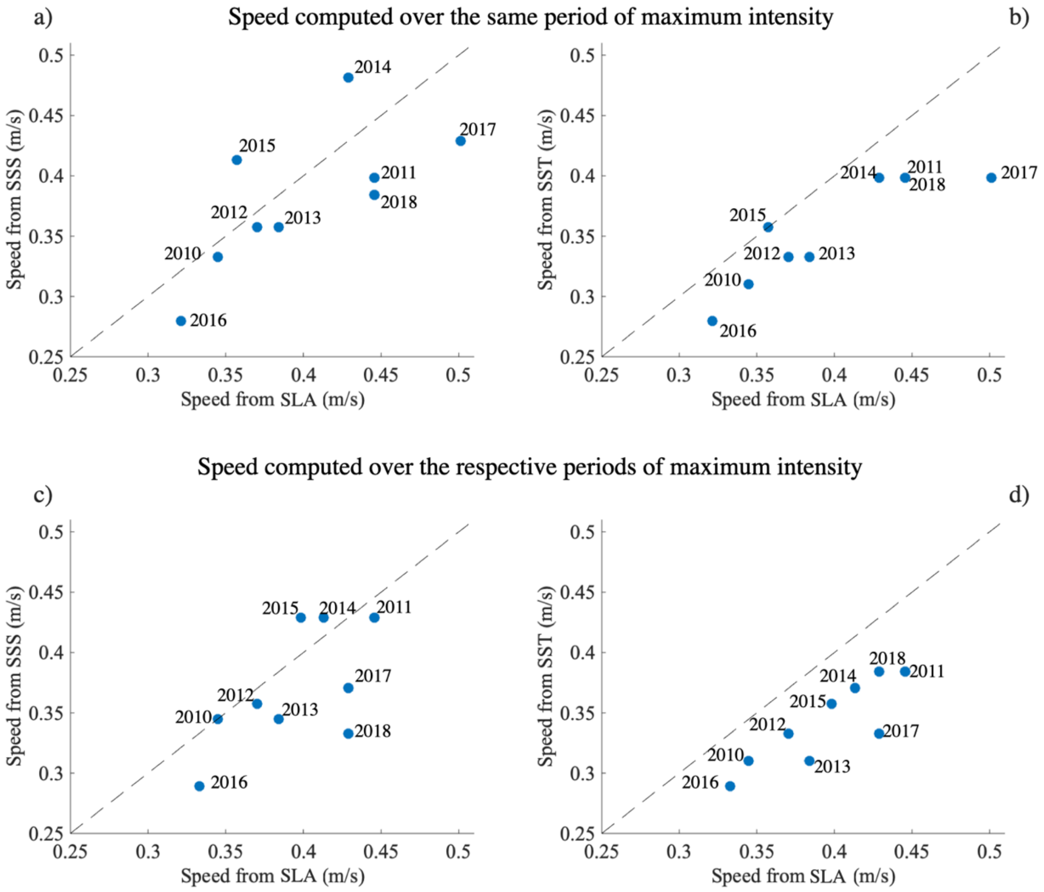

Figure S9. Dispersion diagrams of TIWs westward phase speeds estimated by radon transform for the 01/06-20/07 period and for SSS, SST and SLA (a and b). Dispersions diagrams of TIWs westward phase speeds measured by radon transform for SSS (computed for the 05/05-20/07 period), SLA (computed of the 19/05-11/08 period) and SST (computed for the 01/06-21/08) (c and d).

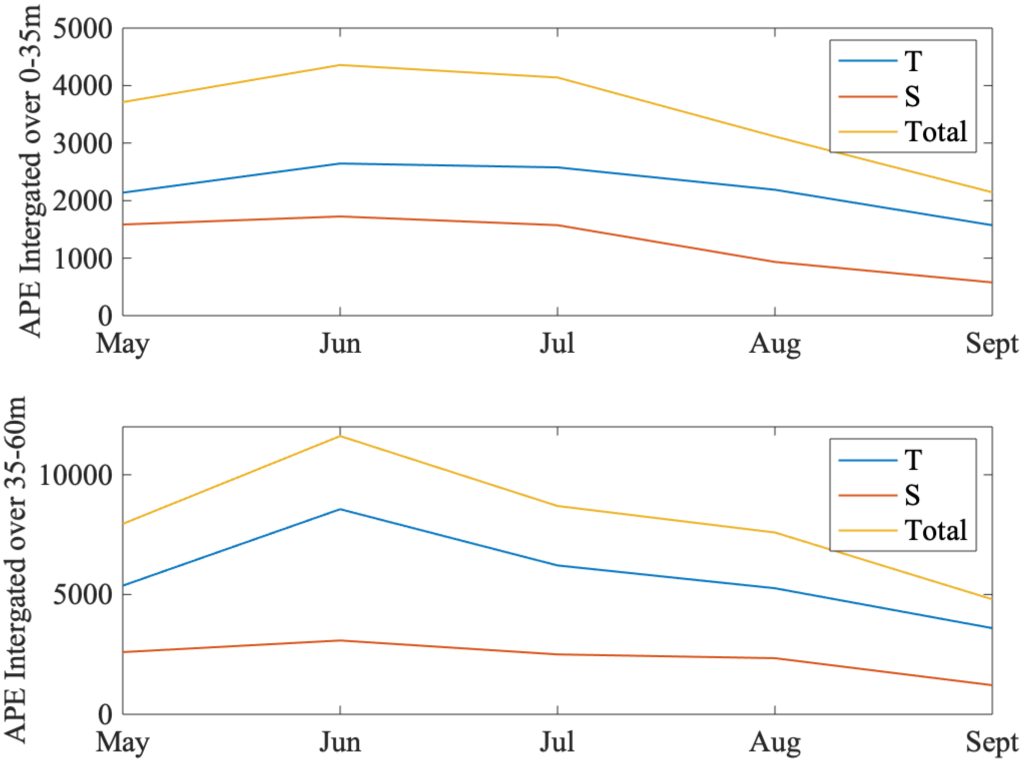

Figure S10. Integrated available perturbation energy for the top 35m of the water column (top) and for the 35-60m layer (bottom). The total APE is represented in yellow; orange and blue describe respectively the contribution of salinity and temperature.

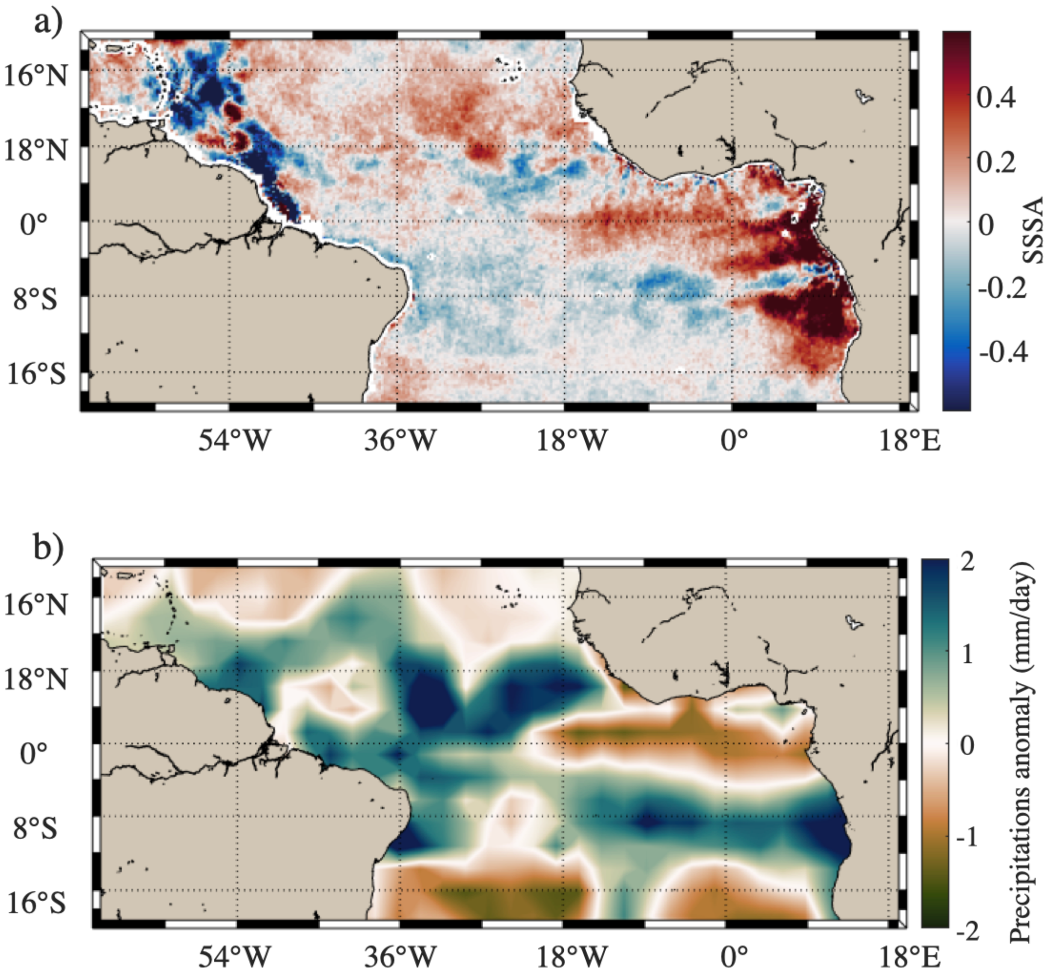

Figure S11. Anomaly to the 2010-2018 climatology for the months of March-April-May-June 2017 in a) SSS, b) precipitations.

B

Supplementary material to the second and third papers

AGU PUBLICATIONS [JGR: Oceans]

Supporting Information for

A freshwater plume in the northwestern tropical Atlantic in February 2020

Reverdin, G.[1], L. Olivier[1], G. R. Foltz[2], S. Speich[3], J. Karstensen[4], J. Horstmann[5], D. Zhang[6], R. Laxenaire[7], X. Carton[8], H. Branger[9], R. Carrasco[5]

[1]LOCEAN-IPSL, Sorbonne Université-CNRS-IRD-MNHN, Paris, France, Paris, France

[2]NOAA/Atlantic Oceanographic and Meteorological Laboratory, Miami, FL, USA,

[3]Laboratoire de Météorologie Dynamique, ENS-Ecole Polytechnique-CNRS-Sorbonne Université, Paris, France.

[4]GEOMAR Helmholz Centre for Ocean Research Kiel, Kiel, Germany

[5]Helmholtz-Zentrum Geesthacht, Geesthacht, Germany

[6]CICOES/University of Washington and NOAA/Pacific Marine Environmental Laboratory, Seattle, WA, USA

[7]Center for Ocean-Atmospheric Prediction Studies, Florida State University, Tallahassee, Florida, USA.

[8]Laboratoire d'Océanographie Physique et Spatiale, UBO-CNRS-IFREMER-IRD, Plouzané, France.

[9]IRPHE, CNRS-AMU, Luminy, France.

Contents of this file

Text S1 to S4 with associated figures S1a, S1b, S2a, S2b, S3 and S4

Introduction

- The supporting information contains: S1, information on the Ocarina profiles used to estimate an average Richardson profile in mixing depth; S2, uncertainties on the currents used to estimate cross-shelf transport; S3, illustration of the 7 other fresh plumes observed in 2010-2019; S4, MSM salinity section on Feb 2 2020

Supporting Information S1: Ocarina on February 03 2020.

On 03 February, the free drifting platform Ocarina (Bourras et al., 2019) was deployed from 06h00 to 17h00 local time (10h00 to 21h00 UTC). On that day, dry easterly trade winds with mesoscale sugar cloud patterns were observed. Measured friction velocity ranged from u*=0.28 m/s (during the first half part of the deployment) to u*=0.18 m/s (during the second part). Aerodynamic roughness height zo varied accordingly from 0.09 mm to 0.06 mm. Reconstructed wind speeds at z=10m from wind speeds recorded on board Ocarina at z=1.5m, taking into account the measured friction velocity and atmospheric stability, ranged from U_{10}=8.5 m/s decreasing to 6.0 m/s. They were mainly directed from WSW, with a maximum at 09h00 local time and a minimum at 15h00 local time. The significant wave height recorded on the platform was around 1.5 m with dominant wave periods around 7s. Ocarina recorded both short-wave and long-wave downwards and upwards radiative fluxes. The net radiation fluxes show a positive budget (heating atmosphere, cooling ocean) with a maximum of 800 Watt/m2 near 13h00 local time. Measured latent heat fluxes were around 175 Watt/m2 from 07h00 to 11h00 local time and around 140 Watt/m2 from 13h00 to 17h00 local time. Buoyancy sensible heat fluxes decreased from 10 Watt/m2 to 7 Watt/m2 during the deployment with large fluctuations at medium time scale (5 min to 20 min). These fluctuations were found to be correlated with wind gusts which had a dominant period of 6 min.

Ocarina drifted westward from (54.14°W,6.83°N) to (54.34°W, 6.83°N), at relatively constant 0.6 m/s (+/- 0.1 m/s) speed. During the drift, the salinity measured at z=-0.2m increased linearly from 34.73 to 34.95 pss, and the reconstructed skin SST increased from 26.58°C to 26.88°C.

The Ocarina platform was equipped with a NORTEK Signature 1200 kHz ADCP to measure water current profiles at 0.5 m resolution between 0.3 m and 17.3m from the sea surface. The current-meter was associated with an inertial unit, compass, magnetometers, and measurements were corrected from platform motion. Data were acquired at a frequency rate of 8 Hz during 3 min, every 5 min. Only measurements with sufficient signal-to-noise-ratio, coherence between beams, and enough acoustic refracted power were retained. All the retained vertical profiles during the 3 minutes were averaged over 3 min to produce an average vertical profile. Thus, 132 'average' vertical profiles were available that day. The ADCP measured an "apparent velocity", i.e. the velocity beneath Ocarina. The "true" current velocity was reconstructed using the GPS drift recorded by the onboard GPS system.

Figure S1a shows the temporal evolution of the vertical profiles of the true velocity computed from the ADCP. There is veering of the direction and amplitude modifications with depth, which might be indicative of Ekman dynamics and coastal upwelling. There is a clear evidence of mixing layer beginning at the surface, with a quite vertical homogeneous profile. The height of the mixed layer seems to increase from 6 -7 m during the first half of the deployment to 13-14 m during the second half. The zonal component of the current is quite large near the surface: it increases from an eastward 45 cm/s at the beginning to an eastward 65 cm/s during the second half of the deployment. Surface eastward current were lower in the morning although friction velocity and wind were stronger, and surface current was higher in the afternoon although wind was lower. Below the mixing layer, a significant vertical shear occurs reaching sometimes 7 cm/s per m of depth.

During the deployment, there were three periods (morning, mid-day, and evening) when the RV Atalante MVP profiles of temperature and salinity and the ADCP current profiles from Ocarina were taken within a few kilometers of each other. The average of these 11 MVP density profiles shows a thoroughly mixed layer between 2 and 6 m thick. Below that it is continuously stratified (Fig. S1b, blue line) with a stratification dominated by salinity increase (from 34.8 pss at the surface to 35.2 pss at 17-m depth, with very weak temperature change in that layer between 26.53°C and 26.67°C). The corresponding currents (S1b, zonal component with black line), which were of 45 cm/s westward in the top 6 m, diminish to 19 cm/s at 17 m, indicating large shear across the salinity-stratified layer (red line). The individual curves are dimensioned in such a way that the blue line reaching the red line corresponds to a Richardson number of 0.2.

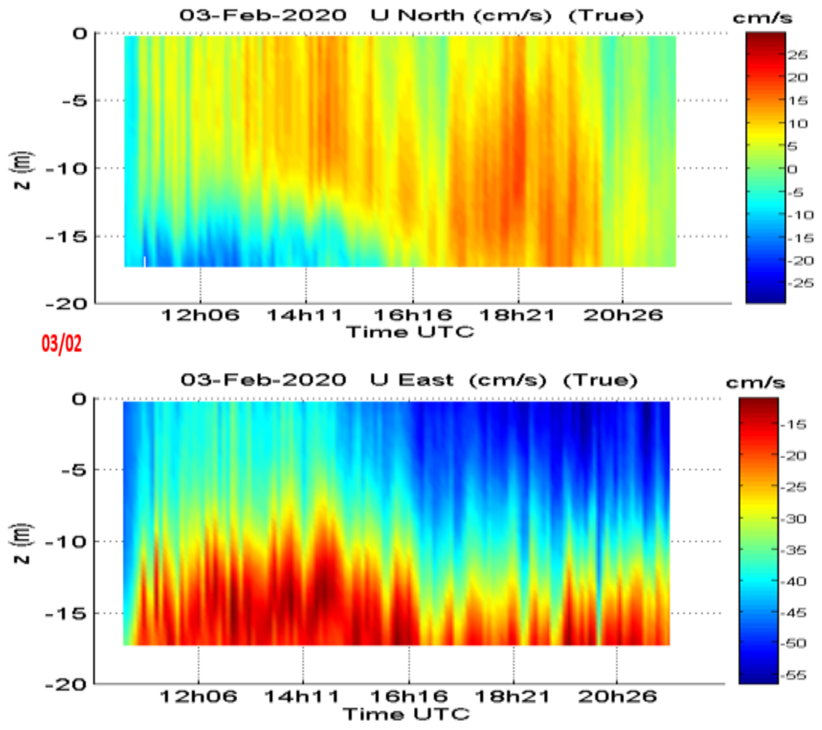

Figure S1a: Temporal evolution of the vertical velocity profiles measured on-board Ocarina on 03 February. Top: True North component, bottom: True East Component.

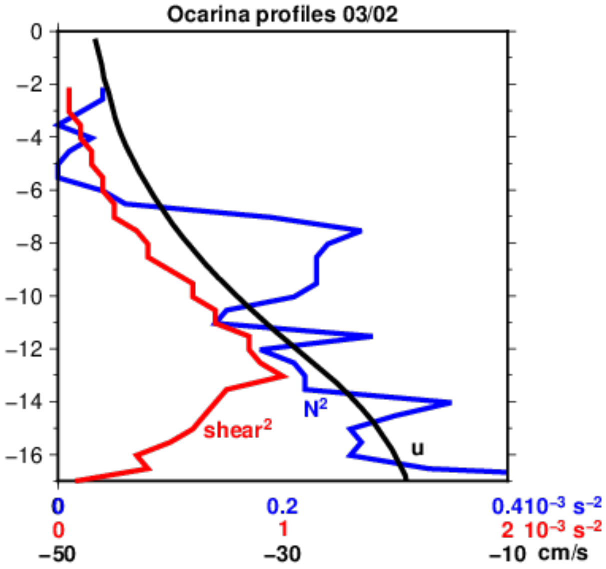

Figure S1b: Average profiles of Ocarina data from 0 to 17-m depth (black, zonal current; red, squared shear) at the times of 11 close-by MVP profiles (squared Brunt-Väisala frequency in blue).

Supporting Information S2: Uncertainties on currents and transports

In part 3.4 and Fig. 10 we presented the advective budget of the fresh water plume. Some approximations were done, and related uncertainties are presented below.

First, the Ekman transport is a large contribution to the transport of fresh water across the shelf break (roughly 50%). We used a constant value of the Ekman depth (20 m) to estimate the budget in Fig. 10. A conservative estimate of the uncertainty of a factor 2 in the actual depth at a given time (see for example the saildrone section in Fig. 9) would thus imply a 25% uncertainty in the flux estimate.

Other large uncertainties are associated with the geostrophic currents near the shelf break. We used near-real time geostrophic DUACS NRT currents derived from altimetry. This product integrates all altimetric data before a given date, but only for the next 6 days after, and thus is less certain than the delayed mode products. In both cases there are also uncertainties resulting from the spatial smoothing applied for the product (close to 100 km), time variability, and possible errors in the mean currents near the shelf and shelf-break.

To illustrate the uncertainties on the DUACS NRT geostrophic velocities, we compared the geostrophic currents derived from altimetry with the ones measured by the vessel mounted ADCPs (VM-ADCP) of RV Atalante and MSM on the 2nd of February, when the vessels were near A1 and the fresh plume and shelf break. To do so, we interpolated the Aviso currents along the RV Atalante and MSM tracks. From comparison between these currents and the ones measured by the top bin of the RV Atalante OS150 kHz VM-ADCP at 28.85-m deep and the MSM OS75kHz VM-ADCP at 18-m, we observe weaker currents in the satellite product away from the shelf. This is particularly true near anticyclone A1 (Fig. S2a) and along the shelf break where a jet visible on the ADCP data is not captured by the altimetry. On average the currents from altimetry are about 25-30% smaller than the ADCP ones for bottom depth greater than 100 m. On the shelf, the situation is different and the magnitude of the altimetric currents is closer to what is observed by MSM at 18-m. They are in some parts even a little bit overestimated. This is not so surprising considering the very shallow fresh surface layer, Ekman currents, and possibility of Ekman upwelling on the inner shelf (thus slope of surface sea level across the shelf), as well as bottom friction. Thus, it is difficult to directly estimate an uncertainty for the currents of this product on the shelf. Although the differences are also related to high frequency variability sensed during the ADCP sections, similar features found with the two ships and the sections crossing the shelf break suggest a conservative estimate of the uncertainty of 30% for the component perpendicular to the shelf. This does not affect the overall conclusion that the geostrophic currents (see Fig. 3) had an off-shelf component near the shelf break in early February (see also fig. S2b) that contributed to the transport of the fresh water from the shelf to the open ocean.

Finally, when estimating the freshwater transport, there is uncertainty due to the mapping of salinity, but it is probably less important for the integration represented in the blue curve of Fig. 10 (uncertainty is on the order or less than 0.5 pss). This uncertainty might modulate the length of the segment of the shelf break over which the fresh water is transported, maybe with an uncertainty of 20% (larger near the beginning and end of the period). Taken together with the current uncertainties, the area advective flux has errors on the order of 50%. Some of it is probably random, but in the worst-case scenario the errors on cumulative flux (blue curve on Fig. 10) are also 50%. If it were just random, the best-case scenario, the resulting uncertainty would be much less (near the end, for example, a 15% error). In all cases, the errors on the area transport are much larger than the error on the area itself, which is difficult to estimate, but could be no more than 10%, based on estimating the daily seasonal product with different corrections, mapping parameters and corrections on the SMAP and SMOS data.

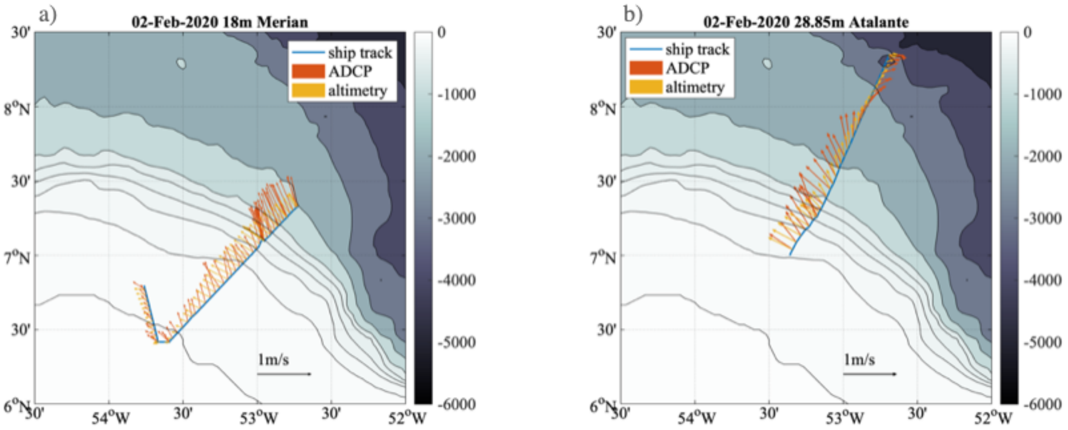

Figure S2a: Geostrophic velocities from altimetry interpolated along the MSM track (a) and RV Atalante (b) for the 2nd of February 2020 (yellow arrows). Red arrows represent the top bin velocities from the MSM (18m, a) and the Atalante VM-ADCP (28.85m, b).

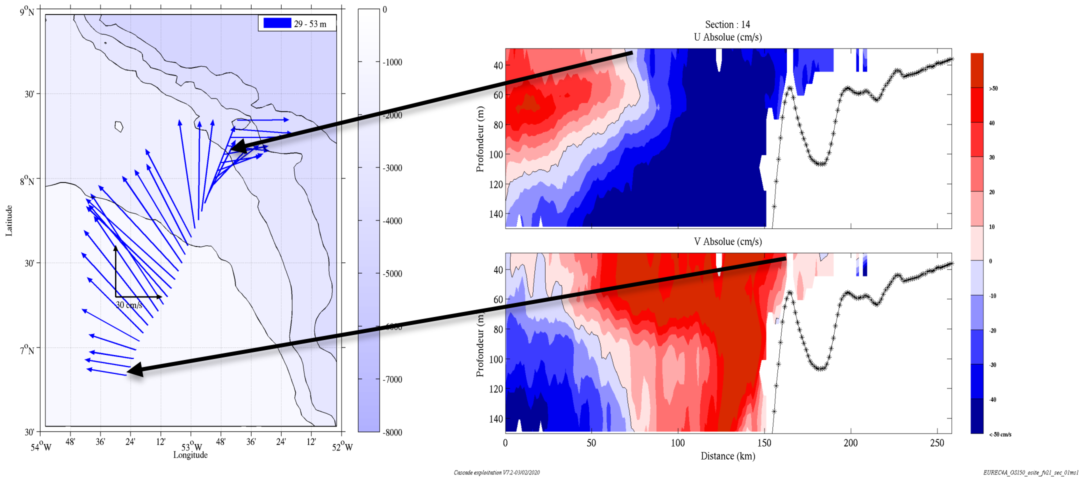

Figure S2b: Current section of RV Atalante on Feb 2 2020. The vertical sections for the two velocity components between 29m and 150m are shown on the right side (notice that shore is to the right), whereas the average currents are plotted on the left map. Notice that it does not extend south to the latitude of the surface front.

Supporting Information S3: freshwater plumes in 2010-2019

We illustrate (Fig. S3) weekly SSS for all occurrences of fresh plumes extending at least to 10°N and east of 56°W in January-March 2010-2019 (note that 2010, 2011 and 2013 don't have events). The weekly SSS fields are generated by the Climate Change Initiative Sea Surface Salinity (CCI+SSS) project (doi:10.5285/4ce685bff631459fb2a30faa699f3fc5). For each event, the week retained corresponds to peak extension of the fresh plume. Notice that most of these plumes suggest the presence of an anticyclone to its east.

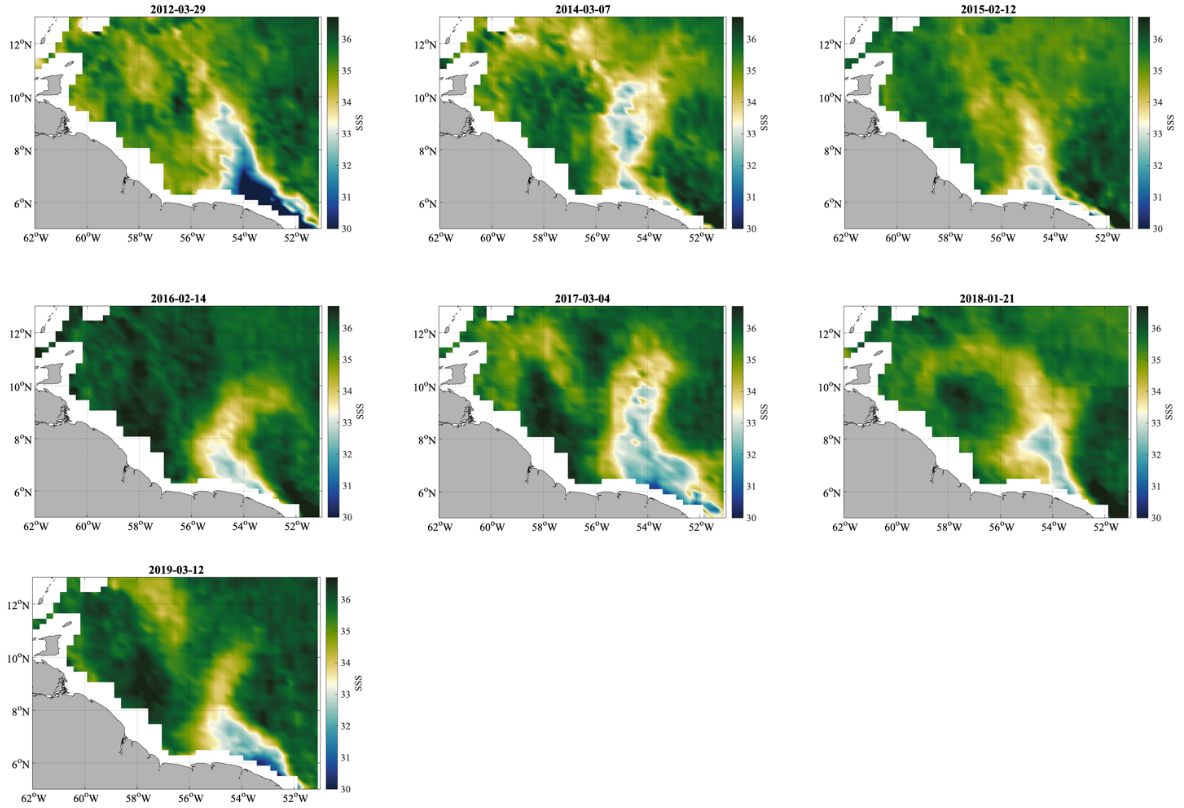

Supporting information S4: MSM salinity section on Feb 2 2020

This figure (S4) complements Fig. 7c (the dotted line here corresponds to the fresh water layer thickness of Fig. 7c). The salinity section combines uCTD profiles south of 53°15’W (squares on top axis) and MVP profiles further west (ticks on top axis). The dashed vertical line corresponds to the surface front location.

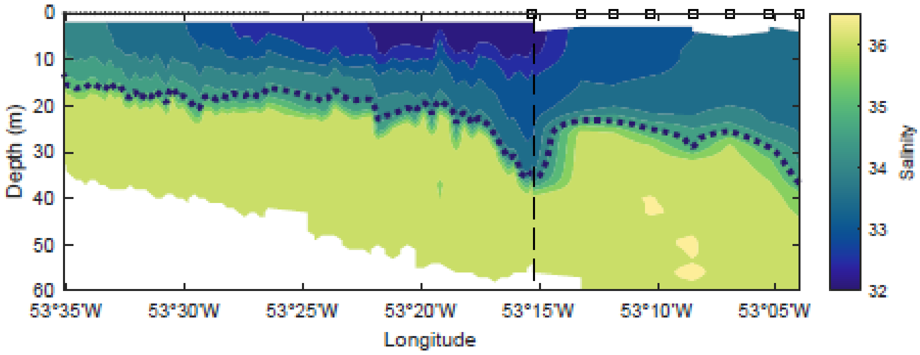

Supporting Information for

Wintertime process study of the North Brazil Current rings reveals the region as a larger sink for CO_2 than expected

L. Olivier[1], J. Boutin[1], G. Reverdin[1], N. Lefèvre[1], P. Landschützer[2], S. Speich[3], J. Karstensen[4], M. Labaste[1], C. Noisel[1], M. Ritschel[2], T. Steinhoff[4] and R. Wanninkhof[5]

[1] LOCEAN-IPSL, Sorbonne Université-CNRS-IRD-MNHN, Paris, France

[2] Max Planck Institute for Meteorology, Hamburg, Germany

[3] Laboratoire de Météorologie Dynamique, ENS-Ecole Polytechnique-CNRS-Sorbonne Université, Paris, France

[4] GEOMAR Helmholtz Centre for Ocean Research, Kiel, Germany

[5] Atlantic Oceanographic & Meteorological Laboratory of NOAA, Miami, USA

Contents of this file

Introduction

The supporting information contains text and figures aiming to detail methods, uncertainties and results presented in the paper. First, the interpolation method used is detailed by text S1. Figure S1 compares the relationship linking salinity and alkalinity used in this paper with the fCO_2 measured during the cruise. Figure S2 presents the repartition of nutrients in the area of interest, and figure S3 follows the evolution of a coastal upwelling along the coast of Guiana.

Text S1.

The fCO_2 associated to the surface T-S-Chl*a* diagram computed from the ship measurement (and collocated satellite Chl*a*) is interpolated using a linear 3D interpolation on a grid of SST, SSS and Chl*a*. The linear 3D interpolation of this scattered dataset on a regular grid is obtained through the griddata matlab function. The method is based on a Delaunay triangulation of the data, often used to generate meshes for space-discretized solvers. The Delaunay triangulation for a given set P of discrete points in a general position is a triangulation DT(P) such that no point in P is inside the circumcircle (circumsphere in 3D) of any triangle (pyramid) in DT(P). In the case of the 3D interpolation, for each query point, the method founds in triangulation data structure the pyramid that encloses the point. The value is then computed from a weighted sum of values of the 4 vertices of the enclosing pyramid (linear interpolation). First averaging data in classes of 0.1°C, 0.1 in SSS and 0.1 in $\log_{10}$(Chl*a*) (yielding about 1000 gridded data points compared with ~20000 original data) did not modify significantly the results of the Delaunay triangulation. This suggests that the resulting 3D interpolation is not strongly influenced by noise and natural variability at small scale in T-S-$\log_{10}$(Chl*a*) space. This dependency on the dataset sampling is further reduced by time averaging the resulting fields over an over 20-day period as is presented in the paper.

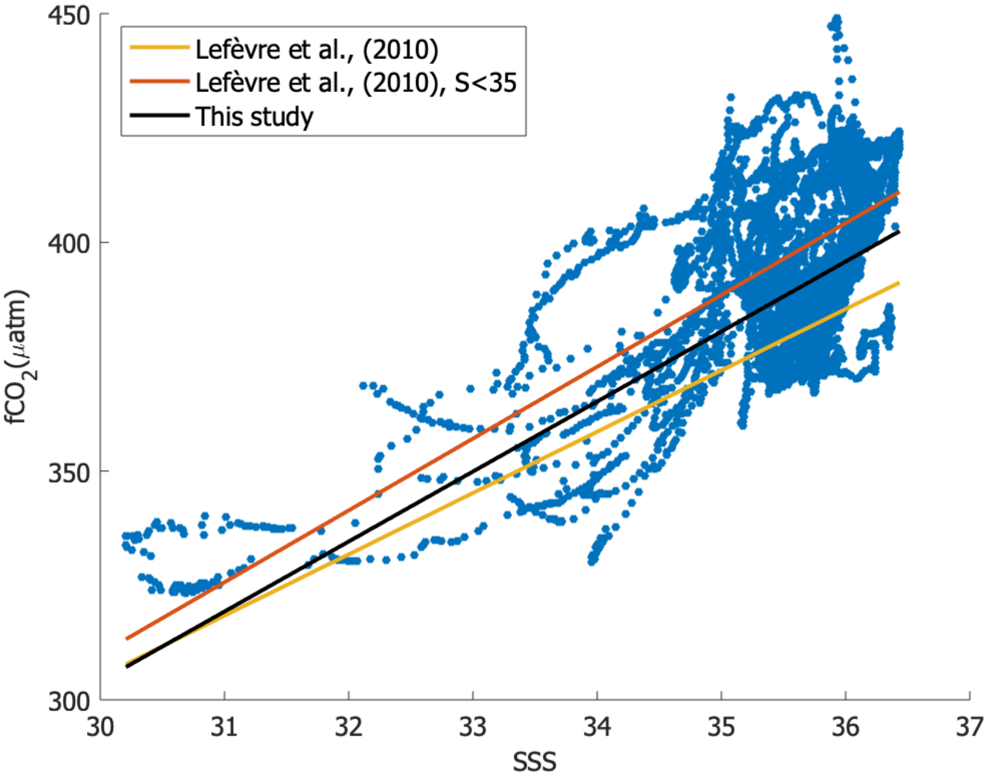

Figure S1. SSS- fCO_2 relation and comparison to Lefèvre et al., (2010)

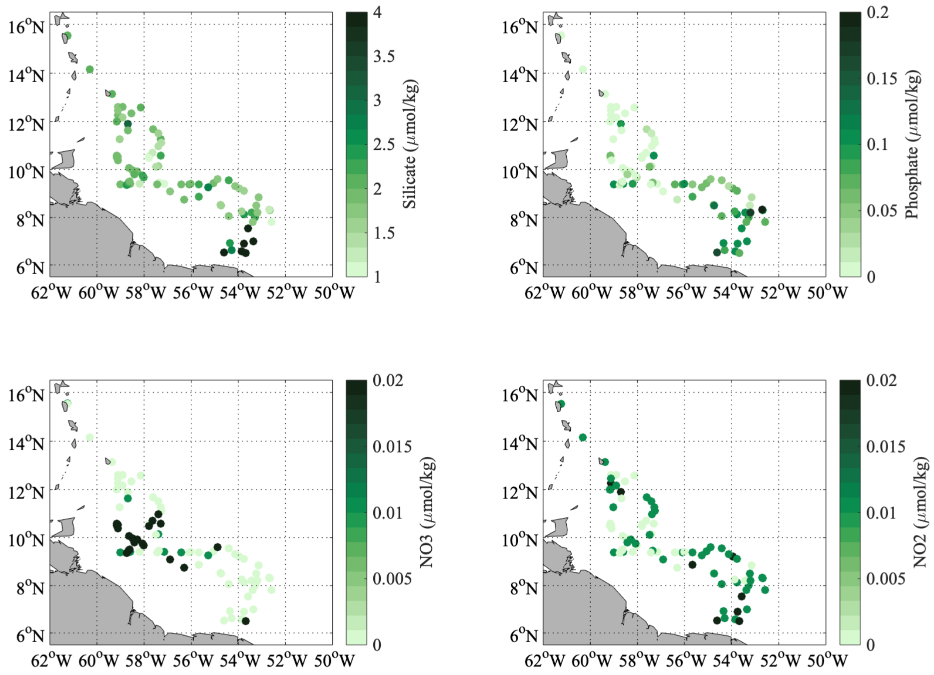

Figure S2. Nutrients (Silicate, Phosphate, Nitrite and Nitrate) measured during the EUREC^{4}A-OA cruise from underway water samples.

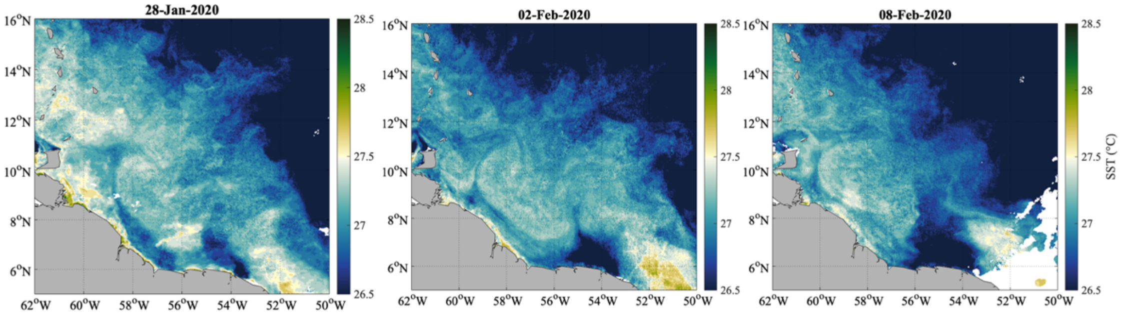

Figure S3. Evolution over 9 days of a local upwelling along the Guyana coast based on SST. SST maps for the 28/01/2020, 02/02/2020 and 08/02/2020.

C

Supplementary material to the fourth paper

Journal of Geophysical Research: Oceans

Supporting Information for

Late summer northwestward Amazon plume pathway under the action of the North Brazil Current rings

L. Olivier[1], G. Reverdin[1], J. Boutin[1], R. Laxenaire[2,3], D. Iudicone[4], S. Pesant[5], Paulo H.R. Calil[6], J. Horstmann[6], D. Couet[7,8], J. M. Erta[9], P. Huber[10], H. Sarmento[10], A. Freire[11], A. Koch-Larrouy[12], J.-L. Vergely[13], P. Rousselot[14], S. Speich[2]

[1]LOCEAN-IPSL, Sorbonne Université-CNRS-IRD-MNHN, Paris, France

[2]Laboratoire de Météorologie Dynamique, ENS-Ecole Polytechnique-CNRS-Sorbonne Université, Paris, France

[3]Laboratoire de l'Atmosphère et des Cyclones, LACy, UMR 8105, CNRS, Université de La Réunion, Météo-France, Saint-Denis de La Réunion, France

[4]Stazione Zoologica Anton Dohrn, Villa Comunale, 80121 Naples, Italy

[5]European Molecular Biology Laboratory, European Bioinformatics Institute, Wellcome Genome Campus, Hinxton, Cambridge CB10 1SD, United Kingdom

[6]Helmholtz-Zentrum Hereon, Max-Planck Straße, 1 Geesthacht, 21502 Germany

[7]CNRS, Research Federation for the study of Global Ocean Systems Ecology & Evolution, FR2022 - GOSEE, Paris, France

[8]Station Biologique de Roscoff, UMR7144, ECOMAP, Roscoff, France

[9]EMS, SLU, C/Teodora Lamadrid 40, E-08022 – Barcelona, Spain

[10]Universidade Federal de São Carlos (UFSCar). Departamento de Hydrobiologia. Rodovia Washington Luiz S/N.São Carlos, S.P., Brazil

[11]Laboratório de Crustáceos e Plâncton, Departamentode Ecologia e Zoologia, Universidade Federal de Santa Catarina, Florianópolis, Santa Catarina, Brasil

[12]Laboratoire d'Etudes en Géophysique et Océanographie Spatiales (LEGOS), UMR5566, CNES, CNRS, IRD, UPS, Toulouse, France

[13]ACRI-st, Biot, France

[14]IRD, UAR IMAGO, Délégation Régionale Ouest, Technopole Pointe du Diable, CS 10070, 29280 PLOUZANE

Contents of this file

Figures S1 to S3

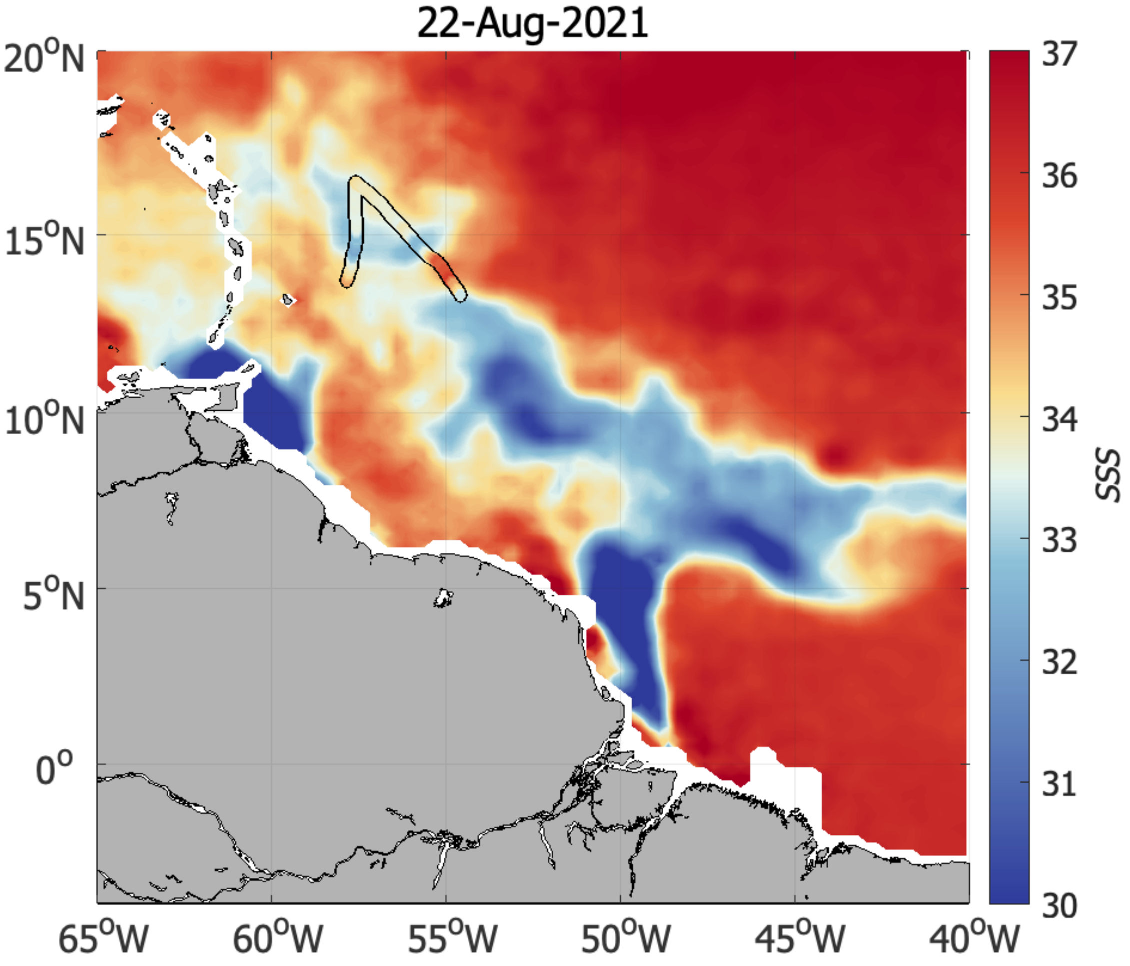

Figure S1. Snapshot of SSS on the 22th of August 2021. Tara's ship track is superimposed, colour-coded by the thermosalinograph salinity from august 21st to august 23rd.

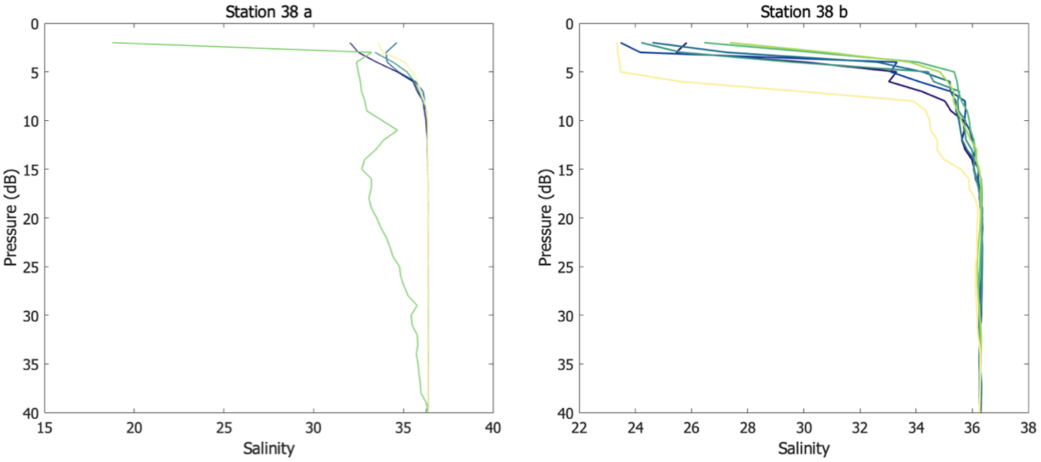

Figure S2. Repeated salinity profiles for *Tara's* stations 38a and 38b.

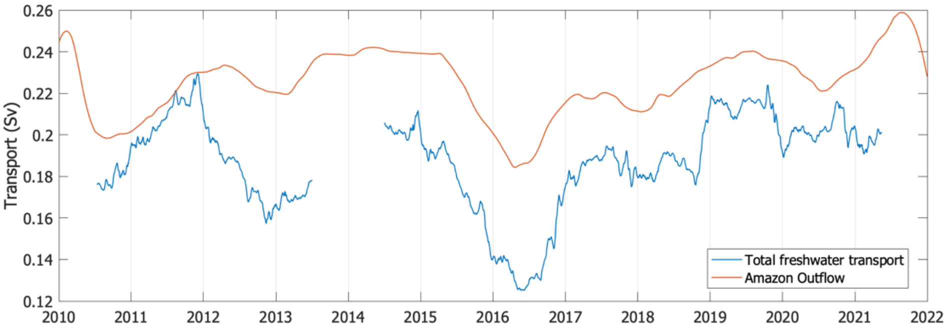

Figure S3. Amazon outflow at Obidos (multiplied by 0.25 following Dai et al., 2009 to represent the outflow at the Amazon mouth) and total freshwater transport (sum of the eastward and northwestward transport) low-passed filtered with a 1-year moving average.

D

Article: Argo floats profiling in the Amazon river plume

Argo floats profiling in the Amazon river plume

Gilles Reverdin[1], Léa Olivier[1], Cécile Cabanes[2], Jacqueline Boutin[1], Clovis Thouvenin[1], Jean-Luc Vergely[3], Nicolas Kolodziejczyk[2], Virginie Thierry[2], Dmitry Khvorostyanov[1], Julien Jouanno[4]

1: LOCEAN, SU/CNRS/IRD/MNHN, Paris, France
2 : LOPS, Univ. Brest/CNRS//IRD/IFREMER, Plouzané, France
3 : ACRI-st, France
4: LEGOS UPS/CNRS/IRD/CNES, Toulouse, France

Submitted to Journal of Applied Atmospheric and Oceanic Technology

Abstract: We investigate the loss of Argo floats profiles, that is instances of profiles which should have happened, but were not transmitted, in the western tropical Atlantic close to the Amazon plume. We find a pattern of losses which fits the seasonal cycle and the occurrence of low surface salinity investigated from a high-resolution satellite salinity product. It appears that Apex and Solo floats were not able to ascend to the surface when surface salinity is on the order of 32.5 pss-78. This results in a loss of profiles from these floats in this region on the order of 6% averaged over the year, and with a peak of 12% in July, when surface salinity (surface density) is lowest. We also find a less common cause of losses, due to aborted descents for Arvor/Provor floats (2.6% in the June to August season). Altogether, the whole set until now includes a maximum loss rate of roughly 6% in July. Because of changes in float technology, the effect was very large until 2010, with an overall decrease afterwards, but with still noticeable loss rates in 2016 and 2018. Refining further the study is hindered by the small number of floats on which one bases these statistics. There is also a suggested small impact of surface temperature through its contribution to surface density, which modifies the seasonal cycle of losses, and the possibility to explore that the climatology based on in situ data to which the average of the surface salinity product from satellite data is adjusted over the period 2010-October 2021 might itself be biased which could result in too high surface salinity in this product, in this very variable region.

1. Introduction

The Argo profiling floats have provided qualified near-real time and delayed mode information on temperature and salinity in the top 2000m of the ocean for now almost 20 years. They currently provide the core observations that are used to follow the evolution of heat and freshwater content in most of ice-free oceans and away from the shelves (Le Traon, 2013; Roemmich et al., 2019; von Shuckmann et al., 2020; Llovel, 2019). The hypothesis done is that they provide random unbiased observations in various mapped products of temperature and salinity (Roemmich and Gilson, 2009; Ishii et al., 2006; Gaillard et al., 2016, Good et al., 2013) that are routinely used to investigate ocean variability and budgets. Nonetheless, in addition to the possibility of inhomogeneous distribution related to ocean circulation horizontal divergence or surface and near-surface drifts of the floats, there have been questions raised on the propensity of the floats to fully sample the ocean freshwater/salinity, and thus of their role in constraining the freshwater budget and the ocean role in changes of the hydrological cycles. This happens, either, because of errors in the salinity measurement, either because they do not always sample close to the sea surface, or because some floats might not be able to cross very large density barriers.

The first issue has been widely documented (Wong et al., 2020. The issue is to detect sensor drifts, correct them by comparison to a reference data set, and provide unbiased absolute calibration of the salinity measurements. Much has been done on that recently, for example using correction methods by comparison with appropriate data bases (Owen and Wong, 2009; Böhme and Send, 2005; Cabanes et al., 2016), or in detecting faulty conductivity cells (Wong et al., 2020).

The second issue is related to the presence of salinity stratification near the surface, in particular in areas of strong surface fresh water input, such as from intense rainfall, river inflow or sea ice melt, which might not be properly sampled by the Argo floats. This has been discussed in the context of the interpretation and validation of surface salinity products based on data collected from band-L radiometric satellite missions (Boutin et al., 2016). Indeed, the bulk of the Argo floats measures S not up to the sea surface, but up to a level 5m below the sea surface, although this is progressively modified with many floats now measuring up to 1 or 2m from the surface. Nonetheless, in areas where the salinity stratification is large close to the sea surface, this partial lack of near-surface sampling might induce biases in surface time series, depending on how the subsurface measurements are extrapolated to the sea surface (Drucker and Riser, 2014; Anderson and Riser, 2014).

The third issue is that because of the float technology used to regulate buoyancy in presence of changing water density or because of software/energetic/set parameters constraints, the float descent and ascend is constrained to a given range of density change. This is the main issue addressed in this paper, where we will focus on the region of the Amazon plume off the South American shelves in the northwestern tropical Atlantic. Very fresh pools of surface water have long been known to spread offshore in this region with a strong seasonally changing pattern (Coles et al., 2013), peaking from May to October. Even during the expected ‘dry/salty’ season, in February, rather fresh water has been observed crossing the shelf break near 7°N that originates from the Amazon and Para river discharge on the shelf near the equator (Reverdin et al., 2021; Olivier et al., 2022a). More recently, in August-September 2021, patches of very fresh surface water have been observed spreading to the northwest on the western side of an anti-cyclonic ring near 7-10°N. Minimal surface salinity was as low as 24 on Practical Salinity Scale of 1978 (hereafter pss-78; UNESCO, 1981,1983), even after this separation from the shelf (Olivier et al., 2022b). Except in boreal winter, this fresh surface water is also usually very warm, thus has a particularly low surface density.

The question we want to address is to which extent such strong haline vertical stratification and unusual low surface density has inhibited Argo floats to cross the intense pycnocline, either while descending to their parking depth (often near 1000dbar) or when they profile upward from usually close to 2000dbar. We will also check the effect this might have on in situ data mapped surface salinity products, and whether there is any impact on the satellite-data based mapped surface salinity due to adjustments to a climatology of in situ data.

For the investigation of surface salinity (SSS) distribution, we will use a high frequency salinity product based on satellite data that should resolve structures of more than 50 km and lasting at least a couple of days. This is required as SSS is highly spatially and temporally variable in this region, so that the lowest SSS patches would not be captured in monthly mean products or low spatial resolution products.

2. Data

2.A Argo data

The Argo float profiles included in the Global Data Assembly Center (GDAC) that we have accessed in Coriolis (Brest, France) originate from different models of floats. In this region, out of a total of close to 10000 profiles, the most common are (name with float type number in first parenthesis, with percentage of the profiles following) are Apex and Alto floats (MRV) (873) (17%), Solo floats (851, 852) (20%), S2A floats (854) (30%), as well as Arvor (841) and Provor floats (838, 845) (31%). The ones deployed early in the program (roughly until 2010) tended to have a 5-m resolution near the surface, with top level near 4 db or deeper (Apex), or 5 db for Solo floats, and near 6 db for Arvor/Provor floats. More recent deployments tend to have higher (typically 1-m) resolution near the surface and end up closer to the sea surface (1-m for S2A floats and 3-m for Arvor/Provor floats). S2A floats appear in this region around 2013, and last occurrences of Solo and Apex floats were in 2016 and 2018 respectively.

All float profiles have been quality controlled in real time, and most in delayed modes, except in the last couple of years. Often (except for S2A floats), there is a high number of uppermost salinity data flagged as bad, but most commonly the flagging is applied not only at the surface, but for a large part of the profile (this is particularly the case for the ARVOR floats, with more than 10% of flagged data). When eliminating those profiles, we have even for Provor/Arvor floats less than 0.4% of profiles which have been flagged as bad only at or near the sea surface. Nonetheless, in the reported statistics, we will also alternatively include data with all quality control (QC) flags.

2.B The satellite salinity product

The SMOS SMAP High Resolution SSS maps we use were developed by the Ocean Salinity Center of Expertise for CATDS (CATDS CEC-OS) (Boutin et al., 2022). This specific version, is a regional product that uses a new methodology aiming at keeping high temporal SMOS and SMAP SSS variability in highly variable regions while filtering outliers in low variability regions.

As for the global 18-day CATDS CEC products, the high resolution (HR) products are built using a temporal interpolation, grid node per grid node. This interpolation is done simultaneously with the estimation of the across-track SSS biases [Boutin et al., 2018]. The main change with respect to the global CEC CATDS products comes from the different kernel used for the temporal smoothing.

The use of an exponential kernel for the temporal smoothing allows:

- an improvement of the spatial contrasts either on the SMOS period alone or on the SMOS + SMAP period on almost all considered regional areas.
- a better restitution of the temporal dynamics for the low SSS at the mouths of the river plumes

There is a substantial gain in the correlation indicators with the in situ data in the SMOS+SMAP period with an exponential core, as can be seen on the documentation available at https://www.catds.fr/Products/Available-products-from-CEC-OS/CEC-Locean-High-Resolution-8-regions.

This was produced for the whole period from 2010 to 2021 and combines level-2 SMOS and SMAP (after April 2015) data. The merged product has a ~50 km x 50 km spatial resolution. Instantaneous rain-effect on surface salinity was preliminary removed based on Supply et al. (2020). Although this is arguable for this application of the data, this is not a major contribution here, except maybe at times in the rainier northernmost part of the region investigated, or at its eastern edge north of the equator under the Inter-tropical Convergence zone (ITCZ).

The product is noisier before May 2015, when only SMOS data are included, resulting in less data coverage. However, even during this SMOS-only period, the random uncertainty that can reach up to 0.5 pss-78 remains small compared with the signals of a few pss-78 we want to detect. There is also some degradation of the SSS product (and larger estimated errors) due to radio-frequency interference signals, in particular from sources at Barbados that are large in 2012-2014. While the product has been able to better remove some of these signals than in earlier CEC CATDS products, this remains an issue, although not so much for detecting the very low salinity patches, as Barbados is usually a little bit off their path.

The bias correction of the product is non-local, as it uses the entire time period of 2010-2021 without separating seasons. It is based on a statistical adjustment to a multi-year quantile of the ISAS product, with quantiles varying from 50% (median) in regions of low variability to 80% in regions of high variability, as described in (Boutin et al., 2021). This adjustment and the land-sea contamination corrections derived at the same time from consistency tests applied to SSS retrieved in various geometries (Kolodziejczyk et al. 2016) implies that the absolute values are less certain close to the coasts. This is particularly true over the Amazon shelf of South America, which is strongly impacted by the Amazon plume, is poorly sampled in the climatology used by ISAS, and recently has not been sampled by many Argo floats.

An advantage of this product compared to other products such as the CCI+SSS weekly product (Boutin et al., 2021) is the higher frequencies resolved when there is enough data, as we have witnessed it close to the shelf break and in the NBC retroflexion region (Reverdin et al., 2021; Olivier et al., 2022a and 2022b). In these regions, SSS changes happen rather quickly, as currents are large, and changes in the wind modify the off-shelf transport of freshwater on time scales of a few days. However, after combining the different satellite data, the effective resolution of the product is probably close to ~50kmx50km which implies that thinner low-salinity filaments are smoothed out in this product.

The validation of this product is done by comparing it with Argo float profiles uppermost pumped salinity value (often near 5m, but more recently, there has been an increase in data closer to the surface near 1 or 2m depth), as well as some validated thermosalinograph data from ships of opportunity. The Argo floats are distributed throughout the region, except over the South American shelves where data coverage is very poor (a region where the product is thus not validated, and for which there is the same lack of data in the in situ-based products, such as ISAS (Gaillard et al., 2016) used to adjust the climatological long-term averaged SSS).

The statistical comparison to in situ data is presented in Figure 1 (upper panel). The dispersion rms variability is only overall 0.58 pss-78 for the joint SMOS-SMAP period, with part of it associated with a tendency for the occurrence of low salinity in Argo floats to correspond to higher salinities than the mapped product. This could be due to the lowest Argo salinities been in small time-space structures not reproduced by the product (see discussion section), but this could also be affected by the reference SSS field over the whole period, the regions with lowest salinities tending to be on the shelf or close to the shelf north of the equator, areas that also correspond to a low climatological salinity. This could also be affected by Argo float upper measurements being often deeper than 4-m below the surface, thus probably at a higher salinity than in the top 1cm near the surface that the satellite salinity senses (note that this would result in a bias, of the other sign as the mean differences illustrated in Figure 1), as well as by Argo floats selectively sampling less some salinity categories, for example the lowest SSS due to the profiling issue that is documented in this paper. It is not completely clear how this last issue would affect the statistics presented, but at least it would certainly modify the average median difference.

2C : APLUME36

The APLUME36 simulation was designed to investigate the Amazon plume dynamics and SSS variability in the western tropical Atlantic. The model grid covers the western tropical Atlantic at 1/36° resolution (5°S–20°N, 70°W–30°W). It provides hourly instantaneous and daily means salinity fields.
The numerical model is the oceanic component of the Nucleus for European Modeling of the Ocean program (Nemo4.2), forced at its boundaries with daily outputs from the MERCATOR global reanalysis GLORYS12, and at the surface with ERA5 hourly wind speed, atmospheric temperature and humidity, long wave, short wave radiation and precipitation. This simulation uses daily and interannual runoff from the JRA reanalysis, and includes a tidal forcing. Here, we only use the simulation for 2017.

3. Results

3.A Statistics of Argo missing profiles

A missing profile is detected when no profile is reported at the expected date of ascent and data transmission. Excluding the rare cases, when the float is at the surface and there is a data transmission issue, this might happen in two different cases:

- either the float does not succeed to surface when ascending, and the full profile is not acquired / transmitted;
- or the float does not succeed to descend, or does only an aborted short descent not reaching its parking depth, thus not providing a full profile. To get relevant statistics, we selected a wide swath of the tropical Atlantic (5°S-15°N, 30°W-80°W), but with a zoom in a more restricted region (0°N-15°N, 59°W-43°W).

1: First (most common) case with missed profiles due to no ascent (or no surface transmission)
The first case in this region is strongly related to the type of floats. In the zoomed region, Apex (846, 847), Solo (851, 852), and Alto (MRV) (873) have the highest percentage of missed ascending profiles (on the order of 6-7%), followed by S2A (854) (3.5%). On the other hand this hardly happened for Arvor and Provor floats. In the case of S2A floats, the missing profiles do not seem to be directly related with any stratification issues, but with some floats missing profiles on a regular basis, and they will not be further investigated. When grouping Apex and Solo floats together, one can plot a map of the percentage of occurrence of missing profiles, chosing a grid of 1°x1° in latitude x longitude (fig. 2a). As there is a relatively low number of profiles, these statistics are rather noisy, and only grid points with more than 10 profiles are retained. This figure indicates an area of large percentage values west of 45°W and east of 59°W, peaking in its southern part near 4°-9°N (notice that the statistics cannot be established on the shelf due to insufficient number of profiles) and with a more scattered presence of missed profiles further east in the 4°N-10°N band. The overall statistics (in the red box, Fig. 2d) indicate a strong seasonal cycle with almost no missed profiles in January-February and a peak in missed profiles, averaging between 11 and 12% in June to August. The spatial distribution is not shared equally between seasons with in January-June (mostly May-June) missing profiles mostly north of 9°N and

west of 50°W, whereas in July-December, there are still missing profiles in this region, but also between 5°N-9°N west of 42°W, and extending further east in lesser concentrations in the 4°N-10°N latitude band.

2: Second (less common) case of missed profiles due to no descent

Missing profiles due to Argo floats not being able to descend in the water column is much less common. It typically happens for floats at the end of their life, such as for some Solo floats that then stayed at the surface. There are also isolated cases for Arvor or Provor floats (altogether 2.6% of all the Arvor/Provor profiles in the June-August season with the lowest salinities) when the float could not descend much, which is often associated with very fresh surface lenses. One such case is for float 6900892, during its drift in the North Equatorial Counter Current (NECC) after a freshwater lens had separated from the North Brazil Current (NBC) retroflection in early to mid-July 2021. For this float, the float already had difficulty going down during cycle 64 (with S=32.818 pss-78 at 8m, and the need of 29 pump actions), whereas the next three profiles were aborted (cycle 65 at 12m with S=30.814 pss-78). When collocating these profiles with the salinity products, we find that at these dates (from 19/07 to 08/08 2021), the float was in freshwater advected to the east in the NECC, east of the NBC retroflection, close to the south-eastern border of the freshwater patch (Fig. 3) but with sometimes very large salinity difference between the in situ and satellite salinity product, as expected from the sharp frontal structure that is certainly smoothed by the close to 50 km resolution of the satellite product.

3.B Uncertain QC for upper level salinity data of Argo floats

We also noticed cases for Arvor/Provor floats (also, some for Solo floats) with low near surface salinity, when the upper level salinity had been flagged as bad. This flagged low surface salinity correspond to at most 0.4% of all Arvor/Provor profiles in June-August, and correspond to surface salinities less than 35 pss-78. This is thus a much smaller percentage than the missed Arvor/Provor profiles due to aborted descent (2.6%), and thus probably a small issue alltogether. However, the origin of these flags will need to be investigated further.

3.C Statistics of low salinity distribution in the SSS product

We considered the frequency of daily salinities (alternatively density) at each grid point below set thresholds for the period January 2010 to November 2021. We averaged those for each calendar month in the red box of fig. 2a in order to get an annual cycle of the frequency of low salinities. This is portrayed on Fig. 4 for different salinity thresholds (32, 32.5, and 33 pss-78 thresholds with a seasonal cycle rather similar as the one of missed profiles on Fig. 2d. The maximum frequency happens in June-August with largest values of Fig. 2d fitting the 32.5 pss-78 salinity threshold. Compared to Fig. 2d, the frequencies are higher in February-April and less in October-December for these salinity thresholds. This seems partially accountable by the seasonal cycle of the contribution of temperature to surface density (not taken into account), which would lower density in October-December compared to January-April, and thus making it harder for the floats to reach the surface during the latter half of the year.

The maps of frequency of salinities lower than the thresholds follow the ones of average salinity (not shown) with a strongly varying seasonal pattern (Fig. 5 for S< 32.5 pss-78). The pattern in the first part of the year (mostly May-June) contrasts with the one in the second half of the year, with north of 4°N a maximum frequency on the shelf, leaving it in a northwestward/northward direction west of 51°W, west of the Demerara Rise, and extending to 12°N/57°W. In the second part of the year, the largest frequencies north of 4°N are off the shelf near 51-54°W extending to 10°N, and mostly then turning clockwise following the northern part of the retroflection of the NBC in the NECC. There is also a less pronounced tongue of high frequency of salinity below the 32.5 pss-78 threshold extending from the retroflection towards the northwest. This freshwater path was discussed in Olivier et al. (2022b), and corresponds to Ekman transports of freshwater patches first geostrophically advected to the northwest of the NBC retroflection. This was particularly pronounced in the late summer of 2021, and is strongly variable interannually.

4. Discussion

Similarities in the seasonal cycle of frequency of missed profiles (Fig. 2d) with the ones of low salinity (fig. 4) is strongly suggestive that the missed profiles (at least the ascending ones) are largely associated with the very low density of the freshest surface waters. It is thus tempting to attribute this roughly to a threshold of surface salinity for this region that Solo, Apex or Alto floats could overcome of 32.5 pss-78. The spatial patterns of missed profiles (Fig. 2a, b) also seem to bear similarities with the ones of the frequency of salinity below a set threshold of 32.5 pss-78 (Fig. 5), but this is only indicative and less reliable, because of the small number of floats and profiles on each grid-point and thus the noisy patterns on the mapped missed profile frequency distributions. Also, the two periods over which the statistics are built are not the same for the Argo floats, which is longer than for the satellite salinity product.

Of course, temperature will also contribute to the surface stratification with respect to the deep ocean. There is not a strong variability in the off-shelf temperature of this region, with high temperatures usually associated with the lowest salinities off the shelf. However, to refine the estimate, we also considered surface density thresholds. In the average, the threshold 32.5 pss-78 is equivalent to a surface sigma of xx kg m-3, thus roughly a surface temperature of 29°C (or 29.5°C?). From the daily SSS fields and daily SST fields, we estimated daily fields of surface density, and reestimated the seasonal cycle of low density occurences (below set thresholds).

This comparison supports the hypothesis that Apex, and to a lesser extent Solo (and Alto?) floats were not capable to ascend across the large salinity/density gradients near the sea surface, when surface salinity was as low or lower than 32.5 pss-78. This is also supported by overall statistics on surface salinities obtained by the different types of Argo floats (Table 1) reported as a percentage of the profiles of that type with SSS lower than set thresholds. If we accept S2A as the norm (the number for June-August fit with the distributions in the surface satellite salinity fields), we find that all other float types have significantly less occurrences of low salinity, and for Solo and Apex float types, even if accepting all QCs. The extreme case is for Apex floats with no occurrence of salinities less than 32 pss-78, and still very small for a threshold at 33 psu. As discussed earlier there is also an issue of missed descents for Arvor/Provor floats (2.6% in June to August) in the very low salinity water, which contributes to the differences with S2A statistics in table 1, as well as the potential that some flags as (probably bad or bad) very low surface salinity data were not correctly applied (for Solo and Arvor/Provor floats). This last point affects only a small number of profiles and would have much less effect.

These different characteristics will all contribute to an under-representation of the low surface salinities in the Argo in situ data base. This will be particularly pronounced in the early period of Argo deployments, when there was a high proportion of Solo and Apex floats. S2A floats became more prominent starting in 2013, and after 2018, there is no more Solo and Apex floats. Thus, after 2018, most floats have a high vertical resolution near the surface, measure (pump-on) closer to the surface, and their surface salinities are less likely to have been flagged as not good. We can provide an estimate of what could be the bias in average monthly surface salinity associated with not sampling low salinities smaller than 32.5 pss-78 (either because profiles do not ascend in these waters or because they are flagged as probably bad), by simulating it in the daily satellite salinity fields. In this case, we obtain for the annual average (Fig. 6c) a large difference in the extended Amazon plume, which often exceeds 1 pss-78. Not surprisingly, the effect is much larger for the season June-August (not shown), where the occurrence of the freshest waters is largest (Fig. 4). This also implies that the seasonal cycle of SSS products based on Argo floats SSS (at least the Apex and Solo floats) would be biased and underestimated, in particular during the early period of the Argo float deployments. It is quite possible that the biases in these products could correspond for that period to an underestimation of the seasonal cycle of surface salinity in the plume by 20 to 30% until at least 2010. On the other hand, in the most recent years (since 2019, in particular), this underestimation of the amplitude of the seasonal cycle should be much smaller and the positive salinity bias in the Argo-based products rather small, with only the issue of some loss of profiles in no-descending Arvor floats remaining.

Because of the change in the types of Argo floats and modes of operation near the surface (Fig. 7 illustrating the rates of missed profiles each year), this will also contribute to trends in in situ surface salinity products. For example, if the transition is from full effect in 2010 at the beginning of the salinity satellite area, and 0 at the end, there would be a trend corresponding to the difference map (Fig. 6c) as pss-78 per decade. The effect will be largest in the freshest season June through August and weakest in January-March. The overall effect is likely to be a little smaller, as even in 2010, there was already a mix of float types.

Precisely, how much of that affects the ISAS fields resulting from the loss of profiles with low SSS in the Argo set is difficult to estimate, and will depend on the proportion of missed profiles, and on how much the incorporated Argo profiles modify the initial climatology that is used. This is of course compounded (in a complicated way) with the lack of Argo data above 5 m depth in the early part of the Argo program, and the way subsurface data information is extrapolated to the surface in the product (when no data are available in a profile in the upper 5-m, it is the value between 5 and 10-m which is taken as a surface value).

The ISAS fields are used to adjust the overall satellite-based product, as a grid-point based correction. In regions that are highly variable, such as the northwestern tropical Atlantic where the fresh water Amazon plume spreads, the adjustment is not done on the median, but by adjusting the 80% highest percentiles in the satellite salinity product time series to the 80th highest percentile in ISAS. Whether this percentile is affected and by how much is difficult to assess, but one can presume, because of the large seasonal cycle, that except on the shelves between the river's mouth and 5°N, this is likely to correspond to the season where profiles with SSS lower than 32.5 pss-78 are absent. Thus, this effect should not have a major effect on the salinity products. On the shelf areas, it possibly could have some effect, but there were also very few Argo profiles in this region, as Argo floats are not designed to sample in these conditions, and the satellite salinity product has other issues there due to possible land contamination.

Thus, this probably does not explain the positive bias of the product relative to Argo profiles at low salinity (Fig. 1). As commented, there could be two other sources for this bias. The first one is the potential salinity stratification above the highest measured level of the Argo floats. The second one is due to resolution of the product which is on the order of 50 km, and which in time is likely to have smoothed the data over a couple of days, due to lack of data in certain days. This would thus smooth out the freshest surface filaments and structures. When there is a good satellite coverage in a day, as is found in half the days during the joint SMAP-SMOS area (since May 2015, except for two short interruptions in the SMAP data), we found that the product is rather close to the satellite data in that day processed as in Reverdin et al (2021) and Olivier et al (2022b), which implies that the time smoothing in the product cannot be very large. A recent model study (APLUME36 simulation) is used to evaluate the impact of the satellite footprint and the time average involved in the gridded surface salinity product. For that the modelled instantaneous grid point salinities are considered as the 'real' salinity data, and they are compared with an averaged version of the simulated salinities to a spatial resolution of 60km, and temporal resolutions of 1 day, 7 days and 30 days. The comparison is sorted as a function of the 'real salinity' and presented averaged in this region (Fig. 8). In all cases, this results in a bias, where for the lowest 'real' salinity data (less than 32 pss-78), the model simulated salinity is higher with a bias that reached 1 pss-78 at 26 pss-78 for weekly data. On the other hand, notice that the bias is much smaller for a 1-day average, but it is still positive in this simulation in the 26-32 pss-78 range.

5. Conclusions

We have found clear evidence that the difficulties for some floats to either ascend or descend through the large salinity/density gradient of the Amazon River plume, has resulted in a significant loss of data in the plume areas, specifically targeting the areas with lowest surface salinity (in particular, for surface salinity smaller than 32.5 pss-78). We also noticed in the Argo data, a small percentage (less than 1% in Arvor/Provor and Solo floats) when low salinity at the surface was flagged, which is suspicious, but difficult to further investigate.

Altogether, probably half the profiles in these low salinity areas have not happened. This was particularly the case for Apex and Solo type floats, but is also present to a lesser extent (and only for descent) on Arvor/Provor floats. Thus, this effect will have been largest in the early years of the program, less since 2013, and very small after 2018. So far, we have neglected the effect of surface temperature on surface density, as it is a smaller contributor in this area to the variations of surface density. Nonetheless, there are some contrasts in eddy structure and seasonal variability in surface temperature which could slightly compound the salinity effect to contribute to profile loss. We suspect that this might contribute to the slight differences between the percentage of profile loss and the statistics of low salinity from the satellite product in spring and fall. During the fall, in particular, the higher temperatures might contribute to further profile loss, which would explain the higher profile loss rate then than in the spring, contrary to what is seen in the satellite salinity statistics. There is still some difficulties in combining the temperature and salinity products due to different time and space resolution, but preliminary attempts are promising.

One important question that needs to be addressed later is whether this selective loss of profiles in regions of low-density surface waters (and large density contrast with the deeper ocean) documented for Apex and Solo floats is happening elsewhere? Although, this is anecdotical, there seems also to be more missed profiles east of 45°W between 4°N and 10°N during July December (4-10°N). This suggests that this phenomenon might also be happening in other areas of the tropical Atlantic with low surface salinity (density). Early in the Argo program, there were also some losses of profiles from Apex floats that could not ascend to the surface in the warm surface layer of the western subtropical Pacific in summer (Steve Riser, personal comm., 2022). There were also Apex floats deployed in the Beaufort gyre that did not return to the surface (J. Morrison, pers. Comm., 2022). We can thus expect that this might have happened in various regions with low surface density, such as other low surface density river plumes, the vicinity of the ITCZ, in particular in particularly strong fresh surface waters, such as observed in the equatorial Pacific during the SPURS2 campaign, maybe also at high latitudes, in situations with extreme surface freshening from sea ice melt or other fresh surface water sources. There is a need to investigate these situations, and find how frequent the losses are. This is a first step to evaluate whether and where it impacts our monitoring of the state of the ocean, and in particular, the evolution of the freshwater content in the upper ocean layers during the Argo program era, and the validation and evaluation of surface salinity products, such as produced by ocean reanalyses or satellite-based products.

Acknowledgments:
Support by JPI-Ocean project EUREC4A-OA is strongly acknowledged, as well as additional support from CNES (the French National Centre for Space Studies) through the TOSCA SMOS-Ocean, and by CATDS. Comments by Anny Wong and Steve Riser were very much appreciated. CATDS SSS are available at the CATDS Production Data Center (CPDC), www.catds.fr. Argo data are available at the ARGO GDAC hosted by Coriolis (Brest, France; http://www.coriolis.eu.org).

References:

Anderson, J. and S. Riser, 2014. Near-surface variability of temperature and salinity in the tropical and subtropical ocean: observations from profiling floats. *Journal of Geophysical Research-Oceans*, **119**, doi:10.1002/2014JC010112.

Boutin, J., Y. Chao, W. Asher, T. Delcroix, R. Drucker, K. Drushka, N. Kolodziejczyk, T. Lee, N. Reul, G. Reverdin, J. Schanze, A. Soloviev, L. Yu, J. Anderson, L. Brucker, E. Dinnat, A. Santos-Garcia, W. Jones, C. Maes, T. Meissner, W. Tang, N. Vinogradova, and B. Ward, 2016. Satellite and In Situ Salinity: Understanding Near-Surface Stratification and Sub-footprint Variability. *Bull. Amer. Meteor. Soc.,* **97**, 1391–1407, doi: 10.1175/BAMS-D-15-00032.1.

Boutin Jacqueline, Vergely Jean-Luc, Olivier Léa, Reverdin Gilles, Perrot Xavier, Thouvenin-Masson Clovis (2022). SMOS SMAP High Resolution SSS maps in regions of high variability, generated by CATDS CEC. SEANOE. https://doi.org/10.17882/90082.

Boutin, J., Reul, N., Koehler, J., Martin, A., Catany, R., Guimbard, S., et al. (2021). Satellite-Based Sea Surface Salinity Designed for Ocean and Climate Studies. *Journal of Geophysical Research: Oceans*, *126*(11), e2021JC017676. https://doi.org/10.1029/2021JC017676.

Boutin, J., J. L. Vergely, S. Marchand, F. D'Amico, A. Hasson, N. Kolodziejczyk, N. Reul, G. Reverdin, and J. Vialard (2018), New SMOS Sea Surface Salinity with reduced systematic errors and improved variability, *Rem. Sens. Environm.*, *214*, 115-134, doi:https://doi.org/10.1016/j.rse.2018.05.022.

Coles, V. J., Brooks, M. T., Hopkins, J., Stukel, M. R., Yager, P. L., & Hood, R. R. (2013). The pathways and properties of the Amazon River Plume in the tropical North Atlantic Ocean. *Journal of Geophysical Research: Oceans*, *118*(12), 6894–6913. https://doi.org/10.1002/2013JC008981

Drucker, R. and S. Riser (2014) Validation of Aquarius sea surface salinity with Argo: analysis of error due to depth of measurement and vertical salinity stratification. *Journal of Geophysical Research-Oceans*, **119**, 4626-4637.

Gaillard, F., T. Reynaud, V. Thierry, N. Kolodziejczyk, and K. von Schuckmann, 2016. In situ-based reanalysis of the global ocean temperature and salinity with ISAS: variability of the heat content and steric height. J. Clim., 29, 1305-1323, doi:10.1175/JCLI-D-15-0028.1

Good SA, Martin MJ, Rayner NA (2013) EN4: quality-controlled ocean temperature and salinity profiles and monthly objective analyses with uncertainty estimates. J Geophys Res Ocean 118(12):6704–6716. https://doi.org/10.1002/2013JC009067

Ishii, M., M. Kimoto, K. Sakamoto, and S.I. Iwasaki, 2006: Steric sea level changes estimated from historical ocean subsurface temperature and salinity analyses. J. Oceanography, 62(2), 155-170. http://link.springer.com/article/10.1007%2Fs10872-006-0041-y

Le Traon, P.-Y., 2013. From satellite altimetry to Argo and operational oceanography: three revolutions in oceanography. *Ocean Science* , 9(5), 901-915 . https://doi.org/10.5194/os-9-901-2013.

Lyer, S., and K. Drushka, 2021. The influence of pre-existing stratification and tropical rain modes on the Mixed Layer salinity response to rainfall. J. Geophys. Res., https://doi.org/10.1029/2021JC017574.

Llovel W., S. Purkey, B. Meyssignac, A. Blazquez, N. Kolodziejczyk and J. Bamber, Global ocean freshening, ocean mass increase and global mean sea level rise over 2005-2015 , Scientific Reports 9, 17717 (2019) doi:10.1038/s41598-019-54239-2

Olivier, L., Boutin, J., Reverdin, G., Lefèvre, N., Landschützer, P., Speich, S., Karstensen, J., Ritschel, M., and R. Wanninkhof, 2022a. Impact of North Brazil Current rings on air-sea CO2 flux variability. Biogeosciences, https://doi.org/10.5194/bg-2021-269

Olivier, L., G. Reverdin, J. Boutin, R. Laxenaire, D. Iudicone, S. Pesant, Paulo Calil, J. Horstmann, D. Couet, J. M. Erta, A. Koch-Larrouy A. Bertrand, P. Rousselot, J.-L. Vergely, S. Speich, M. Araujo, 2022b. Late summer northwestward Amazon plume pathway under the action of the North Brazil Current rings. Submitted to J. Geophys. Res.

Owens, W. B., and Wong, A. P. S. (2009). An improved calibration method for the drift of the conductivity sensor on autonomous CTD profiling floats by Θ-S climatology. Deep Sea Res. Part I. 56, 450–457. doi: 10.1016/j.dsr.2008. 09.008

Reverdin, G., Olivier, L., Foltz, G.R., Speich, S., Karstensen, J., Horstmann, J., Zhang, D., Laxenaire, R., Carton, X., Branger, H., Carrasco, R., J. Boutin, 2020. Formation and evolution of a freshwater plume in the northwestern tropical Atlantic in February 2020. JGR Ocean, doi:10.1029/2020JC016981.

Roemmich, D. and J. Gilson, 2009. The 2004-2008 mean and annual cycle of temperature, salinity, and steric height in the global ocean from the Argo program. Prog. in oceanogr., 82, 81-100, doi:10.1016/j.pocean.2009.03.004

Roemmich, D., et al. (2019), On the Future of Argo: A Global, Full-Depth, Multi-Disciplinary Array, *Frontiers in Marine Science*, *6*, doi:ARTN 439, 10.3389/fmars.2019.00439.

UNESCO, 1981: The Practical Salinity Scale 1978 and the International Equation of State of Seawater 1980. UNESCO technical papers in marine science 36, 25pp.

UNESCO, 1983: Algorithms for computation of fundamental properties of seawater. UNESCO technical papers in marine science 44, 53pp.

Supply, A., J. Boutin, G. Reverdin, J.-L. Vergely, and H. Bellenger (2020a), Variability of Satellite Sea Surface Salinity Under Rainfall, in *Satellite Precipitation Measurement: Volume 2*, edited by V. Levizzani, C. Kidd, D. B. Kirschbaum, C. D. Kummerow, K. Nakamura and F. J. Turk, pp. 1155-1176, Springer International Publishing, Cham, doi:10.1007/978-3-030-35798-6_34.

Von Shuckmann et al., 2020. Copernicus Marine Service Ocean State Report, Issue 4 . *J. Oper. Oceanogr.* , 13(sup1), S1-S172 . Publisher's official version : https://doi.org/10.1080/1755876X.2020.1785097.

Wong, A., et al., 2020. Argo Data 1999–2019: Two Million Temperature-Salinity Profiles and Subsurface Velocity Observations from a Global Array of Profiling Floats. Frontiers in Mar. Sci., 7, Sep. 2020, doi: 10.3389/fmars.2020.00700.

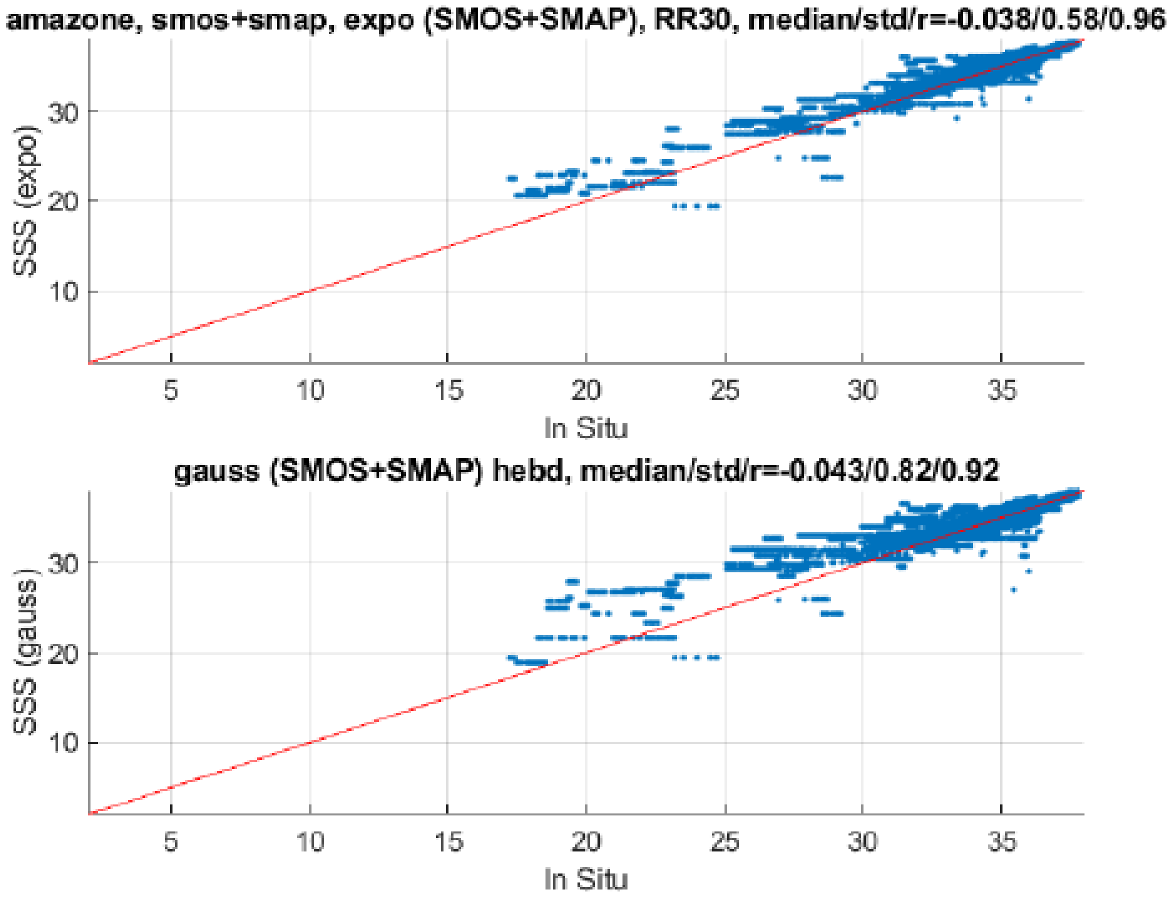

Figure 1. Validation of high time resolution CATDS regional product during the SMOS+SMAP (April 2015-November 2021) period (upper panel with exponential Kernel as used here; lower panel with Guassian panel). A comparison is shown with all the individual collocated data from the Pi-MEP validated database, which includes all Argo floats uppermost pumped data with QC-code less than 2, except for grey-listed floats, as well as data from quality-controlled thermosalinographs (ships on a line from French Guyana to Europe from SNO SSS delayed-mode data base).

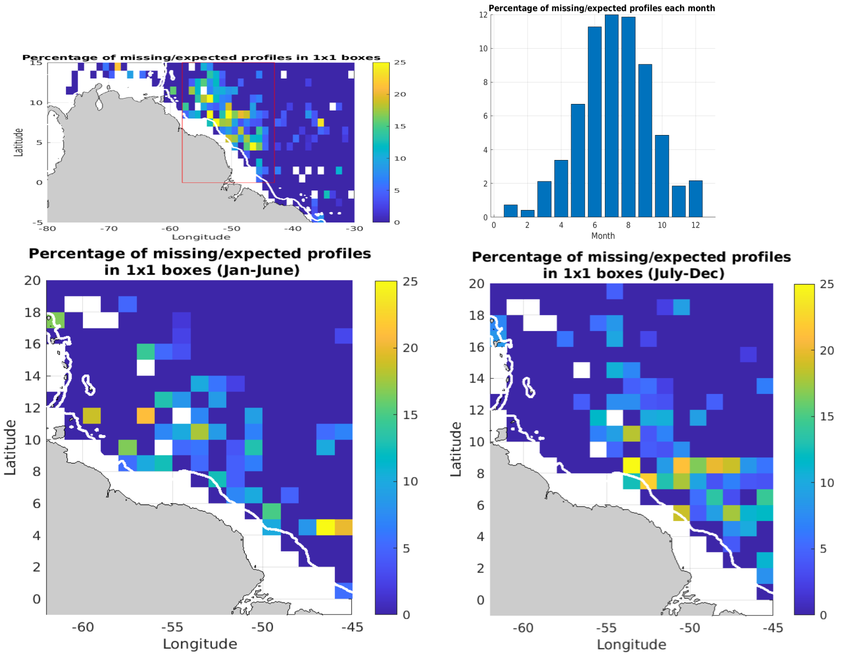

Figure 2: Percentage of missing profiles for Solo and Apex floats. Top left (panel a) present the annual average distribution in 1°*1° boxes, whereas panel b presents the seasonal cycle of the proportion of missing profiles in the red box of panel a. The lower panels present the maps for two six-month seasons.

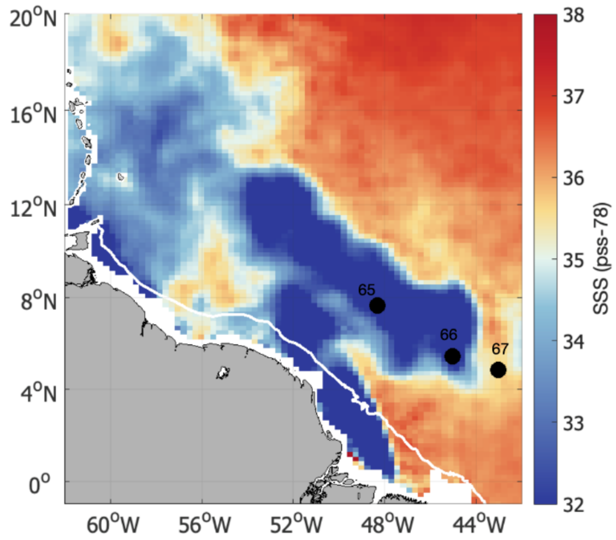

Figure 3: Salinity map (satellite product) on July 29 2021. This corresponds to profile 66 of Arvor float 6900692 (SSS=30.814, SST=29.043) with colocalized satellite salinity of 29.57 pss-78 (cycles 65 on 19/07 and 67 on 08/08 were also affected by the fresh surface water).

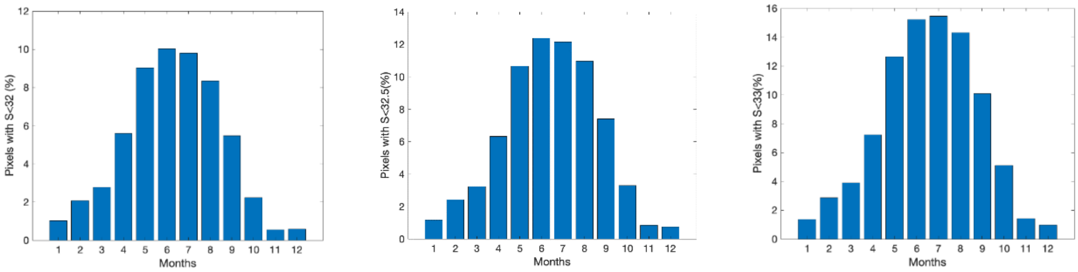

Fig. 4. Frequency of daily gridded salinities less than a salinity threshold in the red box of Fig. 2a (a for S< 32 pss-78; b for S <32.5 pss-78; c for S < 33 pss-78)

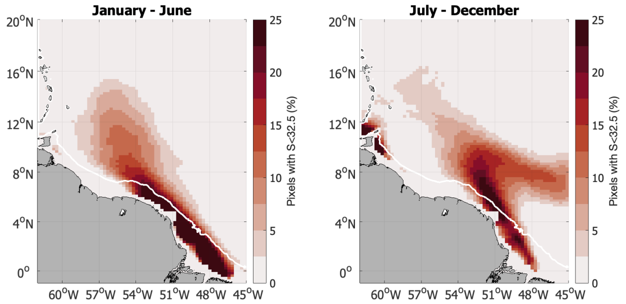

Figure 5: Maps of distribution of frequency of salinity in the daily satellite salinity product below the salinity threshold 32.5 pss-78 (left: for January-June; right for July-December)

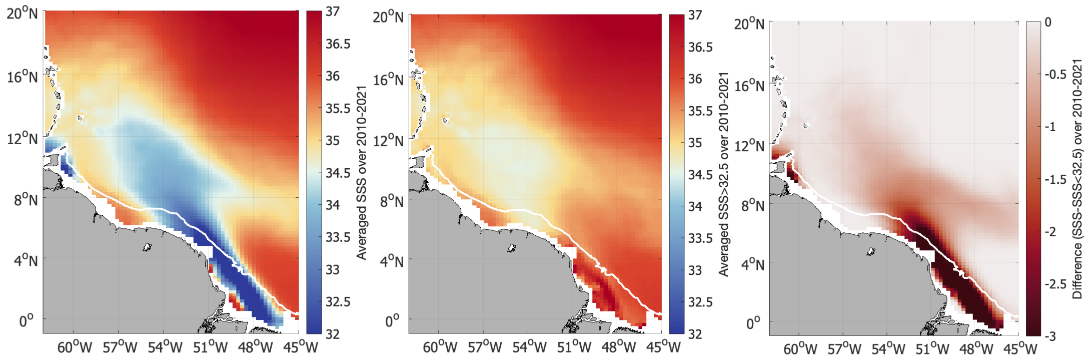

Figure 6: Jan 2010-Nov 2021 salinity of the satellite products. (a) average salinity; 6b, average salinity, but including only salinities over the threshold 32.5 pss-78. C) difference between the two (b-a).

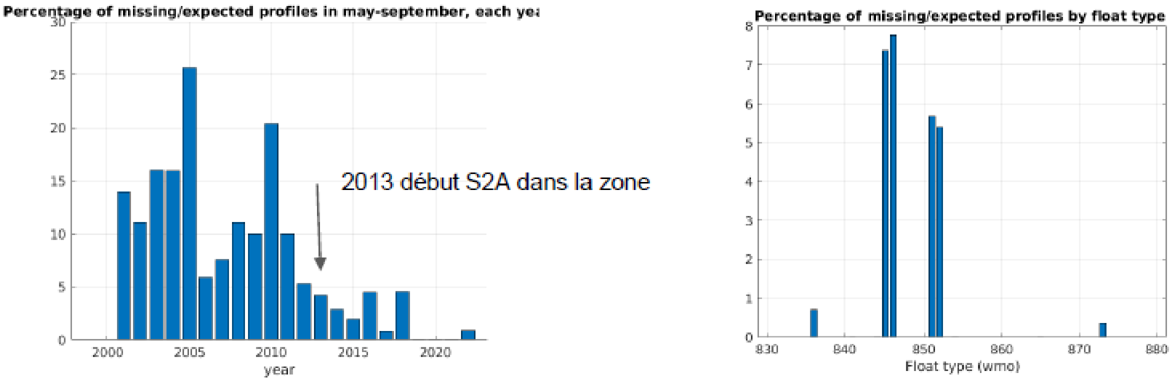

Figure 7: Time distribution of missing ascending profiles due to stratification during May-September, and percentage for each float type for the whole year (red box of figure 2). 2016 and 2018 were the last years with Apex and Solo floats (on the right side: 845-846 for Apex floats and 851-852 for Solo floats)

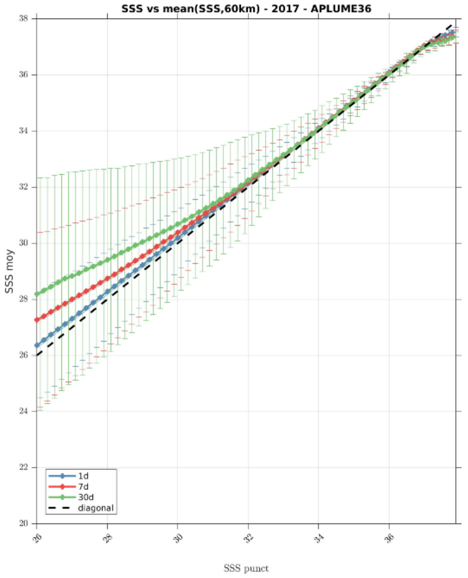

Figure 8: Comparison of measured salinity at satellite-product resolution versus grid-point salinity in the APLUME36 model simulation in 2017 in the whole western Atlantic domain (5°S–20°N, 70°W–30°W). The satellite-product resolution was simulated by averaging model salinity over a 60km radius and over 1 day (blue), 7 days (red) and 30 days (green). The different satellite-product resolution data were sorted as a function by grid-point model salinities by 0.1 pss-78 salinity class; the vertical bars correspond to the standard deviation of the averaged salinities within these point salinity ranges.

	S2A		ARVOR		APEX		SOLO	
	qc <=2	all qc	qc <=2	all qc	qc <=2	all qc	qc <=2	all qc
S<30	1.8	1.8	0.3	1.3	0	0	0.7	2.7
S<31	4.1	4.1	1.1	2.7	0	0	0.7	2.9
S<32	7.9	7.9	4.1	6.8	0	0	1.8	4.2
S<33	15.3	15.5	11.8	18.1	1.2	3.1	5.6	10.3
S<34	25.2	25.4	20.0	29.1	3.0	6.0	10.1	16.1
S<35	34.3	34.5	29.4	40.8	13.3	17.0	19.5	27.5

Ancienne version avec tous les flags. Dessous, nouvelle version où on élimine du décompte tous les profils avec plus de 25% de mauvaises données.

	S2A		ARVOR /PROVOR		APEX		SOLO	
	qc <=2	all qc	qc <=2	all qc	qc <=2	all qc	qc <=2	all qc
S<30	2.2	2.2	0.6	0.7	0	0	0	0
S<31	4.6	4.6	1.5	1.6	0	0	0.2	0.2
S<32	8.4	8.4	5.3	5.4	0	0	1.8	1.8
S<33	15.2	15.3	12.3	12.4	0.7	0.7	6.0	6.3
S<34	24.6	24.7	22.1	22.5	3.3	3.3	10.4	11.2
S<35	35.0	35.0	34.7	34.9	15.7	15.7	20.1	20.2

Table 1: Frequency of uppermost salinity (pump on) less than different salinity thresholds for different types of Argo floats and averaged over the red rectangle region (Fig. 2a) in the June-August season (profiles with more than 25% of QC salinity data larger than 2 (bad or probably bad) have been removed from the count.

E

Carbon footprint

While climate change and its desastrous consequences are well known facts in climate sciences, the work toward a low carbon reasearch is still in progress. Climate scientists, including oceanographers, play a key role in identifying the risks and consquences due to the continually increasing emission of greenhouse gases. They also play a part in warning society and policy maker, through the successive IPCC report for example. However, this same community, and academia globally, is particularly carbon intensive. It raises the question: what is the responsability of the climate scientist community regarding the climate crisis? During my three years at LOCEAN, I have been extremely lucky to work with people passionated about keeping the rising temperature below 1.5 degrees. I am really proud of the measures taken to reduce the LOCEAN's carbon footprint, and the fructuous debates, discussions and actions of our laboratory.

The carbon footprint of climate research is consequent, and the first step in order to reduce it is to identify it. With this in mind, the following section presents the carbon footprint of my PhD thesis, and discusses it.

E.1 Total carbon footprint

With a total carbon footprint of 63 tCO_{2eq}, this PhD thesis is very carbon intensive. It is equivalent to 21 tCO_{2eq}, so almost 3 times the average carbon footprint of a typical french citizen. In order to reach the target fixed by the Paris Agreement, it should be divided by around 10.

My PhD is centered around coupling in situ and satellite observations to better characterize the impact of the ocean small scale. I am very attached to the fact that I collected myself almost all of the in situ data analysed in this PhD. However, oceanographic cruises are very carbon intensive and represent the almost the entirety of my carbon footprint. The second biggest source is the plane taken to join the cruises. Finally, the "life at the laboratory", including the lunch meals, the building heating and electricity, represent a very small amount of the carbon budget.

Even if the carbon footprint of my PhD is still huge, I took several measures to try to make it as small as possible while still going on cruises. I ate only vegertarian food, and attended in person events only if they were accessible by train (for example, I attended the ICOS conference in Reims and Roscoff in person,but not the Ocean Salinity Conference in New-York). The effects are small in the case of my PhD, where oceanographic cruises have such a strong weight, but still significative.

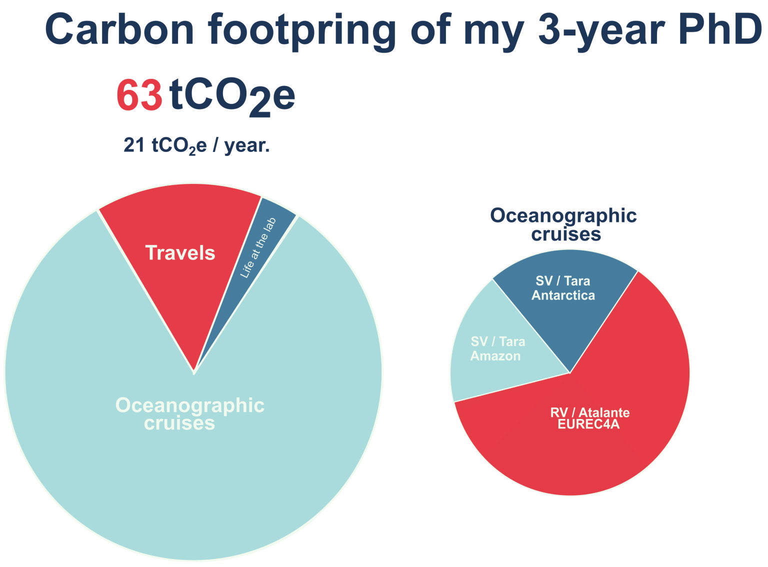

Figure E.1: Carbon budget of my PhD thesis.

The carbon footprint of oceanographic cruises is also to discuss. I have been on three cruises, one on board the research vessel Atalante and two onboard the sailing vessel *Tara*. A day onboard a large size research vessel is equivalent to 1 tCO_{2eq}, so a 30 days cruise already account for half of the carbon footprint of this PhD. The amount of fuel consummed by this type of ship is large, and even if the total carbon footprint is divided among the numerous scientists onboard (30) it stays huge.

Tara is sailing vessel with two motors and 4 to 6 scientists onboard. The ship is sailing is much possible, but depending on the objective of the cruise the motors are often necessary to reach the targeted place. I spent more than 3 months on *Tara*, in places where motors and sails were often combined, and the carbon footprint of these cruises is much smaller than the one of one month on a classic research vessel. Moreover, Tara tries to limit its impact on the ocean by having minimal food waste, composting and using organic products. Plastic waste however is still a huge problem of instumental science and in particular of marine biology and chemistry. An improvement of the mission plan to optimize the sailing time by taking advantage of the winds and currents.

E.2 Toward a low carbon research at LOCEAN

As part of the climaction group since late 2019, we have launched the relection around the carbon footprint of the LOCEAN laboratory, and the need for a low carbon research. We organising several events to educate ourself on these thematics and computed the carbon budget of the lab for 2018. We created inforgraphies based on this carbon budget to raise awareness in the laboratory about our very carbon intensive research, and in particular question the strong contribution of airplane travels (Figure ...). After months of discussion with all lab employes, we submitted to a vote three propositions aiming at reducing the lab carbon footprint :

- The principle of the laboratory's commitment to reduce GHG emissions along a trajectory compatible with the Paris Agreements (i.e. -50% by 2030)
- Favour the train: LOCEAN members will have to take the train for any outward journey of less than 5 hours by train
- Control of air travel: each LOCEAN agent will be allocated an annual carbon quota for their missions, according to the following rules

2021	2022	2023	2024	2025	2026
10 tCO_2e	8 tCO_2e	6 tCO_2e	4 tCO_2e	3 tCO_2e	2.5 tCO_2e

Bibliography

Albert, J. S., & Reis, R. (2011). *Historical Biogeography of Neotropical Freshwater Fishes* [Google-Books-ID: HbLcMtCFdtwC]. University of California Press. (Cited on page 13).

An, S.-I. (2008). Interannual Variations of the Tropical Ocean Instability Wave and ENSO [Publisher: American Meteorological Society]. *Journal of Climate*, *21*(15), 3680–3686. https://doi.org/10.1175/2008JCLI1701.1 (cited on page 18)

Andrié, C., Oudot, C., Genthon, C., & Merlivat, L. (1986). CO2 fluxes in the tropical Atlantic during FOCAL cruises [_eprint: https://agupubs.onlinelibrary.wiley.com/doi/pdf/10.1029/JC091iC10p11741]. *Journal of Geophysical Research: Oceans*, *91*(C10), 11741–11755. https://doi.org/10.1029/JC091iC10p11741 (cited on page 16)

Ardhuin, F., Brandt, P., Gaultier, L., Donlon, C., Battaglia, A., Boy, F., Casal, T., Chapron, B., Collard, F., & Cravatte, S. (2019). SKIM, a candidate satellite mission exploring global ocean currents and waves [ISBN: 2296-7745 Publisher: Frontiers Media SA]. *Frontiers in Marine Science*, *6*, 209 (cited on page 10).

Arostegui, M. C., Gaube, P., Woodworth-Jefcoats, P. A., Kobayashi, D. R., & Braun, C. D. (2022). Anticyclonic eddies aggregate pelagic predators in a subtropical gyre. *Nature*, *609*(7927), 535–540. https://doi.org/10.1038/s41586-022-05162-6 (cited on page 9)

Aroucha, L. C., Veleda, D., Lopes, F. S., Tyaquiçã, P., Lefèvre, N., & Araujo, M. (2020). Intra- and Inter-Annual Variability of North Brazil Current Rings Using Angular Momentum Eddy Detection and Tracking Algorithm: Observations From 1993 to 2016 [_eprint: https://agupubs.onlinelibrary.wiley.com/doi/pdf/10.1029/2019JC
Journal of Geophysical Research: Oceans, *125*(12), e2019JC015921. https://doi.org/10.1029/2019JC015921 (cited on page 20)
e2019JC015921 2019JC015921

Balaguru, K., Chang, P., Saravanan, R., Leung, L. R., Xu, Z., Li, M., & Hsieh, J.-S. (2012). Ocean barrier layers' effect on tropical cyclone intensification [Publisher: Proceedings of the National Academy of Sciences]. *Proceedings of the National Academy of Sciences*, *109*(36), 14343–14347. https://doi.org/10.1073/pnas.1201364109 (cited on page 15)

Bang, N. (1970). Dynamic interpretations of a detailed surface temperature chart of the agulhas current retroflexion and fragmentation area. *South African Geographical Journal*, *52*(1), 67–76 (cited on page 21).

Biber, P. D., Paerl, H. W., Gallegos, C. L., & Kenworthy, W. J. (2004). Evaluating indicators of seagrass stress to light. In *Estuarine indicators* (pp. 215–232). CRC Press. (Cited on page 14).

Bjerknes, V., Bjerknes, J., Solberg, H., & Bergeron, T. (2013). *Physikalische Hydrodynamik: Mit Anwendung auf die Dynamische Meteorologie* [Google-Books-ID: GWaXBwAAQBAJ]. Springer-Verlag. (Cited on page 5).

Boesch, D., Burreson, E., Dennison, W., Houde, E., Kemp, M., Kennedy, V., Newell, R., Paynter, K., Orth, R. J., Ulanowicz, R., et al. (2001). Factors in the decline of coastal ecosystems. *Science* (cited on page 14).

Bourlès, B., Araujo, M., Mcphaden, M. J., Brandt, P., Foltz, G. R., Lumpkin, R., Giordani, H., Hernandez, F., Lefèvre, N., Nobre, P., et al. (2019). Pirata: A sustained observing system for tropical atlantic climate research and forecasting. *Earth and Space Science*, *6*(4), 577–616 (cited on pages 16, 20).

Bracco, A., Provenzale, A., & Scheuring, I. (2000). Mesoscale vortices and the paradox of the plankton [ISBN: 0962-8452 Publisher: The Royal Society]. *Proceedings of the Royal Society of London. Series B: Biological Sciences*, *267*(1454), 1795–1800 (cited on page 10).

Braun, C. D., Gaube, P., Sinclair-Taylor, T. H., Skomal, G. B., & Thorrold, S. R. (2019). Mesoscale eddies release pelagic sharks from thermal constraints to foraging in the ocean twilight zone. *Proceedings of the National Academy of Sciences*, *116*(35), 17187–17192. https://doi.org/10.1073/pnas.1903067116 (cited on page 10)

Brown, O. B., Cornillon, P. C., Emmerson, S. R., & Carle, H. M. (1986). Gulf stream warm rings: A statistical study of their behavior. *Deep Sea Research Part A. Oceanographic Research Papers*, *33*(11-12), 1459–1473 (cited on page 22).

Busecke, J. J. M., & Abernathey, R. P. (2019). Ocean mesoscale mixing linked to climate variability [Publisher: American Association for the Advancement of Science]. *Science Advances*, *5*(1), eaav5014. https://doi.org/10.1126/sciadv.aav5014 (cited on page 9)

Caltabiano, A. C. V., Robinson, I. S., & Pezzi, L. P. (2005). Multi-year satellite observations of instability waves in the Tropical Atlantic Ocean [Publisher: European Geosciences Union]. *Ocean Science Discussions*, *2*(1), 1–35 (cited on page 18).

Chelton, D. B., deSzoeke, R. A., Schlax, M. G., Naggar, K. E., & Siwertz, N. (1998). Geographical Variability of the First Baroclinic Rossby Radius of Deformation [Publisher: American Meteorological Society Section: Journal of Physical Oceanography]. *Journal of Physical Oceanography*, *28*(3), 433–460. https://doi.org/10.1175/1520-0485(1998)028<0433:GVOTFB>2.0.CO;2 (cited on page 6)

Chelton, D. B., Esbensen, S. K., Schlax, M. G., Thum, N., Freilich, M. H., Wentz, F. J., Gentemann, C. L., McPhaden, M. J., & Schopf, P. S. (2001). Observations of Coupling between Surface Wind Stress and Sea Surface Temperature in the Eastern Tropical Pacific [Publisher: American Meteorological Society]. *Journal of Climate*, *14*(7), 1479–1498. https://doi.org/10.1175/1520-0442(2001)014<1479:OOCBSW>2.0.CO;2 (cited on pages 9, 18)

Chelton, D. B., Gaube, P., Schlax, M. G., Early, J. J., & Samelson, R. M. (2011). The Influence of Nonlinear Mesoscale Eddies on Near-Surface Oceanic Chlorophyll, *334*, 6 (cited on pages 7, 8).

Chen, C.-T. A., Huang, T.-H., Fu, Y.-H., Bai, Y., & He, X. (2012). Strong sources of CO2 in upper estuaries become sinks of CO2 in large river plumes. *Current Opinion in Environmental Sustainability*, *4*(2), 179–185. https://doi.org/10.1016/j.cosust.2012.02.003 (cited on page 13)

Chen, Y., Speich, S., & Laxenaire, R. (2022). Formation and Transport of the South Atlantic Subtropical Mode Water in Eddy-Permitting Observations [_eprint: https://onlinelibrary.wiley.com/doi/pdf/10.1029/2021JC017767]. *Journal of Geophysical Research: Oceans*, *127*(1), e2021JC017767. https://doi.org/10.1029/2021JC017767 (cited on page 9)
e2021JC017767 2021JC017767

Chiang, J. C. H., & Vimont, D. J. (2004). Analogous meridional modes of atmosphere–ocean variability in the tropical Pacific and tropical Atlantic. *J. Climate*, *17*(21), 4143–4158 (cited on page 12).

Coles, V. J., Brooks, M. T., Hopkins, J., Stukel, M. R., Yager, P. L., & Hood, R. R. (2013). The pathways and properties of the Amazon River Plume in the tropical North Atlantic Ocean [_eprint: https://agupubs.onlinelibrary.wiley.com/doi/pdf/10.1002/2013JC008981]. *Journal of Geophysical Research: Oceans*, *118*(12), 6894–6913. https://doi.org/10.1002/2013JC008981 (cited on pages 13, 14, 24)

Costanza, R., d'Arge, R., De Groot, R., Farber, S., Grasso, M., Hannon, B., Limburg, K., Naeem, S., O'neill, R. V., Paruelo, J., et al. (1997). The value of the world's ecosystem services and natural capital. *nature*, *387*(6630), 253–260 (cited on page 14).

Cotté, C., d'Ovidio, F., Dragon, A.-C., Guinet, C., & Lévy, M. (2015). Flexible preference of southern elephant seals for distinct mesoscale features within the antarctic circumpolar current. *Progress in Oceanography*, *131*, 46–58 (cited on page 9).

Cotté, C., Park, Y.-H., Guinet, C., & Bost, C.-A. (2007). Movements of foraging king penguins through marine mesoscale eddies. *Proceedings of the Royal Society B: Biological Sciences*, *274*(1624), 2385–2391 (cited on page 9).

Cox, M. D. (1980). Generation and propagation of 30-day waves in a numerical model of the Pacific [ISBN: 1520-0485]. *Journal of Physical Oceanography*, *10*(8), 1168–1186 (cited on page 19).

Cushman-Roisin, B., Tang, B., & Chassignet, E. P. (1990). Westward Motion of Mesoscale Eddies [Publisher: American Meteorological Society Section: Journal of Physical Oceanography]. *Journal of Physical Oceanography*, *20*(5), 758–768. https://doi.org/10.1175/1520-0485(1990)020<0758:WMOME>2.0.CO;2 (cited on page 7)

Dai, A., & Trenberth, K. E. (2002). Estimates of Freshwater Discharge from Continents: Latitudinal and Seasonal Variations [Publisher: American Meteorological Society Section: Journal of Hydrometeorology]. *Journal of Hydrometeorology*, *3*(6), 660–687. https://doi.org/10.1175/1525-7541(2002)003<0660:EOFDFC>2.0.CO;2 (cited on page 13)

Davey, M., Tarran, G. A., Mills, M. M., Ridame, C., Geider, R. J., & LaRoche, J. (2008). Nutrient limitation of picophytoplankton photosynthesis and growth in the tropical north atlantic. *Limnology and Oceanography*, *53*(5), 1722–1733 (cited on page 18).

de Decco, H. T., Torres Junior, A. R., Pezzi, L. P., & Landau, L. (2018). Revisiting tropical instability wave variability in the Atlantic ocean using SODA reanalysis. *Ocean Dynamics*, *68*(3), 327–345. https://doi.org/10.1007/s10236-017-1128-2 (cited on page 19)

Düing, W., Hisard, P., Katz, E., Meincke, J., Miller, L., Moroshkin, K. V., Philander, G., Ribnikov, A. A., Voigt, K., & Weisberg, R. (1975). Meanders and long waves in the equatorial Atlantic [ISBN: 0028-0836 Publisher: Springer]. *Nature*, *257*(5524), 280–284 (cited on page 17).

Duncan, C. P. (1968). An eddy in the subtropical convergence southwest of South Africa [ISBN: 0148-0227 Publisher: Wiley Online Library]. *Journal of Geophysical Research*, *73*(2), 531–534 (cited on page 6).

Edwards, C. A., & Pedlosky, J. (1998). Dynamics of nonlinear cross-equatorial flow. part i: Potential vorticity transformation. *Journal of physical oceanography*, *28*(12), 2382–2406 (cited on page 11).

Ferrari, R., & Wunsch, C. (2009). Ocean Circulation Kinetic Energy: Reservoirs, Sources, and Sinks. *Annual Review of Fluid Mechanics*, *41*(1), 253–282. https://doi.org/10.1146/annurev.fluid.40.111406.102139 (cited on page 8)

Ffield, A. (2005). North Brazil current rings viewed by TRMM Microwave Imager SST and the influence of the Amazon Plume. *Deep Sea Research Part I: Oceanographic Research Papers*, *52*(1), 137–160. https://doi.org/10.1016/j.dsr.2004.05.013 (cited on page 22)

Ffield, A. (2007). Amazon and Orinoco River Plumes and NBC Rings: Bystanders or Participants in Hurricane Events? [Publisher: American Meteorological Society Section: Journal of Climate]. *Journal of Climate*, *20*(2), 316–333. https://doi.org/10.1175/JCLI3985.1 (cited on page 15)

Fieux, M. (2019). *L'océan planétaire*. Les Presses de l'ENSTA. (Cited on page 15).

Foltz, G. R., Hummels, R., Dengler, M., Perez, R. C., & Araujo, M. (2020). Vertical turbulent cooling of the mixed layer in the atlantic itcz and trade wind regions. *Journal of Geophysical Research: Oceans*, *125*(2), e2019JC015529 (cited on page 18).

Foltz, G. R., & McPhaden, M. J. (2009). Impact of Barrier Layer Thickness on SST in the Central Tropical North Atlantic [Publisher: American Meteorological Society Section: Journal of Climate]. *Journal of Climate*, *22*(2), 285–299. https://doi.org/10.1175/2008JCLI2308.1 (cited on page 15)

Fratantoni, D. M., & Glickson, D. A. (2002). North Brazil Current Ring Generation and Evolution Observed with SeaWiFS [Publisher: American Meteorological Society]. *Journal of Physical Oceanography*, *32*(3), 1058–1074. https://doi.org/10.1175/1520-0485(2002)032<1058:NBCRGA>2.0.CO;2 (cited on pages 20, 22)

Fratantoni, D. M., & Richardson, P. L. (2006). The Evolution and Demise of North Brazil Current Rings [Publisher: American Meteorological Society Section: Journal of Physical Oceanography]. *Journal of Physical Oceanography*, *36*(7), 1241–1264. https://doi.org/10.1175/JPO2907.1 (cited on page 20)

Friedlingstein, P., O'Sullivan, M., Jones, M. W., Andrew, R. M., Hauck, J., Olsen, A., Peters, G. P., Peters, W., Pongratz, J., Sitch, S., Le Quéré, C., Canadell, J. G., Ciais, P., Jackson, R. B., Alin, S., Aragão, L. E. O. C., Arneth, A., Arora, V., Bates, N. R., . . . Zaehle, S. (2020). Global Carbon Budget 2020 [Publisher: Copernicus GmbH]. *Earth System Science Data*, *12*(4), 3269–3340. https://doi.org/10.5194/essd-12-3269-2020 (cited on pages 3, 14, 15)

Fuglister, F. C., & Worthington, L. (1951). Some results of a multiple ship survey of the gulf stream. *Tellus*, *3*(1), 1–14 (cited on page 5).

Gaube, P., Barceló, C., McGillicuddy, D. J., Domingo, A., Miller, P., Giffoni, B., Marcovaldi, N., & Swimmer, Y. (2017). The use of mesoscale eddies by juvenile loggerhead sea turtles (Caretta caretta) in the southwestern Atlantic (E. L. Hazen, Ed.). *PLOS ONE*, *12*(3), e0172839. https://doi.org/10.1371/journal.pone.0172839 (cited on page 9)

Gaube, P., J. McGillicuddy Jr., D., & Moulin, A. J. (2019). Mesoscale Eddies Modulate Mixed Layer Depth Globally [_eprint: https://onlinelibrary.wiley.com/doi/pdf/10.1029/2018GL080006]. *Geophysical Research Letters*, *46*(3), 1505–1512. https://doi.org/10.1029/2018GL080006 (cited on page 9)

Giachini Tosetto, E., Bertrand, A., Neumann-Leitão, S., & Nogueira Júnior, M. (2022). The Amazon River plume, a barrier to animal dispersal in the Western Tropical Atlantic [Number: 1 Publisher: Nature Publishing Group]. *Scientific Reports*, *12*(1), 537. https://doi.org/10.1038/s41598-021-04165-z (cited on pages 10, 13)

Gnanadesikan, A., Pradal, M.-A., & Abernathey, R. (2015). Isopycnal mixing by mesoscale eddies significantly impacts oceanic anthropogenic carbon uptake [_eprint: https://onlinelibrary.wiley.com/doi/pdf/10.1002/2015GL064

Geophysical Research Letters, *42*(11), 4249–4255. https://doi.org/10.1002/2015GL064100 (cited on page 9)

Gnanadesikan, A., Russell, A., Pradal, M.-A., & Abernathey, R. (2017). Impact of Lateral Mixing in the Ocean on El Nino in a Suite of Fully Coupled Climate Models. *Journal of Advances in Modeling Earth Systems*, *9*. https://doi.org/10.1002/2017MS000917 (cited on page 9)

Goni, G. J., & Johns, W. E. (2001). A census of North Brazil Current Rings observed from TOPEX/POSEIDON altimetry: 1992–1998 [_eprint: https://onlinelibrary.wiley.com/doi/pdf/10.1029/2000GL011717]. *Geophysical Research Letters*, *28*(1), 1–4. https://doi.org/10.1029/2000GL011717 (cited on page 20)

Gouveia, N. A., Gherardi, D. F. M., Wagner, F. H., Paes, E. T., Coles, V. J., & Aragão, L. E. O. C. (2019). The Salinity Structure of the Amazon River Plume Drives Spatiotemporal Variation of Oceanic Primary Productivity [_eprint: https://onlinelibrary.wiley.com/doi/pdf/10.1029/2018JG004665]. *Journal of Geophysical Research: Biogeosciences*, *124*(1), 147–165. https://doi.org/10.1029/2018JG004665 (cited on page 13)

Grodsky, S. A., Carton, J. A., Provost, C., Servain, J., Lorenzzetti, J. A., & McPhaden, M. J. (2005). Tropical instability waves at 0 N, 23 W in the Atlantic: A case study using Pilot Research Moored Array in the Tropical Atlantic (PIRATA) mooring data [ISBN: 0148-0227 Publisher: Wiley Online Library]. *Journal of Geophysical Research: Oceans*, *110*(C8) (cited on pages 19, 23).

Grodsky, S. A., Reul, N., Lagerloef, G., Reverdin, G., Carton, J. A., Chapron, B., Quilfen, Y., Kudryavtsev, V. N., & Kao, H.-Y. (2012). Haline hurricane wake in the Amazon/Orinoco plume: AQUARIUS/SACD and SMOS observations [_eprint: https://onlinelibrary.wiley.com/doi/pdf/10.1029/2012GL053335]. *Geophysical Research Letters*, *39*(20). https://doi.org/10.1029/2012GL053335 (cited on page 15)

Groeskamp, S., Sloyan, B. M., Zika, J. D., & McDougall, T. J. (2017). Mixing Inferred from an Ocean Climatology and Surface Fluxes [Publisher: American Meteorological Society Section: Journal of Physical Oceanography]. *Journal of Physical Oceanography*, *47*(3), 667–687. https://doi.org/10.1175/JPO-D-16-0125.1 (cited on page 9)

Hamon, B. V. (1965). The East Australian Current, 1960–1964 [Issue: 6], In *Deep sea research and oceanographic abstracts*, Elsevier. Issue: 6. (Cited on page 6).

Hashizume, H., Xie, S.-P., Liu, W. T., & Takeuchi, K. (2001). Local and remote atmospheric response to tropical instability waves: A global view from space [ISBN: 0148-0227 Publisher: Wiley Online Library]. *Journal of Geophysical Research: Atmospheres*, *106*(D10), 10173–10185 (cited on page 9).

Helland-Hansen, B., & Nansen, F. (1909). *The Norwegian Sea: Its physical oceanography based upon the Norwegian researches 1900-1904*. Det Mallingske bogtrykkeri. (Cited on page 5).

Hewitt, H. T., Roberts, M., Mathiot, P., Biastoch, A., Blockley, E., Chassignet, E. P., Fox-Kemper, B., Hyder, P., Marshall, D. P., Popova, E., Treguier, A.-M., Zanna, L., Yool, A., Yu, Y., Beadling, R., Bell, M., Kuhlbrodt, T., Arsouze, T., Bellucci, A., . . . Zhang, Q. (2020). Resolving and Parameterising the Ocean Mesoscale in Earth System Models. *Current Climate Change Reports*, *6*(4), 137–152. https://doi.org/10.1007/s40641-020-00164-w (cited on page 10)

Hobson, L. A. (1989). Paradox of the Phytoplankton—An Overview [Publisher: Taylor & Francis _eprint: https://www.tandfonline.com/doi/pdf/10.1080/01965581.1988.10749547]. *Biological Oceanography*, *6*(5-6), 493–504. https://doi.org/10.1080/01965581.1988.10749547 (cited on page 7)

Hummels, R., Dengler, M., & Bourlès, B. (2013). Seasonal and regional variability of upper ocean diapycnal heat flux in the atlantic cold tongue. *Progress in Oceanography*, *111*, 52–74 (cited on page 18).

Ibánhez, J. S. P., Araujo, M., & Lefèvre, N. (2016). The overlooked tropical oceanic CO2 sink [_eprint: https://agupubs.onlinelibrary.wiley.com/doi/pdf/10.1002/2016GL068020]. *Geophysical Research Letters*, *43*(8), 3804–3812. https://doi.org/10.1002/2016GL068020 (cited on pages 14, 17)

Ibánhez, J. S. P., Flores Montes, M., & Lefèvre, N. (2022). Evidence for enhanced primary production driving significant CO2 drawdown associated with the Atlantic ITCZ. *Science of The Total Environment*, *838*, 156592. https://doi.org/10.1016/j.scitotenv.2022.156592 (cited on page 17)

Im, S.-H., An, S.-I., Lengaigne, M., & Noh, Y. (2012). Seasonality of Tropical Instability Waves and Its Feedback to the Seasonal Cycle in the Tropical Eastern Pacific [ISSN: 2356-6140 Library Catalog: www.hindawi.com Pages: e612048 Publisher: Hindawi Volume: 2012]. https://doi.org/https://doi.org/10.1100/2012/612048. (Cited on page 18)

Iselin, C. O. (1936). A study of the circulation of the western north atlantic (cited on page 5).

Jochum, M., Cronin, M. F., Kessler, W. S., & Shea, D. (2007). Observed horizontal temperature advection by tropical instability waves [_eprint: https://agupubs.onlinelibrary.wiley.com/doi/pdf/10.1029/2007GL029416]. *Geophysical Research Letters*, *34*(9). https://doi.org/10.1029/2007GL029416 (cited on page 18)

Jochum, M., & Malanotte-Rizzoli, P. (2003). On the generation of north brazil current rings. *Journal of Marine Research*, *61*(2), 147–173 (cited on pages 11, 21).

Jochum, M., Malanotte-Rizzoli, P., & Busalacchi, A. (2004). Tropical instability waves in the Atlantic Ocean. *Ocean Modelling*, *7*(1), 145–163. https://doi.org/10.1016/S1463-5003(03)00042-8 (cited on pages 19, 20)

Jochum, M., & Murtugudde, R. (2006). Temperature Advection by Tropical Instability Waves [Publisher: American Meteorological Society]. *Journal of Physical Oceanography*, *36*(4), 592–605. https://doi.org/10.1175/JPO2870.1 (cited on page 18)

Jochumsen, K., Rhein, M., Hüttl-Kabus, S., & Böning, C. W. (2010). On the propagation and decay of North Brazil Current rings [_eprint: https://agupubs.onlinelibrary.wiley.com/doi/pdf/10.1029/2009JC006042]. *Journal of Geophysical Research: Oceans*, *115*(C10). https://doi.org/10.1029/2009JC006042 (cited on page 20)

Johns, W. E., Lee, T. N., Schott, F. A., Zantopp, R. J., & Evans, R. H. (1990). The North Brazil Current retroflection: Seasonal structure and eddy variability [_eprint: https://agupubs.onlinelibrary.wiley.com/doi/pdf/10.1029/JC095iC1 *Journal of Geophysical Research: Oceans*, *95*(C12), 22103–22120. https://doi.org/10.1029/JC095iC12p22103 (cited on pages 20, 21)

Johns, W. E., Zantopp, R. J., & Goni, G. J. (2003). Cross-gyre transport by North Brazil Current rings. In G. J. Goni & P. Malanotte-Rizzoli (Eds.), *Elsevier Oceanography Series* (pp. 411–441). Elsevier. https://doi.org/10.1016/S0422-9894(03)80156-3. (Cited on pages 20–22)

Kelly, B. G., Meyers, S. D., & O'Brien, J. J. (1995). On a generating mechanism for Yanai waves and the 25-day oscillation [_eprint: https://agupubs.onlinelibrary.wiley.com/doi/pdf/10.1029/94JC02911]. *Journal of Geophysical Research: Oceans*, *100*(C6), 10589–10612. https://doi.org/10.1029/94JC02911 (cited on page 19)

Körtzinger, A. (2003). A significant CO2 sink in the tropical Atlantic Ocean associated with the Amazon River plume [_eprint: https://agupubs.onlinelibrary.wiley.com/doi/pdf/10.1029/2003GL018841]. *Geophysical Research Letters*, *30*(24). https://doi.org/10.1029/2003GL018841 (cited on pages 14, 17)

Kouketsu, S., Tomita, H., Oka, E., Hosoda, S., Kobayashi, T., & Sato, K. (2012). The role of meso-scale eddies in mixed layer deepening and mode water formation in the western North Pacific. *Journal of Oceanography*, *68*(1), 63–77. https://doi.org/10.1007/s10872-011-0049-9 (cited on page 9)

LaCasce, J. H., & Groeskamp, S. (2020). Baroclinic Modes over Rough Bathymetry and the Surface Deformation Radius [Publisher: American Meteorological Society Section: Journal of Physical Oceanography]. *Journal of Physical Oceanography*, *50*(10), 2835–2847. https://doi.org/10.1175/JPO-D-20-0055.1 (cited on page 7)

Landschützer, P., Gruber, N., Bakker, D. C. E., & Schuster, U. (2014). Recent variability of the global ocean carbon sink [_eprint: https://agupubs.onlinelibrary.wiley.com/doi/pdf/10.1002/2014GB004853]. *Global Biogeochemical Cycles*, *28*(9), 927–949. https://doi.org/10.1002/2014GB004853 (cited on page 16)

Lee, T., Lagerloef, G., Kao, H.-Y., McPhaden, M. J., Willis, J., & Gierach, M. M. (2014). The influence of salinity on tropical Atlantic instability waves [_eprint: https://agupubs.onlinelibrary.wiley.com/doi/pdf/10.1002/2014JC010100]. *Journal of Geophysical Research: Oceans*, *119*(12), 8375–8394. https://doi.org/10.1002/2014JC010100 (cited on pages 19, 23)

Lefévre, N., Diverrés, D., & Gallois, F. (2010). Origin of CO2 undersaturation in the western tropical Atlantic [Publisher: Taylor & Francis _eprint: https://doi.org/10.1111/j.1600-0889.2010.00475.x]. *Tellus B: Chemical and Physical Meteorology*, *62*(5), 595–607. https://doi.org/10.1111/j.1600-0889.2010.00475.x (cited on pages 14, 17)

Legeckis, R. (1977). Long Waves in the Eastern Equatorial Pacific Ocean: A View from a Geostationary Satellite [Publisher: American Association for the Advancement of Science Section: Reports]. *Science*, *197*(4309), 1179–1181. https://doi.org/10.1126/science.197.4309.1179 (cited on page 18)

Legeckis, R., & Reverdin, G. (1987). Long waves in the equatorial Atlantic Ocean during 1983 [_eprint: https://agupubs.onlinelibrary.wiley.com/doi/pdf/10.1029/JC092iC03p02835]. *Journal of Geophysical Research: Oceans*, *92*(C3), 2835–2842. https://doi.org/10.1029/JC092iC03p02835 (cited on page 18)

Lévy, M., Ferrari, R., Franks, P. J. S., Martin, A. P., & Rivière, P. (2012). Bringing physics to life at the submesoscale [_eprint: https://onlinelibrary.wiley.com/doi/pdf/10.1029/2012GL052756]. *Geophysical Research Letters*, *39*(14). https://doi.org/10.1029/2012GL052756 (cited on page 9)

Lukas, R., & Lindstrom, E. (1991). The mixed layer of the western equatorial pacific ocean. *Journal of Geophysical Research: Oceans*, *96*(S01), 3343–3357 (cited on page 15).

Lumpkin, R., & Garzoli, S. L. (2005). Near-surface circulation in the Tropical Atlantic Ocean. *Deep Sea Research Part I: Oceanographic Research Papers*, *52*(3), 495–518. https://doi.org/10.1016/j.dsr.2004.09.001 (cited on pages 10–12)

Lutjeharms, J., & Gordon, A. (1987). Shedding of an agulhas ring observed at sea. *Nature*, *325*(6100), 138–140 (cited on page 21).

Maes, C., Picaut, J., & Belamari, S. (2002). Salinity barrier layer and onset of el niño in a pacific coupled model. *Geophysical Research Letters*, *29*(24), 59–1 (cited on page 15).

Maes, C., Picaut, J., & Belamari, S. (2005). Importance of the salinity barrier layer for the buildup of el niño. *Journal of Climate*, *18*(1), 104–118 (cited on page 15).

Martin, A. P. (2003). Phytoplankton patchiness: The role of lateral stirring and mixing. *Progress in Oceanography*, *57*(2), 125–174. https://doi.org/10.1016/S0079-6611(03)00085-5 (cited on pages 7, 9)

Martin, A. P., Richards, K. J., Bracco, A., & Provenzale, A. (2002). Patchy productivity in the open ocean [_eprint: https://onlinelibrary.wiley.com/doi/pdf/10.1029/2001GB001449]. *Global Biogeochemical Cycles*, *16*(2), 9–1–9–9. https://doi.org/10.1029/2001GB001449 (cited on page 7)

Martinez, E., Raapoto, H., Maes, C., & Maamaatuaihutapu, K. (2018). Influence of Tropical Instability Waves on Phytoplankton Biomass near the Marquesas Islands [Number: 4 Publisher: Multidisciplinary Digital Publishing Institute]. *Remote Sensing*, *10*(4), 640. https://doi.org/10.3390/rs10040640 (cited on page 19)

Martínez-Moreno, J., Hogg, A. M., & England, M. H. (2022). Climatology, Seasonality, and Trends of Spatially Coherent Ocean Eddies [_eprint: https://onlinelibrary.wiley.com/doi/pdf/10.1029/2021JC017453]. *Journal of Geophysical Research: Oceans*, *127*(7), e2021JC017453. https://doi.org/10.1029/2021JC017453 (cited on page 10)
e2021JC017453 2021JC017453

McCreary Jr, J. P., & Yu, Z. (1992). Equatorial dynamics in a 212-layer model [ISBN: 0079-6611 Publisher: Elsevier]. *Progress in Oceanography*, *29*(1), 61–132 (cited on page 19).

McGillicuddy, D. J. (2016). Mechanisms of Physical-Biological-Biogeochemical Interaction at the Oceanic Mesoscale. *Annual Review of Marine Science*, *8*(1), 125–159. https://doi.org/10.1146/annurev-marine-010814-015606 (cited on page 8)

McGillicuddy, D., Robinson, A., Siegel, D., Jannasch, H., Johnson, R., Dickey, T., McNeil, J., Michaels, A., & Knap, A. (1998). Influence of mesoscale eddies on new production in the sargasso sea. *Nature*, *394*(6690), 263–266 (cited on page 9).

McWilliams, J. C. (1985). Submesoscale, coherent vortices in the ocean. *Reviews of Geophysics*, *23*(2), 165–182 (cited on page 9).

McWilliams, J. C. (2008). The nature and consequences of oceanic eddies. *Ocean modeling in an eddying regime*, *177*, 5–15 (cited on page 8).

Meinen, C. S., & McPhaden, M. J. (2000). Observations of warm water volume changes in the equatorial pacific and their relationship to el niño and la niña. *Journal of Climate*, *13*(20), 3551–3559 (cited on page 15).

Mélice, J.-L., & Arnault, S. (2017). Investigation of the Intra-Annual Variability of the North Equatorial Countercurrent/North Brazil Current Eddies and of the Instability Waves of the North Tropical Atlantic Ocean Using Satellite Altimetry and Empirical Mode Decomposition [Publisher: American Meteorological Society Section: Journal of Atmospheric and Oceanic Technology]. *Journal of Atmospheric and Oceanic Technology*, *34*(10), 2295–2310. https://doi.org/10.1175/JTECH-D-17-0032.1 (cited on page 20)

Menkes, C. E., Kennan, S. C., Flament, P., Dandonneau, Y., Masson, S., Biessy, B., Marchal, E., Eldin, G., Grelet, J., Montel, Y., Morlière, A., Lebourges-Dhaussy, A., Moulin, C., Champalbert, G., & Herbland, A. (2002). A whirling ecosystem in the equatorial Atlantic [_eprint: https://agupubs.onlinelibrary.wiley.com/doi/pdf/10.1029/200 *Geophysical Research Letters*, *29*(11), 48–1–48–4. https://doi.org/10.1029/2001GL014576 (cited on pages 19, 20)

Mignot, J., Lazar, A., & Lacarra, M. (2012). On the formation of barrier layers and associated vertical temperature inversions: A focus on the northwestern tropical Atlantic [_eprint: https://agupubs.onlinelibrary.wiley.com/doi/pdf/1 *Journal of Geophysical Research: Oceans*, *117*(C2). https://doi.org/10.1029/2011JC007435 (cited on page 15)

Mignot, J., de Boyer Montégut, C., Lazar, A., & Cravatte, S. (2007). Control of salinity on the mixed layer depth in the world ocean: 2. Tropical areas [_eprint: https://onlinelibrary.wiley.com/doi/pdf/10.1029/2006JC003954]. *Journal of Geophysical Research: Oceans*, *112*(C10). https://doi.org/10.1029/2006JC003954 (cited on page 15)

Mills, M. M., Ridame, C., Davey, M., La Roche, J., & Geider, R. J. (2004). Iron and phosphorus co-limit nitrogen fixation in the eastern tropical north atlantic. *Nature*, *429*(6989), 292–294 (cited on page 18).

Molinari, R. L. (1983). Observations of near-surface currents and temperature in the central and western tropical atlantic ocean. *Journal of Geophysical Research: Oceans*, *88*(C7), 4433–4438 (cited on page 11).

Moore, C. M., Mills, M. M., Langlois, R., Milne, A., Achterberg, E. P., La Roche, J., & Geider, R. J. (2008). Relative influence of nitrogen and phosphorous availability on phytoplankton physiology and productivity in the oligotrophic sub-tropical north atlantic ocean. *Limnology and Oceanography*, *53*(1), 291–305 (cited on page 18).

Moreau, S., Penna, A. D., Llort, J., Patel, R., Langlais, C., Boyd, P. W., Matear, R. J., Phillips, H. E., Trull, T. W., Tilbrook, B., et al. (2017). Eddy-induced carbon transport across the antarctic circumpolar current. *Global Biogeochemical Cycles*, *31*(9), 1368–1386 (cited on page 9).

Moum, J. N., Lien, R.-C., Perlin, A., Nash, J. D., Gregg, M. C., & Wiles, P. J. (2009). Sea surface cooling at the Equator by subsurface mixing in tropical instability waves [Number: 11 Publisher: Nature Publishing Group]. *Nature Geoscience*, *2*(11), 761–765. https://doi.org/10.1038/ngeo657 (cited on page 18)

Moura, R. L., Amado-Filho, G. M., Moraes, F. C., Brasileiro, P. S., Salomon, P. S., Mahiques, M. M., Bastos, A. C., Almeida, M. G., Silva, J. M., Araujo, B. F., Brito, F. P., Rangel, T. P., Oliveira, B. C. V., Bahia, R. G., Paranhos, R. P., Dias, R. J. S., Siegle, E., Figueiredo, A. G., Pereira, R. C., . . . Thompson, F. L. (2016). An extensive reef system at the Amazon River mouth [Publisher: American Association for the Advancement of Science]. *Science Advances*, *2*(4), e1501252. https://doi.org/10.1126/sciadv.1501252 (cited on page 13)

Muller-Karger, F. E., McClain, C. R., & Richardson, P. L. (1988). The dispersal of the Amazon's water [Bandiera_abtest: a Cg_type: Nature Research Journals Number: 6168 Primary_atype: Research Publisher: Nature Publishing Group]. *Nature*, *333*(6168), 56–59. https://doi.org/10.1038/333056a0 (cited on page 14)

Munk, W. (2002). The evolution of physical oceanography in the last hundred years. *OCEANOGRAPHY-WASHINGTON DC-OCEANOGRAPHY SOCIETY-*, *15*(1), 135–142 (cited on pages 5, 6).

Murray, J. W., Barber, R. T., Roman, M. R., Bacon, M. P., & Feely, R. A. (1994). Physical and Biological Controls on Carbon Cycling in the Equatorial Pacific [Publisher: American Association for the Advancement of Science Section: Articles]. *Science*, *266*(5182), 58–65. https://doi.org/10.1126/science.266.5182.58 (cited on page 18)

Neumann-Leitão, S., Melo, P. A. M. C., Schwamborn, R., Diaz, X. F. G., Figueiredo, L. G. P., Silva, A. P., Campelo, R. P. S., Melo Júnior, M. d., Melo, N. F. A. C., Costa, A. E. S. F., Araújo, M., Veleda, D. R. A., Moura, R. L., & Thompson, F. (2018). Zooplankton From a Reef System Under the Influence of the Amazon River Plume. *Frontiers in Microbiology*, *9* (cited on page 13).

Nof, D. (1981). On the β-Induced Movement of Isolated Baroclinic Eddies [Publisher: American Meteorological Society Section: Journal of Physical Oceanography]. *Journal of Physical Oceanography*, *11*(12), 1662–1672. https://doi.org/10.1175/1520-0485(1981)011<1662:OTIMOI>2.0.CO;2 (cited on page 7)

Orselli, I. B., Kerr, R., de Azevedo, J. L., Galdino, F., Araujo, M., & Garcia, C. A. (2019). The sea-air CO2 net fluxes in the South Atlantic Ocean and the role played by Agulhas eddies [ISBN: 0079-6611 Publisher: Elsevier]. *Progress in Oceanography*, *170*, 40–52 (cited on page 9).

Oudot, C., Andrié, C., & Montel, Y. (1987). Evolution du co2 océanique et atmosphérique sur la période 1982–1984 dans l'atlantique tropical. *Deep Sea Research Part A. Oceanographic Research Papers*, *34*(7), 1107–1137 (cited on page 17).

Paerl, H. W. (1997). Coastal eutrophication and harmful algal blooms: Importance of atmospheric deposition and groundwater as "new" nitrogen and other nutrient sources. *Limnology and oceanography*, *42*(5part2), 1154–1165 (cited on page 14).

Paerl, H. W., & Huisman, J. (2009). Climate change: A catalyst for global expansion of harmful cyanobacterial blooms. *Environmental microbiology reports*, *1*(1), 27–37 (cited on page 14).

Peierls, B. L., Caraco, N. F., Pace, M. L., & Cole, J. J. (1991). Human influence on river nitrogen. *Nature*, *350*(6317), 386–387 (cited on page 14).

Perez, R. C., Lumpkin, R., Johns, W. E., Foltz, G. R., & Hormann, V. (2012). Interannual variations of Atlantic tropical instability waves [_eprint: https://agupubs.onlinelibrary.wiley.com/doi/pdf/10.1029/2011JC007584]. *Journal of Geophysical Research: Oceans*, *117*(C3). https://doi.org/10.1029/2011JC007584 (cited on page 18)

Philander, S. G. H. (1976). Instabilities of zonal equatorial currents [_eprint: https://agupubs.onlinelibrary.wiley.com/doi/pdf/1
Journal of Geophysical Research (1896-1977), *81*(21), 3725–3735. https://doi.org/10.1029/JC081i021p03725 (cited on page 19)

Philander, S. G. H. (1978). Instabilities of zonal equatorial currents, 2 [_eprint: https://agupubs.onlinelibrary.wiley.com/doi/pdf
Journal of Geophysical Research: Oceans, *83*(C7), 3679–3682. https://doi.org/10.1029/JC083iC07p03679 (cited on page 19)

Qiao, L., & Weisberg, R. H. (1995). Tropical instability wave kinematics: Observations from the Tropical Instability Wave Experiment [_eprint: https://agupubs.onlinelibrary.wiley.com/doi/pdf/10.1029/95JC00305]. *Journal of Geophysical Research: Oceans*, *100*(C5), 8677–8693. https://doi.org/10.1029/95JC00305 (cited on page 18)

Radenac, M.-H., Jouanno, J., Tchamabi, C. C., Awo, M., Bourlès, B., Arnault, S., & Aumont, O. (2020). Physical drivers of the nitrate seasonal variability in the Atlantic cold tongue [Publisher: Copernicus GmbH]. *Biogeosciences*, *17*(2), 529–545. https://doi.org/10.5194/bg-17-529-2020 (cited on page 18)

Reul, N., Chapron, B., Lee, T., Donlon, C., Boutin, J., & Alory, G. (2014). Sea surface salinity structure of the meandering Gulf Stream revealed by SMOS sensor [_eprint: https://onlinelibrary.wiley.com/doi/pdf/10.1002/2014GL0592
Geophysical Research Letters, *41*(9), 3141–3148. https://doi.org/10.1002/2014GL059215 (cited on page 6)

Reul, N., Fournier, S., Boutin, J., Hernandez, O., Maes, C., Chapron, B., Alory, G., Quilfen, Y., Tenerelli, J., Morisset, S., Kerr, Y., Mecklenburg, S., & Delwart, S. (2014). Sea Surface Salinity Observations from Space with the SMOS Satellite: A New Means to Monitor the Marine Branch of the Water Cycle. *Surveys in Geophysics*, *35*(3), 681–722. https://doi.org/10.1007/s10712-013-9244-0 (cited on pages 13, 15)

Reverdin, G., & McPhaden, M. J. (1986). Near-surface current and temperature variability observed in the equatorial Atlantic from drifting buoys [_eprint: https://onlinelibrary.wiley.com/doi/pdf/10.1029/JC091iC05p06569]. *Journal of Geophysical Research: Oceans*, *91*(C5), 6569–6581. https://doi.org/10.1029/JC091iC05p06569 (cited on page 11)

Richardson, P. L., & Reverdin, G. (1987). Seasonal cycle of velocity in the Atlantic North Equatorial Countercurrent as measured by surface drifters, current meters, and ship drifts [_eprint: https://onlinelibrary.wiley.com/doi/pdf/
Journal of Geophysical Research: Oceans, *92*(C4), 3691–3708. https://doi.org/10.1029/JC092iC04p03691 (cited on page 11)

Richardson, P. L., & McKee, T. (1984). Average seasonal variation of the atlantic equatorial currents from historical ship drifts. *Journal of Physical Oceanography*, *14*(7), 1226–1238 (cited on page 11).

Richardson, P. L. (1983). Eddy kinetic energy in the north atlantic from surface drifters. *Journal of Geophysical Research: Oceans*, *88*(C7), 4355–4367 (cited on page 6).

Savchenko, V., Emery, W., & Vladimirov, O. (1978). A cyclonic eddy in the antarctic circumpolar current south of australia: Results of soviet-american observations aboard the r/v professor zubov. *Journal of Physical Oceanography*, *8*(5), 825–837 (cited on page 6).

Scales, K. L., Miller, P. I., Embling, C. B., Ingram, S. N., Pirotta, E., & Votier, S. C. (2014). Mesoscale fronts as foraging habitats: Composite front mapping reveals oceanographic drivers of habitat use for a pelagic seabird. *Journal of the Royal Society Interface*, *11*(100), 20140679 (cited on page 9).

Schmitz Jr, W. J., & Richardson, P. L. (1991). On the sources of the florida current. *Deep Sea Research Part A. Oceanographic Research Papers*, *38*, S379–S409 (cited on page 22).

Seo, H., Jochum, M., Murtugudde, R., Miller, A. J., & Roads, J. O. (2007). Feedback of Tropical Instability-Wave-Induced Atmospheric Variability onto the Ocean [Publisher: American Meteorological Society]. *Journal of Climate*, *20*(23), 5842–5855. https://doi.org/10.1175/JCLI4330.1 (cited on page 18)

Servain, J., Wainer, I., McCreary Jr, J. P., & Dessier, A. (1999). Relationship between the equatorial and meridional modes of climatic variability in the tropical atlantic. *Geophysical Research Letters*, *26*(4), 485–488 (cited on page 12).

Shi, W., & Wang, M. (2021). Tropical instability wave modulation of chlorophyll-a in the Equatorial Pacific [Number: 1 Publisher: Nature Publishing Group]. *Scientific Reports*, *11*(1), 22517. https://doi.org/10.1038/s41598-021-01880-5 (cited on page 19)

Smith, W. O., & Demaster, D. J. (1996). Phytoplankton biomass and productivity in the Amazon River plume: Correlation with seasonal river discharge. *Continental Shelf Research*, *16*(3), 291–319. https://doi.org/10.1016/0278-4343(95)00007-N (cited on page 13)

Steele, J. H. (1974). Spatial Heterogeneity and Population Stability [Number: 5443 Publisher: Nature Publishing Group]. *Nature*, *248*(5443), 83–83. https://doi.org/10.1038/248083a0 (cited on page 7)

Steger, J. M., & Carton, J. A. (1991). Long waves and eddies in the tropical Atlantic Ocean: 1984–1990 [_eprint: https://agupubs.onlinelibrary.wiley.com/doi/pdf/10.1029/91JC01316]. *Journal of Geophysical Research: Oceans*, *96*(C8), 15161–15171. https://doi.org/10.1029/91JC01316 (cited on page 18)

Stommel, H. (1948). The westward intensification of wind-driven ocean currents [ISBN: 0002-8606 Publisher: Wiley Online Library]. *Eos, Transactions American Geophysical Union*, *29*(2), 202–206 (cited on page 11).

Stramma, L., & Schott, F. (1999). The mean flow field of the tropical atlantic ocean. *Deep Sea Research Part II: Topical Studies in Oceanography*, *46*(1-2), 279–303 (cited on page 12).

Strutton, P. G., Ryan, J. P., & Chavez, F. P. (2001). Enhanced chlorophyll associated with tropical instability waves in the equatorial Pacific [_eprint: https://agupubs.onlinelibrary.wiley.com/doi/pdf/10.1029/2000GL012166]. *Geophysical Research Letters*, *28*(10), 2005–2008. https://doi.org/10.1029/2000GL012166 (cited on pages 19, 20)

Subramaniam, A., Yager, P. L., Carpenter, E. J., Mahaffey, C., Björkman, K., Cooley, S., Kustka, A. B., Montoya, J. P., Sañudo-Wilhelmy, S. A., Shipe, R., & Capone, D. G. (2008). Amazon River enhances diazotrophy and carbon sequestration in the tropical North Atlantic Ocean [Publisher: National Academy of Sciences Section: Biological Sciences]. *Proceedings of the National Academy of Sciences*, *105*(30), 10460–10465. https://doi.org/10.1073/pnas.0710279105 (cited on page 13)

Swallow, J. C. (1955). A neutral-buoyancy float for measuring deep currents. *Deep Sea Research (1953)*, *3*(1), 74–81 (cited on page 5).

Takahashi, T., Sutherland, S. C., Wanninkhof, R., Sweeney, C., Feely, R. A., Chipman, D. W., Hales, B., Friederich, G., Chavez, F., Sabine, C., Watson, A., Bakker, D. C. E., Schuster, U., Metzl, N., Yoshikawa-Inoue, H., Ishii, M., Midorikawa, T., Nojiri, Y., Körtzinger, A., . . . de Baar, H. J. W. (2009). Climatological mean and decadal change in surface ocean pCO2, and net sea–air CO2 flux over the global oceans. *Deep Sea Research Part II: Topical Studies in Oceanography*, *56*(8), 554–577. https://doi.org/10.1016/j.dsr2.2008.12.009 (cited on page 16)

Tanaka, Y., & Hibiya, T. (2019). Generation Mechanism of Tropical Instability Waves in the Equatorial Pacific Ocean [Publisher: American Meteorological Society Section: Journal of Physical Oceanography]. *Journal of Physical Oceanography*, *49*(11), 2901–2915. https://doi.org/10.1175/JPO-D-19-0094.1 (cited on page 19)

Treguier, A. M., Deshayes, J., Lique, C., Dussin, R., & Molines, J. M. (2012). Eddy contributions to the meridional transport of salt in the North Atlantic [_eprint: https://onlinelibrary.wiley.com/doi/pdf/10.1029/2012JC007927]. *Journal of Geophysical Research: Oceans*, *117*(C5). https://doi.org/10.1029/2012JC007927 (cited on page 8)

Tuchen, F. P., Perez, R. C., Foltz, G. R., Brandt, P., & Lumpkin, R. (2022). Multidecadal Intensification of Atlantic Tropical Instability Waves. *Geophysical Research Letters*, *49*(22). https://doi.org/10.1029/2022GL101073 (cited on page 18)

Tzortzi, E., Josey, S., Srokosz, M., & Gommenginger, C. (2013). Tropical atlantic salinity variability: New insights from smos. *Geophysical Research Letters*, *40*(10), 2143–2147 (cited on page 13).

Uda, M. (1938). Hydrographic fluctuation in the north-eastern sea-region adjacent to Japan of north Pacific ocean.(A result of the simultaneous oceanographical investigations in 1934-1937. *Bull. Imp. Fish. Exp.*, *9*, 1–66 (cited on page 6).

Vialard, J., & Delecluse, P. (1998). An ogcm study for the toga decade. part ii: Barrier-layer formation and variability. *Journal of physical oceanography*, *28*(6), 1089–1106 (cited on page 15).

Vimont, D. J., & Kossin, J. P. (2007). The Atlantic Meridional Mode and hurricane activity [_eprint: https://onlinelibrary.wiley.com/doi/pdf/10.1029/2007GL029683]. *Geophysical Research Letters*, *34*(7). https://doi.org/10.1029/2007GL029683 (cited on page 12)

Vizy, E. K., & Cook, K. H. (2010). Influence of the amazon/orinoco plume on the summertime atlantic climate. *Journal of Geophysical Research: Atmospheres*, *115*(D21) (cited on page 15).

Vörösmarty, C. J., Fekete, B. M., Meybeck, M., & Lammers, R. B. (2000). Global system of rivers: Its role in organizing continental land mass and defining land-to-ocean linkages [_eprint: https://onlinelibrary.wiley.com/doi/pdf/1 *Global Biogeochemical Cycles*, *14*(2), 599–621. https://doi.org/10.1029/1999GB900092 (cited on page 13)

Weisberg, R. H., & Weingartner, T. J. (1988). Instability Waves in the Equatorial Atlantic Ocean [Publisher: American Meteorological Society]. *Journal of Physical Oceanography*, *18*(11), 1641–1657. https://doi.org/10.1175/1520-0485(1988)018<1641:IWITEA>2.0.CO;2 (cited on pages 18, 19)

Wilson, W. D., Johns, W. E., & Garzoli, S. L. (2002). Velocity structure of North Brazil Current rings [_eprint: https://agupubs.onlinelibrary.wiley.com/doi/pdf/10.1029/2001GL013869]. *Geophysical Research Letters*, *29*(8), 114–1–114–4. https://doi.org/10.1029/2001GL013869 (cited on page 21)

Wyrtki, K. (1975). El niño—the dynamic response of the equatorial pacific oceanto atmospheric forcing. *Journal of Physical Oceanography*, *5*(4), 572–584 (cited on page 15).

Wyrtki, K., Magaard, L., & Hager, J. (1976). Eddy energy in the oceans. *Journal of Geophysical Research*, *81*(15), 2641–2646 (cited on page 6).

Zebiak, S. E. (1993). Air–sea interaction in the equatorial Atlantic region [ISBN: 1520-0442]. *Journal of Climate*, *6*(8), 1567–1586 (cited on page 12).

Zhao, J., Bower, A., Yang, J., Lin, X., & Penny Holliday, N. (2018). Meridional heat transport variability induced by mesoscale processes in the subpolar North Atlantic [Number: 1 Publisher: Nature Publishing Group]. *Nature Communications*, *9*(1), 1124. https://doi.org/10.1038/s41467-018-03134-x (cited on page 8)

Acronyms

A
AMM Atlantic Meridional Mode. 12

B
BL Boundary Layer. 14, 15

C
CO_2 Carbon dioxide. 3
CTD Conductivity Temperature Depth. 33, 40, 41

D
DIC Dissolved Inorganic Carbon. 16, 33, 40

E
ENSO El Niño Southern Oscillation. 8, 12
EUC Equatorial UnderCurrent. 11, 18
$EUREC^4A$-OA Elucidating the Role of Cloud-Circulation Coupling in Climate Ocean-Atmosphere. 24, 31, 40

I
IPCC Intergovernmental Panel on Climate Change. 10, 17
ITCZ InterTropical Convergence Zone. 11, 12, 14, 17, 18, 20

M
MLD Mixed Layer Depth. 8, 9
MOC Meridional Overturning Circulation. 3, 8, 10, 22

N
NBC North Brazil Current. 10, 13, 21, 24
NEC North Equatorial Current. 11
NECC North Equatorial Counter Current. 11, 13, 18

R
RV Research Vessel. 31

S
SEC South Equatorial Current. 10, 18
SMOS Soil Moisture and Ocean Salinity. 20
SSS Sea Surface Salinity. 22
SST Sea Surface Temperature. 16, 20
SVP Surface Velocity Program. 34, 38, 39, 41

T
TA Total Alkalinity. 33, 40
TIWs Tropical Instability Waves. 18–20, 24
TSG Thermosalinograph. 31, 35, 36

Alphabetical Index